

DISSERTATION

APPLICATIONS OF EXTREME ULTRAVIOLET COMPACT LASERS TO
NANOPATTERNING AND HIGH RESOLUTION HOLOGRAPHIC IMAGING

Submitted by

Przemyslaw Wojciech Wachulak

Electrical and Computer Engineering Department

In partial fulfillment of the requirements

For the Degree of Doctor of Philosophy

Colorado State University

Fort Collins, Colorado

Fall 2008

UMI Number: 3346487

INFORMATION TO USERS

The quality of this reproduction is dependent upon the quality of the copy submitted. Broken or indistinct print, colored or poor quality illustrations and photographs, print bleed-through, substandard margins, and improper alignment can adversely affect reproduction.

In the unlikely event that the author did not send a complete manuscript and there are missing pages, these will be noted. Also, if unauthorized copyright material had to be removed, a note will indicate the deletion.

UMI[®]

UMI Microform 3346487

Copyright 2009 by ProQuest LLC.

All rights reserved. This microform edition is protected against unauthorized copying under Title 17, United States Code.

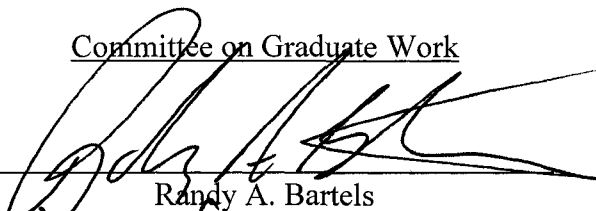
ProQuest LLC
789 E. Eisenhower Parkway
PO Box 1346
Ann Arbor, MI 48106-1346

COLORADO STATE UNIVERSITY

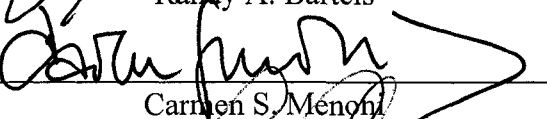
October 23, 2008

WE HEREBY RECOMMEND THAT THE DISSERTATION PREPARED UNDER OUR SUPERVISION BY PRZEMYSŁAW WOJCIECH WACHULAK ENTITLED APPLICATIONS OF EXTREME ULTRAVIOLET COMPACT LASERS TO NANOPATTERNING AND HIGH RESOLUTION HOLOGRAPHIC IMAGING BE ACCEPTED AS FULFILLING IN PART REQUIREMENTS FOR THE DEGREE OF DOCTOR OF PHILOSOPHY.

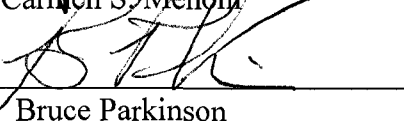
Committee on Graduate Work



Randy A. Bartels



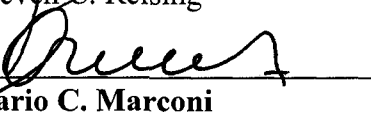
Carmen S. Menoni



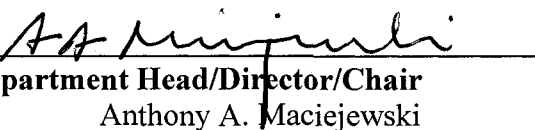
Bruce Parkinson



Steven C. Reising



Advisor **Mario C. Marconi**



Department Head/Director/Chair
Anthony A. Maciejewski

ABSTRACT OF DISSERTATION

APPLICATIONS OF EXTREME ULTRAVIOLET COMPACT LASERS TO NANOPATTERNING AND HIGH RESOLUTION HOLOGRAPHIC IMAGING

This dissertation describes two applications of extreme ultraviolet light in nanotechnology. Using radiation with a wavelength in the extreme ultraviolet (EUV) range allows to reach scales much smaller than with a conventional visible illumination.

The first part of this dissertation describes a series of experiments that allowed the patterning at nanometer scales with sub-100nm resolution. Two types of photoresists (positive tone – PMMA and negative tone – HSQ) were patterned over the areas up to a few mm² with features as small as 45nm using the interferometric lithography approach, reaching resolution equivalent to the wavelength of the illumination – 46.9nm. For the nanopatterning experiments two types of interferometers were studied in detail: Lloyd's mirror configuration and an amplitude division interferometer. Both approaches are presented and their advantages and drawbacks are discussed.

The second part of the dissertation focuses on holographic imaging with ultimate resolution approaching the wavelength of the illumination. Different experiments were performed using Gabor's in-line holographic configuration and its capabilities in the EUV region were discussed. Holographic imaging was performed with different objects:

AFM probes, spherical markers and carbon nanotubes. The holograms were stored in a high resolution recording medium – photoresist, digitized with an atomic force microscope and numerically reconstructed using a code based on the Fresnel propagator algorithm achieving in the reconstructed images the ultimate wavelength resolution. The resolution for the carbon nano-tubes images was assessed by two independent measurements: the knife-edge test resulting 45.8nm and an algorithm based on the correlation between the reconstructed image and a set of templates with variable resolution obtained by successive Gaussian filtering. This analysis yielded a resolution $\sim 46\text{nm}$. A similar algorithm that allowed for the simultaneous assessment of the resolution and the size of the features was used in EUV microscopy images confirming the validity and robustness of the code. A very fast, non-recursive reconstruction algorithm based on fast Fourier transform allowed for three dimensional surface reconstruction of the hologram performed by optical numerical sectioning, with a lateral resolution $\sim 200\text{nm}$ and depth resolution $\sim 2\mu\text{m}$.

Przemyslaw Wojciech Wachulak
Electrical and Computer Engineering Department
Colorado State University
Fort Collins, CO 80523
Fall 2008

ACKNOWLEDGEMENTS

This dissertation is a result of approximately three years of experimental work started in the middle of 2005 and finished in the middle of 2008. During my time at Colorado State University many challenging and demanding experiments were done. The work presented will not be possible without help and support from many people I had a pleasure and luck to meet and to work with and to whom I am very grateful. First of all I would like to thank to my wife Ania. She is a source of constant love, encouragement and support for me and she is my best friend. Without her my journey probably wouldn't even start. Her great patience and understanding was crucial many times in the last years. I would like to thank also to my family for their help, understanding and patience in not seeing me for such a long time.

During my graduate school I needed to switch from "eye-safe" lasers to much shorter wavelength EUV technology. My experience here, at Colorado State University was better than I could imagine. That was mostly because of my great advisor Prof. Mario Marconi. I owe him a lot. He has been a mentor and a friend to me and I am really grateful for all the help and support Mario showed me during my graduate studies. I remember many fruitful discussions we had on various topics and it was great to learn just a little bit of his vast knowledge on the subjects I have studied. Mario's great attitude let me feel like we have been "co-workers" all the time, designing new experiments, processing the data and publishing the results. His great experience and wisdom pointed me in the right direction and allowed me to explore things that interested me. As the results of our studies I have learned much more than I expected about broad range of topics in physics. Mario is one of the most supportive, generous and modest people I know and he is a world-class scientist. It was a privilege and pleasure to work with him over these years. I would like to thank also to his wife Maria-Julia for all her support for me during my time in Fort Collins.

All the holography part of my work probably wouldn't exist without the help from Prof. Randy Bartels. I remember driving to one of the meetings with Mario and Randy when we discussed about using EUV laser in high resolution holographic imaging. That was a great idea and in fact a source of many "one-day" experiments resulting great amount of excitement among all of us. Randy has been like a co-advisor to me in the holography and I really appreciate all the time we spent talking about the new possibilities, new holographic experiment. I have learnt a great deal from Randy taking his courses and from our discussions. He is a great scientist, very good and smart person (one of the smartest I know) and I still have difficulties sometimes to understand, what he is talking about. I am really grateful for the possibility to collaborate with Randy.

I would like to thank also to Prof. Carmen Menoni and Prof. Jorge Rocca for all the help and support I received from them. I remember all the meetings and discussions

about the topics we studied together in particular applying the correlation algorithm to estimate the EUV microscope image parameters and I am grateful for all their valuable input.

During my studies at Colorado State University I had a chance to meet and to work with many incredibly talented scientist, post-docs and students. Dinesh Patel taught me a lot about the equipment I was using routinely later (CAIBE, evaporator, SEM), and he was a great source of information about the fabrication methods. His help was essential in fabrication of the nano-patterns in the photoresist surface and in attempts to transfer the pattern down from the mask to the underlying substrate. I had a great pleasure to work together with Fernando Brizuela and Courtney Brewer (Carmen's and Jorge's students). They have been always helpful to me and I appreciate the time we spent together working on the analysis of the images from their EUV microscope. Erik Anderson and Weilun Chao from Center for X-ray Optics from Lawrence Berkeley National Laboratory both have invaluable knowledge about the nano-fabrication. They also provide us many times with silicon membranes, silicon-nitride samples and samples of the new photoresists to try new ideas. Yong Wang and Miguel Larotonda (Richi) both helped me with preliminary nanopatterning experiments using table-top 13.2 and 13.9nm EUV laser. Mike Grisham, Dale Martz and Scott Heinbuch showed me how to use a desk-top version of the capillary discharge laser in nanopatterning experiments using ADI interferometer and helped me many times when I had problems with this new source. I would like to thank also to Matilda Wheaton for her great attitude, help and patience with my missing receipts. I must also thank to Yun Feng Lu and Prof. Bruce Parkinson for the opportunity to use their AFM necessary for earlier nanopatterning and holography experiments. Lukasz Urbanski is a new Mario's student and I would like to thank him for all his help and support during my last year at Colorado State University and for the time we spent together on designing and performing the last experiments. I am also indebted to Bart for helping me machining all the difficult parts I needed in my setups and to Junior without whom the vacuum chamber we have built wouldn't exist. I must thank to Gustavo Anaya for helping me in nano-fabrication and building the small clean room that was essential in all the patterning work.

I would like to thank also to all the people in the lab I didn't had a chance to work as close as with the others: David Alessi, Mark Berrill, Herman Bravo, Maria Gabriela Capeluto, Sheila Davis, Jorge Filevich, Federico Furch, Patrice Genevet, Eduardo Granados, Jonathan Grava, Hugh Grinolds, Klaus Hartinger, David Hill, David Kemp, Erik Krous, Benjamin Langdon, Peter Langston, Brian Lee, Brad Luther, Omid Masihzadeh, Francesco Pedaci, Mike Purvis, Brendan Reagan, Philip Schlup, Georgiy and Tanya Vaschenko, Jesse Wilson, David Winters, Joseba Yarza, and many more I may have not intentionally omitted for making my experience at Engineering Research Center very positive and enjoyable. Thank you all so much and I wish you all luck.

Last but not least I would like to thank to National Science Foundation for their support in founding our projects through the Engineering Research Center for Extreme Ultraviolet Science and Technology at Colorado State University, where all the experiments presented in this dissertation were performed.

Dedicated to Ania

TABLE OF CONTENTS

CHAPTER 1	1
1 Introduction.....	1
1.1 Motivation for using extreme ultraviolet radiation.....	3
1.2 Overview of the patterning methods.....	6
1.2.1 Patterning	11
1.2.1.1 Writing.....	11
1.2.1.1.1 Writing with rigid stylus	11
1.2.1.1.2 Writing with Beam of Photons and other Energetic Particles	13
1.2.1.1.3 Writing using an Electric Field.....	15
1.2.1.1.4 Writing using a Magnetic Field	16
1.2.1.1.5 Writing by Add-On Process.....	18
1.2.1.2 Self-assembly.....	20
1.2.1.2.1 Phase-Separated Block Copolymers	21
1.2.1.2.2 Nanosphere Lithography.....	21
1.2.2 Replication of patterns	22
1.2.2.1 Duplication with a Mask.....	22
1.2.2.1.1 Masked exposure to photons.....	23
1.2.2.1.2 Masked etching and deposition.....	25
1.2.2.2 Replication with a master.....	26
1.2.2.2.1 Embossing using rigid master.....	27
1.2.2.2.2 Molding with elastomeric master.....	28
1.2.2.2.3 Printing using elastomeric stamp.....	29
1.2.2.2.4 Microfluidic patterning	30
1.2.2.3 Edge lithography.....	31
1.2.3 Three-Dimensional patterning	33
1.2.3.1 Writing using focused laser or electron beams	33
1.2.3.2 Gray scale lithography	34
1.3 Overview of Sources.....	35
CHAPTER 2	47
2 Capillary Discharge Laser description.....	47
2.1 Principle of operation.....	49
2.2 Laser coherence parameters	51
2.3 Summary	53
CHAPTER 3	58
3 Nanopatterning using Interference Lithography (IL)	58
3.1 Introduction.....	58
3.2 Principles of Interferometric Lithography	59
3.3 Previous work in Interference Lithography	61
3.4 Photoresist description and characteristics	65

3.4.1	PMMA photoresist.....	70
3.4.2	HSQ photoresist.....	71
3.5	Table Top Compact Nanopatterning Tool	73
3.5.1	Mirror reflectivity	78
3.6	Limitations to the patterning area due to the coherence of the source.....	83
3.7	Numerical modeling of patterning process	90
3.8	Experimental results.....	98
3.8.1	Patterning of PMMA photoresist	98
3.8.1.1	Different motifs in PMMA	99
3.8.1.2	Smallest features over large patterning area	104
3.8.2	Patterning of HSQ photoresist	106
3.8.2.1	Advantages of HSQ	106
3.8.2.2	Analysis of photosensitivity of HSQ at 46.9 nm	108
3.8.2.3	Multiple exposure IL with HSQ	110
3.9	Summary	115
CHAPTER 4	121
4	Nanopatterning using Amplitude Division Interferometer (ADI)	121
4.1	Interferometer design.....	122
4.2	Spatial and temporal coherence requirements	126
4.3	Transmission diffraction grating fabrication	132
4.4	Desk Top Capillary Discharge Laser in nanopatterning.....	134
4.5	Experimental details.....	135
4.6	Results.....	137
4.7	Influence of the OPD on the pattern quality	139
4.8	Summary	142
CHAPTER 5	145
5	Extreme Ultraviolet Holography.....	145
5.1	Introduction.....	145
5.2	Holographic recording and reconstruction.....	147
5.3	Twin image problem.....	150
5.4	Spatial resolution limitations in high numerical aperture Gabor holography.	152
5.5	Reconstruction algorithm for Gabor holography.....	156
5.5.1	Fresnel propagator	156
5.5.2	Hologram as a lens.....	159
5.5.3	Sampling considerations and the Fresnel propagator	161
5.5.4	Hologram reconstruction code.....	164
5.6	Sampling considerations during the digitization process.....	171
CHAPTER 6	177
6	High spatial resolution holography.....	177
6.1	Holographic imaging of AFM tips.....	179
6.1.1	Introduction.....	179

6.1.2	Experimental details.....	179
6.1.3	Results.....	182
6.1.4	Resolution evaluation.....	185
6.1.4.1	Wavelet analysis	186
6.1.4.2	Binary template generation.....	187
6.1.4.3	Secondary template generation	188
6.1.4.4	Correlation analysis	189
6.1.4.5	Wavelet decomposition and correlation algorithm	190
6.1.4.6	Resolution estimation results	192
6.1.4.7	The influence of the wavelet type on the algorithm results	197
6.2	Wavelength resolution holography	200
6.2.1	Introduction.....	200
6.2.2	Experimental details.....	201
6.2.3	Reconstruction results.....	205
6.2.4	Resolution limitations in wavelength resolution holography	207
6.2.5	Simultaneous estimation of resolution and feature size.....	208
6.2.5.1	Gaussian filtering process	209
6.2.5.2	Correlation methods tests.....	210
6.2.5.3	Correlation and convolution algorithm.....	215
6.2.5.4	Correlation and convolution algorithm results	219
6.3	Summary	221
CHAPTER 7		225
7	3D reconstruction by numerical sectioning	225
7.1	Introduction.....	225
7.2	Experimental details.....	225
7.3	Results.....	228
7.4	Retrieving 3-D information from a single high NA hologram	231
7.5	Surface reconstruction	233
7.6	Summary	236
CHAPTER 8		239
8	Gaussian filtering and correlation analysis in EUV microscopy	239
8.1	Introduction.....	239
8.2	Microscopy of nano-scale periodic patterns at $\lambda=13.2$ nm.....	241
8.3	Algorithm for the simultaneous determination of feature size and resolution	243
8.3.1	Relation to the incoherent Rayleigh criterion	245
8.4	Algorithm results	247
8.5	Summary	249
SUMMARY		252
9	Summary and final thoughts	252
APPENDICES		255

10.1	Appendix I: Reflectivity calculations for the Cr mirror for compact nanopatterning tool using atomic scattering factors	255
10.2	Appendix II: Description of the design of the Gaussian filters and their relation to the image resolution.....	267
10.3	Appendix III: Codes and algorithms used in EUV holography experiments .	270
10.3.1	Reconstruction algorithm for the Gabor holography	271
10.3.2	Wavelet decomposition and correlation algorithm for resolution estimation	277
10.3.3	Three dimensional numerical holographic reconstruction from a single high numerical aperture hologram	280
10.3.4	Carbon nano-tubes holography, resolution and feature size estimation based on Gaussian filtering and correlation code	297
10.4	Appendix IV: Transmission diffraction grating analysis of the diffraction efficiency.....	311

LIST OF PUBLICATIONS ASSOCIATED WITH DISSERTATION:

TECHNICAL PUBLICATIONS in REFEREED JOURNAL:

1. “Soft x-ray laser holography with wavelength resolution“, P. W. Wachulak, M.C. Marconi, R. A. Bartels, C. S. Menoni, J.J. Rocca”, *J. Opt. Soc. Am. B*, **25**, 11, 1811 (2008)
2. “Nanopatterning in a compact setup using table top extreme ultraviolet lasers”, P. W. Wachulak, M.G. Capeluto , C. S. Menoni, J. J. Rocca, M. C. Marconi, *Opto-Electronics Review* **16** (4), 444–450, (2008)
3. “Interferometric lithography with an amplitude division interferometer and a desktop extreme ultraviolet laser”. P. Wachulak, M. Grisham, D. Martz, S. Heinbuch, W. Rockward, D. Hill, J. Rocca, C.S. Menoni, E. Anderson, M.C. Marconi. *JOSA B* **25**, B104, (2008), *this article was also published in The Virtual Journal for Biomedical Optics*, **3**, 8, (2008)
4. “Analysis of extreme ultraviolet microscopy images of patterned nanostructures based on a correlation method”. P.W. Wachulak, C.A. Brewer, F. Brizuela, W. Chao, E. Anderson, R. A. Bartels, C.S. Menoni, J.J. Rocca, M.C. Marconi. *Journal of the Optical Society of America B*, **25**, B20, (2008), *this article was also published in The Virtual Journal for Biomedical Optics*, **3**, 8, (2008)
5. “Nanoscale patterning in high resolution HSQ photoresist by interferometric lithography with table top EUV lasers”. P. W. Wachulak, M.G. Capeluto, M. C. Marconi, D. Patel, C. S. Menoni, J.J. Rocca. *Journal of Vacuum Science and Technology B* **25** (6), 2094, (2007), *this article was also published in Virtual Journal of Nanoscale Science & Technology*, December **24**, 16, 26 (2007)
6. “Volume extreme ultraviolet holographic imaging with numerical optical sectioning”. P. W. Wachulak, M.C. Marconi, R. A. Bartels, C. S. Menoni, J.J. Rocca. *Optics Express* **15**, 10622-10628, (2007).
7. “Patterning of nano-scale arrays by table top extreme ultraviolet laser interferometric lithography”. P.W. Wachulak, M.G. Capeluto, M.C. Marconi, C.S. Menoni, J.J. Rocca. *Optics Express*, **15**, 3465, (2007).
8. “Table Top Nanopatterning with Extreme Ultraviolet laser Illumination”. M.G. Capeluto, P. Wachulak, M.C. Marconi , D. Patel, C.S. Menoni, J.J. Rocca, C. Iemmi, E.H. Anderson, W. Chao, D.T. Attwood. *Microelectronics Engineering*, **84**, 721–724, (2007)
9. “Sub 400 nm spatial resolution extreme ultraviolet holography with a table top laser”. P. W. Wachulak, R. A. Bartels, M. C. Marconi, C. S. Menoni, J.J. Rocca, Y. Lu, B. Parkinson. *Optics Express* **14**, 9636 (2006).

SCIENCE NEWS ARTICLES:

10. "Numerical Optical Sectioning for 3D Holographic Images with EUV Lasers".
P.W. Wachulak, M.C. Marconi, R.A Bartels, C. S. Menoni and J.J. Rocca. Optics and Photonics News. special issue "Optics in 2007" **18**, 12, 22 (2007)

CONFERENCE PROCEEDINGS:

11. P.W. Wachulak, D. Patel, M.G. Capeluto, C.S. Menoni, J.J. Rocca, M.C. Marconi. "Interferometric lithography with sub 100 nm resolution using a table top 46.9 nm laser". SPIE Conference on Soft X-Ray Lasers and Applications VII, SPIE, Vol.6702, (2007).
12. P.W. Wachulak, R.A. Bartels, C.S. Menoni, J.J. Rocca, M.C. Marconi. "Table top soft X-ray holography with sub 200 nm spatial resolution." SPIE Conference on Soft X-Ray Lasers and Applications VII, SPIE, Vol.6702, (2007)
13. M.C. Marconi , M.G. Capeluto, P. Wachulak, G. Vaschenko, H. Bravo, C.S. Menoni, J.J. Rocca , E.H. Anderson, W. Chao, D.T. Attwood, O. Hemberg, B. Frazer, and S. Bloom. "Nanopatterning and nanomachining with table-top extreme ultraviolet lasers". Proceedings Material Research Society Fall Meeting 2006.
14. M.C. Marconi, P. Wachulak, C.S. Menoni, M.G. Capeluto, E. Anderson "Development of a table top nanopatterning tool with Extreme Ultraviolet Lasers". Proceedings of the 2006 NSF Design, Service and Manufacturing G&R Conference.
15. P.W. Wachulak, M. C. Marconi, R. Bartels, C. S. Menoni, J.J. Rocca. "Soft X ray holographic imaging with sub-micron resolution". "X-Ray Lasers 2006". Springer Proceedings in Physics Volume 115. Pag 483-490. P.V. Nickles and K.A. Janulewicz Eds.
16. M. G. Capeluto, P. Wachulak , M.C. Marconi , C.S. Menoni, J.J. Rocca, E.H. Anderson, W. Chao, D.T. Attwood. "Table top nanopatterning using Soft X-Ray lasers". "X-Ray Lasers 2006". Springer Proceedings in Physics Volume 115. Pag 491-496. P.V. Nickles and K.A. Janulewicz Eds.

CONFERENCE ABSTRACTS:

1. F, Brizuela, P. W. Wachulak, C.A. Brewer, C.S. Menoni, W. Chao, E.H. Anderson, R.A. Bartels, J.J. Rocca, M.C. Marconi. "Simultaneous Determination by Correlation of feature size and Spatial Resolution in EUV Images of Patterned Nanostructures". 9th International Conference on X-Ray Microscopy. Zurich, July 21-25 2008.
2. P.W. Wachulak , M.C. Marconi, R. Bartels, C.S. Menoni, J.J. Rocca. "Soft X ray

- Holography with wavelength resolution". 11th International Conference on X-Ray Lasers, Belfast, August 18-22 2008.
3. P.W. Wachulak, M.C. Marconi, W. Rockward, D. Hill, E.H. Anderson, C.S. Menoni, J.J. Rocca. "Interferometric Lithography with a Desk-top size Soft X ray laser". 11th International Conference on X-Ray Lasers, Belfast, August 18-22 2008.
 4. M.C. Marconi, P.W. Wachulak, C. Brewer, F. Brizuela, R. Bartels, C.S. Menoni, J.J. Rocca, E. Anderson, Weilun Chao. "Resolution and Feature Size Assessment in Soft X ray Microscopy Images". 11th International Conference on X-Ray Lasers, Belfast, August 18-22 2008.
 5. P.W. Wachulak, M.C. Marconi, R. Bartels, C.S. Menoni, J.J. Rocca. "Soft X ray Holography with wavelength resolution". 11th International Conference on X-Ray Lasers, Belfast, August 18-22 2008.
 6. M.G. Capeluto, P.W. Wachulak, M.C. Marconi, D. Patel, C.S. Menoni, J.J. Rocca, C. Iemmi, E.H. Anderson, W. Chao, D.T. Attwood. "Table top nanopatterning with compact EUV lasers". 10th International Conference on Near Field Optics and Related Techniques. Buenos Aires. September 1-5 2008.
 7. M.C. Marconi, P.W. Wachulak, C. Brewer, F. Brizuela, R. Bartels, C.S. Menoni, J.J. Rocca, E. Anderson, Weilun Chao. "Analysis of Resolution and Feature Size in Extreme Ultraviolet Microscopy Images". Conference on Lasers and Electro Optics CLEO 08. San Jose, CA. May 4-9, 2008.
 8. P.W. Wachulak, M.C. Marconi, W. Rockward, D. Hill, E.H. Anderson, C.S. Menoni, J.J. Rocca. "Extreme Ultraviolet Interferometric Lithography with a Desk-top system". Conference on Lasers and Electro Optics CLEO 08. San Jose, CA. May 4-9, 2008.
 9. P.W. Wachulak, M.C. Marconi, R. Bartels, C.S. Menoni, J.J. Rocca. "Extreme Ultraviolet Holography with wavelength resolution". Conference on Lasers and Electro Optics CLEO 08. San Jose, CA. May 4-9, 2008.
 10. M.C. Marconi, P.W. Wachulak, W. Rockward, D. Hill, E. Anderson, C.S. Menoni, J.J. Rocca. "Ultra compact interferometric lithography system realized with a desk-top extreme ultraviolet laser". International Conference on Electron, Ion and Photon Beam Technology and Nanofabrication. Portland, May 26-May 31 2008.
 11. F. Brizuela, P.W. Wachulak, C.A. Brewer, C. S. Menoni, W. Chao, E.H. Anderson, R.A. Bartels, J.J. Rocca, M.C. Marconi. "Simultaneous determination by correlation of feature size and spatial resolution in EUV images of patterned nanostructures." 9th International Conference on X-Ray Microscopy - XRM2008, Zürich, Switzerland, July 21 - 25, 2008
 12. M.C. Marconi, P. W. Wachulak, M.G. Capeluto, D. Patel, C. S. Menoni, J.J.

- Rocca “Fabrication of arrays of pillars and holes sub 100 nm size using a table top Soft X-ray laser”. Ultrafast Optics 2007, High fields Short Wavelength 2007. Santa Fe, NM, September 2-7 2007.
13. M.C. Marconi, P. W. Wachulak, R. A. Bartels, C. S. Menoni, J.J. Rocca. “Nanoholography with table top soft X-ray lasers”. Ultrafast Optics 2007, High fields Short Wavelength 2007. Santa Fe, NM, September 2-7 2007.
 14. M. C. Marconi, P. W. Wachulak, R. A. Bartels, C. S. Menoni, J.J. Rocca. “Holographic nano-imaging realized with compact extreme ultraviolet lasers”. LEOS 2007 Annual Conference. Lake Buena Vista, Florida, October 21- 25 2007.
 15. M.C. Marconi, P. W. Wachulak, M.G. Capeluto, D. Patel, C. S. Menoni, J.J. Rocca. “Nanopillars and arrays of nanoholes fabricated by extreme ultraviolet interferometric laser lithography”. LEOS 2007 Annual Conference. Lake Buena Vista, Florida, October 21- 25 2007.
 16. M.C. Marconi, P. Wachulak, D. Patel, M.G. Capeluto, C.S. Menoni, J.J..Rocca, “Interferometric lithography with sub-100-nm resolution using a tabletop 46.9-nm laser”. Soft X-Ray Lasers and Applications VII, San Diego, 29 - 30 August 2007.
 17. P. Wachulak, M.C. Marconi, R.A. Bartels, C.S. Menoni, J.J. Rocca, “Tabletop EUV holography with sub-200-nm spatial resolution”. Soft X-Ray Lasers and Applications VII, San Diego, 29 -30 August 2007.
 18. P. Wachulak, M.G. Capeluto, M.C. Marconi, C.S. Menoni, J.J. Rocca. “Table top Patterning of Arrays of nano-dots with extreme ultraviolet laser interferometric lithography”. International Conference on Electron, Ion and Photon Beam Technology and Nanofabrication. Denver, May 29-June 1st 2007.
 19. M.G. Capeluto, P. Wachulak, M.C. Marconi, D. Patel, C.S. Menoni, J.J. Rocca, C. Iemmi, E.H. Anderson, W. Chao, D.T. Attwood. “Printing arrays of nano-holes with EUV Compact lasers”. 4th Latin-American Symposium on Scanning Probe Microscopy IV LASPM May 2-4 2007. Mar del Plata. Argentina
 20. P.W. Wachulak, R.A. Bartels, M.C. Marconi, C.S. Menoni, J.J. Rocca. “Table Top Extreme Ultraviolet Holography”. Conference on Lasers and Electro optics CLEO 07. Baltimore, May 7-11 2007.
 21. P.W. Wachulak, M.G. Capeluto, M.C. Marconi, C.S. Menoni, J.J. Rocca. “Arrays of Sub-100 nm Features Fabricated with Table Top Extreme Ultraviolet Interferometric Laser Lithography”. Conference on Lasers and Electro optics CLEO 07. Baltimore, May 7-11 2007.
 22. P. Wachulak, M.C. Marconi, R. Bartels, C.S. Menoni, J.J. Rocca. “Table Top Extreme Ultraviolet Holography. Present and future capabilities”. APS March Meeting. Denver, CO, March 5-9 2007
 23. M.C. Marconi, P. Wachulak, D. Patel, M.G. Capeluto, C.S. Menoni, J.J. Rocca. “Sub-100 nm interferometric lithography realized with table top extreme ultraviolet lasers”. APS March Meeting. Denver, CO, March 5-9 2007. Bulletin of the American Physical Society Series II, Vol 52, No 1

24. M.C. Marconi , M.G. Capeluto, P. Wachulak, G. Vaschenko, H. Bravo, C.S. Menoni, J.J. Rocca, E.H. Anderson, W. Chao, D.T. Attwood, O. Hemberg, B. Frazer, S. Bloom. "Nanopatterning and nanomachining with table-top extreme ultraviolet lasers". Fall Meeting Material Research Society, Boston, MA, November 2006.
25. M.G. Capeluto, P. Wachulak, M.C. Marconi , C.S. Menoni, J.J. Rocca , E.H. Anderson, W. Chao, D.T. Attwood. "Development of a table top Nanopatterning tool with Extreme Ultraviolet laser illumination". 32nd International Conference on Micro and Nano Engineering 2006. Barcelona, September 17-21 2006.
26. M. C. Marconi, P. W. Wachulak, R. Bartels, C. S. Menoni, J.J. Rocca. "EUV holographic imaging with sub micron resolution". 10th International Conference on X Ray Lasers. Berlin, August 2006.
27. M.G. Capeluto, P. Wachulak, M.C. Marconi , C.S. Menoni, J.J. Rocca , E.H. Anderson, W. Chao, D.T. Attwood. "Table top Nanopatterning using Soft X Ray lasers". 10th International Conference on X-Ray Lasers. Berlin, August 2006.

INVENTION DISCLOSURES AND PATENTS:

1. "Table top Nanopatterning tool with extreme ultraviolet/soft x ray laser illumination". Mario Marconi, Carmen Menoni, Jorge Rocca, Erik Anderson, Weilun Chao, Przemyslaw Wachulak

TABLE OF FIGURES

Figure 1.1. The electromagnetic spectrum as it extends from the infrared to hard X-rays (HXR)	3
Figure 1.2. Patterning of different length scales. Above the logarithmic scale ruler the ranges of dimensions for specific objects and below the ruler the range of the feature sizes that have been demonstrated for various patterning techniques.	7
Figure 1.3. General description of the patterning process by means of using a mask (a) projected on the surface of the light sensitive material and by means of using a master (b) in a molding or embossing process to copy the pattern from the mask to the responsive medium (usually deformable polymer).....	8
Figure 1.4. Simplified scheme of writing with a rigid stylus. (a) rigid stylus is used to induce deformation or material displacement on a surface. (b) AFM image of the Pablo Picasso's "Don Quixote" in polycarbonate film carved with AFM tip. Picture taken from	12
Figure 1.5. Quantum corral made by positioning 48 iron atoms into a circular ring on the copper surface. Picture taken from [1.].....	13
Figure 1.6. Simplified scheme of writing with a beam of photons, electrons or other energetic particles. (a) The beam is used to induce the changes in the resist surface. (b) SEM image of a pattern written using an electron beam in the PMMA resist. Picture taken from	14
Figure 1.7. Scheme of writing the patterns with electric field. (a) An auxiliary electrode is used to apply an electric field locally to the substrate. (b) AFM image of the cartoon made by oxidizing the silicon surface using conductive scanning probe. Picture taken from	16
Figure 1.8. Writing the patterns using magnetic field. (a) An inductive element mounted on the recording head is used to generate the uniform magnetization in domains in a thin layer of the ferromagnetic material. (b) Image of the magnetization patterns obtained with magnetic force microscopy (MFM) showing the recorded tracks on the hard drive. Picture taken from	17
Figure 1.9. Schematic illustration of three different approaches for writing the patterns that uses add-on process. (a) Writing using laser-induced chemical vapor deposition, (b) inkjet printing, where ink is ejected from the nozzle and dispensed onto the substrate and (c) writing of ink with a pen, where the ink is delivered to the substrate in the tiny ink meniscus formed between tip and the surface.	19
Figure 1.10. Examples of patterns fabricated using self-assembly methods. (a, b) SEM images of two different types of patterns fabricated in silicon nitride by using phase separated copolymer films as the mask for reactive ion etching. (c) SEM image of triangular pillars produced by evaporation of gold in the voids between self-assembled spheres on a silicon substrate. (d) SEM image of gold rings fabricated by spreading ink	

from the edges of silica beads assembled on a gold surface, followed by lift-off and etching. Picture taken from	21
Figure 1.11. (a) Simplified schematic of the stepper. The image of the mask is projected on the surface of the photoresist with demagnification. Movable stage allows to repeat the printing process at different location on the same wafer. (b) Photograph of 12 inch diameter wafer with an array of Pentium IV processors in Intel's 130nm technology. Picture taken from	24
Figure 1.12. Masked deposition and etching. (a) Scheme of the procedure. (b) SEM image of the gold features formed on glass capillary by evaporation and mask removal. (c) SEM image of anisotropically etched pillars in silicon wafer with mask of gold squares patterned on a silicon substrate. Gold mask is still visible on the top of silicon pillars. Picture taken from	25
Figure 1.13. Embossing using rigid master scheme (a) to imprint the features into a deformable material using mechanical force. (b) SEM image of lines embossed in the thin layer of polymer. Picture taken from	28
Figure 1.14. Replica molding scheme (a), liquid polymer is cast into the mold and cured into a solid state. (b) SEM image of the microstructures made in polyurethane with the use of PDMS mold. Picture taken from	28
Figure 1.15. Scheme of microcontact printing (a). Stamp is used to define the pattern on the surface of the substrate. SEM image (b) of the patterns made in thin layer of silver by microcontact printing, followed by selective chemical etching of the regions unprotected by the ink. Picture taken from	30
Figure 1.16. Microfluidic patterning (μ FN) scheme. (a) Small channels of microfluidic network are used to transport and deposit material on the surface of the substrate with spatial control. (b) A fluorescence microscopy of labeled proteins deposited on a PDMS substrate using sets of parallel channels made in silicon mold. Picture taken from	31
Figure 1.17. Examples of edge lithography. (a) SEM image of silicon rings fabricated using near-field, phase-shifting optical lithography. (b) SEM image of platinum nanowires fabricated using superlattice nanowire pattern transferring. Picture taken from	32
Figure 1.18. SEM image of 3D structure of tungsten bars fabricated in layer-by-layer fashion using multiple mask scheme. Picture taken from	33
Figure 1.19. The SEM image of the bull sculpture fabricated in the polymer resist by two-photon absorption in the resist induced by raster scanning of a laser beam. Picture taken from	34
Figure 1.20. SEM image of the photoresist line with triangular profile produced by photolithography using gray-scale mask. Picture taken from	35
Figure 1.21. Advanced Photon Source, Argonne National Lab	36
Figure 1.22. Example of high harmonic generation source from	38

Figure 1.23. Capillary Discharge Laser generates ns laser pulses with energy up to 0.8mJ/pulse, high repetition rate. The laser beam has very good spatial and temporal coherence properties.	40
Figure 1.24. Desk-top version of the Capillary Discharge Laser. Much more compact ..	40
Figure 2.1. Capillary Discharge Laser, compact device with 0.4x1m ² footprint. In the back Marx generator used to charge the water dielectric capacitor.....	49
Figure 2.2. Schematic diagram of a table-top capillary discharge laser based on a water dielectric capacitor. The liquid dielectric capacitor is charged to ~ 200 kV and rapidly discharged through the spark-gap switch by the capillary load.	49
Figure 2.3. Capillary Discharge Laser characteristics: a) 46.9nm laser beam footprint with Al filter and supporting mesh, b) spectrum of the laser output emission shows high monochromaticity of this source ($\lambda/\Delta\lambda > 10^4$) [2.12].	51
Figure 2.4. Color interferogram and corresponding lineout showing the spatial coherence of the laser beam with capillary length 36cm, resulting full spatial coherence at this capillary length. (Figure and data from [2.12]).....	52
Figure 3.1. Two beams interference lithography, schematic description.	59
Figure 3.2. Positive photoresist processing scheme. The portion of the photoresist exposed to light becomes soluble to the photoresist developer and the portion of the photoresist that is unexposed remains insoluble to the developer.	66
Figure 3.3. Negative photoresist processing scheme. The portion of the photoresist exposed to light becomes relatively insoluble to the photoresist developer. The unexposed portion of the photoresist is dissolved easily by the developer.	66
Figure 3.4. The example of the contrast curves for the photoresist showing the difference between high and low contrast (from [3.26]).....	68
Figure 3.5. Influence of high and low photoresist contrast on the developed pattern.	69
Figure 3.6. a) schematic description of the PMMA molecular composition. Long chains of polymers (one of the molecules are depicted bold) contain carbon, hydrogen and oxygen atoms in depicted configuration. The PMMA molecular composition after the photon or e-beam exposure (b). The bonds between the molecules in long polymer chain are broken creating the shorter chains.	71
Figure 3.7. Cage-like structure of HSQ (a) before exposing it to light or e-beam. Hydrogen, oxygen and silicon atoms constitute to form the hydrogen silsesquioxane, which changes its chemical structure after the exposure. Networked structure of HSQ after exposing HSQ to light or e-beam (b).....	72
Figure 3.8. Lloyd's mirror interferometer explanation. Top part of the beam illuminates the sample coated with the resist and the bottom part illuminates the mirror's surface, reflects from it and superposes with the top part of the beam creating the intensity modulation at the sample plane.....	74
Figure 3.9. Compact nanopatterning tool based on Lloyd's mirror configuration.	75
Figure 3.10. Photograph of the nanopatterning tool showing all major components.	75

Figure 3.11. Zoomed area of the mirror and aperture assembly showing those components in details. Inset images show the aperture cut in the stainless steel shim and the alignment of the aperture with the use of an optical microscope,	77
Figure 3.12. Optical micrograph showing the results of using the aperture and possibility to pattern many different shapes and sizes in the single sample both 1D (right-lower square with single exposure) and 2D patterns.	77
Figure 3.13. Reflectivity of various materials at 41nm wavelength vs. grazing incidence angle for a) s-polarization (TE) perpendicular to the incidence plane,.....	79
Figure 3.14. Fringe visibility in the interference pattern vs. grazing incidence angle for small grazing incidence Θ angles from 0 to 30 degrees.	80
Figure 3.15. The photograph of the setup used to measure the chromium mirror reflectivity vs. the grazing incidence angle. Laser beam reflects from the measured surface and illuminates the photodiode.....	82
Figure 3.16. Chromium mirror reflectivity vs. grazing incidence angle measured at 46.9nm wavelength.	83
Figure 3.17. Filtering of spatially and temporally incoherent radiation from thermal source (a). Spatial filtering using a pinhole increases the spatial coherence of the source (b) while spectral filtering increases the temporal coherence of the source (c). Spectral filtering and a pinhole produces a temporally and spatially coherent beam (d). Please notice greatly diminished power after the filtering is performed. Based on [3.].....	85
Figure 3.18. The schematic description of the Lloyd's mirror interferometer useful to study the spatial and temporal coherence influence on the patterning area.....	86
Figure 3.19. Period of the interference pattern and patterned features vs. grazing incidence angle a) and the calculated spatial and temporal coherence limitations to the patterning width vs. grazing incidence angle b).	89
Figure 3.20. The intensity patterns generated by the described model, (a, b) intensity patterns in each of two exposures, the total intensity pattern generated by incoherent addition of the doses for angle between the exposures equal to 90° c).....	92
Figure 3.21. The intensity patterns generated by the described model, (a, b) intensity patterns in each of two exposures, the total intensity pattern generated by incoherent addition of the doses for angle between the exposures equal to 30° c).....	92
Figure 3.22. The intensity patterns generated by the described model, (a, b) intensity patterns in each of two exposures with periods equal to 448nm and 168nm respectively, the total intensity pattern generated by incoherent addition of the doses for angle between the exposures equal to 90° c).	93
Figure 3.23. Photoresist response curve for PMMA in terms of the normalized	94
Figure 3.24. Results of the PMMA photoresist model for various conditions: a) $2 \times 2 \mu\text{m}^2$ area with pillars made high dose ($\sim 170 \text{mJ/cm}^2$) with the angle between the exposure $\alpha = 90^\circ$, b) $1.4 \times 1.4 \mu\text{m}^2$ area with holes in the surface made with lower dose ($\sim 110 \text{mJ/cm}^2$) with the angle between the exposure $\alpha = 90^\circ$, c) $3 \times 3 \mu\text{m}^2$ area with elongated pillars in the surface made with the angle between the exposure $\alpha = 30^\circ$, d) $2 \times 2 \mu\text{m}^2$ area	

with elongated holes in the surface made with the angle between the exposure $\alpha = 90^\circ$ and two different periods in two consecutive exposures 150 and 220nm. 97

Figure 3.25. a) Fabricated arrays of cone-shaped nano-dots patterned in PMMA by double exposure with a Lloyd's mirror configuration, with $\alpha = \pi/2$ and high ($166\text{mJ}/\text{cm}^2$, 60+60 laser shots) photon dose, b) detailed image showing in details 58nm FWHM the nano-dots..... 100

Figure 3.26. Fabricated array of holes patterned in PMMA by double exposure with a Lloyd's mirror configuration, $\alpha = \pi/2$ and low ($110\text{mJ}/\text{cm}^2$, 40+40 laser shots) photon dose showing in details 60nm FWHM holes. 101

Figure 3.27. Double exposure scheme with an angle between exposures equal to $\alpha=\pi/6$. Depending on the dose holes or pillars will be fabricated after the developing procedure. 102

Figure 3.28. Fabricated array of oval-shaped nano-dots patterned in PMMA by double exposure with a Lloyd's mirror configuration, with $\alpha = \pi/6$. Pillars - FWHM $80 \times 160\text{nm}^2$ were obtained with periods 160nm and 320nm, respectively..... 102

Figure 3.29. a) Double exposure scheme with an angle between exposures equal to $\alpha=\pi/2$, but with different period in each exposure adjusted by changing the interferometer angle. b) Fabricated arrays of oval-shaped nano-dots patterned in PMMA by double exposure with a Lloyd's mirror configuration, with $\alpha = \pi/2$ and different periods in each exposure 150nm and 220nm. Pillars - FWHM $75 \times 110\text{nm}^2$ were obtained in this experiment..... 103

Figure 3.30. The examples of the smallest patterns obtained with compact nanopatterning tool in the surface of the PMMA. Two dimensional pattern a) obtained in two exposures showing pillars 45nm FWHM diameter and 90nm period in the PMMA surface. One dimensional pattern b) obtained with single exposure showing 47nm FWHM lines and $\sim 95\text{nm}$ period. Because of the patterning tool visibility limitations at higher interferometer angles the patterns quality is reduced. 104

Figure 3.31. The examples of the features patterned over large areas in the PMMA photoresist. Pillars a) with 70nm FWHM diameter and 140nm period are shown over $10 \times 10\mu\text{m}^2$. Lines b) 47nm FWHM with 95nm period over the $7 \times 7\mu\text{m}^2$ are depicted. The quality of the pattern distribution is high. 105

Figure 3.32. Chemical composition of PMMA and HSQ photoresists. Limiting component in case of PMMA is carbon with $\sim 25\text{nm}$ attenuation length at 41nm wavelength. HSQ is inorganic and has silicon instead, which allow to obtain taller structures (8 times higher attenuation length)..... 107

Figure 3.33. Spinning curves for HSQ form manufacturer's specifications (lines) for various concentrations and with the measured data (points) obtained using AFM. Numbers are indicating the precise values..... 109

Figure 3.34. One and two dimensional patterns in the surface of HSQ photoresist. Lines 106nm FWHM a) in HSQ made in single exposure with dose at the sample plane

~41mJ/cm ² and holes b) 130nm FWHM diameter patterned in HSQ with depth exceeding 110nm made in two step exposure with dose ~41mJ/cm ²	111
Figure 3.35. Array of nanodots a) obtained with low dose (14mJ/cm ²) illumination and array of holes developed in HSQ with a high dose (41mJ/cm ²) illumination b).	111
Figure 3.36. Two dimensional Fourier transform of the image Figure 3.35b	112
Figure 3.37. Large arrays of holes patterned in HSQ photoresist. Holes are 120nm	113
Figure 3.38. Modulation depth for an array of holes with ~500nm period as a function of the developing time for different exposure doses.	114
Figure 4.1. Schematic description of the amplitude division interferometer used for nanopatterning with transmission diffraction grating. Two equally intense diffraction orders are recombined at the sample plane using two mirrors. In the overlapping area interference intensity modulation exposes the photoresist.	122
Figure 4.3. Scheme for OPD calculations in amplitude division interferometer.	127
Figure 4.4. Sequence of steps for the fabrication of the transmission diffraction grating using electron beam lithography in a photoresist layer deposited on top of a 100nm Si membrane.	132
Figure 4.5. AFM image of the transmission diffraction grating.	133
Figure 4.6. a) photograph of the “desk-top” capillary discharge laser (right) connected using vacuum manifold to the experimental chamber (left) housing the ADI interferometer. b) desk-top version of the capillary discharge laser. Much more compact source with energy per pulse up to 13μJ and repetition rate up to 12Hz.	135
Figure 4.7. Photograph of the set up a). Purple lines illustrate the optical path of the two beams (+/-1 st diffraction orders from the beamsplitter – transmission diffraction grating). Laser beam – green line, 0 th diffraction order is blocked by beam block (light blue line). More detailed image of the interferometer showing mirror – sample assembly b).	136
Figure 4.8. a) AFM image of a 145nm period grating printed by interferometric lithography using an EUV laser. b) AFM image of a 95nm period grating. Both images were obtained with the AFM working in “tapping” mode over a small section of the printed grating.	138
Figure 4.9. Translation stage was incorporated in the previous ADI setup to allow the grating displacement in the direction perpendicular to the interferometer’s axis.	140
Figure 4.10. AFM scans of the patterned photoresist surface 1.5x1.5μm ² size for various displacements of the transmission diffraction grating. Lines are 125nm period. All samples were processed in the same way to provide good comparison.	141
Figure 4.11. The visibility of the patterns obtained by rotating the image to have vertical lines and by binning the image vertically as a function of the optical path difference between both interferometer arms.	142
Figure 5.1. Holographic recording scheme a) using Gabor’s in-line configuration. The interference pattern between flat wavefront reference beam and beam diffracted from the object – object beam is stored in the recording medium (PMMA photoresist). Optical reconstruction b), where the transmission hologram is illuminated by the reconstruction	

beam (the same as reference beam) and the image of the object appears where the object was located during the recording phase.	148
Figure 5.2. FZP pattern is illuminated by the flat wavefront. Generation of real and virtual images.	150
Figure 5.3. Formulation of twin image in Gabor holography.	151
Figure 5.4. Schematic description of the spatial coherence limitation to the hologram resolution.	153
Figure 5.5. Schematic description of the temporal coherence limitation to the hologram resolution.	154
Figure 5.6. Schematic description of the scanning limitation to the hologram resolution.	155
Figure 5.7. The hologram of a point object. The interference between the spherical wavefront and plane wavefront produces the Fresnel zones. The phase between two wavefronts changes producing constructive and destructive interference radially outwards the z-axis.	157
Figure 5.8. Fresnel zones pattern a), and the focusing property of this pattern b).	158
Figure 5.9. Fresnel propagator derivation in spatial domain. Flat wavefront is focused by the lens or other focusing system to a single point at focal distance away from the lens principle plane a). The optical path difference in the spherical wavefront created by focusing lens at the lens plane between the center point and the second point separated from the center of the lens b) is depicted as γ	160
Figure 5.10. Setup for recording Gabor's in-line hologram of a point with a distances z_m , z_p and z_0 indicated.	165
Figure 5.11. Flowchart representing the hologram reconstruction code based on Fresnel propagator.	167
Figure 5.12. The example of the hologram scanned with AFM a), reconstructed image b) at the distance $z_p \sim 120\mu\text{m}$ that results in having a sharp image of the original object. ...	170
Figure 5.13. A few examples of results of running the code at different distances between the object and recording medium – z_p	170
Figure 5.14. Synthesized hologram of a point object (FZP pattern) the outermost circular zone has.	171
Figure 6.1. Schematic description of the Gabor's in-line holographic scheme for hologram recording.	180
Figure 6.2. Photograph of the laser system used to make the holograms.	181
Figure 6.3. An example of AFM tip used as the object for Gabor holography.	182
Figure 6.4. a) Hologram scanned with AFM at $z_p \sim 4\text{mm}$. The image is composed by 9 sub scans to cover a total area $270 \times 290 \mu\text{m}^2$, b) numerical reconstruction of the hologram obtained with the Fresnel propagator with zoomed area of the end of the reconstructed tip.	183

Figure 6.5. a) Hologram scanned with AFM at $z_p \sim 120\mu\text{m}$. Single scan image to cover a total area $42 \times 42 \mu\text{m}^2$, b) numerical reconstruction of the hologram obtained with the Fresnel propagator with zoomed area of the end of the reconstructed tip.	184
Figure 6.6. Line section through the example of reconstructed image showing sharp edges and roughly 160-170nm resolution.	184
Figure 6.7. The 0 th order template generated for resolution estimation. This binary image resembles.....	187
Figure 6.8. Wavelet decomposition: templates with reduced resolution obtained from the 0 th order template. a) 1 st order, resolution reduced 2x, b) 2 nd order, resolution reduced 4x, c) 3 rd order, resolution reduced 8x,	189
Figure 6.9. Flowchart representing the EUV holography reconstruction and resolution estimation code. AFM image after removing artifacts and noise is reconstructed with the reconstruction algorithm mentioned in previous section. Template of the image is generated and subsequently decomposed using wavelet analysis to produce a set of templates. Then to estimate the resolution each reconstruction image is correlated with set of templates and the results are plotted.	191
Figure 6.10. Image correlation between reconstructed images at different distances between the object and recording medium z_p and wavelet decomposition levels for $z_p \sim 4\text{mm}$ separation.	193
Figure 6.11. Image correlation between reconstructed images at different distances between the object and recording medium z_p and wavelet decomposition levels for $z_p \sim 120\mu\text{m}$ separation.	194
Figure 6.12. Correlation coefficients as a function of z_p distance for different wavelet decomposition levels for $z_p \sim 4\text{mm}$ separation.	195
Figure 6.13. Correlation coefficients as a function of z_p distance for different wavelet decomposition levels for $z_p \sim 120\mu\text{m}$ separation.	196
Figure 6.14. Image correlation between reconstructed images at different distances between the object and recording medium z_p and wavelet decomposition levels for $z_p \sim 4\text{mm}$ separation (a) and for $z_p \sim 120\mu\text{m}$ separation (c) decomposed using “db3” wavelet. Correlation coefficients as a function of z_p distance for different wavelet decomposition levels for $z_p \sim 4\text{mm}$ separation (c) and for $z_p \sim 120\mu\text{m}$ separation (d) decomposed using “db3” wavelet.	199
Figure 6.15. Gabor’s in-line configuration for high resolution hologram recording (a). The EUV laser beam illuminates the object composed of carbon nanotubes deposited in a Si membrane. The recording medium is a high resolution photoresist. On the other side of the membrane a high resolution photoresist was placed almost in contact with the membrane ($z_p \sim$ a few micrometers). Three dimensional view of the scheme (b).....	202
Figure 6.16. SEM images of 50-80nm diameter carbon nanotubes. The tubes were deposited on top of a thin Si membrane and used as the object in holographic imaging.	203

Figure 6.17. Sample holder assembly for high resolution holographic imaging. a) holder disassembled showing all the parts, b) holder assembled.....	204
Figure 6.18. Optical micrograph of the hologram recorded in the surface of the photoresist after developing procedure. Only big clusters are visible, while single nanotube holograms are impossible to see.....	205
Figure 6.19. Holograms (a to c) and reconstructed images (d to f) of 50-80nm diameter carbon nanotubes. The holograms were obtained by digitizing of the small area of the photoresist with AFM showing the complicated interference pattern stored in the photoresist surface. In the reconstructed images, single nanotubes and clusters of nanotubes are depicted.....	206
Figure 6.20. Knife edge test applied to estimate the resolution of the image a). The intensity lineout through the image from A to B is shown in b) indicating a 10-90% intensity modulation over approximately 4.5 pixels, corresponding to 45.8nm.....	207
Figure 6.21. Testing the capability of the 2D correlation to compare and find best match between the images.....	210
Figure 6.22. Different binary images used for testing the correlation part of the code. Images a-d are magnified for better appearance. All dots are 1 pixel. a) variable dot separation, b) horizontal dots, c) vertical dots, d) four dots, e) arbitrary image with four dots in the center.....	211
Figure 6.23. Applying the Gaussian filter with various widths to decrease the resolution of the binary image. a) binary arbitrary shape image, b) resolution set to 50nm, c) resolution set to 100nm, when one pixel is 10nm.....	212
Figure 6.24. Correlation coefficient as a function of the filter width ratio for different binary test images. The maximum of the correlation coefficient is equal to one for all tested input images and, as expected, for filter width ratio equal to one.....	212
Figure 6.25. Testing the capability of the correlation code to distinguish between different resolutions in the processed image.....	213
Figure 6.26. Template image for the multiresolution test a) and the result of applying Gaussian filter with two different widths to the different part of the test image b). Left image resolution was set to be 32nm and right has 87nm resolution.....	214
Figure 6.27. The results of applying Gaussian filter with variable width to the test image, Figure 6.26a) resulting in resolution decreasing. Resolution was set to be 12nm – a), 27nm – b), 42nm – c), 57nm – d), 72nm – e) and 87nm – f).....	214
Figure 6.28. Correlation coefficient as a function of the resolution showing the averaging effect of the correlation algorithm.....	215
Figure 6.29. Algorithm designed for resolution and feature size estimation from reconstructed images in EUV holographic imaging of carbon nanotubes.....	216
Figure 6.30. Description of the convolution procedure responsible for making the templates with various thicknesses. a) The image is filtered to remove the low frequency background fluctuations. b) With a skeletonizing algorithm the position of the nanotube is found. c) Various radii circles are convolved with the skeleton image to simulate the	

change of the tube diameter. d) High resolution template of the nanotubes (binary image) with given tube diameter $D_i=2r_c$	217
Figure 6.31. Description of the correlation code used to obtain the correlation coefficient to assess the image resolution and feature size. a) Template with a given thickness is convolved with a 2D Gaussian filter to obtain a degraded resolution template b). This template is correlated with original data image to construct a 2D plot in the resolution/tube diameter space shown in c). Both the resolution and tube diameter are found by localizing a global maximum in this plot.	218
Figure 6.32. Resolution and feature size estimation using the correlation algorithm for sub image a) obtained from Figure 6.31c), the localization of the global maximum in the correlation coefficient plot b).....	219
Figure 6.33. Resolution and feature size estimation using the correlation algorithm for different reconstructed image a), the localization of the global maximum in the correlation coefficient plot b).....	220
Figure 7.1. Scheme of the experimental set up.....	226
Figure 7.2. Detailed scheme of the test object used in volume holographic imaging. ...	226
Figure 7.3. Transmission of the 100nm thick pure aluminum foil (based on calculations from [7.1].	227
Figure 7.4. a) Hologram of the 3-D object with a random distribution of 465nm diameter latex spheres (markers) over the tilted surface of an Al foil recorded in the photoresist surface and digitized with an atomic force microscope. b) Digital reconstruction of the hologram. Intensity cuts in the vertical direction of one “in focus” marker c) and one “out of focus” marker d). The white dotted lines indicate the region in the reconstruction that is “in focus”.....	229
Figure 7.5. Reconstruction of the small portion of the hologram of the tilted surface with markers on the top a). Magnified regions of the reconstructed image at different reconstruction distances b). Arrows indicate markers close to the sharpest image, in focus.....	230
Figure 7.6. Simplified flowchart describing the algorithm used to retrieve 3D information from a single EUV high resolution hologram. The algorithm is based on 2D correlation between reconstructed images at different planes and template generated based on previous knowledge about the markers used.	231
Figure 7.7. Reconstructed image with all considered markers indicated with blue circles a) and correlation coefficients for only two indicated spheres (orange and violet) as a function of the reconstruction distance z_p showing the global maximum indicated with gray lines b).....	232
Figure 7.8. Al foil surface reconstruction for the region close to the edge of the spacer where a high slope is revealed a), position of each marker in 3D space obtained from the correlation algorithm b), projection of all markers on a x-z plane emphasizing the Al foil higher slope in one direction and line fitted to the data c), surface topography obtained from (b) using surface fitting algorithm d).	234

Figure 7.9. Al foil surface reconstruction for the region approximately 200 μm away from the edge of the spacer where a low slope is revealed a), position of each marker in 3D space obtained from the correlation algorithm b), projection of all markers on a x-z plane emphasizing the Al foil lower slope in one direction and line fitted to the data c), surface topography obtained from (b) using surface fitting algorithm d).	235
Figure 8.1. Schematic diagram of the 13nm wavelength imaging system. A condenser zone plate collects the laser light and focuses it onto the test pattern. An objective zone plate forms the image of the test pattern onto a back-illuminated charge coupled detector (CCD). Picture was taken from [8.10]......	241
Figure 8.2. EUV microscope image of a) a 100nm full period grating, b) 200nm full period grating, and c) 100nm full period elbow-shaped grating obtained with 13.2nm wavelength laser illumination. d), e) and f) are the corresponding SEM images of the test objects.	242
Figure 8.3. a) EUV image of the 200 nm full period grating. b) Image of the 200nm period grating with the threshold applied. c) Skeleton obtained from the image shown in (b). d) Binary template generated by convolution of the skeleton image with a circle with diameter $D=50\text{nm}$	243
Figure 8.4. Set of templates obtained applying Gaussian filters of different FWHM yielding different resolutions δ . a) $\delta=15\text{ nm}$, b) $\delta=45\text{ nm}$, c) $\delta=75\text{ nm}$, d) $\delta=105\text{nm}$, e) $\delta=135\text{nm}$ and f) $\delta=165\text{nm}$	244
Figure 8.5. Resolution estimated from the optimum Gaussian filter size.....	246
Figure 8.6. Correlation coefficients plotted in the feature size-resolution space showing a global maximum for each of the three different images of Figure 8.2. The dashed lines indicate the coordinates of the global maxima for each of the data sets: a) 100nm full period grating linewidth $31\pm 5\text{nm}$, and Rayleigh resolution $54.8\pm 5\text{nm}$. b) 200nm full period grating, linewidth $53.6\pm 5\text{nm}$ and $59.2\pm 5\text{nm}$ resolution c) 100nm full period elbow-shaped grating, linewidth $29\pm 5\text{nm}$ and $58.3\pm 5\text{nm}$ resolution.	247
Figure 10.1.1. The coordinate system and the symbols used in the analysis of the reflection coefficient from the Cr mirror. The incident wave k strikes plane interface separating two media and gives rise to the reflected k'' and refracted k' wave.	255
Figure 10.1.2. Reflection and refraction with polarization perpendicular to the plane of incidence (TE).....	259
Figure 10.1.3. Reflection and refraction with polarization parallel to the plane of incidence (TM).....	262
Figure 10.1.4. Scattering diagram for atom that contains many electrons.	265
Figure 10.1.5. A vector scattering diagram for incident wave vector \vec{k}_i and scattered wave vector \vec{k}	265
Figure 10.1.6. Comparison plot for the reflectivity of the chromium mirror between the data obtained from CXRO database and calculated using complex atomic scattering factors for various polarizations.....	267
Figure 10.3.1. Detailed flowchart of the reconstruction code.....	271

Figure 10.3.2. Detailed flowchart of the wavelet decomposition and correlation algorithm for resolution estimation.....	277
Figure 10.3.3. Detailed flowchart of the 3D holographic imaging algorithm (part 1) ...	280
Figure 10.3.4. Detailed flowchart of the 3D holographic imaging algorithm (part 2) ...	287
Figure 10.3.5. Detailed flowchart of the 3D holographic imaging algorithm (part 3) ...	291
Figure 10.4.1. Transmission diffraction grating diffraction efficiency calculations. a) normalized interference function for N=20 sources, b) normalized intensity function of the slit, c) normalized intensity function of a grating consisting of N similar, equally spaced and parallel slits, d) relative intensities in each diffracted order normalized to the intensity in the 0 th order for duty cycle of 50% d).....	312
Figure 10.4.2. a) Normalized interference function for N=300 sources (grooves), b) relative intensities in each diffracted order normalized to the intensity in the 0 th order for duty cycle of 48.5%.	313

TABLE OF TABLES

Table 3.1. Photoresist processing conditions. PAB is a baking condition using hotplate after the spinning is done to assure that the solvent in the photoresist has completely evaporated completely (data from [3.29]).	94
Table 3.2. Etching rates for various materials obtained using CAIBE system.....	108
Table 3.3. Measured HSQ thickness for various concentrations and spinning velocities using AFM.	109
Table 3.4. Measured modulation depth after exposing HSQ photoresist with different doses.....	109
Table 3.5. Comparison table showing required exposure doses to fabricate pillars or pattern of holes in both PMMA and HSQ photoresists.	113
Table 6.1. Coherence limitation to the resolution, AFM sampling limitations and the experimentally obtained resolutions estimated based on correlation analysis.....	197
Table 6.2. Summary of the results for high resolution EUV holographic imaging using carbon nanotubes as the object for three different reconstructions.....	221
Table 8.1. Comparison of linewidth size and image resolution determined by the correlation algorithm with measurements from the SEM images and grating test respectively for three different test images obtained with the EUV microscope at 13.2nm illumination.	248

CHAPTER 1

1 Introduction

Nanoscience and nanotechnology describes the field of applied science and technology that deals with controlling matter at the atomic and molecular scales, 100 nanometers or smaller, and fabrication of the devices with critical dimensions within that size range. It is a multidisciplinary field, having its roots in applied physics, materials science, molecular chemistry, robotics, electrical engineering, mechanical engineering, chemical engineering and biology. Nanotechnology in general can also be considered as an extension of existing sciences into nanometer scales.

Nanoscience and nanotechnology became recently a very important part of modern people's everyday lives. There are many examples of importance of these fields for all of us such as smaller, faster and less power consuming computer processors, hard drives with higher capacity, materials with increased strength and durability, solar panels with increased efficiency of conversion of light to electrical energy, super bright light emitting diodes (LED) in the headlights of modern cars among others. It is expected, that the importance of nanosciences will grow in the future. Potential applications in the future may result in a huge increase in speed of the computers with transistor sizes approaching size of a few atoms, larger data storage capacity, much more efficient lighting and battery storage, therapies for different kinds of cancer, more efficient water

filters, clothes that never stain or glass that never requires cleaning, nano-robots, etc. These amazing possibilities are the main driving force of the development of nanosciences over the last few decades.

Nanotechnology means understanding and controlling the matter at dimensions below 100 nanometers. It involves measuring, imaging, modeling and manipulating matter at this length scales. There are many different ways to reach the realm of nanometer scales. One way to manipulate the matter in this length scale is to generate the patterns by means of direct interactions between the atoms, molecules, such as pattern writing, self assembly on nanostructures or pattern replication. Other approach is to use beams of particles (electrons, ions) or photons. Shorter wavelengths of photons or particles are capable of fabricating and resolving smaller features and enable studies of the atoms and molecules in the nanometer scales. Interacting and controlling the matter is possible by changing the matter and by seeing these changes, which acts as a feedback mechanism necessary to learn and to draw the important conclusions. Shorter wavelengths of the photons allow us to see and to control the matter on the nanometer scales.

The importance of the shorter wavelengths to the nanoscience and nanotechnology as well as exploiting the capabilities of new table top extreme ultraviolet (EUV) lasers producing short wavelength photons is the main motivation of this dissertation. The applicability of the short wavelength photons to study the matter on the nanometer scales by means of seeing and controlling the nano-world will be presented.

1.1 Motivation for using extreme ultraviolet radiation

Extreme ultraviolet and soft x-ray radiation boundaries are not precisely established however it is generally agreed that EUV light encompass photon energies between $\sim 25\text{eV}$ and $\sim 250\text{eV}$, corresponding to wavelengths extending 5nm to $\sim 50\text{nm}$ while the soft x-ray region extends from the photon energies between 250eV to several keV as seen in Figure 1.1. The optical region of electromagnetic spectrum is well understood and historically thoughtfully studied because of its importance for humans to perceive their environment.

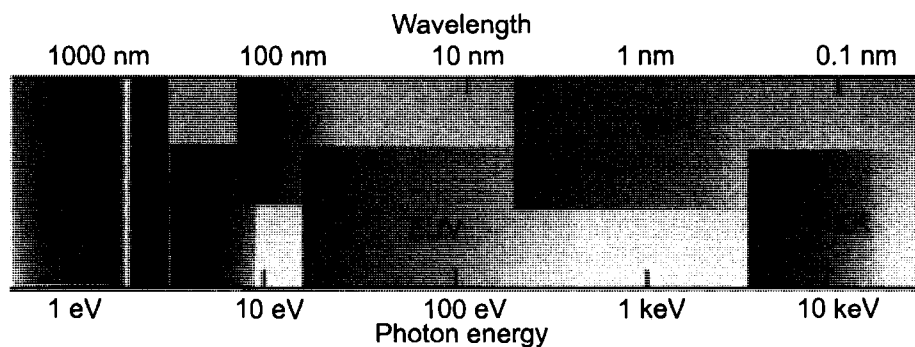


Figure 1.1. The electromagnetic spectrum as it extends from the infrared to hard X-rays (HXR)

Also hard x-rays are widely used for long time in scientific and medical applications. The EUV region of the electromagnetic spectrum although quite well understood by extension of well known laws from the visible spectral range (laws of optics), was unexploited mainly because the difficulties to implement applications due to the high absorption in the matter in this spectral range. Atomic resonances existing in this region lead to high absorption of radiation very close to the surface (nanometers to micrometers) in all materials. That was the main reason why the interest in EUV light was not significant.

Simultaneously the lack of sufficiently bright and coherent sources was an obstacle to fully explore the shorter wavelength possibilities of the EUV region.

Although the inconvenience of EUV radiation to perform conventional applications due to the high absorption, that were described before, EUV has distinctive advantages. Photons with shorter wavelengths have higher photon energies and are able to interact with matter differently than visible photons. EUV photon has much larger penetration depth in plasmas that allow for the investigation of regimes that cannot be studied with visible photons. The interferometry of dense plasmas is a unique application where EUV has distinctive advantages over other optical techniques. Also the shorter wavelength of the EUV radiation scales down the limits of the visible optics in applications like imaging and patterning. Ten to fifty times shorter wavelength is an obvious advantage that allows patterning and resolving smaller features, in the case of holographic imaging or classical imaging with the use of diffractive optics [1.1]. Shorter wavelength thus pushes the diffraction limits beyond what can be achieved with visible photons.

In this dissertation two applications of EUV light will be presented that allow to control the matter on nano-meter scales: nanopatterning of periodic motifs and EUV holographic imaging with high spatial resolution. Transferring applications like nanopatterning and holography to the EUV range allows to push the limits of resolution towards the nanometer scale, making the new technology very appealing to the future development of nanosciences.

This work is organized as follows. In the first chapter a detailed description of the current patterning methods will be presented to set the frame of reference for the work

done in the EUV table-top nanopatterning. The last section of this chapter will discuss various types of EUV sources used commonly for these applications. Advantages and drawbacks of these sources will be discussed in terms of size, flux and coherence of the beam. Chapter two will describe the table-top capillary discharge laser. This source was used in almost all experiments presented in this work. In chapter three nanopatterning using the technique of interferometric lithography will be discussed. Previous work and the principles of interferometric lithography will be presented in detail. One of the contributions of this work is a complete characterization of two e-beam photoresists: PMMA (poly-methyl methacrylate) and HSQ (hydrogen silsesquioxane) at the EUV laser wavelength. Both photoresists were used in the nanopatterning experiments. A compact table-top nanopatterning tool capable of patterning sub-100nm period one and two dimensional patterns will be presented and described in detail. Finally the results of patterning using a compact patterning tool for the two photoresists will be shown. Different, periodic motifs in PMMA and HSQ as well as the analysis of photosensitivity of the HSQ photoresist at 46.9nm wavelength will be presented. Chapter four describes the nanopatterning results obtained with an amplitude division interferometer (ADI). The spatial and temporal coherence requirements will be discussed in detail showing the advantages of that scheme. The transmission diffraction grating used as a beam splitter in the ADI and fabrication process of the grating will be described in this chapter as well as the interferometer design. Patterns obtained with the amplitude division interferometer will be presented and the interferometer optimization and the influence of the optical path difference on the pattern quality will be discussed.

The second application described in this dissertation is high resolution holographic imaging with few tens of nanometers spatial resolution. In chapter five a general overview of holography will be presented. An important part of this chapter is also devoted to the reconstruction algorithm, based on Fresnel propagator, used to reconstruct the images of the objects from high numerical aperture holograms. In chapter six two different holographic experiments will be presented: imaging of AFM tips and the resolution estimation algorithm using wavelet decomposition and a correlation method, and ultimate wavelength resolution holographic imaging of carbon nanotubes where the resolution and the size of the tubes were simultaneously assessed using a Gaussian filtering and correlation analysis. Chapter seven is devoted to the three dimensional numerical reconstruction of the surfaces from single high numerical aperture hologram and to the algorithm used for the three dimensional reconstruction. Chapter eight describes the application of the Gaussian filtering and correlation analysis, employed previously for resolution and feature size estimation in wavelength resolution holography and now used to characterize the EUV microscope images. Chapter nine is the summary of this dissertation.

1.2 Overview of the patterning methods

Nano structures and nanometer size objects had found new application in a variety of fields that includes among others material sciences, biology, surface chemistry and technology - semiconductor industry, protective coatings, etc. The capability to reliably print nanometer size structures had opened new horizons for example in storage devices,

integrated circuits, display devices, micromechanical devices (MEMS) [1.2], sensors [1.3], biochips [1.4], microfluidic devices [1.5] to photonic crystals [1.6] and diffractive optics [1.7], etc. Figure 1.2. shows the typical sizes of the patterned features from a millimeter in size down to angstroms using different patterning techniques.

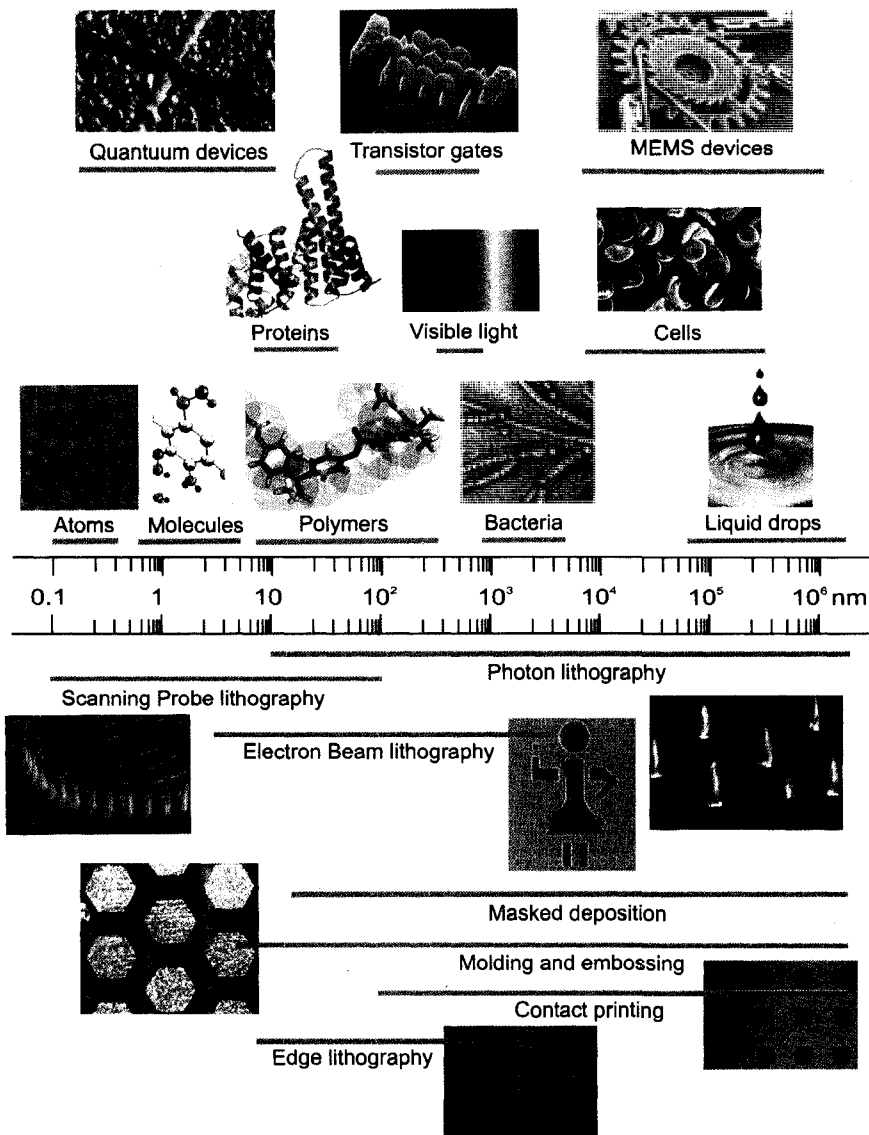


Figure 1.2. Patterning of different length scales. Above the logarithmic scale ruler the ranges of dimensions for specific objects and below the ruler the range of the feature sizes that have been demonstrated for various patterning techniques.

Generally lithographic techniques consist of several elements. Firstly there has to be a set of patterns in the form of a mask or a master. The idea can be easily understood considering two distinct techniques such as projection lithography and embossing technique, both shown in Figure 1.3. The mask is used in projection lithography to modulate the intensity of the light by introduction of amplitude or phase changes to the light that exposes a light sensitive material. This idea can be seen in Figure 1.3a. A master is a rigid or flexible substrate with a surface modulation that is used later to replicate by molding or embossing techniques. This is schematically depicted in Figure 1.3b.

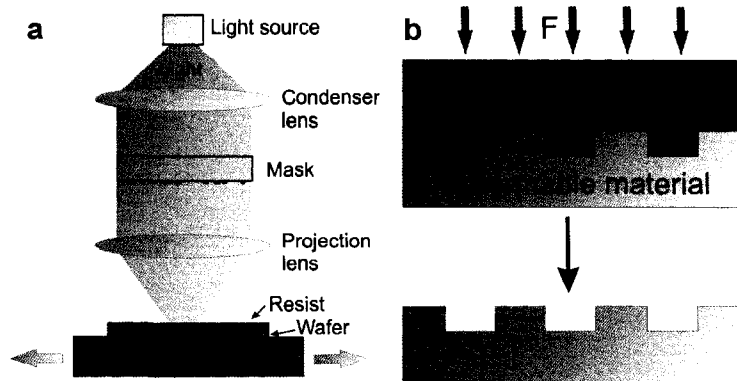


Figure 1.3. General description of the patterning process by means of using a mask (a) projected on the surface of the light sensitive material and by means of using a master (b) in a molding or embossing process to copy the pattern from the mask to the responsive medium (usually deformable polymer)

Secondly there has to be a method to transfer or to replicate the patterns. In projection lithography, Figure 1.3a, the spatially modulated light transfers the pattern from the mask to the substrate. In the case of a master, Figure 1.3b, the mechanical force causes to transfer the pattern from the master to the substrate by mechanically deforming the soft substrate in the case of embossing.

The third element is the responsive medium, usually light sensitive or particle beam sensitive resist to store the information and to serve for subsequent steps in the case of projection lithography, or the mechanically deformable soft polymer for the embossing process.

The requirements for a successful lithographic process are different depending on the application. The most obvious constrain is the feature size that selects the proper lithographic technique. However the fabrication of more complex structures like integrated circuits, storage devices or displays involves many steps and sophisticated technologies to satisfy the downsizing trend.

Probably the best established technology for patterning is optical lithography or photo-lithography. The foundations for this technique were established in microelectronics for the fabrication of integrated circuits. A photosensitive film (photoresist) is first patterned by the spatially intensity modulated light with wavelengths ranging from visible range to X-rays. This generates the sacrificial layer, sometimes called mask, used for subsequent processing. Pattern transfer to the substrate can be done in different ways like selective growth of the material in the unmasked areas of the substrate by electroplating or removing the exposed surface of the substrate by wet or dry etching. Photoresists are usually organic or inorganic polymers, whose molecular chains are degraded, cross-linked or rearranged when they are exposed to particles or photons having sufficient energy to induce the chemical reaction [1.8]. Photolithography is a very common and effective way to pattern these materials. However it can be only applied to pattern directly a limited number of materials, usually photoresists, and is not efficient in

three-dimensional (3D) fabrication. These limitations triggered the development of alternative methods and techniques [1.9].

Herein a general review of the various patterning techniques used in the nanopatterning will be presented. The scope of this review will be to illustrate the different ideas and principles involved in defining patterns on the surface of the substrate. In a very general way patterning can be divided into generation and replication. These two approaches are different and somehow complimentary.

Generation of the patterns is intrinsically a serial process of writing the patterns using focused laser or particle beams. It is a relatively slow approach useful for fabrication of a few copies of the original sample. These originals might be used later as a mask or master in the replication process.

The replication is an intrinsically parallel process, thus is much faster than the pattern generation. The replication allows the patterned features to be transferred into other materials in a single step, fast and inexpensively with high fidelity. Precise fabrication of masks combined with rapid duplication techniques might be the most practical protocol for high throughput patterning.

Another possibility is to separate the patterning techniques into “bottom-up” and “top-down”. In the first one the devices and materials are built from chemically assembled molecular components that grow or self assemble directly in the surface of the substrate. An example of this approach is self-assembly. In the second one the nano-sized objects are fabricated from larger objects without having the control on the atomic length scales. The example can be photolithography.

1.2.1 Patterning

1.2.1.1 Writing

Writing patterns is done using sharp tips in contact with the substrate by mechanical engraving of the surface with or without ink. The ink is an extra material deposited during the writing process. Writing might be also done in proximity to the substrate material by the interactions between the tip and the substrate. This process is intrinsically serial, thus the pattern generation is slow. Writing the patterns allows to generate arbitrary shaped patterns on the surface of the substrate. Writing techniques don't necessary need any ink to accomplish the task and depending on the sharpness of the tip the resolution achieved might range from micrometer scale down to the atomic scale. These techniques have a common mechanism associated with reversible or irreversible local changes of the substrate material. Practically changes to the substrate surface might be done mechanically, optically, chemically, electrically and magnetically or by any combination of these mechanisms.

1.2.1.1.1 Writing with rigid stylus

This technique involves mechanical displacement of the material from the surface of the substrate. The surface modification is produced in a controllable way, as schematically depicted in Figure 1.4a. Sometimes this method is called micromachining. The process is based on direct contact between a rigid stylus and the substrate. The stylus is moved across the surface to engrave a relief pattern. Because considerable forces might

be involved in this process, with time the stylus sharpness will change thus the resolution of the relief patterns will degrade.

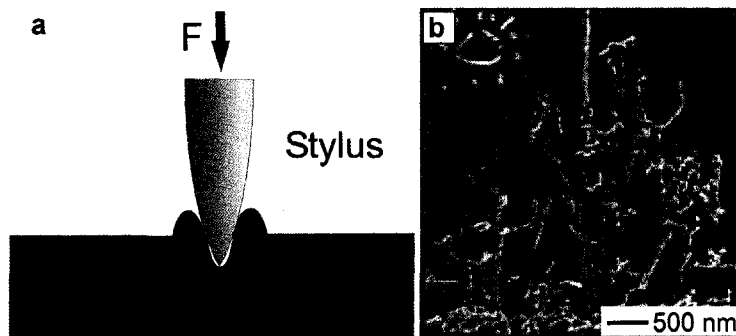


Figure 1.4. Simplified scheme of writing with a rigid stylus. (a) rigid stylus is used to induce deformation or material displacement on a surface. (b) AFM image of the Pablo Picasso's "Don Quixote" in polycarbonate film carved with AFM tip. Picture taken from [1.10].

High resolution patterns require using scanning probe techniques, mainly scanning tunneling microscopy (STM) or atomic force microscopy (AFM). Both techniques employ ultrasharp tips [1.11]. The achievable resolution can vary significantly from the size of individual atoms, to micron size scales. If the film is relatively thick the resulting holes or trenches are surrounded by the displaced material forming walls. This technique was successfully used to write patterns in polymers [1.12], shown in Figure 1.4b, on self-assembled monolayers (SAM) [1.13] and metals or oxides [1.14].

Some of the weakly adsorbed molecules or small particles might also be grabbed by the stylus or tip and moved to another region on the sample to form structures and patterns [1.15]. This technique however is difficult to control and slow in grabbing moving and releasing the particles, however it is the only technique, to the author's knowledge, capable of resolution at the atomic scale [1.16]. An example of this technique capable of operating on single atoms is the quantum corral [1.17] made with a scanning tunneling microscope (STM), depicted in Figure 1.5. Forty eight iron atoms were

positioned by grabbing, moving and releasing them to create a circular ring on the top of copper substrate.

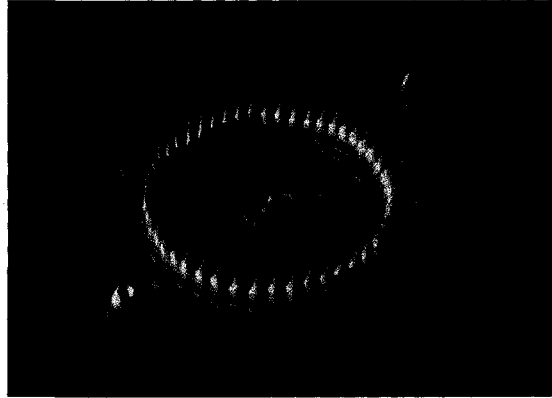


Figure 1.5. Quantum corral made by positioning 48 iron atoms into a circular ring on the copper surface.
Picture taken from [1.18]

1.2.1.1.2 Writing with Beam of Photons and other Energetic Particles

In this approach a tightly focused beam is scanning the surface of the susceptible material. The schematic description of the process is shown in Figure 1.6a. The energy of the beam is dissipated in this material and leads to various types of physical and chemical changes dependent on the type of radiation utilized, dose and material. Generally, the patterning process can be additive when the species are deposited in the vicinity of the beam, subtractive when leads to removal of the material from the surface or it might induce the physical or chemical reactions that lead to a latent image formation in the surface of the substrate.

Focused laser beams have been used in many fabrication schemes. The laser micro- and nano-ablations of a solid surface are based on selective removal of the material. This technique can be applied to many different materials both organic and

inorganic. Photoablation was even being used for commercial mask fabrication where the feature size was not an important requirement (1-2 μm) [1.19].

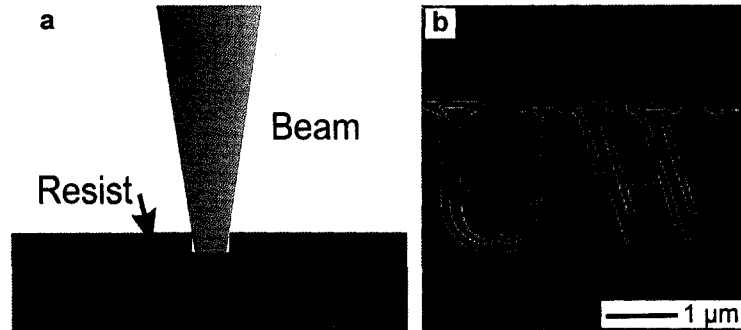


Figure 1.6. Simplified scheme of writing with a beam of photons, electrons or other energetic particles. (a) The beam is used to induce the changes in the resist surface. (b) SEM image of a pattern written using an electron beam in the PMMA resist. Picture taken from [1.10].

Lithography based on near field scanning microscopy (NSOM) uses a tiny waveguide to direct the light from the laser source to the surface. The waveguide is usually a transparent probe coated with thin layer of aluminum [1.20]. If the tip is very close to the substrate, even for apertures much smaller than the illumination wavelength the exposure will be localized to the area that is substantially smaller than the diffraction limit in the far field. This approach was proved to be useful to selectively polymerize the photoresists [1.21] and in other experiments like localized melting, evaporation or activation of the reactive species [1.22].

Focused beams of energetic particles are usually electrons or ions. These techniques have extremely high resolution due to the fact of short wavelengths associated with particle beam ($<1\text{\AA}$) and large depth of focus. Electron beam lithography is a well known approach and has become a standard tool for writing arbitrary shape patterns. The resolution of e-beam patterning mainly depends on the beam spot size and on the scattering associated with the generation of the secondary electrons. PMMA was a main

resist used for e-beam lithography for a long time. The SEM image in Figure 1.6b is an example of using PMMA in high resolution e-beam lithography. Recently photoresists such as HSQ became more popular. However a variety of materials were used including inorganic materials [1.23]. Reactions in the polymer photoresist include polymerization, cross-linking, or more complex processes such as chemical amplification with acids or bases [1.24].

Focused beam of ions (FIB) is a related technique to electron beam lithography. The higher mass of ions results in decreasing of the patterning distortions due to back-scattering from the substrate. Other possibilities of FIB is highly localized doping, ion-induced deposition, ion milling, but those methods still have worse resolution than e-beam lithography.

1.2.1.1.3 Writing using an Electric Field

In this method the surface of the substrate is locally modified using an electric field or a current [1.25]. An electric field is generated between two electrodes: the conductive probe that moves above the conductive surface. This is schematically depicted in Figure 1.7a. The field induces physical or chemical changes to the patterned surface by charge accumulation or by Ohmic heating due to the current established between the substrate and the tip. To introduce the surface changes on the nano-meter scales, conductive (metal or metal coated) ultrasharp tips of atomic force microscopes are used.

STM and AFM techniques were used to demonstrate positioning of the metal clusters [1.26], fabrication of holes and pits [1.27] and manipulations of single atoms and

molecules [1.28]. Electrochemical processes include the oxidation of the silicon (Figure 1.7b) and other materials, modifications of the resist films [1.29] and organic thin films [1.30].

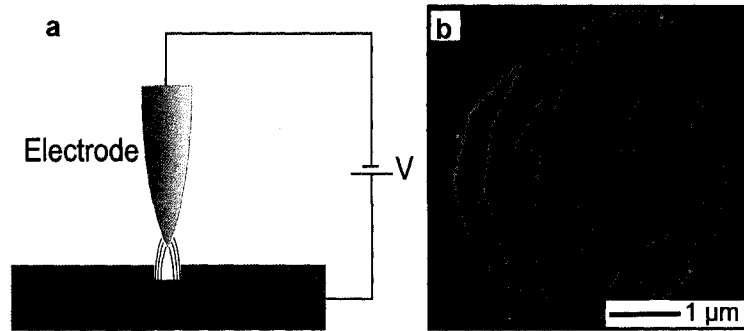


Figure 1.7. Scheme of writing the patterns with electric field. (a) An auxiliary electrode is used to apply an electric field locally to the substrate. (b) AFM image of the cartoon made by oxidizing the silicon surface using conductive scanning probe. Picture taken from [1.10].

1.2.1.1.4 Writing using a Magnetic Field

Magnetic surfaces can be patterned with magnetic fields. In this patterning technique an inductive device mounted on the recording head is used to magnetize locally and selectively small areas of the magnetic medium. The magnetic surface can be a flat substrate or flexible tapes made by deposition of the magnetic particles such as iron oxide or polycrystalline alloys composed from cobalt, chromium or platinum. The idea of writing using magnetic fields is schematically depicted in Figure 1.8a.

Magnetization patterns are made in the ferromagnetic surface by the head. Reading back the information is a reverse process and is usually done using magneto-resistive sensors mounted on the same head. The most important fact about this method is that the patterning process induces reversible changes. This is the approach used to store the information in a reversible, dynamic way, in the computer hard drives. The lateral

density of bits on a hard drive disks increased significantly over last decades by making the heads smaller, decreasing the head-surface distance, and decreasing the thickness of the recording medium and the grain size.

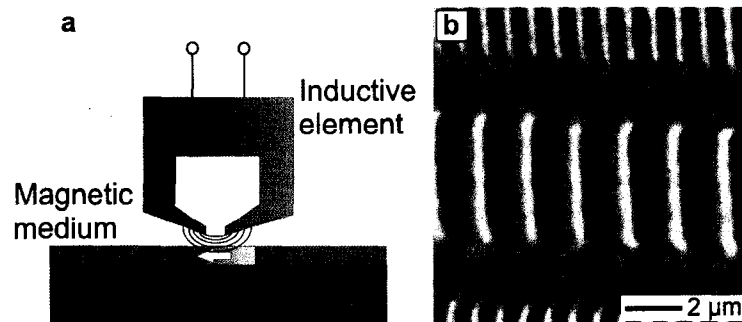


Figure 1.8. Writing the patterns using magnetic field. (a) An inductive element mounted on the recording head is used to generate the uniform magnetization in domains in a thin layer of the ferromagnetic material. (b) Image of the magnetization patterns obtained with magnetic force microscopy (MFM) showing the recorded tracks on the hard drive. Picture taken from [1.10].

Using magnetic particles with smaller grain size is very important in increasing the information storage density, however reduction of the size of the grain might be constrained by superparamagnetism. This is a phenomenon by which magnetic materials may behave similarly to paramagnetic materials even below the Curie temperature. On small length-scales the energy required to change the direction of the magnetic moment of a particle is small and comparable to the ambient thermal energy. That means that the rate of randomly reversed magnetic moment direction becomes significant. This effect limits the grain size due to the fact, that the grains cannot retain the induced magnetization because of the thermal agitation as the grains became too small [1.31]. One of the approaches to overcome this limitation is to use patterned magnetic media with arrays of single domain particles [1.32], however this is still a challenge to fabricate such devices.

1.2.1.1.5 Writing by Add-On Process

So far the techniques presented were based on removing the material from the surface. Another way is to add material in a precise controllable way. The spatial coordinates and the volume of the added material have to be known precisely. There are a few add-on methods used in patterning. Three of them will be described here, based on the fixing of the precursor with the laser beam, printing on the substrate using ink, or writing with the ink and stylus.

Laser-induced chemical vapor deposition (LCVD) was widely used as a patterning method for solid substrates. The idea of this method is depicted in Figure 1.9a. Gaseous precursors are deposited on the surface due to the photon absorption and cleavage of the chemical bonds or by heating and dissecting of the precursor compounds. As a precursor alkyl or carbonyl metals are used. This is a fast way to deposit many different materials on planar and nonplanar surfaces. The smallest feature size is limited to the focused spot size of the beam and sizes as small as 500nm were deposited with laser beams. Better spatial resolution is possible with the use of NSOM lithography in conjunction with CVD deposition of various materials [1.33]. Also instead of focused laser beams, beams of electrons and ions can be used to locally deposit different materials from the gaseous precursors onto the substrate [1.34]. Focused ion beam based deposition of the materials on the substrate is so successful that it is a commonly used technique for repairing the defects on the photomasks or integrated circuits.

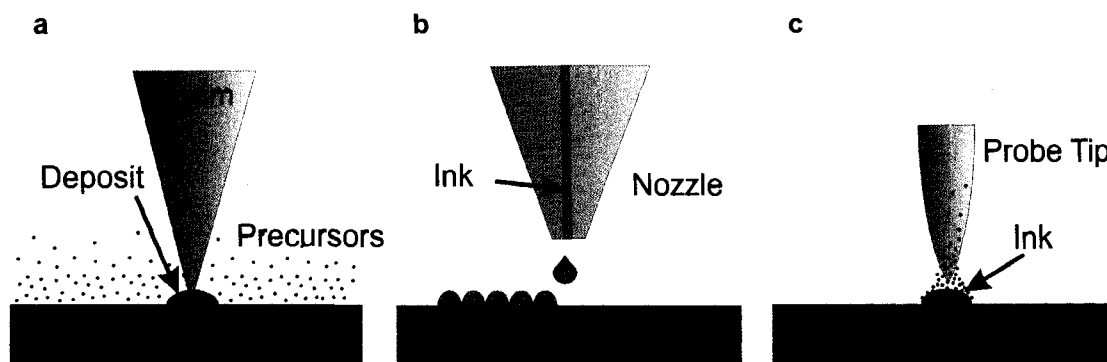


Figure 1.9. Schematic illustration of three different approaches for writing the patterns that uses add-on process. (a) Writing using laser-induced chemical vapor deposition, (b) inkjet printing, where ink is ejected from the nozzle and dispensed onto the substrate and (c) writing of ink with a pen, where the ink is delivered to the substrate in the tiny ink meniscus formed between tip and the surface.

Inkjet printing (IJP) is another technique for deposition of small amount of material on the substrate. The idea behind IJP is schematically depicted in Figure 1.9b. In this technique a small amount of liquid ink is ejected from a nozzle onto the substrate. The liquid ink can be deposited either as a continuous jet or in small droplets by applying acoustic or thermal pulses. The advantages of this technique are that this is a contact free technique, provides high throughput if many nozzles are used (parallel printing), allows to print simultaneously different materials from different nozzles and finally provides good control over the volume deposited. Nozzles typically 20-30 μm in diameter can deliver drop volumes about 10-20pl. The limitation to the resolution is mainly due to the statistical variations of the flight direction and the spreading of droplets on the surface and is limited to about 20-50 μm .

Dip-pen nanolithography (DPN) is a high resolution method for writing with liquid ink on substrates [1.35]. The ink is loaded on the AFM tip and delivered to the substrate through a thin liquid meniscus formed between the tip and the substrate with nanometer dimensions. The idea behind this approach is shown in Figure 1.9c. DPN was

successfully used to pattern a variety of materials such as gold [1.36], metal salts [1.37] and polymers [1.38].

Add-on writing is a useful technique for patterning materials that are not compatible with the resists or etching processes. It can also provide very good pattern control over the entire substrate.

1.2.1.2 Self-assembly

A system will self-assemble if appropriate interaction capabilities of its building blocks will aggregate them into well defined, stable structures. The size of the structures may vary from nanometers to millimeters. The final structure is created by equilibrium to the lowest energy state, when both repulsion and attraction forces are balanced. The building blocks can be divided in three categories depending on their length scales. The first one is molecular self-assembly. It uses interactions between molecules based on van der Waals, surface or electrostatic interactions [1.39]. The second category of building blocks is the assembly of nanoscale objects such as nanowires, nanotubes and related objects that form ordered arrays and lattices [1.40]. The third category is the objects with macroscale dimensions such as directed self-assembly of small objects (1 to 10mm in length) into regular, two-dimensional arrays as reported in [1.41].

Self-assembly of objects in the second and third categories rely mostly on external electromagnetic fields, gravitational forces or physical confinement to direct the assembly process.

1.2.1.2.1 Phase-Separated Block Copolymers

Block copolymers (BC) consist of two or more immiscible and chemically distinct polymer fragments joined by covalent bond [1.42]. These systems develop many different patterns at equilibrium with size and period of the structures typically 10-100nm [1.43]. Chemical differences between polymers allow for selective removal of one of them leaving porous array composed from the other polymer on the substrate that can serve as a mask for further processing. Typical equilibrium patterns with high density of nanometer size arrays are depicted in Figure 1.10a, b.

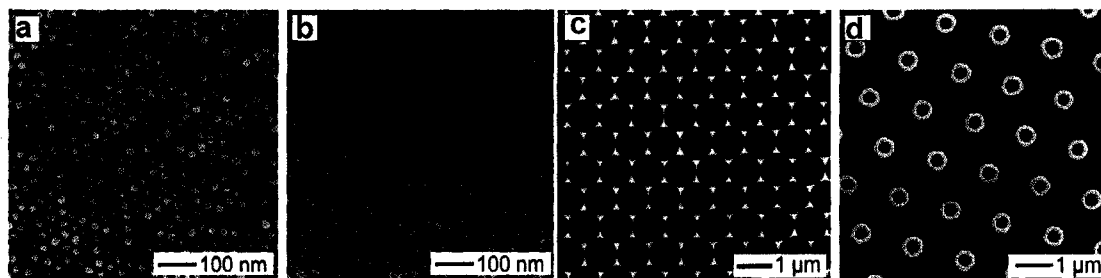


Figure 1.10. Examples of patterns fabricated using self-assembly methods. (a, b) SEM images of two different types of patterns fabricated in silicon nitride by using phase separated copolymer films as the mask for reactive ion etching. (c) SEM image of triangular pillars produced by evaporation of gold in the voids between self-assembled spheres on a silicon substrate. (d) SEM image of gold rings fabricated by spreading ink from the edges of silica beads assembled on a gold surface, followed by lift-off and etching. Picture taken from [1.10].

1.2.1.2.2 Nanosphere Lithography

Nanosphere lithography (NSL) is based on self-assembly of the monodispersed spherical beads on the surface forming a single layer with hexagonal symmetry that serves as a mask for subsequent processing [1.44]. By evaporation of the metal on the top of the mask and lift-off of the layer of beads, the arrays of triangular pillars can be

fabricated on the substrate. The results of nanosphere lithography are depicted in Figure 1.10c. It is also possible to use self-assembled spherical beads to spread a liquid ink on the surface of the substrate to form ring patterns, as depicted in Figure 1.10d. The advantage of NSL is that large areas can be patterned in a parallel fashion, however this technique is very sensitive to the defects and distortions in self-assembly and it is limited in terms of pattern design and complexity.

1.2.2 Replication of patterns

Pattern replication allows to reproduce the information stored in the surface of the mask or master onto the surface of the substrate in a single step, rapidly with high quality. The replication can be divided in three categories. The first category uses a mask placed between the source and the substrate that modulates the flux of the electromagnetic radiation or particles moving towards the substrate. The second category uses a master, against which patterns are duplicated using molding, embossing or printing. The last category combines all the techniques used to reproduce the edges of the structures known as edge lithography.

1.2.2.1 Duplication with a Mask

The key component is a photomask. It consists of alternating opaque and transparent features. The mask is imaged on or modulates the intensity of light that

illuminates the photoresist film. Photomasks are usually fabricated in quartz substrates, but flexible substrates such as foils might be also used if feature size is large (more than 50 μm).

1.2.2.1.1 Masked exposure to photons

This technique is also called photolithography or optical lithography [1.45]. It has been a driving force for the high volume manufacturing in semiconductor industry. Optical lithography can be carried out in three different modes depending on the relative position between the mask and the substrate. If the mask is in contact with the photoresist, this technique is called contact printing, if the mask is very close to the substrate it is called proximity printing and finally if the mask is imaged on the sample plane it is called projection lithography. Contact printing is often used in small volume prototyping usually in research laboratories, but is not well suited for high throughput manufacturing, high resolution and accuracy. Physical contact causes contamination and damage of the mask, as the replication is repeated many times, replication can be done always with 1:1 scale thus requires masks with the same resolution as the expected features in the wafer. Lateral shifts between the mask and the substrate during the exposure also may cause the degradation of the printed features. Proximity printing overcomes some of those limitations, but is still limited to 1:1 reproduction scheme. In the projection lithography an optical system is used to project the mask on the substrate plane. The mask is imaged on the sample plane with a de-magnification typically by a factor four. That releases some constraints about the mask fabrication. In the

semiconductor industry printing is based on step-and-repeat lithographic process using the tool called stepper, schematically depicted in Figure 1.11a.

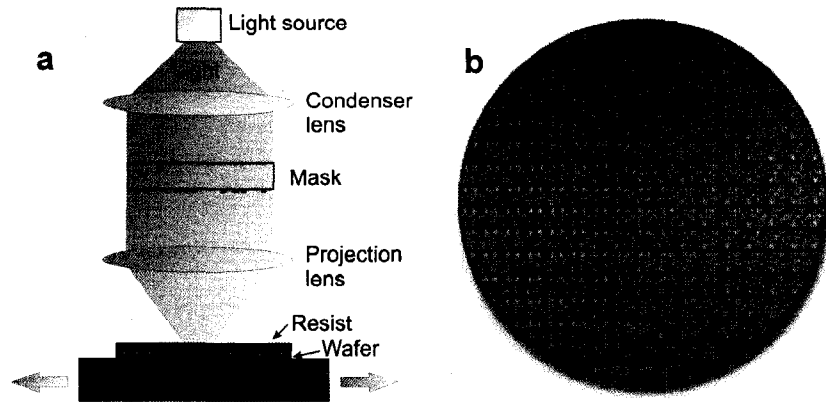


Figure 1.11. (a) Simplified schematic of the stepper. The image of the mask is projected on the surface of the photoresist with demagnification. Movable stage allows to repeat the printing process at different location on the same wafer. (b) Photograph of 12 inch diameter wafer with an array of Pentium IV processors in Intel's 130nm technology. Picture taken from [1.10].

These tools provide very good uniformity, accuracy and resolution over the whole surface of the wafer. The example of such a patterned wafer using photolithography process is shown in Figure 1.11b. Projection lithography is restricted by the diffraction limit. To keep pace with downsizing trend in the feature size one avenue has been to decrease the illumination wavelength. However the transition to shorter illumination wavelengths requires overcoming new technical challenges associated with development of the sources, new materials for the optical system, materials for the coatings and for masks, efficient photoresists, etc.

1.2.2.1.2 Masked etching and deposition

This approach is sometimes called dry lift-off. It involves the use of a stencil mask that contains void regions and directs the deposition or etching processes. The idea of the masked etching and deposition is schematically depicted in Figure 1.12a.

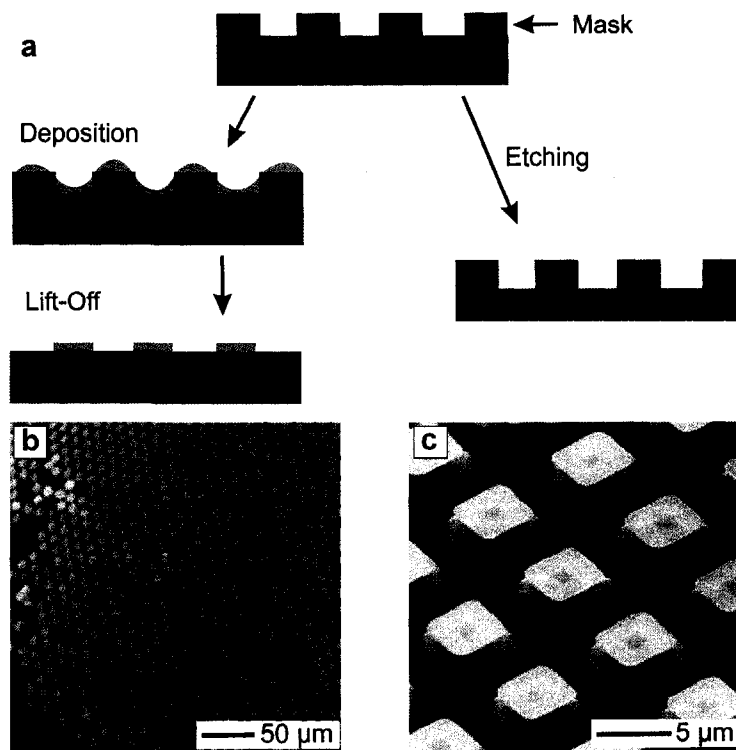


Figure 1.12. Masked deposition and etching. (a) Scheme of the procedure. (b) SEM image of the gold features formed on glass capillary by evaporation and mask removal. (c) SEM image of anisotropically etched pillars in silicon wafer with mask of gold squares patterned on a silicon substrate. Gold mask is still visible on the top of silicon pillars. Picture taken from [1.10].

Typically the mask is rigid and placed in proximity to the sample, sometimes the mask is made by patterning directly on the substrate. Features with sizes down to 20nm were demonstrated with the use of highly ordered and porous anodic alumina [1.46] used as a high resolution stencil mask. Polymers are also used as masks, when the substrate is

curved or uneven. Masked deposition works well with a variety of vaporizable metals, semiconductors and dielectrics. SEM image of the gold features formed on glass capillary (~1mm in diameter) by the evaporation using polymeric mask followed by the mask removal is depicted in Figure 1.12b. The disadvantage of the rigid masks is that they have to be freestanding and there is always a possibility of having a small gap between the mask and the substrate that will cause decreasing of edge resolution because of lateral diffusion of deposited material in the gap. Also deposition from the liquid phase is difficult.

In masked etching, the mask acts as a physical barrier to block the exposure to reactive etchant or particle bombardment. The etching rate depends on the material's crystallographic orientation and can result in selective etching in a given crystallographic orientation. Patterned features in the mask during the etching are transferred to the substrate with high fidelity and the depth in the direction normal to the sample plane can be controlled knowing the etching rate for both mask and material. If wet etching is used with crystal substrates like silicon, due to the anisotropy in etching rates for different crystallographic planes, tapered profiles might be obtained. This can be seen in Figure 1.12c that depicts the SEM image of anisotropically etched pillars in a silicon wafer with gold squares mask.

1.2.2.2 Replication with a master

A replication process with a master can be used to produce identical patterns or complimentary patterns to those on the master. It depends on the procedure used in the

experiment. Examples of this method include patterning of nonplanar substrates, large area fabrication or using materials that are incompatible with resists or developers. Using elastomeric masters instead of rigid ones also allow to modify the pattern by mechanical deformation of the master, which is another degree of freedom in controlling the pattern. By changing the applied pressure to the elastomeric master, change in the feature shape and size might be obtained.

1.2.2.2.1 Embossing using rigid master

This technique generates the patterns in the polymer by mechanical deformation. The polymer has to be thermoplastic, thermally or UV-curable or deformable to adapt to the master's surface. This is schematically depicted in Figure 1.13a where a rigid master is used to imprint the features into a deformable material using pressure.

A well known thermoplastic material often used is PMMA. The substrate coated with PMMA is heated above the glass-transition temperature during the mechanical imprinting and cooled below that temperature before separation from the master. This process is sometimes called hot embossing. If a thermally or UV-curable material is used, then the imprint is in the liquid phase and the material is then hardened by temperature or UV radiation. The resolution in this method depends on the mechanical properties of the master and the polymer properties such as wetting, adhesion, and viscosity. This technique was successfully used to pattern feature sizes up to tens on nanometers.

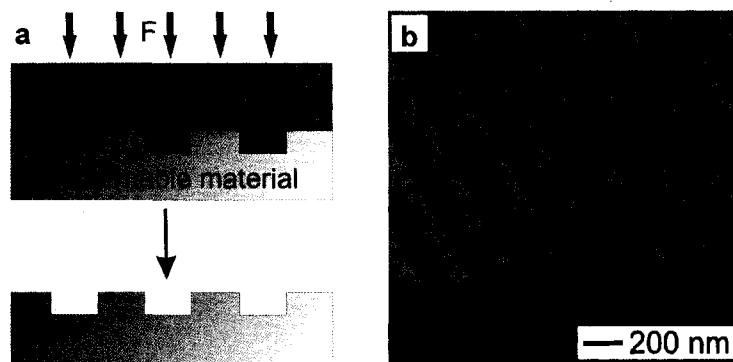


Figure 1.13. Embossing using rigid master scheme (a) to imprint the features into a deformable material using mechanical force. (b) SEM image of lines embossed in the thin layer of polymer. Picture taken from [1.10].

1.2.2.2.2 Molding with elastomeric master

In this process structures are formed in the void areas of the master or mold. Replica molding scheme is shown in Figure 1.14a where a liquid polymer is cast into the mold and cured into a solid state. This well known in macroscale technique was successfully applied to nanometer size patterning. With the use of proper materials the pattern of the mold can be transferred to the replica with very good accuracy.

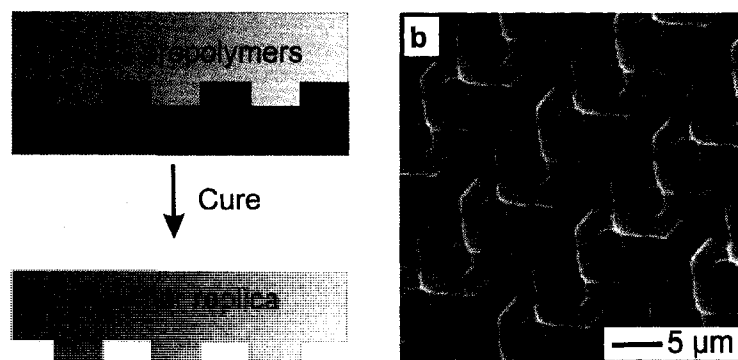


Figure 1.14. Replica molding scheme (a), liquid polymer is cast into the mold and cured into a solid state. (b) SEM image of the microstructures made in polyurethane with the use of PDMS mold. Picture taken from [1.10].

This technique has an important advantage because it allows to duplicate 3D structures in a single step, just by filling the empty spaces in the 3D mold. This is something that cannot be easily done using the other patterning techniques. Replica molding (REM) of organic polymers with polydimethylsiloxane (PDMS) molds is one method that gives very good overlay accuracy and pattern quality as shown in the SEM image of the microstructures made in polyurethane with the use of PDMS mold in Figure 1.14b. Elastomeric molds ensure easy releasing of the replicas. Features with vertical dimensions (height) down to ~2nm were fabricated in this way in PMMA, PDMS and polyurethane [1.47].

Solvent assisted micromolding (SAMIM) is another method in which a solvent is used to soften a polymeric material that can adopt in this way to the shape of the mold. With time, solvent evaporates or dissipates in other ways causing the polymer to be hard again preserving the pattern from the mold. SAMIM was successfully applied to various polymers including cellulose-acetate, Novolac-based photoresists and conducting polymers [1.48].

1.2.2.2.3 Printing using elastomeric stamp

This method involves a stamp to transfer patterned ink on a flat substrate. The scheme of microcontact printing is shown in Figure 1.15a. This is an additive process. Relief printing is one of the schemes using elastomeric stamps. It includes letterpress printing and flexographic techniques, in which the pattern is transferred from the raised regions of the stamp.

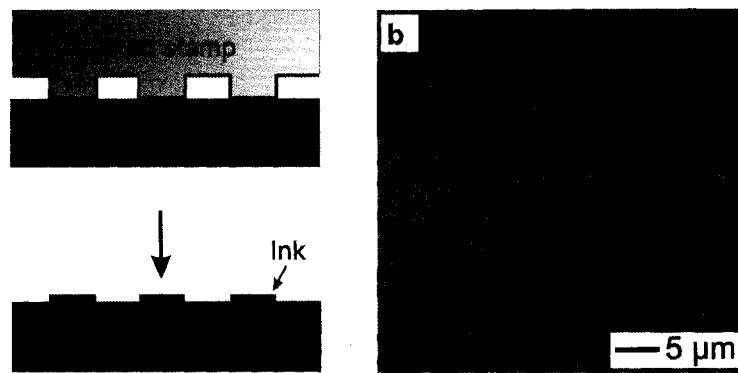


Figure 1.15. Scheme of microcontact printing (a). Stamp is used to define the pattern on the surface of the substrate. SEM image (b) of the patterns made in thin layer of silver by microcontact printing, followed by selective chemical etching of the regions unprotected by the ink. Picture taken from [1.10].

Microcontact printing (μ CP) belongs to the same category. It is based on inking the stamp with ink in liquid state, then drying the ink and finally bringing the stamp prepared in this way into contact with the surface of the substrate. Microcontact printing was demonstrated for a first time for self assembled monolayers (SAMs) alkanethiols on gold [1.49] but it works as well on other metals such as silver. An SEM image of the patterns made in a thin layer of silver by microcontact printing, followed by selective chemical etching of the regions unprotected by the ink is shown in Figure 1.15b. A feature size from $\sim 350\text{nm}$ to a couple of millimeters can be achieved with μ CP, while features with sub-100nm still remain a challenge.

1.2.2.2.4 Microfluidic patterning

Microfluidic patterning is based on the changing of liquid flow in small channels of microfluidic networks (μ FN). The size of these channels varies from 1-100 μm . The liquid is necessary to transport and to deposit very small amounts of materials on the

surface of the substrate. The scheme of the microfluidic patterning where small channels of microfluidic network are used to transport and deposit the material on the surface of the substrate or to remove some material from the surface by dissolution is depicted in Figure 1.16. Capillary forces dominate the motion of the liquid in the microchannels. Anyway external pumps are often necessary to mediate the flow of the liquid particularly if the distances are long. This type of patterning is often used in biology and biochemistry.

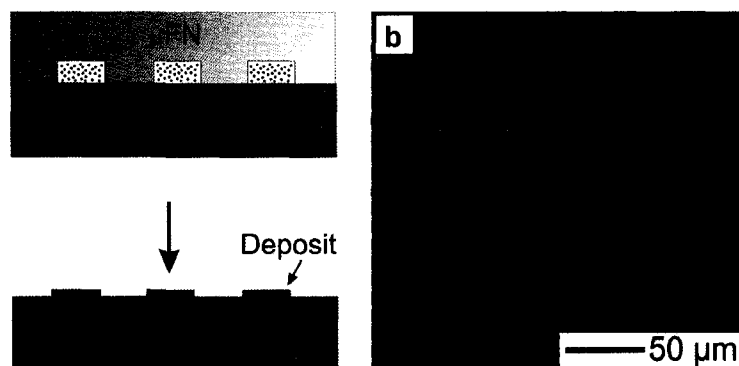


Figure 1.16. Microfluidic patterning (μ FN) scheme. (a) Small channels of microfluidic network are used to transport and deposit material on the surface of the substrate with spatial control. (b) A fluorescence microscopy of labeled proteins deposited on a PDMS substrate using sets of parallel channels made in silicon mold. Picture taken from [1.10].

1.2.2.3 Edge lithography

It is a common name for all the techniques in which the edges of the structures are the patterned features. These approaches are attractive alternatives to the other techniques when high resolution lines, circles, trenches or wires are the features one is looking for. One of these techniques is called near-field phase-shifting photolithography [1.50]. It is similar to the approach of contact lithography, but uses an elastomeric mask to have a

better contact with the photoresist film. The relief features in the mask are transparent to the illumination wavelength, but induce a phase change in the light that changes the intensity distribution at the photoresist surface. This leads to large unexposed or overexposed regions in the photoresist generating the sharp edges due to destructive and constructive interference in different regions. It is possible to obtain 50nm lines with 248nm illumination using this technique. An SEM image of silicon rings fabricated using near-field, phase-shifting optical lithography is depicted in Figure 1.17a.

Another interesting method is based on introducing the steps to metal surface or to use boundaries between different metal films that are submicron in width as the templates for deposition of other materials. Cross-section of the multilayered film fabricated using molecular beam epitaxy (MBE) was used as a template to deposit extremely thin lines in the selected regions. An SEM image of platinum nanowires fabricated using this technique is depicted in Figure 1.17b.

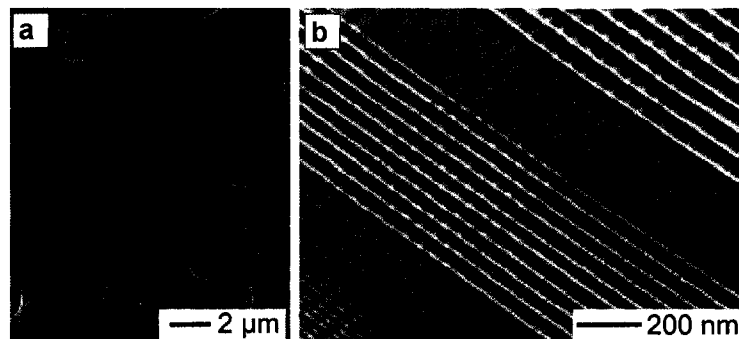


Figure 1.17. Examples of edge lithography. (a) SEM image of silicon rings fabricated using near-field, phase-shifting optical lithography. (b) SEM image of platinum nanowires fabricated using superlattice nanowire pattern transferring. Picture taken from [1.10].

This is called superlattice nanowire pattern transfer (SNAP) [1.51] and allows to transfer those lines onto the other substrates or stacking into multilayer lattices.

1.2.3 Three-Dimensional patterning

Precise control of all three dimensions is required to form 3D structures. 3D fabrication of microelectronic devices relies mainly on a layer-by-layer scheme in which the crucial step is to have an accurate alignment between masks.

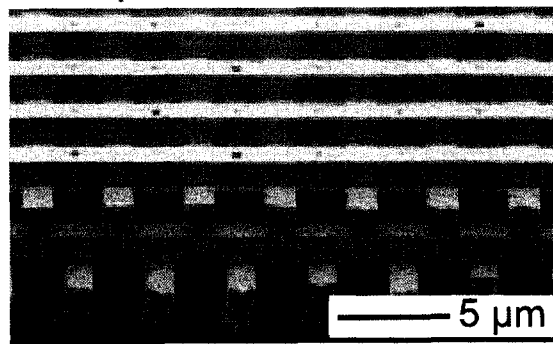


Figure 1.18. SEM image of 3D structure of tungsten bars fabricated in layer-by-layer fashion using multiple mask scheme. Picture taken from [1.10].

Although this scheme is universal and allows to fabricate arbitrary structures, the accumulation of defects increases with the number of layers.

1.2.3.1 Writing using focused laser or electron beams

A very interesting example of 3D writing using two-photon polymerization (TPA) was reported as an attractive tool for the fabrication of arbitrary patterns. The polymerization will occur only at the focal point of the laser beam creating a voxel. Voxel is a three dimensional (volume) element of the polymerized resist. Patterning of arbitrary structures is performed by raster scanning the focal spot in the resist in

three dimensional space according to designed and preprogrammed pattern (matrix of voxels). The SEM image of the bull sculpture fabricated in the polymer resist by two-photon absorption in the resist induced by raster scanning of a laser beam is depicted in Figure 1.19. The voxel size depends on the focal spot size and energy of the laser beam.

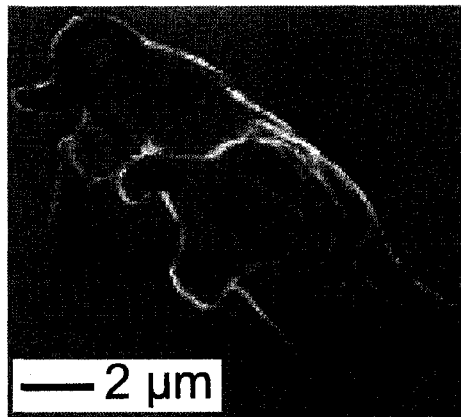


Figure 1.19. The SEM image of the bull sculpture fabricated in the polymer resist by two-photon absorption in the resist induced by raster scanning of a laser beam. Picture taken from [1.10].

1.2.3.2 Gray scale lithography

In conventional lithography masks are usually binary consisting of alternating opaque and transparent regions, with the same transmission coefficients. This results in having all the features approximately of the same height. Using binary masks for 3D fabrication is not efficient because requires multiple exposures with precise realignment of each mask. This is very time consuming, expensive and might have many defects in the resulting pattern. Photolithography using gray-scale masks overcomes these limitations allowing patterning 3D profiles similar to Figure 1.20.

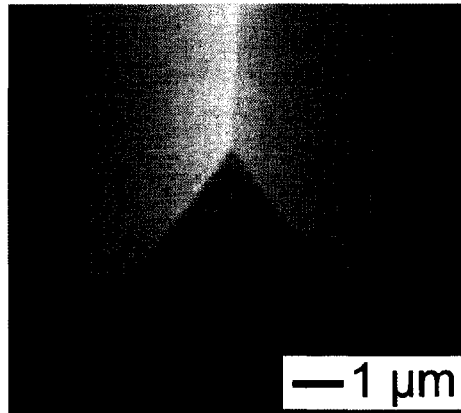


Figure 1.20. SEM image of the photoresist line with triangular profile produced by photolithography using gray-scale mask. Picture taken from [1.10].

In this case the grayscale mask has variable transparency and encodes the final shape proportional to the optical density map of the mask and variable intensity exposing the resist. Gray scale masks are usually made of chromium deposited on the glass. The thickness of the chromium film, that absorbs the light, defines the gray levels in the mask. Another approach is to use glass doped with silver atoms for example. The density of the dopant changes the transmission of the mask and sets the gray scale levels.

1.3 Overview of Sources

Synchrotron and free electron lasers (FEL) are able to provide high intensity EUV pulses and tunable output wavelengths. Synchrotrons utilize a narrow confined beam of charged particles like electrons for example (sometimes other particles like protons) redirected by the magnetic field that travels in a closed loop. The particles in synchrotron have to be accelerated to velocities approaching the speed of light. Magnetic field redirects the particle beam, while electric field accelerates them. Charged particles under

acceleration emit photons, and lose the energy. The limiting beam energy is reached when the energy lost to the lateral acceleration required to maintain the circular beam path equals the energy added in each cycle.

In a FEL a beam of electrons is accelerated to relativistic speeds. The beam passes through a periodic, alternating transverse magnetic field. This field is produced by an assembly of magnets with alternating poles along the beam path. This array of magnets (“wiggler”) forces the beam of electrons to travel in a sinusoidal path. The acceleration due to changing the direction of propagation of the electrons results in losing the energy by releasing photons.

The main limitation of synchrotrons or FEL devices is their size. Both facilities are the size of a large building and cost millions of dollars. The scale of the synchrotron facility like Advanced Photon Source in Argonne National Lab for example is depicted in Figure 1.21.

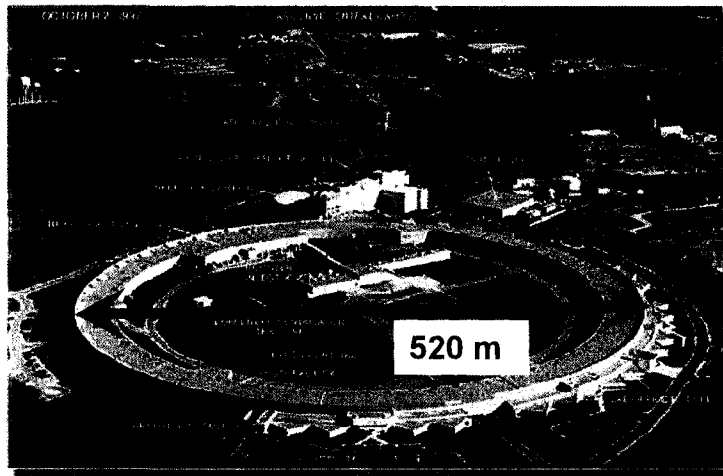


Figure 1.21. Advanced Photon Source, Argonne National Lab [1.52]

The experimental testbed must be brought to the facility and the beam-time has to be booked before the experiment begins which in fact might be inconvenient in some cases. To have a fully spatially coherent beam often pinholes with micrometer size diameter have to be used, that limits the useful photon flux. The bandwidth of the emitted radiation changes between 2.5% and 4% depending on the photon energies [1.53], $\lambda/\Delta\lambda \sim 25-40$ and the temporal coherence length may be in micrometer range. The remedy to that is to use the interferometry station that includes a spherical grating monochromator for example which reduces the spectral bandwidth to about $\Delta\lambda/\lambda \sim 0.1\%$ or use the selective optics, for example multilayer mirrors which will narrow the bandwidth after each reflection. This is however also associated with serious photon flux loss.

The development of the tabletop sources has made important advances in the EUV research field. The tabletop source is usually small in size and may be set up conveniently in the lab. EUV sources, high harmonic generation (HHG) and soft X-ray lasers are the three most notable ones that can be called tabletop sources.

EUV sources are often based on Z-pinch. Z-pinch is a type of plasma confinement that uses an electrical current flowing in the plasma to compress it by the generation of a magnetic field. The electrons in the plasma are all pulled toward each other by the Lorentz force and the plasma contracts in the direction perpendicular to the direction of the current flow. The plasma in the source is magnetically confined far away from the electrodes which helps minimizing the heat load and reducing debris from the heated surfaces.

These EUV sources can be used for metrology, resist evaluation, EUV microscopy or defect inspection. They are compact and can easily be fitted in a small

laboratory. They also provide very high output power, but emit incoherent radiation into a wide bandwidth and a large solid angle, thus the usable power is much smaller than the total output power.

High harmonic generation (HHG) sources are tabletop sources capable to fit on a single optical table. The example of high harmonic generation source is shown in Figure 1.22. HHG produces short wavelength radiation in the EUV region down to soft X-rays. It is a nonlinear process that involves a laser capable of producing femtosecond pulses (typically a Ti:sapphire oscillator with a single stage amplifier) and a noble gas. In the classical picture, the electric field of the ultrafast laser pulse interacts with the individual gas atoms pulling their electrons apart from the nucleus. As the electrons change their paths, de-accelerate and travel back towards the nucleus. The change in the electron's path results in the emission of photons. Usually monoatomic gasses are used, having intrinsic symmetry. Due to a comb-like excitation of the atoms and their symmetric responses on the driving electric field the resulting burst of radiation from the atom occurs twice in an optical cycle and transformed to the spectral domain has only odd harmonics.



Figure 1.22. Example of high harmonic generation source from James R. Macdonald Laboratory, An Atomic, Molecular & Optical Physics Research Facility [1.54].

Complex (having a non symmetric response on the driving electric field) gasses can have also even harmonics. Although only a tiny fraction of the laser power can be converted into higher harmonics, this can still be used for measurements down to wavelengths in EUV or even in the X-ray spectral region. Also those sources generate pulses with attosecond durations in the EUV spectral region. Intensities of the laser pulse are below ionization intensities, usually 10^{14} - 10^{15} W/cm² with typical pulse duration of 20-100fs [1.55]. Harmonics typically appear in a narrow forward radiation cone. Also those sources generate pulses with attosecond durations in the EUV spectral region. The divergence half angle is usually less than ~ 1 rad [1.55]. High harmonics sources are a very elegant solution with tunable short wavelength output and coherence similar to that of synchrotrons. It is also very compact with high repetition rate (up to 100kHz) and requires very low maintenance as compared with large facilities. The pulse width from this source has femto-second time duration. The main disadvantage however is the small flux. The energy per pulse is in nJ range. Experiments often require a few hours of operating at 30kHz repetition rate to acquire necessary exposure dose.

A very unique EUV source is the table top capillary discharge laser developed at Colorado State University. The photograph of the laser is shown in Figure 1.23. A bright laser source produces 46.9 nm wavelength radiation with energy per pulse up to 0.8mJ with 36cm capillary length and repetition rate up to 4Hz [1.56]. The source emits a highly spatially and temporarily coherent beam.

A smaller version of this laser was demonstrated by Heinbuch et al. [1.57]. The desk-top version shown in Figure 1.24 is capable to produce nano-second laser pulses at 46.9nm with energy per pulse up to 13 μ J and repetition rate up to 12Hz.

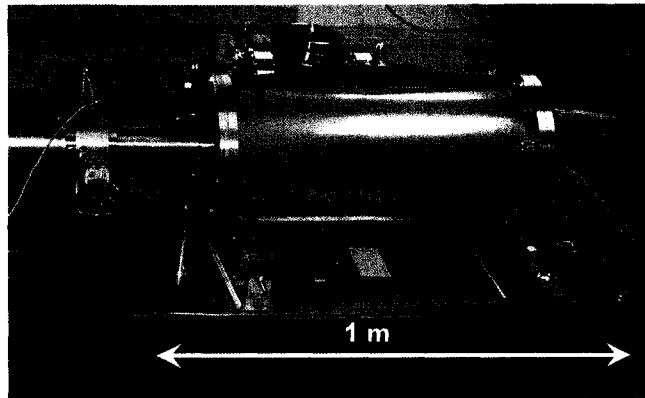


Figure 1.23. Capillary Discharge Laser generates ns laser pulses with energy up to 0.8mJ/pulse, high repetition rate. The laser beam has very good spatial and temporal coherence properties.

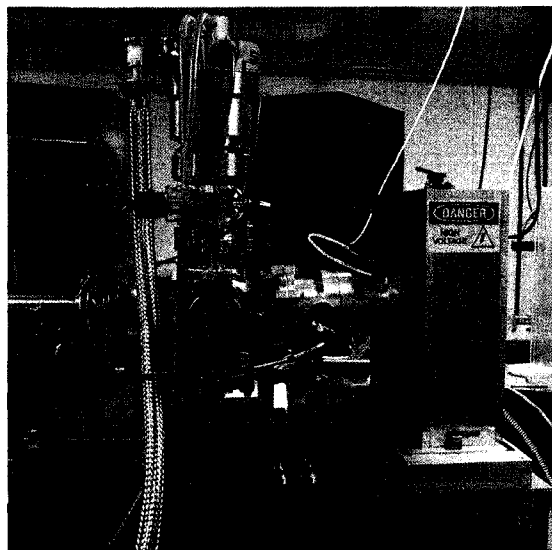


Figure 1.24. Desk-top version of the Capillary Discharge Laser. Much more compact with energy per pulse about 13 μ J and repetition rate up to 12Hz.

Capillary discharge lasers provide the highest temporal and spatial coherence among the all table top sources considered in this section (a fraction of a millimeter coherence radius and coherence length). The systems are very compact, comfortably fitting on the optical table or are even the size of a desktop computer. These sources provide the highest brightness at the particular emission wavelength, high energy per pulse in mJ region, but

are not tunable. Both EUV laser sources were used in the experiments presented in this dissertation and described in detail in the next chapters.

-
- [1.1] F. Brizuela, G. Vaschenko, C. Brewer, M. Grisham, C. S. Menoni, M. C. Marconi, J. J. Rocca, W. Chao, J. A. Liddle, E. H. Anderson, D. T. Attwood, A. V. Vinogradov, I. A. Artioukov, Y. P. Pershyn and V. V. Kondratenko, "Reflection mode imaging with nanoscale resolution using a compact extreme ultraviolet laser," *Optics Express* **13**, 3983 (2005)
- [1.2] *Microelectromechanical Systems: Technology and Applications*, a special issue of *MRS Bull.* **26**, 282 (2001)
- [1.3] I. Fraden, *Handbook of Modern Sensors: Physics, Design and Applications*, 3rd ed., (Springer Verlag, New York, 2004)
- [1.4] *Nanofabrication and Biosystems: Integrating Materials, Science, Engineering, and Biology*, (Eds: H. C. Hoch, L. W. Jelinski, H. G. Craighead), (Cambridge University Press, New York 1996)
- [1.5] L. Baharudin, "Microfluidics: Fabrications and applications", *Instrumentation Science and Technology*, **36**, 222 (2008)
- [1.6] D. J. Campbell, K. E. Korte, Y. N. Xia, "Fabrication and analysis of photonic crystals", *Journal of Chemical Education*, **84**, 1824 (2007)
- [1.7] E. H. Anderson, D. L. Olynick, B. Harteneck, E. Veklerov, G. Denbeaux, W. L. Chao, A. Lucero, L. Johnson, D. Attwood, "Nanofabrication and diffractive optics for high-resolution x-ray applications", *Journal of Vacuum Science and Technology B*, **18**, 2970, (2000)
- [1.8] E. Reichmanis, L. F. Thompson, "Polymer materials for microlithography", *Chem. Rev.* **89**, 6, 1273 (1989)
- [1.9] Y. Xia, J. A. Rogers, K. E. Paul, G. M. Whitesides, "Unconventional Methods for Fabricating and Patterning Nanostructures", *Chem. Rev.* **99**, 7, 1823 (1999)
- [1.10] M. Geissler, Y. Xia, "Patterning: Principles and Some New Developments", *Adv. Matter*, **16**, 15 (2004)
- [1.11] R. M. Nyffenegger, R. M. Penner, "Nanometer-Scale Surface Modification Using the Scanning Probe Microscope: Progress since 1991", *Chem. Rev.* **97**, 4, 1195 (1997)
- [1.12] G. Binnig, M. Despont, U. Drechsler, W. Häberle, M. Lutwyche, P. Vettiger, H. J. Mamin, B. W. Chui, T. W. Kenny, " Ultrahigh-density atomic force microscopy data storage with erase capability", *Appl. Phys. Lett.* **74**, 1329 (1999)

-
- [1.13] S. Xu, S. Miller, P. E. Laibinis, G. Y. Liu, "Fabrication of Nanometer Scale Patterns within Self-Assembled Monolayers by Nanografting", *Langmuir* **15**, 21, 7244 (1999)
- [1.14] T. Sumomogi, T. Endo, K. Kuwahara, R. Kaneko, T. Miyamoto, "Micromachining of metal surfaces by scanning probe microscope", *J. Vac. Sci. Technol. B* **12**, 1876 (1994)
- [1.15] R. Resch, C. Baur, A. Bugacov, B. E. Koel, A. Madhukar, A. A. G. Requicha, P. Will, "Building and Manipulating Three-Dimensional and Linked Two-Dimensional Structures of Nanoparticles Using Scanning Force Microscopy", *Langmuir*, **14**, 23, 6613 (1998)
- [1.16] A. A. Tseng, Z. Li, "Manipulations of atoms and molecules by scanning probe microscopy", *Journal of Nanoscience and Nanotechnology*, **7**, 2582 (2007)
- [1.17] M.F. Crommie, C.P. Lutz, D.M. Eigler, "Confinement of electrons to quantum corrals on a metal surface", *Science* **262**, 218-220 (1993)
- [1.18] <http://spiff.rit.edu/classes/phys314/lectures/stm/stm.html> as in July 2008
- [1.19] *Laser Processing and Chemistry*, (Ed: D. Bäuerle), 3rd ed., (Springer Verlag, Berlin, Germany, 2000)
- [1.20] H. Heinzelmann, D. W. Pohl, "Scanning near-field optical microscopy (SNOM)", *Appl. Phys. A* **59**, 89 (1994)
- [1.21] I. I. Smolyaninov, D. L. Mazzoni, C. C. Davis, "Near-field direct-write ultraviolet lithography and shear force microscopic studies of the lithographic process", *Appl. Phys. Lett.* **67**, 3859 (1995)
- [1.22] S. Sun, K. S. L. Chong, G. J. Leggett, "Nanoscale Molecular Patterns Fabricated by Using Scanning Near-Field Optical Lithography", *J. Am. Chem. Soc.* **124**, 2414 (2002)
- [1.23] J. Fujita, H. Watanabe, Y. Ochiai, S. Manako, J. S. Tsai, S. Matsui, "Sub-10 nm lithography and development properties of inorganic resist by scanning electron beam", *Appl. Phys. Lett.* **66**, 3065 (1995)
- [1.24] D. R. Medeiros, A. Aviram, C. R. Guarnieri, W. S. Huang, R. Kwong, C. K. Magg, A. P. Mahorovala, W. M. Moreau, K. E. Petrillo, M. Angelopoulos, "Recent progress in electron-beam resists for advanced mask-making", *IBM J. Res. Dev.* **45**, 639 (2001)

-
- [1.25] A. J. Bard, G. Denauld, C. Lee, D. Mandler, D. O. Wipf, "Scanning electrochemical microscopy - a new technique for the characterization and modification of surfaces", *Acc. Chem. Res.* **23**, 11, 357 (1990)
- [1.26] G. S. Hsiao, R. M. Penner, J. Kingsley, "Deposition of metal nanostructures onto Si(111) surfaces by field evaporation in the scanning tunneling microscope", *Appl. Phys. Lett.* **64**, 1350 (1994)
- [1.27] S. Kondo, S. Heike, M. Lutwyche, Y. Wada, "Surface modification mechanism of materials with scanning tunneling microscope", *J. Appl. Phys.* **78**, 155 (1995)
- [1.28] D. M. Eigler, E. K. Schweizer, "Positioning single atoms with a scanning tunnelling microscope", *Nature* **344**, 524 (1990)
- [1.29] K. Wilder, C. F. Quate, D. Adderton, R. Bernstein, V. Elings, "Noncontact nanolithography using the atomic force microscope", *Appl. Phys. Lett.* **73**, 2527 (1998)
- [1.30] H. Lee, S. A. Kim, S. J. Ahn, "Positive and negative patterning on a palmitic acid Langmuir-Blodgett monolayer on Si surface using bias-dependent atomic force microscopy lithography", *Appl. Phys. Lett.* **81**, 138 (2002)
- [1.31] C. L. Dennis, R. P. Borges, L. D. Buda, U. Ebels, J. F. Gregg, M. Hehn, E. Jouguelet, K. Ounadjela, I. Petej, I. L. Prejbeanu, M. J. Thornton, "The defining length scales of mesomagnetism: a review", *J. Phys. Condens. Matter*, **14**, R1175 (2002)
- [1.32] C. A. Ross, "Patterned magnetic recording media", *Annu. Rev. Mater. Sci.* **31**, 203 (2001)
- [1.33] D. Bäuerle, R. Denk, J. D. Pedaring, K. Piglmayer, J. Heitz, G. Schrems, "Perspectives of laser processing and chemistry", *Appl. Phys. A* **77**, 203 (2003)
- [1.34] M. T. Reetz, M. Winter, G. Dumpich, J. Lohau, S. Friedrichowski, "Fabrication of Metallic and Bimetallic Nanostructures by Electron Beam Induced Metallization of Surfactant Stabilized Pd and Pd/Pt Clusters", *J. Am. Chem. Soc.* **119**, 19, 4539 (1997)
- [1.35] D. S. Ginger, H. Zhang, C. A. Mirkin, "The Evolution of Dip-Pen Nanolithography", *Angew. Chem. Int. Ed.* **43**, 30, (2003)
- [1.36] R. D. Piner, J. Zhu, F. Xu, S. Hong, C. A. Mirkin, "Dip-Pen" Nanolithography", *Science*, **283**, 661 (1999)
- [1.37] Y. Li, B. W. Maynor, J. Liu, "Electrochemical AFM "Dip-Pen" Nanolithography", *J. Am. Chem. Soc.* **123**, 2105 (2001)

-
- [1.38] J. H. Lim, C. A. Mirkin, "Electrostatically Driven Dip-Pen Nanolithography of Conducting Polymers", *Adv. Mater.* **14**, 1474 (2002)
- [1.39] H. Ringsdorf, B. Schlarb, J. Venzmer, "Molecular Architecture and Function of Polymeric Oriented Systems: Models for the Study of Organization, Surface Recognition, and Dynamics of Biomembranes", *Angew. Chem. Int. Ed. Engl.*, **27**, 1, 113 (1998)
- [1.40] S. Park, J. H. Lim, S. W. Chung, C. A. Mirkin, "Self-Assembly of Mesoscopic Metal-Polymer Amphiphiles", *Science*, **303**, 348 (2004)
- [1.41] N. Bowden, A. Terfort, J. Carbeck, G. M. Whitesides, "Self-Assembly of Mesoscale Objects into Ordered Two-Dimensional Arrays", *Science* **276**, 5310, 233 – 235 (1997)
- [1.42] F. S. Bates, G. H. Fredrickson, "Block Copolymers—Designer Soft Materials", *Phys. Today*, **52**, 2, 32 (1999)
- [1.43] H. Yokoyama, T. E. Mates, E. J. Kramer, "Structure of Asymmetric Diblock Copolymers in Thin Films", *Macromolecules*, **33**, 5, 1888 (2000)
- [1.44] C. B. Roxlo, H. W. Deckman, B. Abeles, "Molecular Confinement in Nanometer-Size Superlattice Microstructures", *Phys. Rev. Lett.* **57**, 2462 (1986)
- [1.45] Optical lithography, a special issue of *IBM J. Res. Dev.* **41**, 1-2 (1997)
- [1.46] D. H. Pearson, R. J. Tonucci, "Parallel patterning with nanochannel glass replica membranes", *Adv. Mater.* **8**, 12, 1031 (1996)
- [1.47] B. D. Gates, G. M. Whitesides, "Replication of Vertical Features Smaller than 2 nm by Soft Lithography", *J. Am. Chem. Soc.* **125**, 49, 14986 (2003)
- [1.48] J. A. Rogers, Z. Bao, L. Dhar, "Fabrication of patterned electroluminescent polymers that emit in geometries with feature sizes into the submicron range", *Appl. Phys. Lett.* **73**, 294 (1998)
- [1.49] A. Kumar, G. M. Whitesides, "Features of gold having micrometer to centimeter dimensions can be formed through a combination of stamping with an elastomeric stamp and an alkanethiol "ink" followed by chemical etching", *Appl. Phys. Lett.* **63**, 2002 (1993)
- [1.50] Y. Yin, B. Gates, Y. Xia, "A soft lithographic approach to the fabrication of nanostructures of single crystalline silicon with well-defined dimensions and shapes", *Adv. Mater.* **12**, 1426 (2000)

-
- [1.51] Y. C. Chang, L. L. Chang, L. Esaki, "A new one-dimensional quantum well structure", *Appl. Phys. Lett.* **47**, 1324 (1985)
- [1.52] <http://www.anl.gov>, as in October 2007,
- [1.53] H. H. Solak, D. He, W. Li, F. Cerrina "Nanolithography using extreme ultraviolet lithography interferometry: 19 nm lines and spaces", *J. Vac. Sci. Technol. B* **17**, 6, (1999)
- [1.54] <http://jrm.phys.ksu.edu/scripts/beam-gallery.pl?KLS-Apr2006>, as in October 2007,
- [1.55] D. Attwood, *Soft X-rays and Extreme Ultraviolet Radiation: Principles and Applications*, (Cambridge Univ. Press, 1999).
- [1.56] C.D. Macchietto, B.R. Benware, and J.J. Rocca, "Generation of millijoule-level soft-x-ray laser pulses at a 4-Hz repetition rate in a highly saturated tabletop capillary discharge amplifier," *Optics Letters* **24**, 1115, (1999).
- [1.57] S. Heinbuch, M. Grisham, D. Martz, and J.J. Rocca, "Demonstration of a desk-top size high repetition rate soft x-ray laser", *Optics Express* **13**, 4050, (2005).

CHAPTER 2

2 Capillary Discharge Laser description

The idea of capillary discharge lasers was born in 1988 when the development of soft X-ray lasers was first proposed by Rocca et al. [2.1]. As amplification media for soft X-ray radiation plasmas generated by direct current discharge excitation in long capillaries with large length-to-diameter ratios ($L/d > 100$) were proposed. The capillary geometry was thought to provide a small volume and a resistance for Ohmic heating. Heat conduction to the capillary walls responsible for rapid plasma cooling during the decaying of the excitation current pulse allowed a large recombination rate and a population inversion.

The capillary discharge laser used in this work is based on the same idea of creating the plasma in a long channel (capillary) and rapid plasma excitation by a fast current discharge. The energy stored in the capacitor is suddenly released by the spark-gap switch and further excites pre-ionized gas inside the capillary. Low inductance capacitor and fast spark-gap switch allows to obtain current pulses of approximately tens of kA with a current rise time typically 10-40ns [2.2]. The fast current pulse flowing through the plasma inside the capillary by means of Lorentz force compresses the plasma column towards the axis of the capillary to achieve very hot filamentary plasma channel.

Inside this channel a population inversion is created and due to the relaxation of the ions to the ground level high energy photons are released and EUV radiation is produced. The geometry of the capillary may have stabilizing effect on the plasma column creating highly symmetrical initial conditions as it is compressed inward by the Lorentz force down to 200-300 μm diameter generating high aspect ratio (1000:1) plasma column. The short current rise time leads to faster plasma compression generating strong population inversion and generation of the short wavelength radiation and minimizing the amount of material ablated from the capillary walls by the magnetic field that detaches the plasma from the walls [2.2].

So far two approaches were most successful in generating high intensity soft X-ray radiation. One of them was by creating plasma inside the capillary from the gas medium. Argon lasers emitting at 46.9nm [2.3] and chlorine table top EUV lasers radiating at 52.9nm [2.4] were demonstrated. The second approach proved that high amplification in the discharge created plasmas is also possible in the elements that are solid at the room temperature. Neon like sulfur lasing at 60.84nm [2.5] was performed by ablating auxiliary sulfur capillary and injecting the sulfur vapor into the main capillary channel through the hole in a ground electrode and subsequently exciting the vapors by the fast current pulse. The most successful and with the highest energy per laser pulse system with the shortest wavelength was based on argon plasma. Argon based capillary discharge laser is a bright laser source producing 46.9nm wavelength radiation. A compact discharge-pumped Ne-like Ar capillary laser occupies a footprint of 0.4 x 1m². The laser is depicted in Figure 2.1.

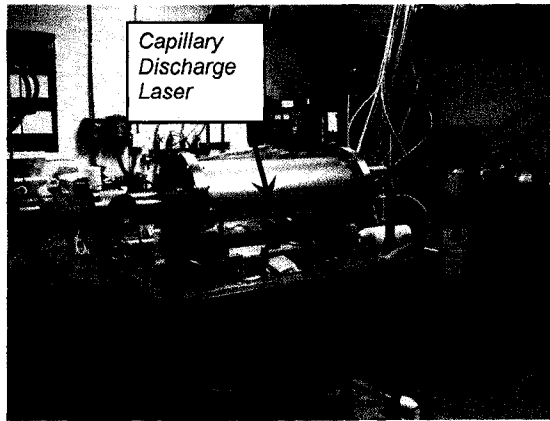


Figure 2.1. Capillary Discharge Laser, compact device with 0.4x1m² footprint. In the back Marx generator used to charge the water dielectric capacitor.

2.1 Principle of operation

The table-top size Ne-like Ar laser is based on a pulsed excitation produced by a high current pulse delivered by a discharge of a large liquid dielectric capacitor that is charged to high voltage about 200kV by a multistage voltage amplifier - Marx generator [2.6, 2.7]. The schematic of the capillary discharge laser is shown in Figure 2.2 where main components such as the capillary and the spark-gap switch attached to the capacitor's inner electrode are indicated.

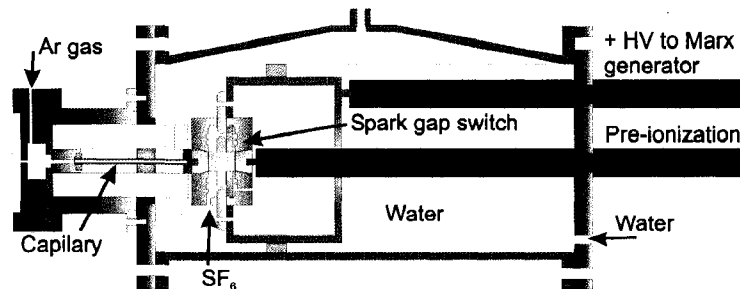


Figure 2.2. Schematic diagram of a table-top capillary discharge laser based on a water dielectric capacitor. The liquid dielectric capacitor is charged to ~ 200 kV and rapidly discharged through the spark-gap switch by the capillary load.

Lasing takes place in the $3s\ ^1P_1 - 3p\ ^1S_0$ transition of Neon-like Ar by exciting Ar in an alumina capillary 3.2mm in diameter with a current pulse having an amplitude of ≈ 24 kA [2.3, 2.8]. The fast current pulse (10% to 90% rise time of ~ 50 ns for 27cm capillary length) is produced by discharging a water dielectric cylindrical capacitor through a spark gap switch connected in series with the capillary load. The current pulse rapidly compresses the plasma column to achieve a dense and hot filamentary plasma channel where a population inversion is created by strong monopole electron impact excitation of the laser upper level and rapid radiative relaxation of the laser lower level [2.9]. The water serves as the dielectric for the capacitor ($\epsilon_r \sim 78.4$ at 25 °C) and also cools the capillary. A continuous flow of Ar is injected in the front of the capillary. The laser was operated in most experiments with 27cm long capillaries and an optimum Ar gas pressure of 490 mTorr maintained in the capillary channel to produce ~ 0.15 mJ laser pulses with half angle divergence of ~ 4.5 mrad at a repetition rate of 1Hz. The laser beam footprint shows a characteristic annular shaped beam. To obtain highest intensity the argon pressure in the capillary should be ~ 500 mTorr. At this argon pressure larger plasma density gradients and higher electron densities are generated as the result of higher compression [2.10]. With the decrease of the gas pressure the beam refraction from the axis increases due to the larger plasma density gradients in the capillary plasma column. Detailed computer simulations show that as the pressure decreases, the refraction losses and the gain coefficient become larger generating more intense laser beam and deflecting a central portion of the laser beam away from the axis producing a region of lower intensity in the center of the beam footprint as can be seen in Figure 2.3a. The

emission is highly monochromatic as can be seen in the spectrum of the laser output [2.9] depicted in Figure 2.3b.

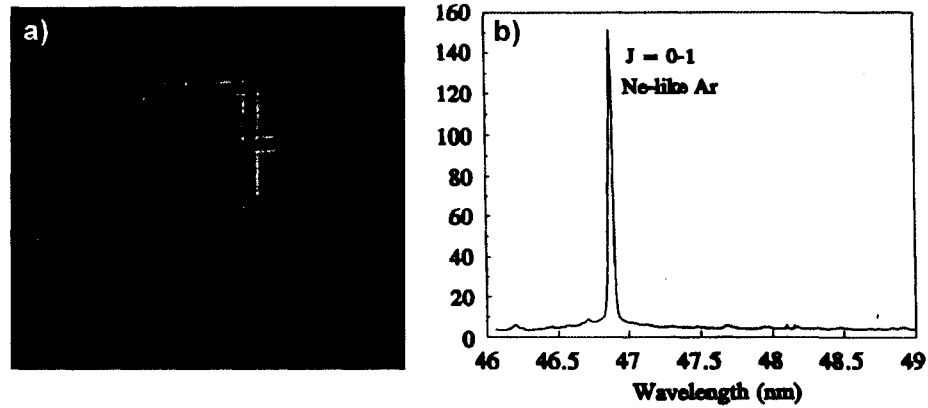


Figure 2.3. Capillary Discharge Laser characteristics: a) 46.9nm laser beam footprint with Al filter and supporting mesh, b) spectrum of the laser output emission shows high monochromaticity of this source ($\lambda/\Delta\lambda > 10^4$) [2.12].

2.2 Laser coherence parameters

The laser beam has very high spatial and temporal coherence. The longitudinal coherence length of $\sim 470\mu m$ is determined by the linewidth that is mainly limited by the Doppler broadening of the laser transition.

The degree of spatial coherence is calculated from the fringe visibility from the measurements made using a Young's double slit interferometer. According to [2.11] the intensity at the CCD location shown in Figure 2.4a can be expressed in terms of the complex degree of coherence $I = I_1 + I_2 + 2\sqrt{I_1}\sqrt{I_2}|\gamma_{12}(\tau)|\cos[\alpha_{12}(\tau) - \delta]$, where $\tau = \frac{s_2 - s_1}{c}$ is a delay time between two interferometer's arms and $\delta = k(s_2 - s_1)$ is a relative phase accumulation between the arms. Assuming that the light is quasi-

monochromatic, $\gamma_{12}(\tau)$ and $\alpha_{12}(\tau) = 2\pi f\tau + \arg \gamma_{12}(\tau)$ change slowly compared to $\cos(\delta)$. Also, if the openings in the pinhole mask are small enough, one can assume the intensities $I_1 = I_2 = I_0$ introducing a uniform background I_0 with superimposed sinusoidal intensity modulation with constant amplitude $2\sqrt{I_1}\sqrt{I_2}|\gamma_{12}(\tau)|$. This leads to the intensity minima $I_{\min} = I_1 + I_2 - 2\sqrt{I_1}\sqrt{I_2}|\gamma_{12}(\tau)|$ and intensity maxima $I_{\max} = I_1 + I_2 + 2\sqrt{I_1}\sqrt{I_2}|\gamma_{12}(\tau)|$. Consequently the fringe visibility is equal to $V = \frac{I_{\max} - I_{\min}}{I_{\max} + I_{\min}} = \frac{2\sqrt{I_1}\sqrt{I_2}}{I_1 + I_2}|\gamma_{12}(\tau)|$ and with the assumption of equal beam intensities $I_1 = I_2 = I_0$ will lead to the fact, that the measured visibility of the fringes is equivalent to the degree of coherence $V = |\gamma_{12}(\tau)|$.

The spatial coherence was measured by Liu et al. [2.12] in the following experiment. A masks consisted of two 10 μm diameter laser-drilled pinholes at different separations on 12.5 μm thick stainless-steel substrates were placed in front of the laser beam and the interference pattern was recorded in the CCD camera placed 3m away from the mask, as schematically depicted in Figure 2.4a.

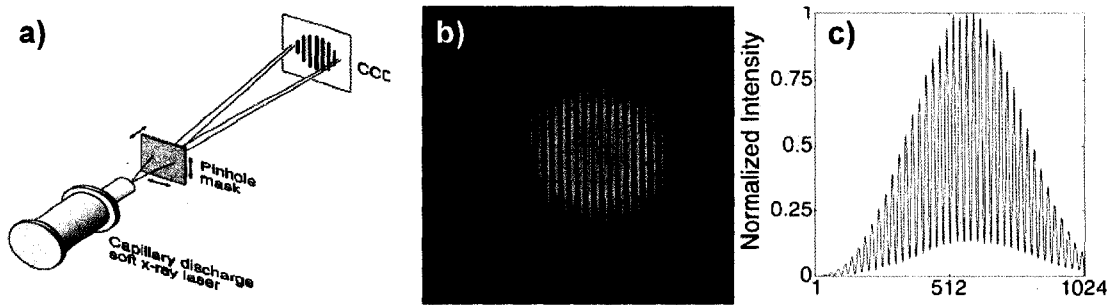


Figure 2.4. Color interferogram and corresponding lineout showing the spatial coherence of the laser beam with capillary length 36cm, resulting full spatial coherence at this capillary length. (Figure and data from [2.12])

The masks were placed at distances of 15 and 40cm from the exit of the capillary and aligned using *x-y* translation stage. From the visibility measurements it was observed that the spatial coherence improved as a function of capillary length, and for 36cm long capillaries a nearly fully coherent beam was emitted from the laser. This is illustrated by the high fringe modulation in Figure 2.4 (b, c).

These lasers have been used in numerous applications, including nanopatterning [2.13-2.16], holographic imaging [2.17, 2.18], interferometry of dense plasmas [2.19-2.21], the measurement of optical constants [2.22], ablation of the materials [2.23], the characterization of soft x-ray optics [2.24], imaging [2.25] and nanomachining [2.26].

2.3 Summary

A very compact 46.9nm wavelength discharge-pumped laser that can be operated at a repetition of several Hz, capable to produce millijoule-level pulses with an average power up to 3.5mW was described [2.8]. The laser produces a high spatially and temporarily coherent beam with average power per unit bandwidth comparable to the radiation generated by a third generation synchrotron beam line. A peak coherent power however is several orders of magnitude larger, making it one of the brightest soft X-ray sources that it is entirely contained on a single optical table.

The reduction in the size complexity and cost of EUV/SXR sources resulting from development of the capillary discharge lasers lead to the widespread use of these sources in numerous scientific and technological applications. Capillary discharge laser with its

unique properties opened the way for high resolution holographic imaging and nanopatterning that will be the subject of this dissertation.

-
- [2.1] J. J. Rocca, D. C. Beetle, M. C. Marconi, "Proposal for soft-x-ray and XUV lasers in capillary discharges", *Opt. Lett.* **13**, 565 (1988)
- [2.2] J. J. Rocca, "Table top soft x-ray lasers", *Review of Scientific Instruments*, **70**, 10, 3799 (1999)
- [2.3] B.R. Benware, C.D. Macchietto, C.H. Moreno, and J.J. Rocca, "Demonstration of a High Average Power Tabletop Soft X-Ray Laser," *Physical Review Letters* **81**, 5804, (1998)
- [2.4] M. Frati, M. Saminario, J. J. Rocca, "Demonstration of a 10- μ J tabletop laser at 52.9nm in neon like chlorine", *Optics Letters* **25**, 14, 1022 (2000)
- [2.5] F. G. Tomasel, J. J. Rocca, V. N. Shlyaptsev, C. D. Macchietto, "Lasing at 60.8 nm in Ne-like sulfur ions in ablated material excited by a capillary discharge", *Physical Review A*, **55**, 2, 1437 (1997)
- [2.6] J.J. Rocca, D.P. Clark, J.L.A. Chilla, V.N. Shlyaptsev, "Energy extraction and achievement of the saturation limit in a discharge-pumped table-top soft x-ray amplifier", *Phys. Rev. Lett.* **77**, 1476 (1996)
- [2.7] A. Ritucci, G. Tomassetti, A. Reale, L. Palladino, L. Reale, F. Flora, L. Mezi, S.V. Kukhlevsky., A. Faenov, T. Pikuz, "Investigation of a highly saturated soft X-ray amplification in a capillary discharge plasma waveguide," *Applied Phys. B* **78**, 965 (2004)
- [2.8] C.D. Macchietto, B.R. Benware, and J.J. Rocca, "Generation of millijoule-level soft-x-ray laser pulses at a 4-Hz repetition rate in a highly saturated tabletop capillary discharge amplifier," *Optics Letters* **24**, 1115, (1999)
- [2.9] J.J. Rocca, V.N. Shlyaptsev, F.G. Tomasel, O.D. Cortazar, D. Hartshorn, and J.L.A. Chilla, "Demonstration of a Discharge Pumped Table-Top Soft-X-Ray Laser," *Physical Review Letters* **73**, 2192, (1994)
- [2.10] C. H. Moreno, M. C. Marconi, V. N. Shlyaptsev, B. R. Benware, C. D. Macchietto, J. L. A. Chilla, J. J. Rocca, and A. Osterheld, "Two-dimensional near-field and far-field imaging of a Ne-like Ar capillary discharge table-top soft-x-ray laser", *Phys. Rev. A* **58**, 1509 (1998)
- [2.11] M. Born, E. Wolf, *Principles of Optics*, 7th edition, (Cambridge University Press, 1999)

-
- [2.12] Y. Liu, M. Seminario, F.G. Tomasel, C. Chang, J.J. Rocca, and D.T. Attwood, "Achievement of essentially full spatial coherence in a high-average-power soft-x-ray laser," *Physical Review A* **63**, 033802, (2001)
- [2.13] P. W. Wachulak, M. G. Capeluto, M. C. Marconi, C. S. Menoni, and J. J. Rocca, "Patterning of nano-scale arrays by table-top extreme ultraviolet laser interferometric lithography", *Optics Express* **15**, 6, 3465 (2007)
- [2.14] M.G. Capeluto, G. Vaschenko, M. Grisham, M.C. Marconi et al., "Nanopatterning with interferometric lithograph using a compact $\lambda=46.9$ nm laser", *IEEE Transac. on Nanotechnology*, **5**, 1, (2006)
- [2.15] M. G. Capeluto, P. Wachulak, M.C. Marconi, D. Patel, C.S. Menoni, J.J. Rocca, C. Iemmi, E.H. Anderson, W. Chao, D.T. Attwood, "Table top nanopatterning with extreme ultraviolet laser illumination", *Microelectronic Engineering* **84**, 5, 721 (2007),
- [2.16] P. W. Wachulak, M. G. Capeluto, M. C. Marconi, D. Patel, C. S. Menoni, J. J. Rocca, "Nanoscale patterning in high resolution HSQ photoresist by interferometric lithography with table top EVU lasers", *Journal of Vacuum Science & Technology B* **25**, 6, 2094 (2007)
- [2.17] P. W. Wachulak, R. A. Bartels, M. C. Marconi, C. S. Menoni, J. J. Rocca, Y. Lu, and B. Parkinson, "Sub 400 nm spatial resolution extreme ultraviolet holography with a table top laser", *Optics Express* **14**, 21, 9636 (2006)
- [2.18] P. W. Wachulak, M.C. Marconi, R. A. Bartels, C. S. Menoni, J.J. Rocca, "Volume extreme ultraviolet holographic imaging with numerical optical sectioning", *Optics Express* **15**, 17, 10622 (2007)
- [2.19] J. Filevich, K. Kanizay, M.C. Marconi, J.L.A. Chilla, and J.J. Rocca., "Dense plasma diagnostics with an amplitude-division soft-x-ray laser interferometer based on diffraction gratings," *Optics Lett.* **25**, 356 (2000)
- [2.20] J. Filevich J, J. Grava, M. Purvis, M. C. Marconi, J. J. Rocca, J. Nilsen, J.Dunn, W. R. Johnson, "Prediction and observation of tin and silver plasmas with index of refraction greater than one in the soft x-ray range", *Phys. Rev. E* **74**, 1 (2006)
- [2.21] E. Jankowska, E. C. Hammarsten, J. Filevich, M. C. Marconi, J. J. Rocca, "Table-top soft X-ray laser interferograms of dense laser-created plasma", *IEEE Transactions on Plasma Science* **30**, 1, 46-47 (2002)
- [2.22] A. Artiukov, B.R. Benware, J.J. Rocca, M. Forsythe, Y.A. Uspenskii, A.V. Vinogradov, "Determination of XUV optical constants by reflectometry using a high-repetition rate 46.9-nm laser," *IEEE J. of Selected Topics in Quant. Elec.* **5**, 1495 (1999)

[2.23] B.R. Benware, A. Ozols, J.J. Rocca, I.A. Artioukov, V.V. Kondratenko and A.V. Vinogradov, "Focusing of a tabletop soft-x-ray laser beam and laser ablation," *Optics Lett.* **24**, 1714 (1999)

[2.24] M. Seminario, J.J. Rocca, R. Depine, B. Bach, and B. Bach, "Characterization of Diffraction Gratings by use of a Tabletop Soft-X-Ray Laser," *Appl. Optics* **40**, 5539 (2001)

[2.25] F. Brizuela, G. Vaschenko, C. Brewer, M. Grisham, C. S. Menoni, M. C. Marconi, J. J. Rocca, W. Chao, J. A. Liddle, E. H. Anderson, D. T. Attwood, A. V. Vinogradov, I. A. Artioukov, Y. P. Pershyn and V. V. Kondratenko, "Reflection mode imaging with nanoscale resolution using a compact extreme ultraviolet laser," *Optics Express* **13**, 3983 (2005)

[2.26] G. Vaschenko, A. Garcia Etxarri, C.S. Menoni, J.J. Rocca, O. Hemberg, S. Bloom, W. Chao, E.H. Anderson, D. T. Attwood, Y. Lu, and B. Parkinson, "Nanometer scale ablation with a table-top soft x-ray laser," *Optics Letters* **31**, 3615, (2006)

CHAPTER 3

3 Nanopatterning using Interference Lithography (IL)

3.1 Introduction

The fabrication of large arrays of nanometer size metallic or semiconductor pillars, rings and holes with sub 100nm sizes has attracted great attention because of the unique optical, electrical and magnetic properties of these structures and its possibility to play an important role in many technological developments in the future [3.1-3.5].

One promising approach for patterning uniformly large areas is based the interference phenomenon and is called interference lithography (IL). In this approach two or more mutually coherent beams are made to interfere in a surface coated with a photo-sensitive material. In the overlapping region the interference pattern is created with an intensity distribution which can be characterized by the wavelength used in the experiment, the geometry and number of combined laser beams. In the simplest case, when two plane wavefronts with the same intensity are overlapped, the period of the interference pattern can be expressed by a simple equation:

$$p = \frac{\lambda}{2\sin(\Theta)} \quad (3.1)$$

For example, using light beams with a wavelength 257 nm and incident angle $\theta = 80^\circ$, lines and spaces with period of 130nm can be obtained. The ultimate limit for IL can be achieved when the two beams are traveling in opposite directions. In this case a fringe period equal to half of the wavelength is obtained.

3.2 Principles of Interferometric Lithography

IL is a mask-less photolithographic technique that can be easily implemented when a coherent light source is available. It is based on the activation of a photoresist by the interference pattern generated by two or more mutually coherent light beams. A simplified description of the interferometric lithography principle is depicted in Figure 3.1 for two mutually coherent beams.

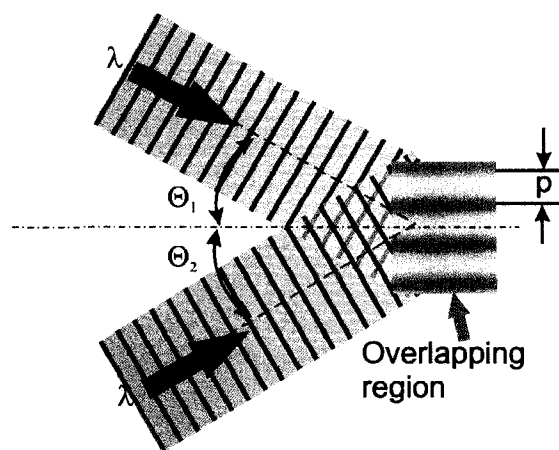


Figure 3.1. Two beams interference lithography, schematic description.

In the overlapping region an interference pattern is created. Based on the coherence properties of the source, the superposition of two beams may or may not lead to

interference. If the two beams originate from the same source the amplitude and phase fluctuations in each beam are correlated and the degree of correlation sets up the degree of coherence. If the two beams are emitted from different sources, those fluctuations are not correlated and a stable interference will not occur. The intensity in the interference pattern created by two interfering beams is given by [3.6]

$$I = I_1 + I_2 + 2\sqrt{I_1 I_2} \cos \delta \quad (3.2)$$

The phase difference is equal to $\delta = \frac{2\pi}{\lambda} \Delta S$, where ΔS is the optical path difference for the two waves from their common source to the point where they are superposed. If the intensities of the two interfering beams are equal $I_1 = I_2$ the intensity in the interference pattern reduces to

$$I = 4I_1 \cos^2 \frac{\delta}{2} \quad (3.3)$$

For this simple case the intensity varies between $I_{\max} = 4I_1$ and $I_{\min} = 0$. Often the incident beams are unpolarized. In this case the light might be considered as a superposition of two linearly polarized and mutually perpendicular components. The two polarization components may be considered separately and the total intensity is the addition of the intensities of each component.

The period of the interference pattern depends on the wavelength of the illumination, the index of refraction of the surrounding environment and the incidence angle set by the geometry of the interferometer. The optical path difference between two consecutive interference maxima is equal to a multiple of the illumination wavelength. That can be expressed by

$$\Delta S = m\lambda \quad (3.4)$$

where m is an integer. Simply by the geometry the optical path difference can be described in terms of both beam angles and for $m = 1$ is equal to

$$p \sin \Theta_1 + p \sin \Theta_2 = \lambda \quad (3.5)$$

where p is the period of the interference pattern. By rearranging the terms this period is equal to

$$p = \frac{\lambda}{\sin \Theta_1 + \sin \Theta_2} \quad (3.6)$$

If one assumes that the geometry is symmetric then both angles are equal $\Theta = \Theta_1 = \Theta_2$ and that leads to equation 3.1 that determines the period of the intensity pattern created by interference. The smallest period can be achieved when the two beams are traveling in opposite direction at $\Theta = \pi/2$. In this case a fringe period is equal to half of the wavelength. This represents the ultimate limit in resolution for any interferometric lithography system.

Equation 3.1 also indicates that reducing the wavelength of the illumination to EUV region may lead to realizing interference patterns with dimensions of tens of nanometer and below. This was the main motivation for using ultraviolet light, extreme ultraviolet (EUV) and even shorter wavelength soft X-rays (SXR) light for nanometer scale fabrication [3.7-3.12].

3.3 Previous work in Interference Lithography

The advantages of IL had been recognized by many groups and extensive work had been done in the field demonstrating the capabilities of this approach. Savas et al. [3.13] using an ArF laser ($\lambda = 193nm$) and phase gratings were able to demonstrate sub-100nm

periodic structures patterned in the surface of a photoresist. The highly coherent beam from an ArF laser was expanded creating patterns about 10cm^2 . Zaidi et al. [3.14] using a multiple exposure interferometric lithography scheme showed the possibility of patterning 1D and 2D features with sub-micron resolution. A cw Ar⁺-ion laser was used in this experiment. Light with the wavelengths $\lambda = 488\text{ nm}$ or $\lambda = 364\text{ nm}$ was expanded and impinged on a Fresnel mirror placed in contact and perpendicularly to the sample. Part of the expanded laser beam illuminated a sample consisted of a photoresist coated silicon wafer and other part was reflected from the Fresnel mirror and overlapped with the undeflected part of the beam. Because the sample and the mirror were perpendicular to each other the undeflected portion of the beam and the reflected beam from the mirror are overlapped at the sample at equal angles of incidence and generated a 1D interference pattern. The sample was positioned on an XY translation and rotation stage to change the position and angle in successive exposures. Patterns as small as $0.6\mu\text{m}$ period were fabricated in KTI 1350 and AZ 1350B photoresists. Switkes et al. [3.15] have implemented an interference lithography tool using 157nm F₂ lasers, capable of patterning dense line patterns with a spatial period of 91nm . No complicated optics was required, only calcium fluoride (CaF₂) plates and flat mirrors. Hinsberg et al. [3.16] described the design and operating characteristics of a DUV interferometric lithography tool. This tool was designed particularly for the study of the high resolution chemically amplified resists. Patterns as small as sub- 100nm were fabricated to address the critical issues in a resist performance.

An extension of the simple two beam interference lithography was reported by Fernandez et al. [3.11]. Image reversal and multiple-beam interference were used to

fabricate arrays of holes. Optical image reversal process allowed to fabricate holes as small as 100nm diameter with 2:1 aspect ratio. Multiple-beam interference has the advantage of a higher throughput based on an increased dose from many interfering beams however the shape and modulation depth of the profiles are sensitive to relative phase variations between each of the beams. This phase dependence makes the application of multiple-beam techniques for patterning features more complicated.

Further feature size reduction can be achieved using shorter wavelengths provided by synchrotron facilities. Synchrotron sources provide a large photon flux and tunable output however the beam spatial and temporal coherence are not as good as compared to laser sources. Additional filtering is needed in order to obtain good interference contrast at the sample plane and large patterning areas. This is associated with serious flux reduction. Regardless these disadvantages the synchrotrons were always attractive for leading-edge IL experiments because its capability to provide radiation with wavelength as short as a few nanometers. Solak et al. [3.12, 3.17] have developed an EUV IL system for testing resists by exposing with high resolution patterns. The system was based on undulator radiation from an electron storage ring and a Lloyd mirror interferometer. 19nm line and space patterns (37nm period) were achieved using this system with 13.4nm wavelength in PMMA (polymethyl methacrylate). The same authors demonstrated 2D arrays of holes and pillars made in UV6 and PMMA using a more complicated setup based on four beam interference originated from four cross-shaped grating arrangement [3.18]. The interference pattern made by the diffracted beams was recorded in a photoresist coated substrate. Arrays of holes in a square pattern with period equal to 141nm were patterned in initial tests. Interference lithography and synchrotron

radiation were also used by Glovkina et al. [3.19] to explore the ultimate resolution of Shipley XP9947W-100 and XP99146-V, two positive-tone chemically amplified resists. In this work studies were presented that allowed to pattern XP99146-V photoresist with 26nm line/space patterns with the use of a transmission grating EUV interferometer and multiple beam IL. Further extension of multiple beam IL up to eight beams and all the consideration associated with this technique as well as the use of wideband sources were presented by Solak et al. [3.20]. In this paper 2D periodic structures and more complicated patterns were made in the surface of the photoresist for example patterns with defined cell shapes, such as arrays of circular rings. The method used by Solak et al. combined coherent and incoherent addition of interference fields. That produces high-resolution, space-invariant intensity patterns in a single exposure. Using wideband light, instead of highly monochromatic sources like lasers it was possible to eliminate the periodic variation of the intensity pattern as multiple beams interfered. Nanometer scale arrays of circular rings and dots in PMMA were obtained.

There is another way to increase the resolution of the system to be able to pattern smaller features. It is done by increasing the numerical aperture of the optical system. This is often done in projection tools, by using high numerical aperture objectives with larger acceptance angle or in immersion lithography. Frauenglass et al. [3.21] with the use of 22x reduction imaging interferometric lithography testbed demonstrated printing arbitrary 86nm half-pitch patterns. The key element of the optical system was the 0.9 NA “cheetah” lens (TROPEL). A frequency doubled Ar-ion laser (244nm) illuminated the arbitrary shape mask and its image was projected by the high numerical aperture objective onto the sample plane resulting 22x demagnification and less than 90nm lines.

The use of immersion media liquids to extend optical resolution was used for a long time in oil-immersion optical microscopy. Raub et al. [3.22, 3.23] show that through the use of de-ionized water as an immersion liquid with $n \sim 1.44$ at 193nm wavelength [3.24] it is possible to reduce the minimum feature size compared with traditional air/vacuum exposures media by a factor of 44%. He addressed the impact of water immersion on the patterning capabilities using different resist formulations. The resists were evaluated by imaging line-space structures at a 65nm half-pitch both in air and with water immersion to show the improvement using immersion techniques. Also in this work 45nm half-period lines were patterned into resist using liquid immersion lithography (LIL) with a $NA = 1.18$ and $\lambda = 213nm$.

In summary the interference lithography technique is a simple approach for the EUV region that allows to pattern relatively large areas in short exposure times. This method is useful in applications where periodically repeated cell structures, holes, pillars, lines and other periodic features are needed such as optical filters, photonic crystals, display units, electronic memories, logic circuits and magnetic storage devices among others.

3.4 Photoresist description and characteristics

A photoresist is a light-sensitive polymer. The photoresist changes its chemical properties as is exposed to photons (radiation) or to a beam of particles. After the exposure, the photoresist is developed changing the surface morphology of the resist. Photoresists are classified into two groups based on their response: positive resists and negative resists. A positive resist is such that the region exposed to light becomes soluble

to a chemical (developer) and the region that is unexposed remains insoluble. This is schematically depicted in Figure 3.2. In a negative resist the region exposed to light becomes relatively insoluble to the developer while the unexposed region is dissolved easily as schematically shown in Figure 3.3.

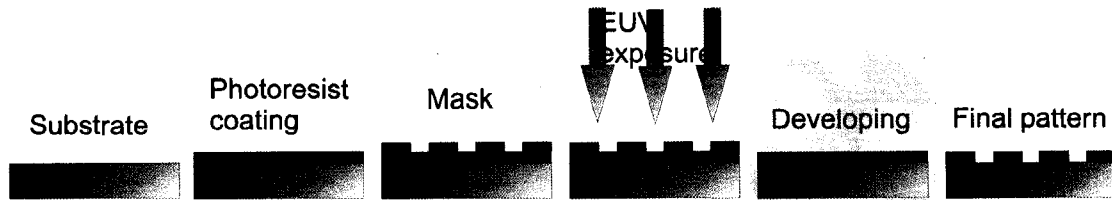


Figure 3.2. Positive photoresist processing scheme. The portion of the photoresist exposed to light becomes soluble to the photoresist developer and the portion of the photoresist that is unexposed remains insoluble to the developer.

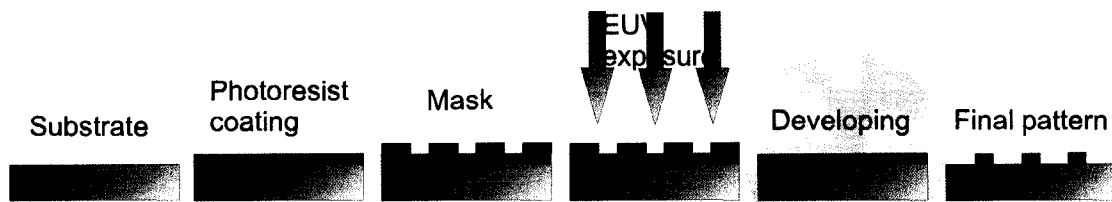


Figure 3.3. Negative photoresist processing scheme. The portion of the photoresist exposed to light becomes relatively insoluble to the photoresist developer. The unexposed portion of the photoresist is dissolved easily by the developer.

Photoresists also can be exposed by beam of electrons. The exposure by electron beam (e-beam writers or electron microscopes) produces the same results as exposure by light. There is one difference however. While photons are absorbed, depositing all their energy at once, electrons deposit a little bit of their energy in the photoresist each time they interact with the photoresist molecules. The energy of the electron is thus deposited into the volume of the photoresist during this process. Similar to photons with high-energy many transitions are excited by high energy electron beams. The typical carbon

based photoresist is composed from long carbon polymer chains. The average length of the chains is often expressed in terms of its molecular weight (MW). Molecular weight describes the mass of the macro-polymers composed from many polymer molecules. The larger the MW is, the longer the polymer chains composing the photoresist. The dissociation energy for a carbon C-C bond is 3.6eV. The electrons may have energies sufficient to dissociate this bond, causing scission. The low-energy electrons have a longer photoresist interaction time because of their lower speed. Scission breaks the original polymer chains into segments with lower molecular weight, which are more readily dissolved in a developer acting as a solvent [3.25].

One important characteristic of the photoresist is the contrast. This can be evaluated measuring the remaining photoresist thickness, which is the thickness measured after the developing procedure. The contrast curve measures the remaining thickness after the developing in relation to the initial thickness d'/d_0 as a function of the exposure dose. A typical contrast curve can be seen in Figure 3.4. Quantitatively the contrast can be expressed in terms of the dosage necessary to activate the resist D_0 and to completely saturate the resist - D_c , [3.26].

$$\gamma = \frac{1}{\log_{10} \left(\frac{D_c}{D_0} \right)} \quad (3.7)$$

For a positive type photoresist, if the exposure dose is low, below the threshold D_0 the resist will not be activated and after developing the resist thickness will not or almost not change. Larger exposure leads to reducing the remaining resist thickness after developing

and finally if the exposure dose is above the D_c all exposed resist will be removed by the developer. For the negative tone resist the curves in Figure 3.4 is reversed.

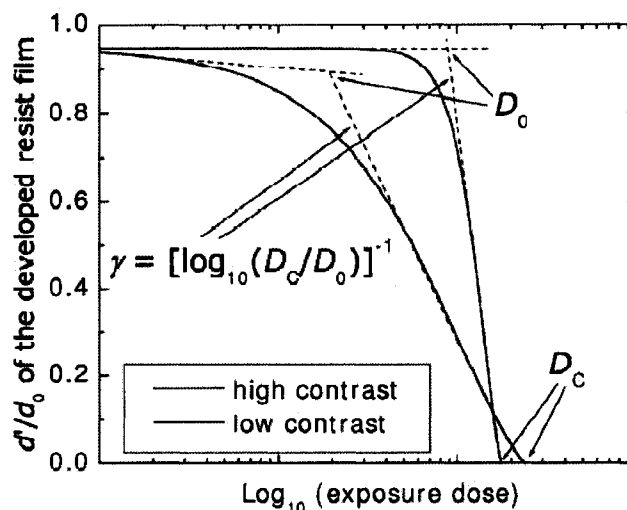


Figure 3.4. The example of the contrast curves for the photoresist showing the difference between high and low contrast (from [3.26]).

The contrast of a photoresist represents the slope of the linear portion of the decreasing or increasing section of the photoresist response curve (normalized remaining thickness of the photoresist as a function of the exposure dose). Figure 3.5 helps to visualize the influence of the contrast on the final surface pattern. The exposing light intensity was assumed to be $I_{\max} \cdot \sin^2(x)$. If the photoresist contrast is low, then the slope between D_0 and D_c is small. The large difference between those values results in a large dynamic range of the photoresist and means that it may accept larger dosage span during the exposure. If the exposure dose is within the dynamic range of the resist then the resist will respond linearly with the intensity. On the contrary if the contrast of the resist is high, the response curve has a steep transition between D_0 and D_c . For the same exposure like in the first case the dose span will be far above D_c in saturation range and

below D_0 in non-activation range. That will cause the pattern to look more like a binary (or square) function as depicted in Figure 3.5.

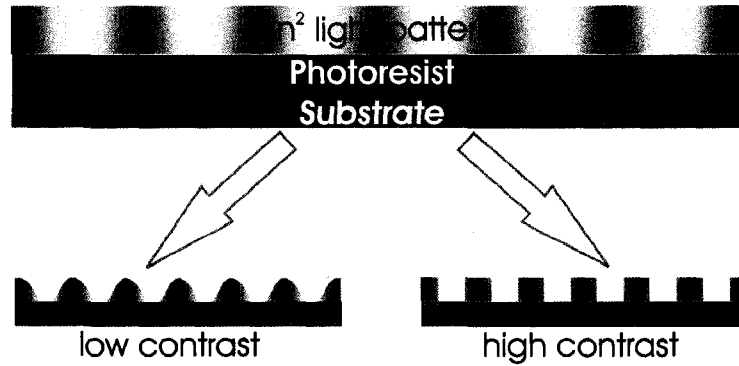


Figure 3.5. Influence of high and low photoresist contrast on the developed pattern.

The sensitivity of a resist is often defined as the minimum exposure dose of radiation that is required to produce useful structures from the lithographic point of view [3.27]. For positive-tone photoresists complete removal of resist in the exposed region is required for pattern to be considered as a functional mask for further processing. Negative-tone resists require sufficient feature thickness to serve as an etching mask for patterned structures to be considered as lithographically useful. This threshold defining the “functional mask” is more arbitrary and is always a fraction of the initial resist thickness. That is why the sensitivity of the resist will always be the exposure dose between D_0 and D_c depending on the criterion defining “useful structures” for various photoresists. However no matter how is defined, there is a tendency for the sensitivity (minimum required exposure) to have as small value as possible. This is required for efficient fabrication enabling the high throughput of the patterning process.

3.4.1 PMMA photoresist

PMMA is most commonly used as a high resolution positive resist for e-beam writing as well as X-ray and deep UV micro and nano lithographic processes. PMMA is also used as a protective coating for wafers, a bonding adhesive and as a sacrificial layer in some of lithographic processes. Standard PMMA resist is formulated with 495,000 & 950,000 molecular weight (MW) resins in chlorobenzene or the anisole solvent. PMMA dissolved in anisole or chlorobenzene is a colorless liquid that can be deposited on the surface of the substrate by spin-coating. A small amount of the PMMA solution is placed in the center of the substrate. By rotating the wafer at high acceleration rate and holding the constant speed for a few tens of seconds up to a minute the liquid uniformly spreads outwards coating the substrate with uniform thickness layer. After spinning the deposited layer is pre-baked using a hotplate or a convection oven. The pre-baking is necessary to remove the remaining solvent from the photoresist layer. After baking a very smooth and low roughness surface is achieved. Figure 3.6a shows schematically a chain of a PMMA molecules. PMMA requires doses $>500\text{mJ}/\text{cm}^2$ at wavelength 248nm and is even less sensitive in X-ray region $\sim 1\text{-}2\text{ J}/\text{cm}^2$ at 8.3\AA [3.28]. The sensitivity increases at longer X-ray wavelengths and in the EUV region. The PMMA properties were studied extensively by Junarsa et al. [3.29]. The PMMA activation threshold was found to be $\sim 7.4\text{mJ}/\text{cm}^2$.

Both photons and electrons break the bonds between the PMMA molecules decreasing locally the average molecular weight as depicted schematically in Figure 3.6b. This increases rapidly the dissolution rate and causes the developer to wash out the exposed part of the resist much easier creating the relief pattern in the photoresist surface.

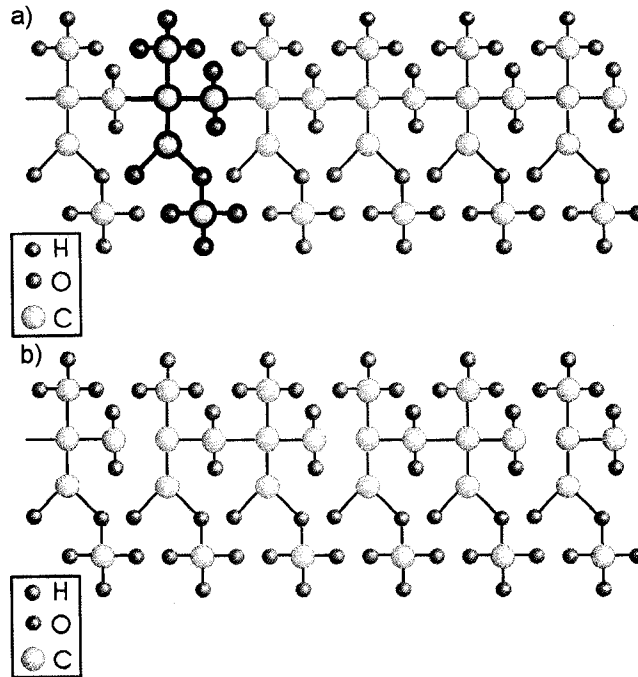


Figure 3.6. a) schematic description of the PMMA molecular composition. Long chains of polymers (one of the molecules are depicted bold) contain carbon, hydrogen and oxygen atoms in depicted configuration. The PMMA molecular composition after the photon or e-beam exposure (b). The bonds between the molecules in long polymer chain are broken creating the shorter chains.

3.4.2 HSQ photoresist

Hydrogen silsesquioxane is a highly ordered polymer with a cage-like structure schematically depicted in Figure 3.7a. It is commonly used as a spin-on-glass dielectric in integrated circuits [3.30, 3.31]. The cross-linking occurs at temperatures above 400 °C. At that temperature Si–H bonds are converted to form silanol (Si–OH) groups [3.32, 3.33]. These groups are not stable and rapidly degrade to form siloxane bonds (Si–O–Si) whereby the caged structure is transformed into a networked structure schematically depicted in Figure 3.7b. The resulting film has a very low surface roughness and chemistry of a glass.

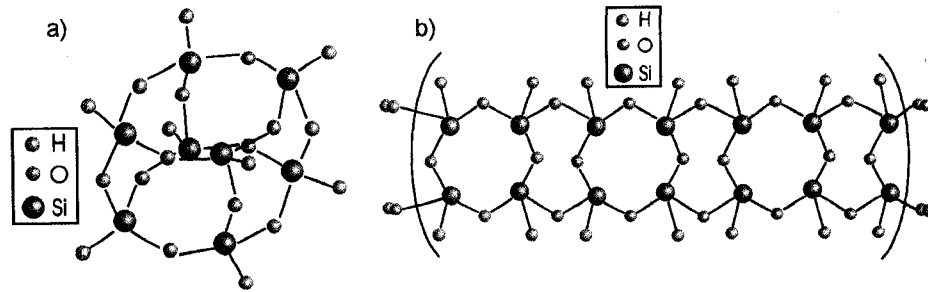


Figure 3.7. Cage-like structure of HSQ (a) before exposing it to light or e-beam. Hydrogen, oxygen and silicon atoms constitute to form the hydrogen silsesquioxane, which changes its chemical structure after the exposure. Networked structure of HSQ after exposing HSQ to light or e-beam (b).

A chemical reaction similar to the thermal curing process occurs when HSQ is exposed to high energy radiation [3.34] making the exposed regions of the HSQ resist insoluble in the developers such as tetramethylammonium hydroxide (TMAH), that is aqueous based, leaving relief structures in the patterned region [3.35]. Junarsa et al. [3.29] measured the contrast and the sensitivity for HSQ. The sensitivity of HSQ at 13.4nm wavelength was defined to be the incident dose at which 70% of the resist thickness remained insoluble after exposure and development. The HSQ sensitivity was $11.5\text{mJ}/\text{cm}^2$ at 13.4nm. HSQ is about three times more sensitive to EUV radiation than PMMA. The sensitivity of both photoresists in the EUV region is much higher than in DUV or X-ray. Both resists have also very good spatial resolution that allows to fabricate feature size below 50nm. That makes both of those resists very useful and interesting alternatives for e-beam nanopatterning.

3.5 Table Top Compact Nanopatterning Tool

The utilization of a compact table-top EUV laser opens the opportunity to realize compact nanopatterning tools using the IL approach. The main advantages of IL as compared with conventional projection systems are that the feature size that can be printed is only limited by the wavelength and that it is independent on the expensive and sophisticated optics necessary to project sub 50nm features. In this work an IL system was implemented combining a capillary discharge laser and a Lloyd's mirror interferometer.

The idea behind this approach is very simple. As in all interferometers two or more mutually coherent beams are superposed to generate an intensity modulation. In the case of the Lloyd's mirror interferometer the two beams are generated with a single flat mirror placed in front of the laser beam. The laser beam illuminates the mirror's edge as depicted in Figure 3.8. The beam is split by reflection in the mirror. One half of the beam is reflected in the mirror and illuminates a photoresist coated silicon sample attached to the end of the mirror (see Figure 3.8), while the other half illuminated the sample directly. Both the reflected beam and the transmitted are combined in the sample plane. The superposition of the two mutually coherent beams creates the interference pattern with a period $p = \lambda / (2 \sin \Theta)$. If the two beams have equal intensities, the interference maxima are up to four times the intensity in the single beam while the minima are equal to zero. Here obviously the two beams have different intensities since one of them is reflected in the mirror surface and is slightly attenuated. This reduces the contrast below the optimum value of one.

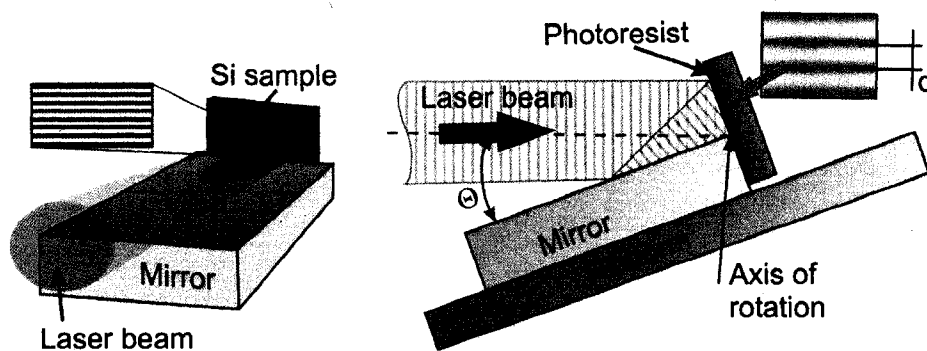


Figure 3.8. Lloyd's mirror interferometer explanation. Top part of the beam illuminates the sample coated with the resist and the bottom part illuminates the mirror's surface, reflects from it and superposes with the top part of the beam creating the intensity modulation at the sample plane.

The interference pattern consists of lines parallel to the mirror's edge as depicted in Figure 3.8. After the first exposure the sample is rotated around an axis perpendicular to the sample's surface and a second exposure is realized creating a second line pattern in the same region of the photoresist. This simple approach allows to make 2D periodic patterns. Generalizing the idea it is possible to make multiple exposures to create more complicated patterns.

Figure 3.9 shows a schematic of the nanopatterning tool. A rectangular $16 \times 22 \text{ mm}^2$ Cr coated silicon substrate (mirror) was mounted at grazing incidence in front of the laser beam on a pivoting platform, with its axis coincident with the farther edge of the mirror. Using the silicon as the mirror's substrate has the advantage of low roughness that allows to evaporate a very uniform layer of chromium. The mirror was attached to $30 \times 50 \text{ mm}^2$ brass holder as can be seen in Figure 3.10. The mirror assembly was placed on a second translation stage to provide a spring-loaded mount necessary to avoid accidental crushing the sample on the mirror's edge during approaching the sample to the mirror. The sample consisting of a Si wafer coated with photoresist was mounted at the

edge of the mirror in a motorized rotation stage that allows for controlled rotation by an angle α around an axis normal to the sample's surface.

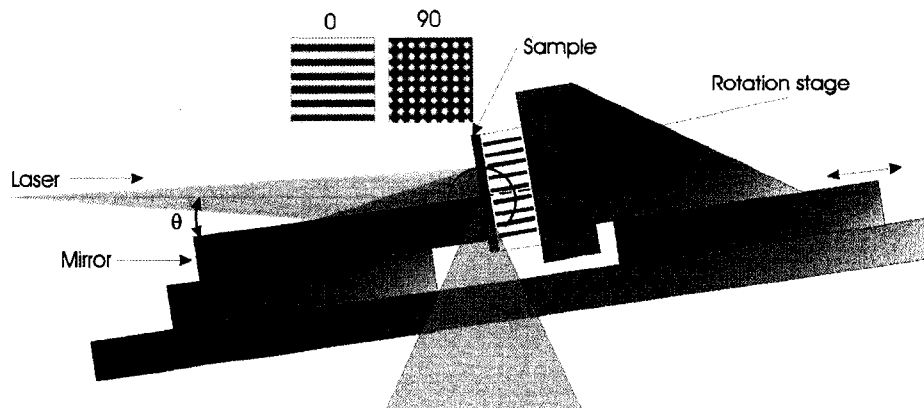


Figure 3.9. Compact nanopatterning tool based on Lloyd's mirror configuration.

The photograph of the patterning tool is depicted in Figure 3.10 where all the main components are indicated.

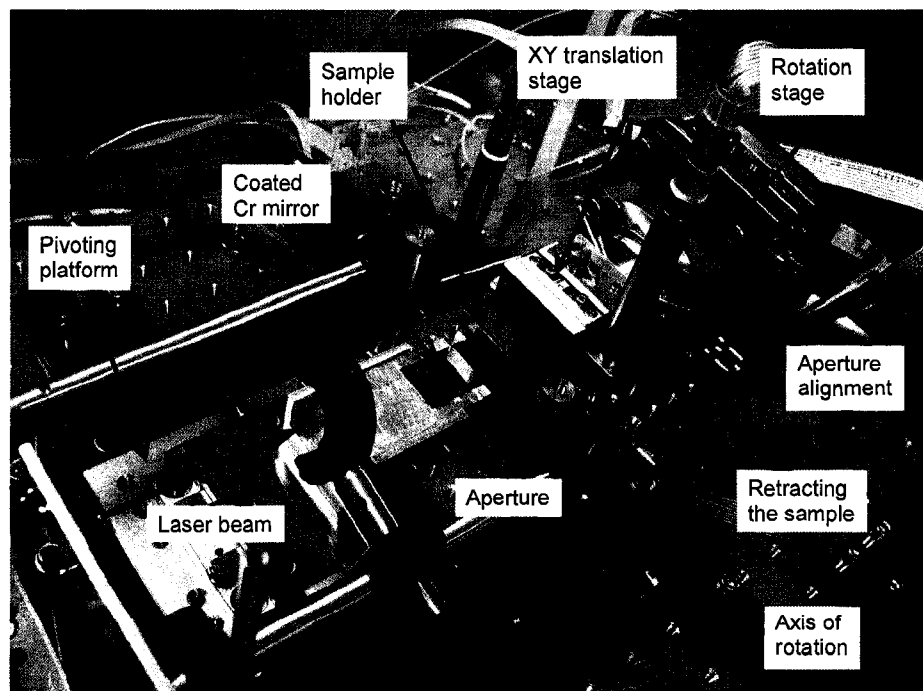


Figure 3.10. Photograph of the nanopatterning tool showing all major components.

The entire system was mounted on a motorized pivoting platform to change the incidence angle Θ . The nanopatterning tool allowed to change the incident angle from $\sim 1^\circ$ up to 15° . These angles correspond to periods in the interference pattern between $\sim 90.6\text{nm}$ and $\sim 1.4\mu\text{m}$.

This system allows to pattern the photoresist surface, although to allow multiple exposures in the same sample two more components were added to the final version of the tool. Because of the coherence limitations discussed later in this section the patterning area was limited to approximately $500 \times 500 \mu\text{m}^2$. The rectangular aperture $0.5 \times 0.9 \text{mm}^2$ was laser cut in a $25\mu\text{m}$ thick $2 \times 2 \text{cm}^2$ size stainless steel shim. The aperture was mounted at the mirror's edge with the help of microscope to have approximately the $500 \times 500 \mu\text{m}^2$ square opening next to the edge of the mirror. Using $20\times$ magnification microscope, the center of this aperture was aligned with the axis of the rotation stage. That allows to align multiple $500 \times 500 \mu\text{m}^2$ exposures in a single substrate. A small x-y translation stage allows for the displacement of the sample to make many $500 \times 500 \mu\text{m}^2$ patterned regions. The zoomed area of the mirror, aperture and sample is shown in Figure 3.11. The inset images show also the aperture and the alignment process.

The aperture in front of the beam limits the area where the patterning is produced. This was very convenient for a systematic study when the dose or the incident angle was changed because assures identical post processing conditions in all the exposures such as the developing or postbaking.

Figure 3.12 is the optical micrograph showing the results of using the limiting aperture. It is possible in the single sample to make patterns with different shapes and periods.

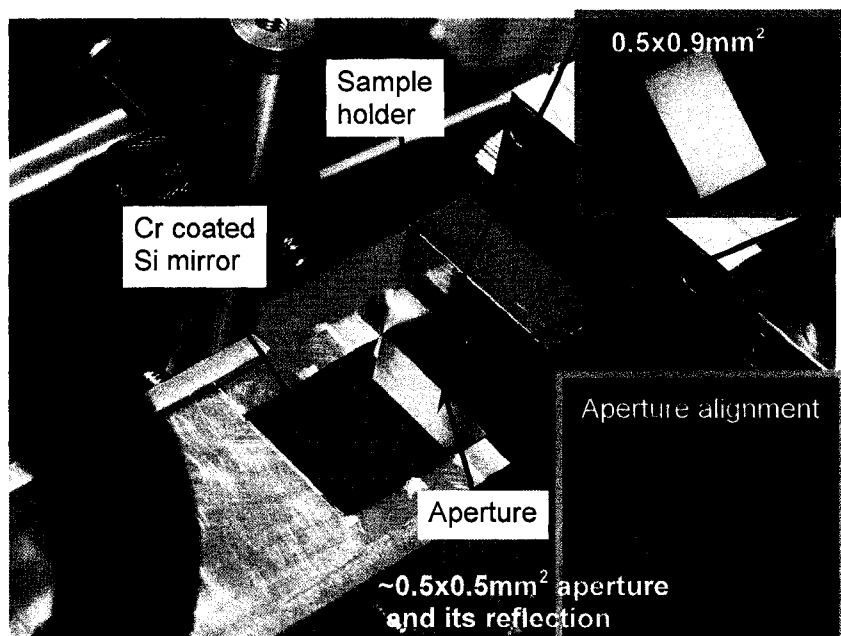


Figure 3.11. Zoomed area of the mirror and aperture assembly showing those components in details. Inset images show the aperture cut in the stainless steel shim and the alignment of the aperture with the use of an optical microscope,

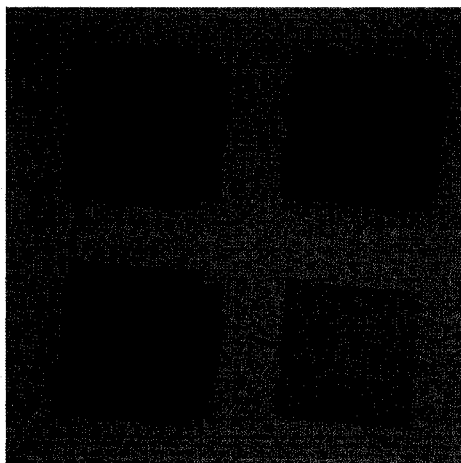


Figure 3.12. Optical micrograph showing the results of using the aperture and possibility to pattern many different shapes and sizes in the single sample both 1D (right-lower square with single exposure) and 2D patterns.

The small square in the right lower portion of the image shows a single exposure which results in a 1-D line pattern. The other squares show double exposure (two overlapped squares) which result in nanofabrication of 2-D patterns like holes or pillars. It can be

observed that the axis of rotation of the sample was slightly misaligned with respect to the center of the aperture $\sim 20\mu\text{m}$ however it was not influencing the performance of the tool significantly.

The tool is housed in vacuum chamber $0.45\times 0.55\times 0.40\text{m}^3$ with aluminum walls and stainless steel frame that was built for that purpose. To achieve a vacuum on a $10^{-5} - 10^{-6}$ Torr level one scroll (oil-free) vacuum pump and one turbomolecular pump were used. The whole system was remotely controlled using vacuum actuators without the necessity to break the vacuum during the exposures. The entire EUV interferometry instrument has a footprint of $0.7\times 2.6\text{m}^2$.

3.5.1 Mirror reflectivity

The mirror is the main component of the nanopatterning tool based on the Lloyd's interferometer. The reflectivity of the mirror has a crucial role in the determination of the interferometric pattern visibility; consequently the discussion presented in this section is important to understand the performance limitation of the tool.

Different materials for the mirror were considered. Based on the online database of the Center for X-ray Optics [3.36] (CXRO) the reflectivity of different materials were used to calculate the expected visibility in the interference pattern. A detailed derivation of the calculations done by CXRO can be found in Appendix I. The materials taken under the consideration were silicon and gallium arsenide as a possible substrates and chromium, gold, silver and nickel as possible coatings. The reflectivity of each material for the two different polarizations was obtained from the database for 30eV photons

which corresponds to 41.3nm wavelength. That was the smallest photon energy available in the database but it is close enough to 46.9nm that we can expect the results to be valid. The thickness assumed for the metallic coatings was always larger than a few wavelengths, about 100nm. The reflectivity for polarizations s and p at a $\lambda=41\text{nm}$ for different materials versus the grazing incidence angle Θ was plotted in Figure 3.13.

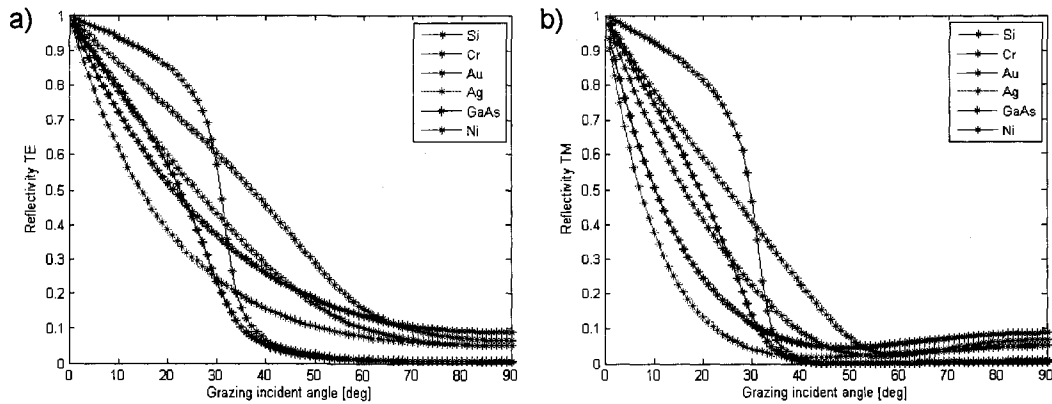


Figure 3.13. Reflectivity of various materials at 41nm wavelength vs. grazing incidence angle for a) s -polarization (TE) perpendicular to the incidence plane, b) p -polarization (TM) in the incidence plane.

The interference maxima and minima are polarization dependent. The equations describing the maximum and minimum intensity in the interference pattern illuminating the photoresist depending on the reflectivity coefficients for both polarizations can be expressed as:

$$I_{\max} = \frac{1}{2} \left(I + R_{TE} \cdot I + 2I\sqrt{R_{TE}} \right) + \frac{1}{2} \left(I + R_{TM} \cdot I + 2I\sqrt{R_{TM}} \cdot \cos(2\Theta) \right) \quad (3.8)$$

$$I_{\min} = \frac{1}{2} \left(I + R_{TE} \cdot I - 2I\sqrt{R_{TE}} \right) + \frac{1}{2} \left(I + R_{TM} \cdot I - 2I\sqrt{R_{TM}} \cdot \cos(2\Theta) \right) \quad (3.9)$$

In the Lloyd's mirror interferometer the two beams are overlapped at the sample plane, one unaffected and the second one reflected from the mirror's surface. The intensity of

the reflected beam is reduced by limited reflectivity of the mirror. The total intensity incident on the sample can be expressed in terms of only one intensity as $I = I_2 = R(\Theta) \cdot I_1$. The total intensity of the interfering beams will be a superposition of the TM and TE polarizations. For the TE polarization the electric field vectors of the two interfering beams are always parallel to each other and independent of the incidence angle. This is not a case for the TM polarization, where the angle between both interfering beams is equal to 2Θ . Considering this, the interference fringe visibility as a function of the grazing incidence angle can be expressed as

$$V = \frac{I_{\max} - I_{\min}}{I_{\max} + I_{\min}} = \frac{2(\sqrt{R_{TE}} + \sqrt{R_{TM}} \cos(2\Theta))}{2 + R_{TE} + R_{TM}} \quad (3.10)$$

The calculated visibility values for small grazing incidence angles used in the Lloyd's interferometer are depicted in and Figure 3.14.

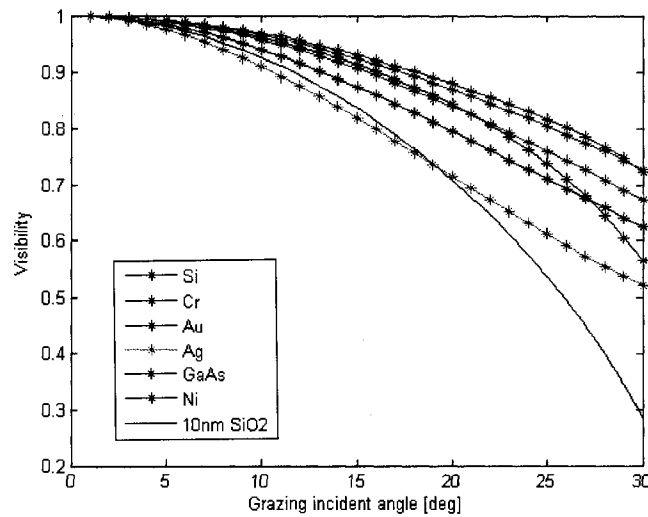


Figure 3.14. Fringe visibility in the interference pattern vs. grazing incidence angle for small grazing incidence Θ angles from 0 to 30 degrees.

For silicon and gallium arsenide (red and black curves with * marker respectively) the fringe visibility decreases rapidly for Θ around 30° while the metal coatings, although might produce smaller visibility at the lower grazing incidence angles, don't show this rapid decrease for larger Θ . This is the reason why a chromium coating was chosen to be the reflective surface in the Lloyd's mirror nanopatterning tool and silicon substrate was used because of very low surface roughness (few angstroms) that provides very good coating quality. Layer of chromium 400nm thick was coated on the silicon wafer using evaporation. Another consideration regarding silicon is the fact that the silicon often has a thin (up to tens of nanometers thick) layer of silicon oxide on the top. This layer further reduces the reflectivity and consequently the fringe visibility as shown in Figure 3.14 (black solid line) for 10nm thick layer of SiO_2 .

The average reflectivity of the Cr-coated mirror for unpolarized light was measured at $\lambda=46.9\text{nm}$ using the capillary discharge laser. A small piece of a silicon wafer was coated with chromium and placed in front of the laser beam in the vacuum chamber at $\sim 1.5\text{m}$ from the capillary end. The laser beam impinged the chromium coated silicon and reflected from it. The reflected beam impinges the photodiode and the signal was measured using vacuum photodiode with an Al cathode. The polarization voltage for the diode was 1kV assuring that the diode was not saturated by the signal. The mirror was then rotated to change the grazing incidence angle and the measurements were repeated. Series of 20 measurements were taken for each grazing incidence angle and for the laser beam. The reflectivity of the mirror for each angle was estimated as a ratio between the average amplitude of the reflected pulse and the average of the amplitude of the laser beam. For each angle the error was evaluated as the standard deviation of the value from

its average. The photograph of the setup used to measure the mirror reflectivity is shown in Figure 3.15.

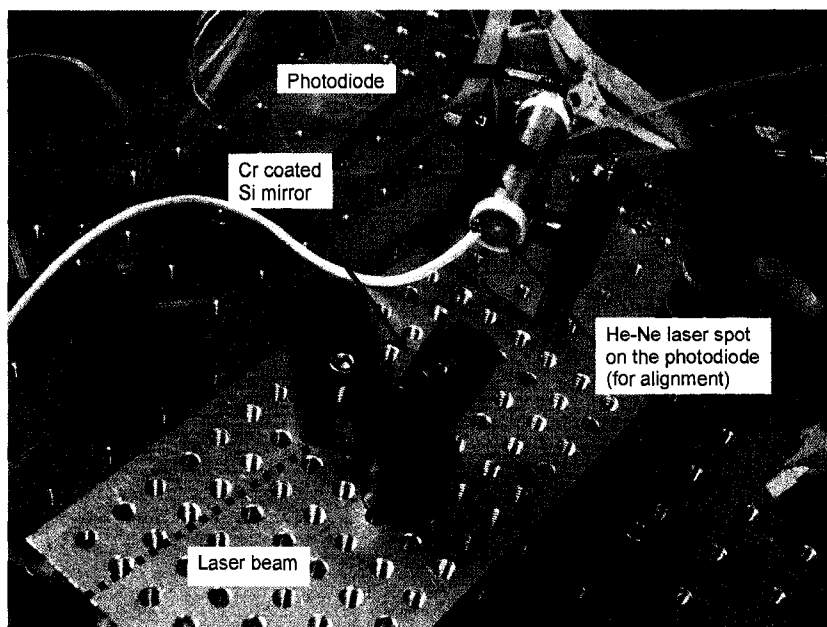


Figure 3.15. The photograph of the setup used to measure the chromium mirror reflectivity vs. the grazing incidence angle. Laser beam reflects from the measured surface and illuminates the photodiode.

The reflectivity of the chromium mirror vs. the grazing incidence angle is shown in Figure 3.16. The reflectivity of the chromium mirror decreases as the grazing incidence angle increases producing features with smaller periods. The mirror reflectivity is high (about 90%) at the grazing incidence angles less than 10° . At the maximum possible grazing incidence angle for the tool $\sim 15^\circ$ the reflectivity of the mirror is $\sim 86\%$. This reflectivity measured for unpolarized light is in good agreement with the reflectivity obtained for both polarizations at 41nm from CXRO database as can be seen if compared to Figure 3.13.

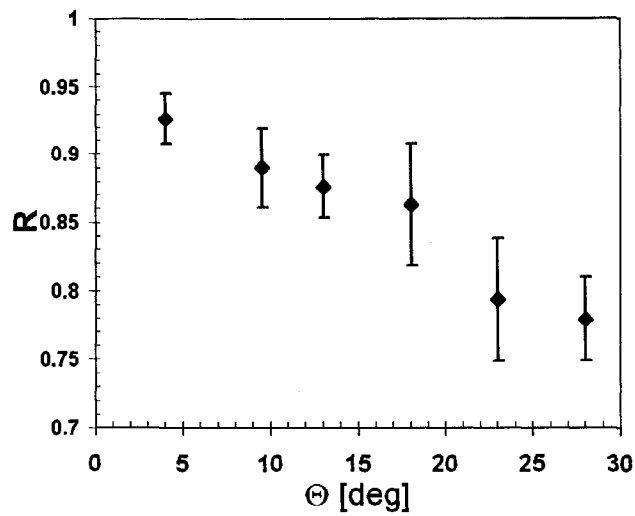


Figure 3.16. Chromium mirror reflectivity vs. grazing incidence angle measured at 46.9nm wavelength.

The reflectivity of the mirror and polarization are the two most important factors that reduce the modulation depth in the patterned surface. Other factors like the contribution of mechanical vibrations during exposure from mechanical and turbo-molecular pumps, scattering due to the mirror's surface roughness further reduces the intensity of the reflected beam and the visibility.

3.6 Limitations to the patterning area due to the coherence of the source

Both the spatial and the temporal coherence of the laser source limit the patterning area that can be obtained in a wavefront division interferometer. Spatial coherence describes the phase relationship between one spatial position on the wavefront and the other spatial position on the same wavefront and is related to the size of the light

source. Theoretically a point source of zero diameter emits fully spatially coherent light because the wavefront spreading out was created at the same point in space thus there is a fixed phase relationship between all the points on the wavefront. The light from a source of finite diameter will have lower coherence caused by the fact that the wavefront does not originate from exactly the same point in space. The spatial coherence of the finite size and shape source can be estimated using van Cittert-Zernike theorem [3.37]. To characterize the spatial coherence of the source at a given distance a parameter defined as radius of coherence (R_c) is often used. The interference between two points on the wavefront can be produced only within the circular coherence area characterized by this radius R_c .

If a wave is superposed with a delayed copy of itself (as it is often done using any amplitude division interferometers) the duration of the delay over which they produces stable interference is known as the coherence time of the wave, τ_c . If the delay between two copies of the same wavefront increases, then the interference pattern fringe visibility at the observation plane decreases. This time corresponds to the spatial dimension called coherence length which can be calculated: $l_c = c \cdot \tau_c$, where c is the speed of light. The temporal coherence of a wave is inversely proportional to the spectral bandwidth of the source.

$$l_c = \lambda \frac{\lambda}{\Delta\lambda} = \frac{\lambda^2}{\Delta\lambda} \quad (3.11)$$

An ideally monochromatic (single frequency) wave would have an infinite coherence time and length as $\Delta\lambda \rightarrow 0, l_c \rightarrow \infty$. In practice, no wave is truly monochromatic and has some associated bandwidth.

The idea of the spatial and temporal coherence of the light can be easily understood in terms of increasing the coherence of the source performing a suitable filtering. The idea of spatial and spectral filtering is presented in Figure 3.17.

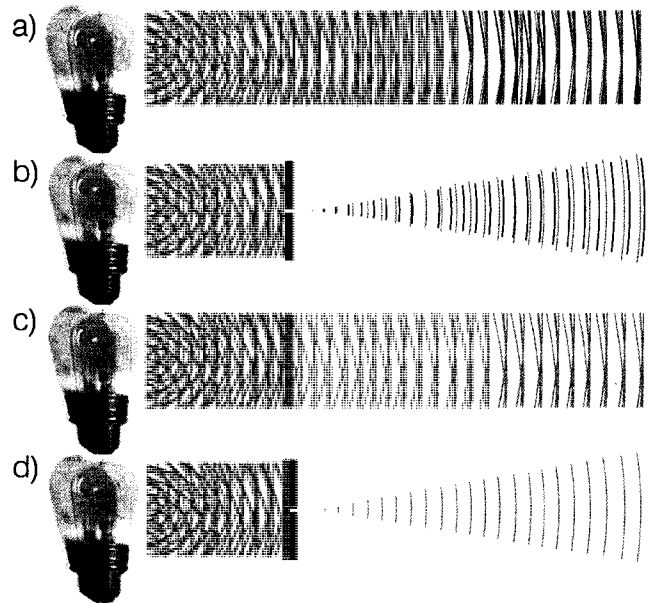


Figure 3.17. Filtering of spatially and temporally incoherent radiation from thermal source (a). Spatial filtering using a pinhole increases the spatial coherence of the source (b) while spectral filtering increases the temporal coherence of the source (c). Spectral filtering and a pinhole produces a temporally and spatially coherent beam (d). Please notice greatly diminished power after the filtering is performed. Based on [3.38].

The illustration shows an extended source that produces a thermal radiation with a broad spectrum. This situation is depicted in Figure 3.17a. The radiation may be filtered in two ways. If a pinhole is used as shown in Figure 3.17b spatial filtering is performed and the degree of spatial coherence of the radiation increases. The radiation is spatially coherent over some angular extent that can be described using $d \cdot \Theta = \lambda / 2\pi$, where d is the diameter of the pinhole used for spatial filtering, and Θ the divergence half angle. If a spectral filter is used, as depicted in Figure 3.17c, to narrow the spectral bandwidth, the

degree of longitudinal coherence described by the longitudinal coherence length l_c increases according to equation 3.11. The combination of both pinhole and filter results in a spatially and temporally coherent radiation as can be seen in Figure 3.17d. However the useful coherent power is only a small fraction of the total power radiated by the source.

To analyze both the spatial and the temporal coherence influence on the area of patterning in the Lloyd's mirror interferometer, consider the scheme shown in Figure 3.18.

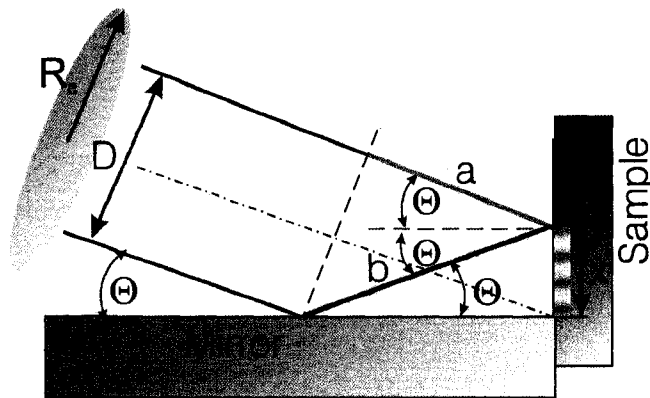


Figure 3.18. The schematic description of the Lloyd's mirror interferometer useful to study the spatial and temporal coherence influence on the patterning area.

If we define x as the distance measured on the sample from the edge of the mirror to the point where we should still expect to see interference, the spatial coherence will limit the patterning width x if $D \leq 2R_c$. That imposes that the laser beam will produce the interference pattern at the sample plane only within the area of coherence described by the radius of coherence $A_c = \pi R_c^2$.

From the geometry of the problem it is easy to see that

$$\frac{D}{b} = \sin(2\Theta) = 2 \sin \Theta \cos \Theta \Rightarrow b = \frac{D}{2 \sin \Theta \cos \Theta} \quad (3.12)$$

also

$$\frac{x}{b} = \sin \Theta \Rightarrow x = b \sin \Theta \quad (3.13)$$

by combining these two equations

$$x = \frac{D}{2 \cos \Theta} \quad (3.14)$$

to satisfy the spatial coherence requirement

$$x \leq \frac{R_c}{\cos \Theta} \quad (3.15)$$

The equation 3.15 relates the patterning width with the spatial coherence of the source.

On the other hand the temporal coherence imposes that the time delay between two interfering beams cannot be larger than Δt_c . In space this can be translated to the fact that the optical path difference between two interfering beams cannot exceed the coherence length. This can be expressed as

$$b - a \leq l_c \quad (3.16)$$

It can be shown that

$$\frac{D}{a} = \tan(2\Theta) = \frac{\sin(2\Theta)}{\cos(2\Theta)} \quad (3.17)$$

also

$$D^2 + a^2 = b^2 \Rightarrow D^2 = b^2 - a^2 = (b - a)(b + a) \quad (3.18)$$

using equation 3.16

$$D^2 \leq l_c(b + a) \quad (3.19)$$

that reduces to

$$D^2 \leq l_c \frac{D(1 + \cos(2\Theta))}{\sin(2\Theta)} \Rightarrow D \leq l_c \frac{1 + \cos(2\Theta)}{\sin(2\Theta)} \quad (3.20)$$

knowing that $b = \frac{D}{\sin(2\Theta)}$ and $a = \frac{D}{\tan(2\Theta)} = \frac{D \cos(2\Theta)}{\sin(2\Theta)}$. From previous considerations using equation 3.19

$$x \leq l_c \frac{1 + \cos(2\Theta)}{2 \sin(2\Theta) \cos(\Theta)} \quad (3.21)$$

assuming $\sin(2\Theta) = 2 \sin \Theta \cos \Theta$ and $\cos(2\Theta) = \cos^2 \Theta - \sin^2 \Theta$ the final expression will be:

$$x \leq \frac{l_c}{2 \sin \Theta} \quad (3.22)$$

Equation 3.22 relates the patterning width with the coherence length of the source that is a measure of the temporal coherence. There is another way to look at the coherence length influence on the patterning width. From section 3.5 one can see that the patterning period in the Lloyd's mirror interferometer depends on the illumination wavelength and the grazing incidence angle Θ :

$$p = \frac{\lambda}{2 \sin \Theta} \Rightarrow 2 \sin \Theta = \frac{\lambda}{p} \quad (3.23)$$

also we know that $x \leq \frac{l_c}{2 \sin \Theta}$ and by substitution $x \leq \frac{l_c p}{\lambda}$. Using equation 3.11

$$x \leq p \frac{\lambda}{\Delta \lambda} \quad (3.24)$$

This equation indicates that the patterning width is limited by the inverse bandwidth of the source, roughly by a factor $\frac{\lambda}{\Delta \lambda}$. For the capillary discharge laser $\frac{\lambda}{\Delta \lambda} \sim 10^4$ so the patterning width is limited by the temporal coherence to roughly 10'000 periods in the interference pattern.

The radius of coherence of the source at the plane where the interference was obtained was estimated to be $R_c \sim 0.5\text{mm}$. The laser beam linewidth was limited mainly by the Doppler broadening in the argon plasma. This gives the coherence length $l_c \sim 470\mu\text{m}$. In both cases for the spatial and temporal coherence the patterning width is dependent on the value of grazing incidence angle. Knowing the coherence parameters the patterning width was plotted versus the grazing incidence angle. This can be seen in Figure 3.19a.

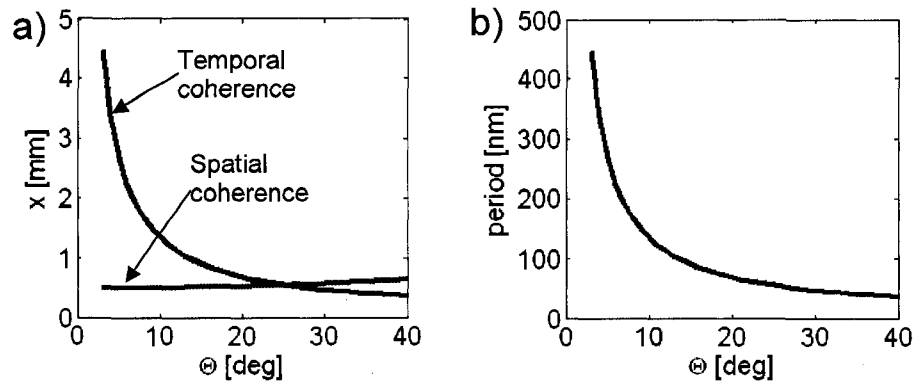


Figure 3.19. Period of the interference pattern and patterned features vs. grazing incidence angle a) and the calculated spatial and temporal coherence limitations to the patterning width vs. grazing incidence angle b).

Figure 3.19a indicates, that the main limitation to the patterning width x at the low grazing incidence angles is the spatial coherence. At about $\Theta = 24^\circ$ the temporal coherence starts to limit the patterning width as the period of the features gets smaller with the same number of patterned periods. For small angles however (in the angle span limited by the nanopatterning tool) the patterning width is no less than 0.5mm. In a double exposure the area patterned with the features with the period p is $0.5 \times 0.5 \text{mm}^2$. The period of the features as a function of the grazing incidence angle is shown in Figure

3.19b. At low angles the period is very sensitive to the angle while at the angles larger than $\sim 20^\circ$ slowly, asymptotically approaches $\lambda/2$.

3.7 Numerical modeling of patterning process

The behavior of the photoresists although might be very complicated generally can be modeled using simple approaches and in most of the cases a crude and simple model can predict the behavior of the photoresists accurately. In this section a simple model of the PMMA photoresist will be described based on its response obtained from [3.29]. The model simulates the Lloyd's mirror interferometer and multiple exposures scheme to generate 1-D and 2-D patterns in the surface of the photoresist. This model was used exclusively for PMMA, although may work for all types of resists as soon as the response curve is known. It simulates up to three consecutive exposures. Each exposure creates 1D intensity modulation at the sample plane. For each of three exposures the number of laser shots (exposure dose), the interferometer incidence angle Θ and the rotation angle α were defined. For each exposure the intensity patterns were generated using the simple equation shown below:

$$I_i(x, y) = \frac{1}{2}(I_{\max i} - I_{\min i}) \cos\left(\frac{2\pi R_i(x, y)}{d_i}\right) + \frac{1}{2}(I_{\max i} + I_{\min i}), i = 1, 2, 3 \quad (3.25)$$

where the first term describes the $\cos(x)$ type of intensity modulation and the second term is a scaling factor required for normalization of the intensity distribution for each of

the exposures i . The period of the modulation is described by $d_i = \frac{\lambda}{2 \sin(\Theta_i)}$, the rotation of the intensity pattern in each exposure:

$$R_i(x, y) = x \cdot \cos(\alpha_i) + y \cdot \sin(\alpha_i) \quad (3.26)$$

Each of the components $I_{\max i}$ and $I_{\min i}$ describes the maximum and minimum value of the intensity in the interference pattern based on the reflectivity of the Lloyd's interferometer mirror for each polarization TE and TM. Those components can be expressed as below:

$$I_{\max i} = I_i \left[1 + \sqrt{R_{TEi}} + \sqrt{R_{TMi}} \cdot \cos(2\Theta_i) + \frac{1}{2}(R_{TEi} + R_{TMi}) \right] \quad (3.27)$$

$$I_{\min i} = I_i \left[1 - \sqrt{R_{TEi}} - \sqrt{R_{TMi}} \cdot \cos(2\Theta_i) + \frac{1}{2}(R_{TEi} + R_{TMi}) \right] \quad (3.28)$$

To compute the total unpolarized intensity incident on the sample, the reflected portion of the beam was expressed in terms of the beam that illuminates the sample directly $I_{2i} = R(\Theta_i) \cdot I_{1i}$. The intensity of the interfering beams was calculated as a superposition of the TM and TE polarizations.

The intensity distributions in each exposure $I_i(x, y)$ are then added up incoherently. To visualize the idea the intensity patterns in each directions and the total intensity pattern generated by the code for arbitrary conditions are depicted in Figure 3.20. The angle Θ was chosen to be 8° resulting the period of the intensity pattern to be 168nm. The angle between exposures is $\alpha = 90^\circ$. Only small regions $1.4 \times 1.4 \mu\text{m}^2$ were generated to help to visualize the idea behind this model.

If the angle between the exposures changes the total intensity pattern looks different, as can be seen in Figure 3.21. The exposure conditions were exactly the same in both cases but the angle between the exposures was changed to $\alpha = 30^\circ$.

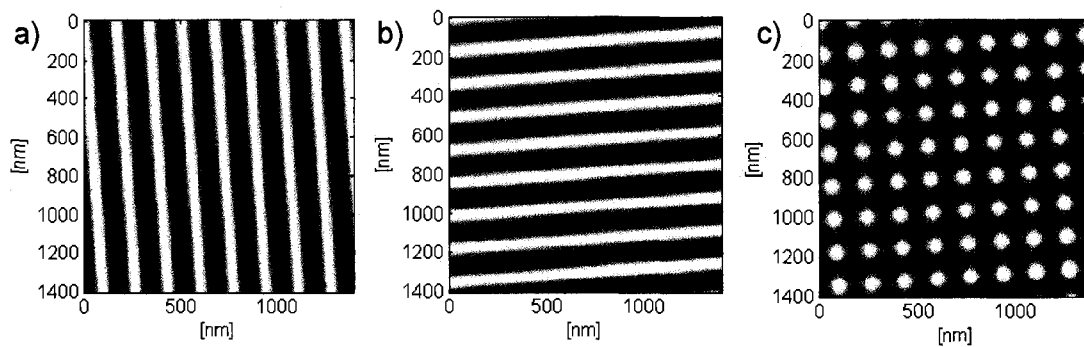


Figure 3.20. The intensity patterns generated by the described model, (a, b) intensity patterns in each of two exposures, the total intensity pattern generated by incoherent addition of the doses for angle between the exposures equal to 90° c).

The features are not circular any more and the resulting intensity pattern will give after the photoresist developing elongated pillars or holes depend on the tone of the photoresist. The angle of the features can be described by the half of the relative angle between the exposures. In this case is equal to 15° relative to both exposures.

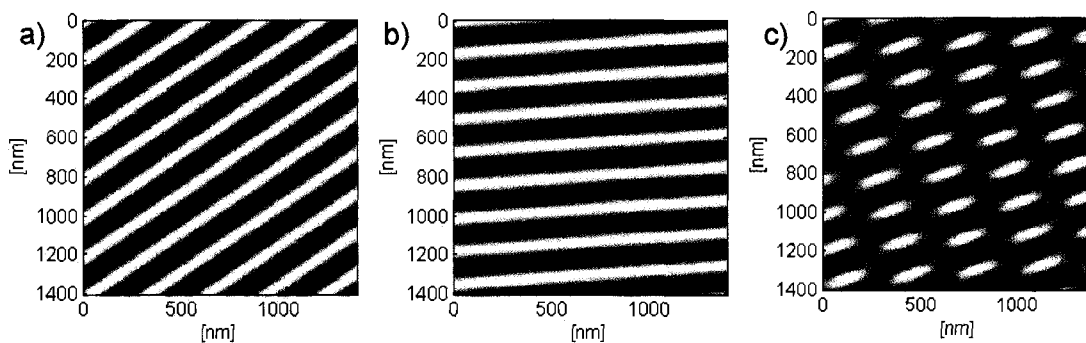


Figure 3.21. The intensity patterns generated by the described model, (a, b) intensity patterns in each of two exposures, the total intensity pattern generated by incoherent addition of the doses for angle between the exposures equal to 30° c).

Another possibility is to change the period d of the intensity pattern just by changing the angle Θ . Doing that in each exposure gives the intensity patterns shown in Figure 3.22.

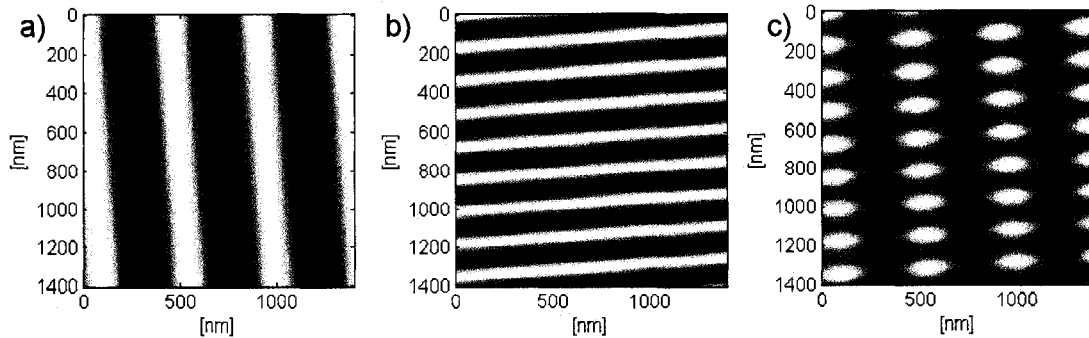


Figure 3.22. The intensity patterns generated by the described model, (a, b) intensity patterns in each of two exposures with periods equal to 448nm and 168nm respectively, the total intensity pattern generated by incoherent addition of the doses for angle between the exposures equal to 90° c).

The resulting pattern also gives elongated shape features just by changing the periods in each exposure. There is a lot of flexibility in choosing the patterns made in this way as soon as they are symmetric. Due to the different response curves of the photoresists the final surface profile after developing may change. The invariant can be only the intensity illuminating the photoresist and this makes also this description more intuitive.

The intensity patterns are then expressed in terms of the exposure dose. Based on the exposure dose matrix and the response of the PMMA (discussed in detail later in this section) the normalized amount of the photoresist removed after developing procedure was calculated. Finally the normalized matrix was multiplied by the assumed thickness of the photoresist, and corrected for the penetration depth factor.

Junarsa et al. [3.29] determined the sensitivity and contrast of PMMA by exposing the resists over large areas to different doses of EUV radiation. A beamline's

undulator radiated photons with an energy centered at 92.5eV, $\lambda=13.4\pm 0.1\text{nm}$. After the resist was processed under the specified conditions, shown in

Table 3.1, the thickness of the residual resist left in the exposed area was measured as a function of exposure dose.

Table 3.1. Photoresist processing conditions. PAB is a baking condition using hotplate after the spinning is done to assure that the solvent in the photoresist has completely evaporated completely (data from [3.29]).

Resist	Solution	Spin-coat	Thickness	PAB	Development
PMMA	PMMA (4 wt %) :Chlorobenzene=3:7	3000 rpm, 60s	~55nm	130C, 5 min	MIBK: IPA=1:3, 30s

The PMMA photoresist response curve in terms of the normalized residual thickness (thickness of the photoresist remained after developing procedure) of the resist as a function of dose can be seen in Figure 3.23. Exposures of various doses were performed through a blank mask to find the resist response curves for PMMA [3.39].

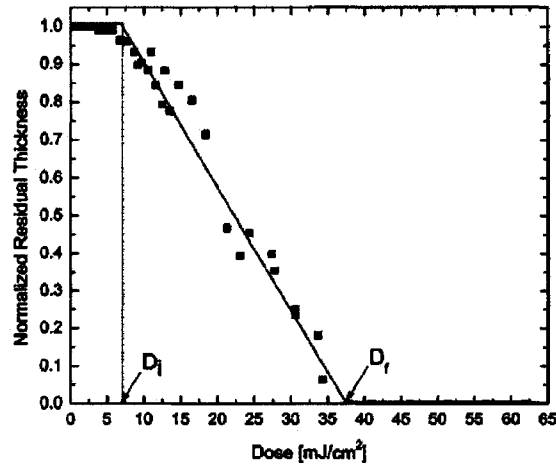


Figure 3.23. Photoresist response curve for PMMA in terms of the normalized residual thickness as a function of dose (figure from [3.29]).

The sensitivity of PMMA for EUV exposures was found to be $38.2\text{mJ}/\text{cm}^2$. The response of the PMMA can be easily approximated by horizontal lines below the D_i and above D_f points. The dose below D_i means that the photoresist was not activated resulting that all residual thickness of the resist is left after the developing process.

On the other hand if the dose is higher than D_f the resist is activated completely and the developing will remove all the photoresist down to the penetration depth of the photons at given wavelength. Between D_i and D_f the photoresist response of the PMMA can be approximated using linear function. This is the linear response region of the PMMA. In the case of PMMA D_i was estimated to be $\sim 7.5\text{mJ}/\text{cm}^2$ and $D_f \sim 37.5\text{mJ}/\text{cm}^2$.

The exposure dose necessary for the model was recalculated in terms of number of laser shots. The energy per shot was calculated for the capillary discharge laser by integrating the response to the EUV radiation of the photodiode equipped with gold photocathode according to the equation:

$$E = \frac{V_{\text{int}} \cdot \Delta t \cdot E_{\text{ph}} [\text{eV}]}{R_{\text{osc}} \cdot q_{\text{eff}}} \cdot \text{Att}_{\text{ph}} \cdot \frac{\text{Att}_{\text{beam}}}{\text{Att}_{\text{ocs}}} \quad (3.29)$$

where V_{int} is the integrated voltage based on the response of the photodiode to the EUV laser pulse, $\Delta t = 0.5\text{ns}$ is the time step, energy of the photon $E_{\text{ph}} = 26.5\text{eV}$, wavelength $\lambda = 46.9\text{nm}$, $R_{\text{osc}} = 50\Omega$ is the resistance of the oscilloscope's channel, $q_{\text{eff}} = 0.06$ is a quantum efficiency in [electrons/photons] for a gold photocathode at 26.5eV obtained from [3.40], the beam was attenuated with 3 stainless steel meshes. By the geometry and size of the holes the transmission of these meshes was estimated to be 33%. Three

meshes were used resulting $Att_{beam} = 0.33^3 = 3.59 \cdot 10^{-2}$. The oscilloscope has an additional 3x attenuator $Att_{osc} = 0.33$. The photodiode used in this measurement was equipped with acceleration mesh with a transmission equal to $Att_{ph} = 0.33$. The energy of the laser pulse was found to be equal to 0.1mJ with a 27cm capillary length. At the distance 2.1m from the exit of the capillary, assuming the total divergence of the laser beam is $\Theta = 9mrad$, the radius of the beam was estimated to be $\sim 9.5mm$. From the size of the beam and the pulse energy, the dose in the single shot was calculated as a ratio between the energy and the area equal to be $3.56 \cdot 10^{-2} mJ/cm^2$. This dose multiplied by the number of laser shots gives the total dose for each exposure.

Figure 3.24 shows the results of the model's predictions for PMMA for various conditions. Figure 3.24a shows small area $2 \times 2 \mu m^2$ with pillars with a dose $\sim 170 mJ/cm^2$ and the angle between two exposures $\alpha = 90^\circ$. A high exposure causes that the resist will be activated everywhere except the regions where two interference minima are overlapped. In these regions small pillars of non activated photoresist will remain after developing. Figure 3.24b shows $1.4 \times 1.4 \mu m^2$ area with holes, with lower exposure dose $\sim 110 mJ/cm^2$ and $\alpha = 90^\circ$. A lower exposure dose causes that the resist will be activated only in the regions where interference maxima are overlapped. In these regions small holes will be formed after the developing. Figure 3.24c shows $3 \times 3 \mu m^2$ area with asymmetric pillars with $\alpha = 30^\circ$, which creates elongated pillars and finally Figure 3.24d shows another possibility to fabricate elongated shaped pillars or holes by changing the periods in the two exposures. A $2 \times 2 \mu m^2$ area with elongated holes in the surface made with the angle between the exposure $\alpha = 90^\circ$ and two different periods in two consecutive exposures 150 and 220nm is shown in Figure 3.24d.

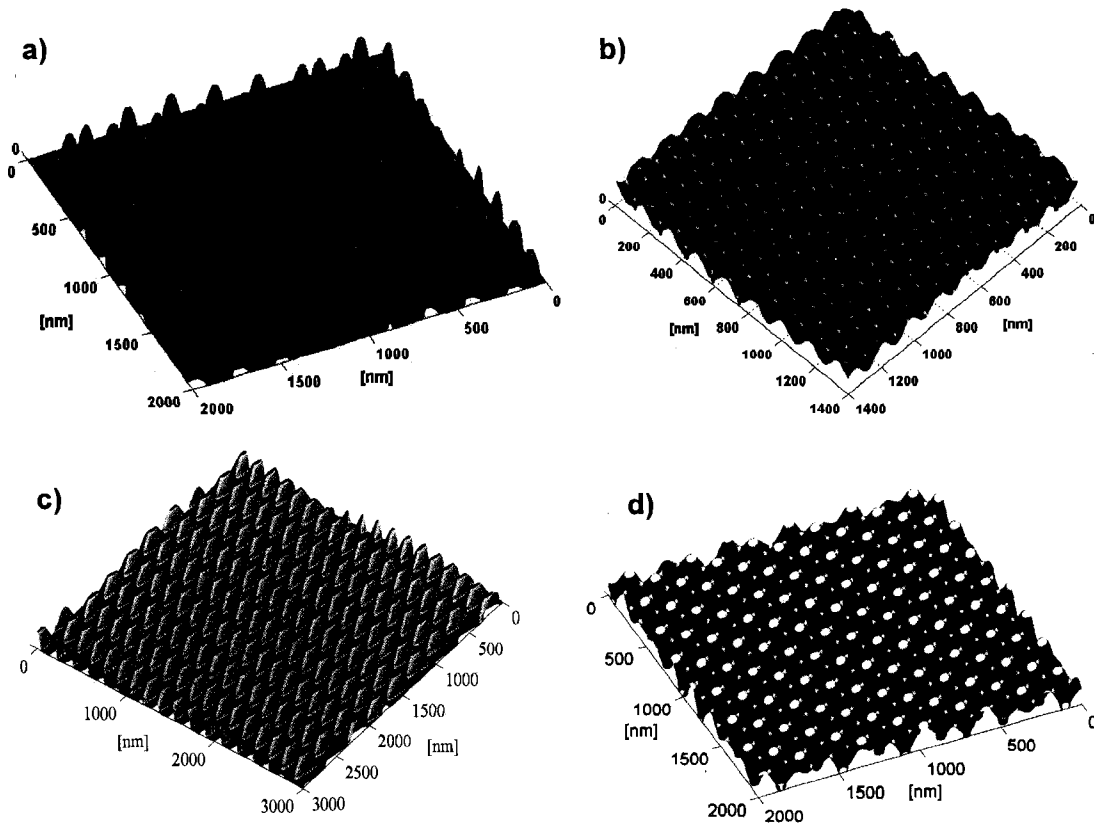


Figure 3.24. Results of the PMMA photoresist model for various conditions: a) $2 \times 2 \mu\text{m}^2$ area with pillars made high dose ($\sim 170 \text{ mJ/cm}^2$) with the angle between the exposure $\alpha = 90^\circ$, b) $1.4 \times 1.4 \mu\text{m}^2$ area with holes in the surface made with lower dose ($\sim 110 \text{ mJ/cm}^2$) with the angle between the exposure $\alpha = 90^\circ$, c) $3 \times 3 \mu\text{m}^2$ area with elongated pillars in the surface made with the angle between the exposure $\alpha = 30^\circ$, d) $2 \times 2 \mu\text{m}^2$ area with elongated holes in the surface made with the angle between the exposure $\alpha = 90^\circ$ and two different periods in two consecutive exposures 150 and 220 nm.

This simple model describing the photoresist behavior was based on the photoresist response curve. The model is capable of simulating 1-D and 2-D periodic patterns. More complicated cases can be modeled as well as using various types of positive and negative photoresists knowing its response curves.

3.8 Experimental results

This section will describe the results of nanopatterning using the compact patterning tool based on the Lloyd's mirror interferometer. Two types of photoresists will be discussed: PMMA and HSQ and different motifs patterned in the surface of both photoresists will be presented.

3.8.1 Patterning of PMMA photoresist

This is a positive tone photoresist composed from carbon, oxygen and hydrogen atoms. The sample consisting of a Si wafer coated with PMMA was mounted at the edge of the mirror on a magnetic mount in a motorized rotation stage. During the patterning step a PMMA coated sample was initially exposed to produce an interference pattern consisting of regular lines parallel to the mirror's edge. This was followed by a second exposure in which the sample was rotated *in situ* by an angle α . The results of the patterning experiment using PMMA and the compact nanopatterning tool based on the Lloyd's mirror interferometer were reported in [3.41].

Typically single exposure required 30-50 seconds. Multiple exposures were used to print periodic patterns over surface areas approximately $500 \times 500 \mu\text{m}^2$. Ultra thin photoresist layers, with thickness approximately 30nm [3.42], were deposited on the silicon sample to match the thickness of the photoresist layer to the penetration depth of the 46.9nm photons in PMMA, allowing the photolithographic pattern to reach the

substrate. This was accomplished by spin coating the substrate with diluted 1% PMMA in anisole at 5000 rpm in a standard spin coater.

After the exposure the PMMA was developed with the standard procedure consisting of an immersion in a 1:3 solution of MIBK-methyl isobutyl ketone (4-Methyl-2-Pentanone) with IPA- isopropyl alcohol for 35 seconds, followed by rinsing with IPA. The sample was subsequently dried using compressed nitrogen.

3.8.1.1 Different motifs in PMMA

The pattern motif can be controlled by:

- I. Changing the exposure dose: a high dose produces pillars and low dose – holes.
- II. Changing the angle α between exposures: this angle changes the geometry of the pattern allowing for elongated (oval shaped) features.
- III. Changing the interferometer angle Θ – this angle is the pivoting platform angle on the top of which the interferometer is mounted and changes the period of the interference pattern in each exposure.

I. Changing the exposure dose.

The photon dose applied in each exposure, calculated as the energy per unit area, allows control over the shape of the imprinted features. If the applied dose is $166\text{mJ}/\text{cm}^2$ (high dose), which corresponds to about 60 laser shots in each exposure, the only not activated region of the photoresist is the region of overlapping of two interference

minima in two consecutive exposures. In this case the activated volume generates after developing a regular array of trenches in two perpendicular directions that leave small non activated spots at the intersections. The experimental pattern is shown in Figure 3.25a and corresponds to a very regular array of cone-shaped dots that closely resembles the simulation (Figure 3.24a).

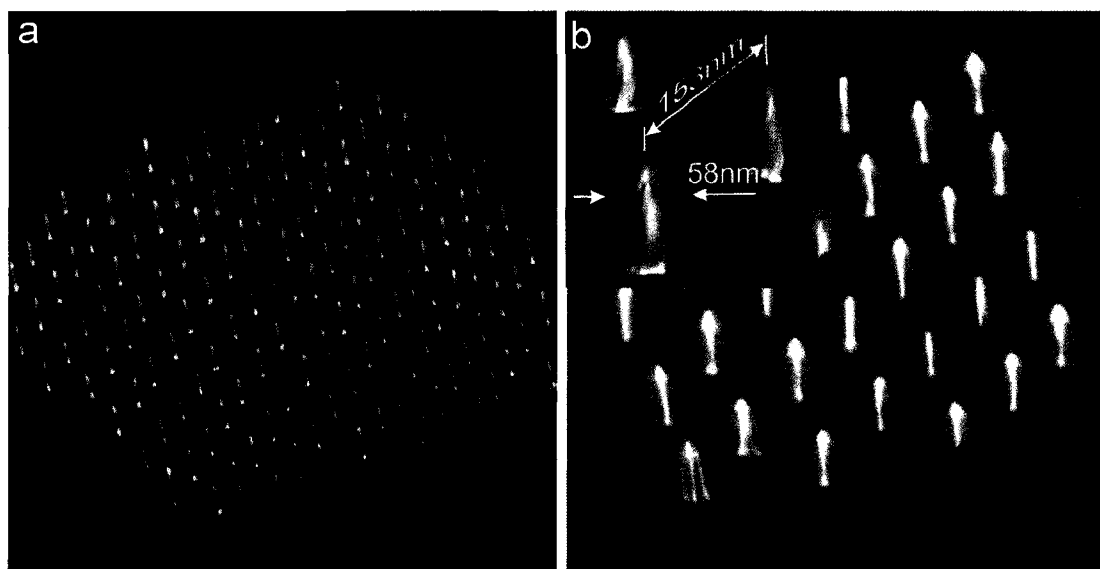


Figure 3.25. a) Fabricated arrays of cone-shaped nano-dots patterned in PMMA by double exposure with a Lloyd's mirror configuration, with $\alpha = \pi/2$ and high ($166\text{mJ}/\text{cm}^2$, 60+60 laser shots) photon dose, b) detailed image showing in details 58nm FWHM the nano-dots.

The period, 153nm in this example, can be continuously changed by varying the incidence angle Θ . The FWHM of the features is equal to 58nm. An atomic force microscope (AFM, Novascan 3D) scan with a size $1.2 \times 1.2 \mu\text{m}^2$ is shown in Figure 3.25b. The period and the FWHM of the cone-shaped dots are indicated. Cones with FWHM down to 58nm (1.2λ) were obtained with period 153nm. The height of the cones corresponds to the penetration depth of the 46.9 nm light in the PMMA, approximately 30nm.

Figure 3.26 shows the holes fabricated in a PMMA layer for a low dose exposure around $110\text{mJ}/\text{cm}^2$. This dose corresponds to approximately 40 laser shots in each exposure.



Figure 3.26. Fabricated array of holes patterned in PMMA by double exposure with a Lloyd's mirror configuration, $\alpha = \pi/2$ and low ($110\text{mJ}/\text{cm}^2$, 40+40 laser shots) photon dose showing in details 60nm FWHM holes.

For that dose the photoresist is only activated along lines coincident with the interference maxima, leaving in the crossing points small regions where small holes are developed. A small $1.4 \times 1.4\mu\text{m}^2$ section of the total printed surface was scanned with an AFM in tapping mode with a 10nm tip radius AFM probe. 60nm FWHM diameter holes were fabricated that closely resemble the simulation shown in Figure 3.24b.

II. Changing the rotation angle α .

This situation is depicted in Figure 3.27, where a double exposure scheme is presented for the angle between the exposures equal to $\alpha = \pi/6$. If the rotation angle

was for example $\alpha = \pi/6$, an array of oval dots was patterned as shown in Figure 3.28. AFM scan size was $3 \times 3 \mu\text{m}^2$.

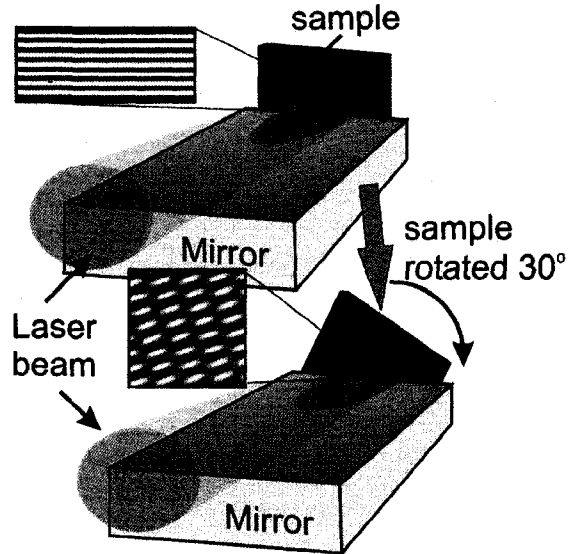


Figure 3.27. Double exposure scheme with an angle between exposures equal to $\alpha = \pi/6$. Depending on the dose holes or pillars will be fabricated after the developing procedure.

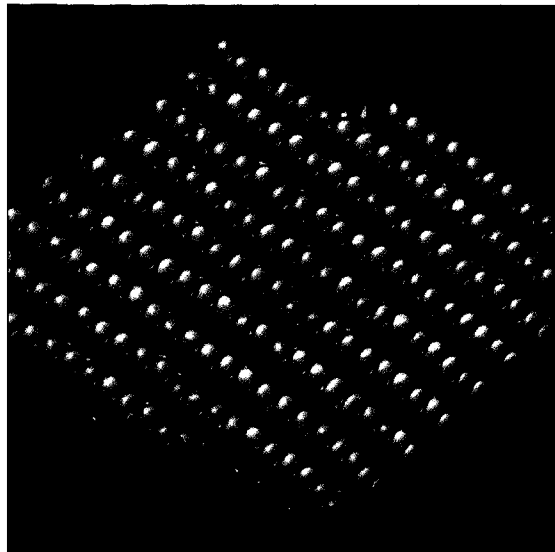


Figure 3.28. Fabricated array of oval-shaped nano-dots patterned in PMMA by double exposure with a Lloyd's mirror configuration, with $\alpha = \pi/6$. Pillars - FWHM $80 \times 160 \text{nm}^2$ were obtained with periods 160nm and 320nm, respectively.

The oval-shaped nano-dots were fabricated with periods 160nm and 320nm. The size of the oval dots is equal to half of the periods: 80nm and 160nm, respectively. The oval dots are similar to the simulation shown previously in Figure 3.24c.

III. Changing the incidence angle Θ .

In this case the angle between the exposures was $\alpha = \pi/2$, which will give square or rectangular feature distribution, but instead, in each exposure the period of the patterned features was changed by changing the interferometer angle Θ . This situation is depicted in Figure 3.29a.

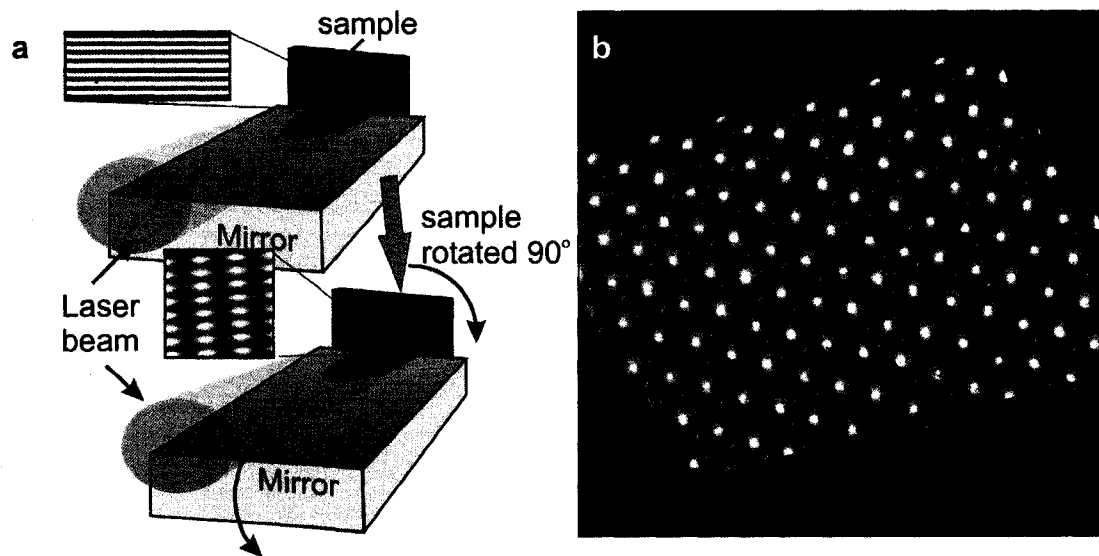


Figure 3.29. a) Double exposure scheme with an angle between exposures equal to $\alpha = \pi/2$, but with different period in each exposure adjusted by changing the interferometer angle. b) Fabricated arrays of oval-shaped nano-dots patterned in PMMA by double exposure with a Lloyd's mirror configuration, with $\alpha = \pi/2$ and different periods in each exposure 150nm and 220nm. Pillars - FWHM $75 \times 110 \text{ nm}^2$ were obtained in this experiment.

The photoresist surface, scanned with AFM was depicted in Figure 3.29b. In the first exposure the angle was set to have 150nm period in the pattern while in the second

exposure the period was slightly increased to 220nm. That gave $75 \times 110 \text{nm}^2$ (1.6×2.3) λ pillars in the surface of the photoresist that closely resemble the simulated case shown in Figure 3.24d.

3.8.1.2 Smallest features over large patterning area

The examples of the smallest patterns obtained in the surface of the PMMA are depicted in Figure 3.30. Two dimensional pattern, Figure 3.30a, obtained in two exposures shows pillars 45nm FWHM diameter and 90nm period in the PMMA surface. Figure 3.30b shows one dimensional pattern (lines) obtained with single exposure, 47nm lines ($\sim 95\text{nm}$ period).

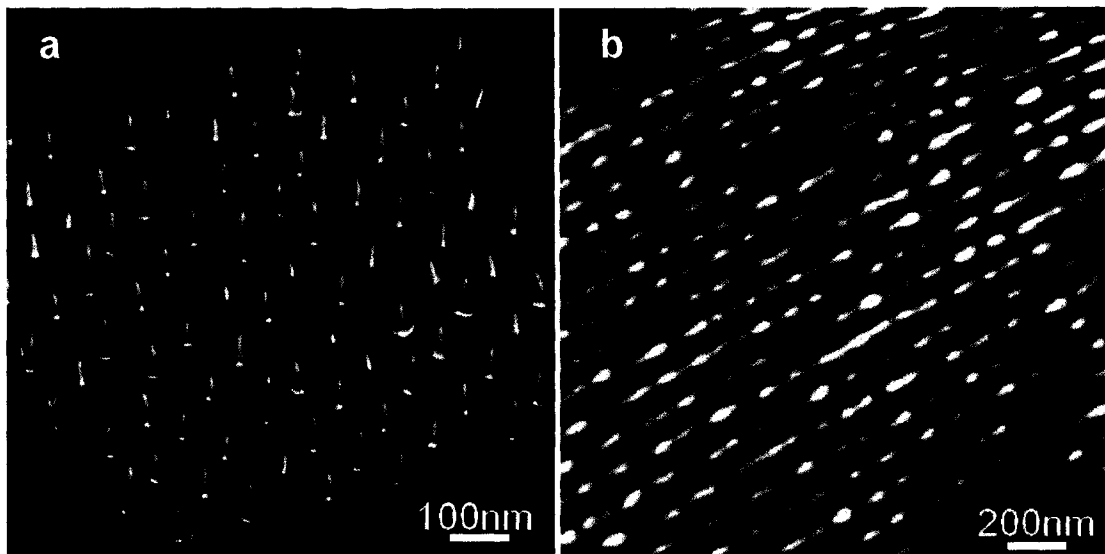


Figure 3.30. The examples of the smallest patterns obtained with compact nanopatterning tool in the surface of the PMMA. Two dimensional pattern a) obtained in two exposures showing pillars 45nm FWHM diameter and 90nm period in the PMMA surface. One dimensional pattern b) obtained with single exposure showing 47nm FWHM lines and $\sim 95\text{nm}$ period. Because of the patterning tool visibility limitations at higher interferometer angles the patterns quality is reduced.

Because reduction of the reflectivity at higher interferometer angles, that reduces the visibility of the interference patterns, the quality of the fabricated features is less than optimal. However these small patterns indicate the features with sizes equal or even smaller than the illumination wavelength of the EUV source.

Figure 3.31 shows the examples of the features patterned over large areas. Pillars in Figure 3.31a with 70nm FWHM diameter and 140nm period are depicted over $10 \times 10 \mu\text{m}^2$ and lines in Figure 3.31b with 47nm FWHM and 95nm period over the $7 \times 7 \mu\text{m}^2$. Both lines and pillars are distributed very uniformly over the large areas $\sim 500 \times 500 \mu\text{m}^2$.

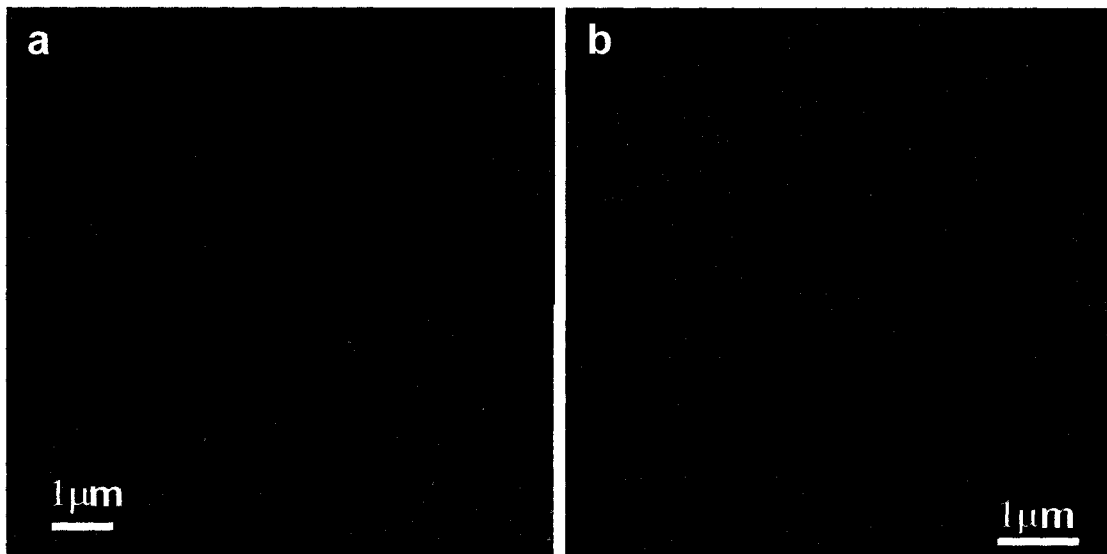


Figure 3.31. The examples of the features patterned over large areas in the PMMA photoresist. Pillars a) with 70nm FWHM diameter and 140nm period are shown over $10 \times 10 \mu\text{m}^2$. Lines b) 47nm FWHM with 95nm period over the $7 \times 7 \mu\text{m}^2$ are depicted. The quality of the pattern distribution is high.

3.8.2 Patterning of HSQ photoresist

This is a negative tone photoresist composed from silicon, oxygen and hydrogen atoms.

3.8.2.1 Advantages of HSQ

The advantage of this inorganic resist, as compared with the carbon-based photoresist PMMA, is its lower attenuation in the EUV region where all organic materials exhibit strong atomic absorption. The chemical constituents of PMMA are hydrogen, oxygen and carbon, HSQ instead of carbon has silicon and similarly oxygen and hydrogen. Using the CXRO database [3.36] the attenuation length (e^{-1} intensity drop) was found for each of the elements at the closest available in the database wavelength, 41nm. The limiting factor in PMMA is the carbon, which has the attenuation length of 25nm, while the other PMMA components hydrogen and nitrogen are not limiting the pattern depth because their attenuation lengths are in micro-meter range, 200 μ m and 18 μ m respectively, as shown in the scheme in Figure 3.32.

Hydrogen and oxygen are also components of HSQ, but silicon instead of carbon allows for up to an 8 times larger penetration depth. Another important advantage is that the HSQ is more resistant to ion beam etching. That was demonstrated by etching using chemically assisted ion beam etching (CAIBE) with identical etching parameters two samples coated with PMMA and HSQ. For the particular case of chlorine in the etching chamber, about 4scm flow, and argon (2.5scm flow) with ion beam parameters: beam current $I_D = 0.28A$, beam voltage $V_B = 250V$, beam current $I_B = 19mA$, acceleration

voltage $V_A = 500V$ it was found that PMMA etching rate is about 1.08-1.15nm/s while for HSQ the etching rate was equal to 0.41-0.53nm/s.

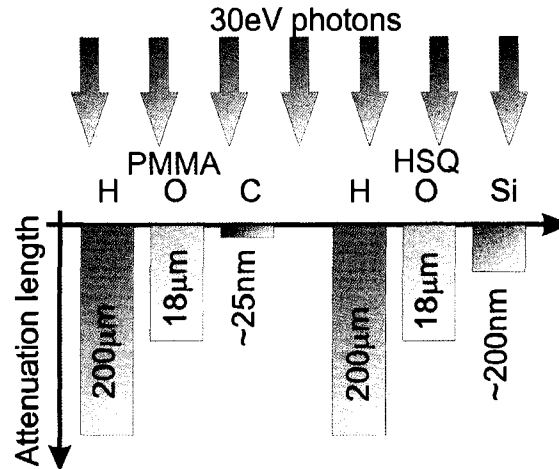


Figure 3.32. Chemical composition of PMMA and HSQ photoresists. Limiting component in case of PMMA is carbon with ~25nm attenuation length at 41nm wavelength. HSQ is inorganic and has silicon instead, which allow to obtain taller structures (8 times higher attenuation length).

The range of the etching rates corresponds to different experiments repeated at the same conditions. The ratio between the etching rates of PMMA and HSQ is between 2 and 2.8. HSQ is more resistant to ion beam etching and allows to transfer the pattern from the photoresist to the substrate more efficiently (deeper into the substrate) than the PMMA. For future reference the etching rates for other materials at exactly the same etching conditions as above were also estimated and are presented in Table 3.2.

Another important advantage of HSQ is its spatial resolution. It was reported in [3.43] that lines of 5.3nm width were successfully obtained using e-beam lithography. That value exceeds the resolution of PMMA that was estimated to be around 10nm [3.44, 3.45]. Moreover, as it will be discuss later, HSQ requires less exposure dose at 46.9nm than PMMA. This characteristic makes HSQ an attractive alternative as a high resolution photoresist.

Table 3.2. Etching rates for various materials obtained using CAIBE system.
Etching conditions are shown on the top of the table.

conditions: $I_D = 0.28A, V_B = 250V, I_B = 19mA$ $V_A = 500V, Cl_2 = 4scm, Ar = 2.5scm$	
Material	Etching rate [$\text{\AA}/s$]
PMMA (polymethyl methacrylate)	10.8-11.5
HSQ (hydrogen silsesquioxane)	4.17-5.3
Si (silicon)	12.1-13.3
Cr (chromium)	0.67
Ni (nickel)	1.33
Ag (silver)	5.1-8.6
Au (gold)	7.3-8.3
Si ₃ N ₄ (silicon nitride)	7.4

3.8.2.2 Analysis of photosensitivity of HSQ at 46.9 nm

To evaluate the exposure conditions necessary to activate the photoresist, samples consisting of Si wafers spin coated with HSQ (XR-1541) at different concentrations were prepared. Several Si wafers were spun with HSQ 1% solids, 4% solids and 6% solids obtaining resist thickness ranging from 35 to 150nm, which is in good agreement with the spinning curves published by the photoresist manufacturer [3.46] and depicted in Figure 3.33. The spinning parameters for the different samples are summarized in Table 3.3.

After spinning, the samples were pre-baked for 5 minutes at 90 °C. Later the samples were exposed with different doses and after the exposure post-baked during 15 minutes at 110 °C. The developing was performed in LDD26W, 2.38% tetra-methyl-ammonium hydroxide (TMAH) in water for 45 seconds, rinsed with de-ionized water for 30 seconds and dried with compressed nitrogen. Table 3.4 summarizes the results of this test.

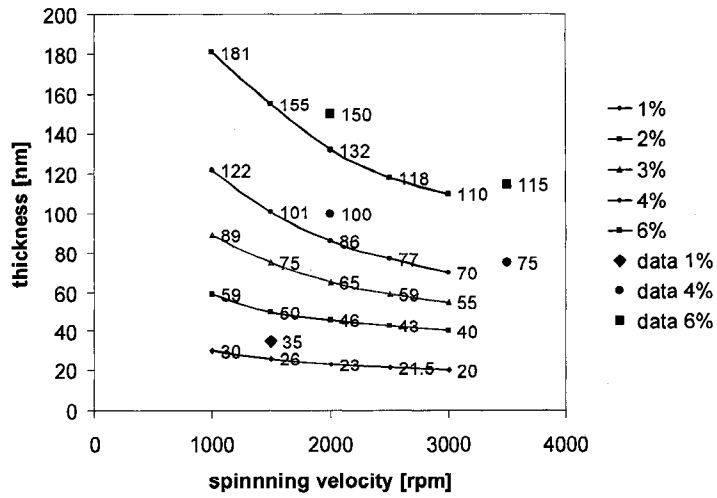


Figure 3.33. Spinning curves for HSQ form manufacturer's specifications (lines) for various concentrations and with the measured data (points) obtained using AFM. Numbers are indicating the precise values.

Table 3.3. Measured HSQ thickness for various concentrations and spinning velocities using AFM.

HSQ concentration	Spinning velocity [rpm]	Resist layer thickness [nm]
1% solids	1500	35
4% solids	2000	100
4% solids	3500	75
6% solids	2000	150
6% solids	3500	115

Table 3.4. Measured modulation depth after exposing HSQ photoresist with different doses and for different HSQ concentrations. The developing conditions were kept unchanged.

HSQ concentration	Exposure [mJ/cm ²]	Modulation depth [nm]
1% solids	30	33
1% solids	60	40
1% solids	90	40
4% solids	30	101
4% solids	45	107
6% solids	30	153
6% solids	45	153

An average exposure of 100 laser shots that corresponds to a dose in the sample surface of approximately $35\text{mJ}/\text{cm}^2$ completely activates the HSQ. The sample was illuminated with a small section of the laser beam corresponding to the maximum intensity in the beam profile. Based on the statistical shot to shot variation of the laser pulse energy the uncertainty of 12% [3.47] of the exposure dose was estimated. This test also demonstrated that the penetration depth of the $\lambda=46.9\text{ nm}$ photons is at least 150nm.

3.8.2.3 Multiple exposure IL with HSQ

Multiple exposures IL were implemented with HSQ coated samples. The energy density in the laser beam is the total energy of the laser pulses divided by the surface area and the dose at the sample plane is the energy per unit area enhanced by the interference. At small interferometer angles Θ the enhancement is approximately equal to 4. Changing the energy density of the laser beam in each exposure allows for printing different features. In the case of single exposure, lines parallel to the mirror's edge are obtained as shown in Figure 3.34a. This figure shows lines 106nm FWHM that were made with a dose $\sim 41\text{mJ}/\text{cm}^2$ at the sample plane. Two dimensional structures were made by multiple exposures. An example of hole pattern in HSQ is depicted in Figure 3.34b showing 130nm FWHM diameter holes 110nm deep made with two exposures with doses $\sim 20\text{mJ}/\text{cm}^2$ each.

When the laser energy density is equal to approximately $3.5\text{mJ}/\text{cm}^2$, corresponding to the dose $\sim 14\text{mJ}/\text{cm}^2$, the photoresist was only activated in small

volumes in the intersections of the interference maxima, developing in this case an array of small dots (pillars), as shown in Figure 3.35a.

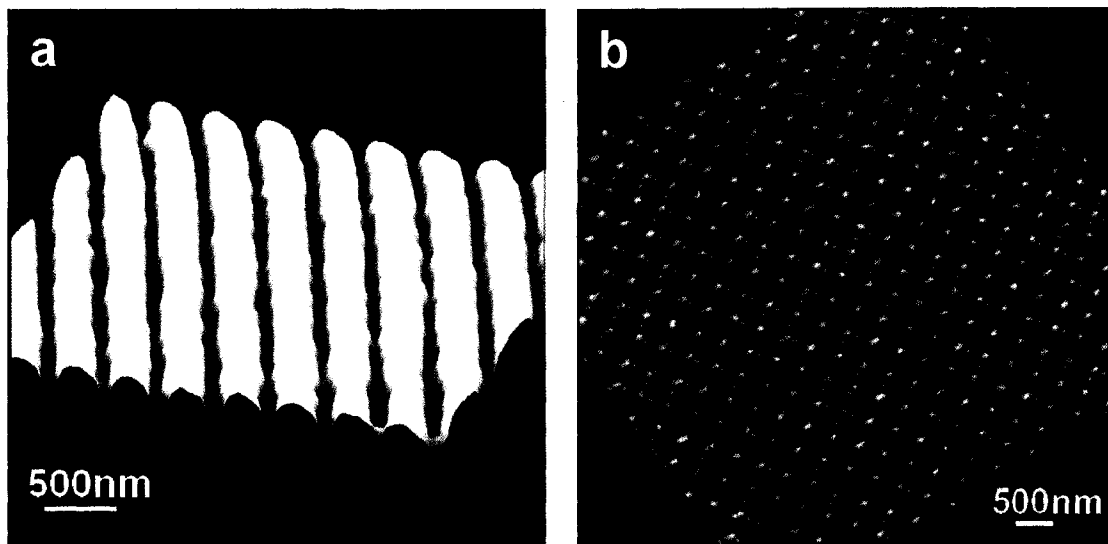


Figure 3.34. One and two dimensional patterns in the surface of HSQ photoresist. Lines 106nm FWHM a) in HSQ made in single exposure with dose at the sample plane $\sim 41\text{mJ}/\text{cm}^2$ and holes b) 130nm FWHM diameter patterned in HSQ with depth exceeding 110nm made in two step exposure with dose $\sim 41\text{mJ}/\text{cm}^2$.

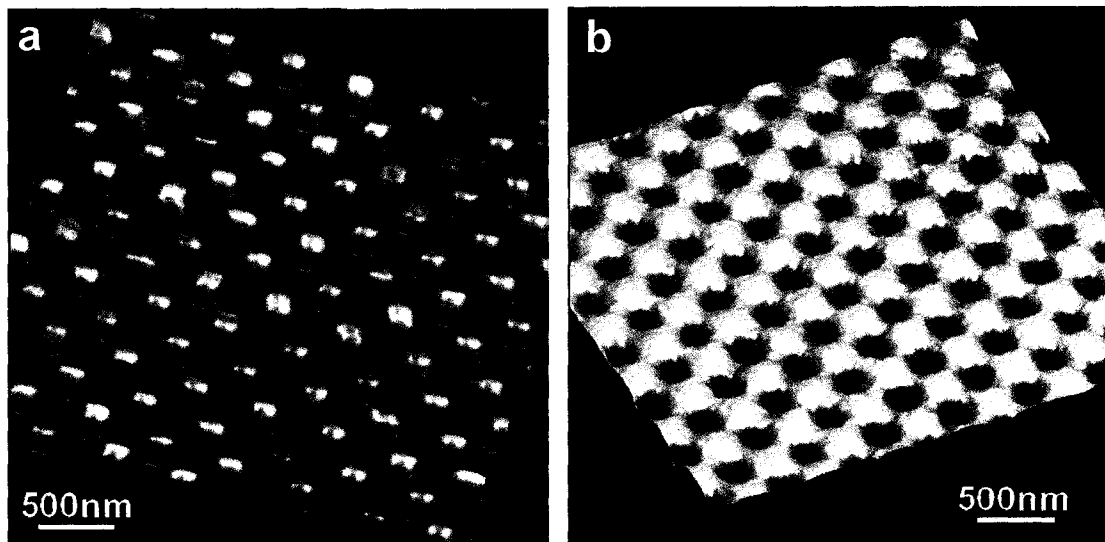


Figure 3.35. Array of nanodots a) obtained with low dose ($14\text{mJ}/\text{cm}^2$) illumination and array of holes developed in HSQ with a high dose ($41\text{mJ}/\text{cm}^2$) illumination b).

That means that the lithographic activity of the HSQ starts at doses around $14\text{mJ}/\text{cm}^2$. The results of the HSQ patterning were reported in [3.48]. If the energy density is increased to approximately $14\text{mJ}/\text{cm}^2$, (dose $\sim 40\text{mJ}/\text{cm}^2$), the resist was activated in wide strips that develop in the intersections small holes as shown in Figure 3.35b.

The versatility of this IL set up allows changing the feature characteristics (holes or dots) very easily by changing the applied dose and the periodicity by changing the incidence angle on the mirror. The size and distribution of the holes and nano-dots in the array were very homogeneous as can be observed in the 2-D Fourier transform of the AFM image. This plot, shown in Figure 3.36, has only significant contributions at the hole spacing spatial frequency and its harmonics.

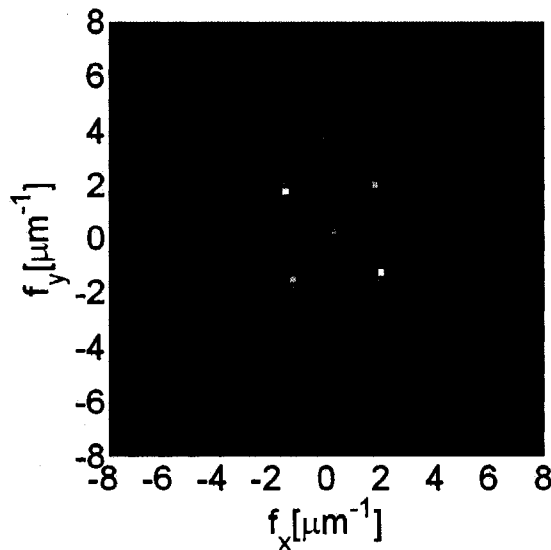


Figure 3.36. Two dimensional Fourier transform of the image Figure 3.35b showing only significant contributions at the hole spacing spatial frequency and its harmonics.

As it can be seen, the required exposure doses at the sample plane for HSQ are much lower than in the case of PMMA. The comparison Table 3.5 shows the combined results for patterning the PMMA and HSQ.

Table 3.5. Comparison table showing required exposure doses to fabricate pillars or pattern of holes in both PMMA and HSQ photoresists.

pattern/photoresist	PMMA	HSQ
holes	110mJ/cm ²	41mJ/cm ²
pillars	166mJ/cm ²	14mJ/cm ²

As it was mentioned before the HSQ requires less exposure dose at 46.9nm than PMMA. This is quantitatively shown in the table above. In the worst case (hole pattern) PMMA requires 2.7 times more photons to be activated than HSQ, while in the case of pillars the exposure ratio increases up to 11.8.

As in the case of PMMA the patterned area is dependent on the coherence parameters of the EUV laser and it is possible to print uniform arrays of features up to 0.5x0.5mm². The patterns obtained in this way are very uniform as can be seen in Figure 3.37. Holes 100nm FWHM diameter and 120nm deep over 20x20μm² scanned area are depicted.

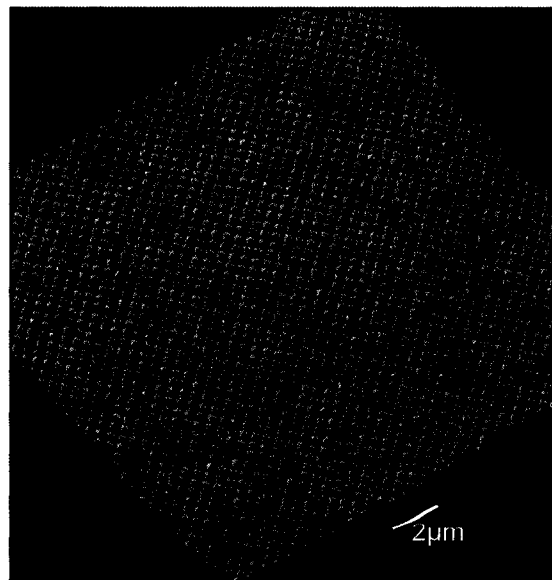


Figure 3.37. Large arrays of holes patterned in HSQ photoresist. Holes are 120nm deep and ~100nm FWHM diameter. Scan size 20x20μm², dose ~80mJ/cm².

We observed that the modulation depth that can be obtained in the exposed HSQ, measured as the difference between the maximum and minimum heights in the photoresist surface, depends on the applied dose at the surface of the photoresist and also on the developing time. Figure 3.38 is a plot of the modulation depth in a double exposure sample for different exposure and developing conditions.

These curves were obtained for a photoresist layer $\sim 100\text{nm}$ thick with the use of 4% solution (solids). The samples were patterned with holes with a period approximately 500nm . Large period was chosen to avoid having any AFM tip influence on the measured modulation depth that can be significant at very small scales. The maximum modulation depth was obtained with the energy density of $8.5\text{mJ}/\text{cm}^2$. This energy density corresponds to a dose equivalent to $33\text{mJ}/\text{cm}^2$ measured at the photoresist surface, due to the intensity enhancement produced by the interference effect.

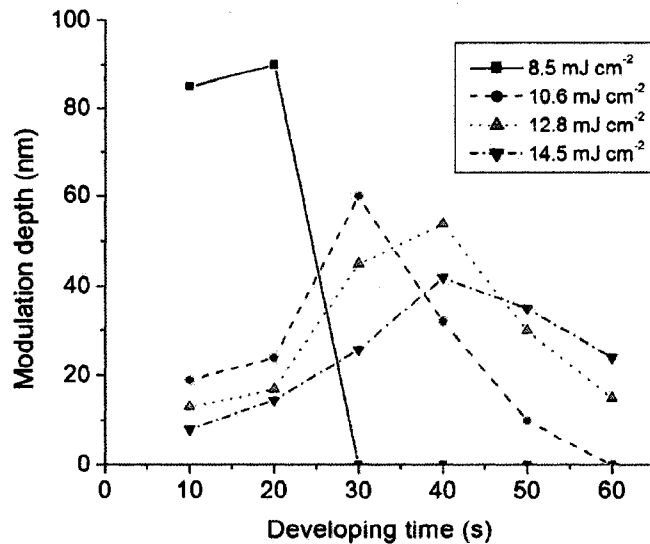


Figure 3.38. Modulation depth for an array of holes with $\sim 500\text{nm}$ period as a function of the developing time for different exposure doses.

To calculate the interference enhancing factor the reflectivity of the mirror at the incidence angle used in this test $\Theta = 2.8^\circ$ was assumed to be 96% [3.36]. For this dose the optimum developing time is between 10 and 20 seconds with 2.38% concentration of TMAH. These curves indicate that at the lowest energy density ($8.5\text{mJ}/\text{cm}^2$), the photoresist is not completely activated and it is completely removed by the TMAH solution when the developing time is prolonged more than the optimum developing time. In the regions corresponding to the minima of interference, the low energy density assures that the photoresist is completely removed even for short developing times thus achieving the maximum modulation depth. At larger doses the optimum developing time increases, but also a lower modulation depth is obtained indicating an overexposure of the resist. This can be produced by a partial activation of the photoresist in the regions corresponding to the interference minima, which are not null due to the difference in intensities between the two interfering beams. This effect produces an even dissolution of the polymer layer in the TMAH, obtaining an increasingly lower modulation depth.

3.9 Summary

A nanometer-scale patterning tool using a table-top EUV laser and interferometric lithography was presented. Lines and dense arrays of holes and nanodots with sub-100nm feature size and a modulation depth more than 100nm were obtained. The periodicity of the structures was controlled by changing the incidence angle of laser beam at the mirror while changing the applied dose and the developing time made possible the printing of holes or dots. It was found that HSQ has sensitivity at $\lambda=46.9\text{nm}$ illumination starting the

photolithographic activity at doses of approximately $14\text{mJ}/\text{cm}^2$ at the surface of the photoresist. We also measured a penetration depth of approximately 150nm , an almost one order of magnitude larger than the penetration depth obtained at the same wavelength in PMMA. These results show that HSQ holds distinctive advantages when used with EUV photons and is an interesting alternative to realize table-top nanopatterning with EUV lasers. The overall results of nanopatterning using EUV laser in PMMA and HSQ photoresists may be found in a review article [3.49].

-
- [3.1] J. Aizpurua, P. Hanarp, D. S. Sutherland, M. Käll, W. Bryant, Garnett, F. J. García de Abajo, "Optical properties of gold nanorings", *Physical Review Letters*, **90**, 5, (2003)
- [3.2] F. J. Castaño, D. Morecroft, W. Jung, C. A. Ross, "Spin-dependent scattering in multilayered magnetic rings", *Physical Review Letters*, **95**, 13 (2005)
- [3.3] F. J. Castaño, C. A. Ross, A. Eilez, W. Jung, C. Frandsen, "Magnetic configurations in 160-520-nm-diameter ferromagnetic rings", *Physical Review B* **69**, 14 (2004)
- [3.4] Y. Chen, A. Lebib, S. P. Li, M. Natali, D. Peyrade, E. Cambril, "Nanoimprint fabrication of micro-rings for magnetization reversal studies", *Microelectronic Engineering* **57-58**, 405 (2001)
- [3.5] A. Lebib, S. P. Li, M. Natali, Y. Chen, "Size and thickness dependencies of magnetization reversal in Co dot arrays", *Journal of Applied Physics* **89**, 7, 3892 (2001)
- [3.6] M. Born, E. Wolf, *Principles of Optics*, 7th edition, (Cambridge University Press, 1999)
- [3.7] W. Fan, S. Zhang, K. J. Malloy, S. R. J. Brueck, "Large-area, infrared nanophotonic materials fabricated using interferometric lithography", *J. Vac. Sci. Technol. B* **23**, 2700 (2005)
- [3.8] H. H. Solak, C. David, "Patterning of circular structure arrays with interference lithography", *J. Vac. Sci. Technol. B* **21**, 2883 (2003)
- [3.9] H. H. Solak, C. David, J. Gobrecht, L. Wang, F. Cerrina, "Multiple-beam interference lithography with electron beam written gratings", *J. Vac. Sci. Technol. B* **20**, 2844 (2002)
- [3.10] M. Switkes, M. Rothschild, "Immersion lithography at 157 nm", *J. Vac. Sci. Technol. B* **19**, 2353 (2001)
- [3.11] A. Fernandez, J. Y. Decker, S. M. Herman, D. W. Phillion, D. W. Sweeney, M. D. Perry, "Methods for fabricating arrays of holes using interference lithography", *J. Vac. Sci. Technol. B* **15**, 2439 (1997)
- [3.12] H. H. Solak, D. He, W. Li, S. Singh-Gasson, F. Cerrina, B. H. Sohn, X. M. Yang, P. Nealey, "Exposure of 38 nm period grating patterns with extreme ultraviolet interferometric lithography", *Appl. Phys. Lett.* **75**, 2328 (1999)

-
- [3.13] T. A. Savas, M. L. Schattenburg, J. M. Carter, Henry I. Smith, "Large-area achromatic interferometric lithography for 100 nm period gratings and grids", *J. Vac. Sci. Technol. B* **14**, 4167 (1996)
- [3.14] S.A. Zaidi, S.R.J. Brueck, "Multiple-exposure interferometric lithography", *J. Vac. Sci. Technol. B* **11**, 658 (1993)
- [3.15] M. Switkes, T. M. Bloomstein, M. Rothschild, "Patterning of sub-50 nm dense features with space-invariant 157 nm interference lithography", *Appl. Phys. Lett.*, **77**, 3149 (2000)
- [3.16] W. Hinsberg, F. A. Houle, J. Hoffnagle, M. Sanchez, G. Wallraff, M. Morrison, S. Frank, "Deep-ultraviolet interferometric lithography as a tool for assessment of chemically amplified photoresist performance", *J. Vac. Sci. Technol. B* **16**, 3689 (1998)
- [3.17] H. H. Solak, D. He, W. Li, F. Cerrina, "Nanolithography using extreme ultraviolet lithography interferometry: 19 nm lines and spaces", *J. Vac. Sci. Technol. B* **17**, 3052 (1999)
- [3.18] H. H. Solak, C. David, J. Gobrecht, L. Wang, F. Cerrina, "Four-wave EUV interference lithography", *Microelectronic Engineering* **61-62**, 77 (2002)
- [3.19] V. N. Golovkina, P. F. Nealey, F. Cerrina, J. W. Taylor, H. H. Solak, C. David, J. Gobrecht, "Exploring the ultimate resolution of positive-tone chemically amplified resists: 26 nm dense lines using extreme ultraviolet interference lithography", *J. Vac. Sci. Technol. B* **22**, 99 (2004)
- [3.20] H. H. Solak, "Space-invariant multiple-beam achromatic EUV interference lithography", *Microelectronic Engineering* **78-79**, 410 (2005)
- [3.21] A. Frauenglass, S. Smolev, A. Biswas, S. R. J. Brueck, "244-nm imaging interferometric lithography", *J. Vac. Sci. Technol. B* **22**, 3465 (2004)
- [3.22] A. K. Raub, S. R. J. Brueck, "Deep UV Immersion Interferometric Lithography", *Proc. SPIE* **5040**, 667 (2003)
- [3.23] A. K. Raub, A. Frauenglass, S. R. J. Brueck, W. Conley, R. Dammel, A. Romano, M. Sato, W. Hinsberg, "Imaging capabilities of resist in deep ultraviolet liquid immersion interferometric lithography", *J. Vac. Sci. Technol. B* **22**, 3459 (2004)
- [3.24] J. H. Burnett, S. Kaplan, "Measurement of the refractive index and thermo-optic coefficient of water near 193 nm", *Proc. SPIE* **5040**, 1742 (2003).
- [3.25] D. van Steenwinckel, J. H. Lammers, T. Koehler, R. L. Brainard, P. Trefonas, "Resist effects at small pitches", *J. Vac. Sci. Technol. B* **24**, 316 (2006)

-
- [3.26] www.microchemicals.eu/technical-information as in October 2007
- [3.27] L. F. Thompson, C. G. Willson, and M. J. Bowden, *Introduction to Microlithography*, 2nd ed. (American Chemical Society, Washington, D.C., 1994).
- [3.28] PMMA datasheet from Microchem Corp.
http://www.microchem.com/products/pdf/PMMA_Data_Sheet.pdf as in May 2008
- [3.29] I. Junarsa, M. P. Stoykovich, P. F. Nealey, "Hydrogen silsesquioxane as a high resolution negative-tone resist for extreme ultraviolet lithography", *J. Vac. Sci. Technol. B* **23**, 138 (2005)
- [3.30] M. J. Loboda, G. A. Toskey, "Understanding hydrogen silsesquioxane-based dielectric film processing", *Solid State Technol.* **41**, 99 (1998)
- [3.31] M. J. Loboda, C. M. Grove, R. F. Schneider, "Properties of a-SiO_x:H Thin Films Deposited from Hydrogen Silsesquioxane Resins", *J. Electrochem. Soc.* **145**, 2861 (1998)
- [3.32] Y. K. Siew, G. Sarkar, X. Hu, J. Hui, A. See, C. T. Chua, "Thermal Curing of Hydrogen Silsesquioxane", *J. Electrochem. Soc.* **147**, 335 (2000)
- [3.33] C. C. Yang, W. C. Chen, "The structures and properties of hydrogen silsesquioxane (HSQ) films produced by thermal curing", *J. Mater. Chem.* **12**, 1138 (2002)
- [3.34] H. Namatsu, Y. Takahashi, K. Yamazaki, T. Yamaguchi, M. Nagase, K. Kurihara, "Three-dimensional siloxane resist for the formation of nanopatterns with minimum linewidth fluctuations", *J. Vac. Sci. Technol. B* **16**, 69 (1998)
- [3.35] H. Namatsu, T. Yamaguchi, M. Nagase, K. Yamasaki, K. Kurihara, "Nanopatterning of a hydrogen silsesquioxane resist with reduced linewidth fluctuations", *Microelectron. Eng.* **41-42**, 331 (1998)
- [3.36] <http://www-cxro.lbl.gov/> as in December 2006
- [3.37] F. Zernike, "The Concept of Degree of Coherence and its Application to Optical Problems," *Physica* **5**, 785 (1938)
- [3.38] A. L. Schawlow, "Laser Light", *Sci. Amer.* **219**, 120 (1968)
- [3.39] H. H. Solak, C. David, J. Gobrecht, V. Golovkina, F. Cerrina, S. O. Kim, P. F. Nealey, "Sub-50 nm period patterns with EUV interference lithography", *Microelectron. Eng.* **67-68**, 56 (2003)

-
- [3.40] R. H. Day, P. Lee, E. B. Saloman, D. J. Nagel, "Photoelectric quantum efficiencies and filter window absorption coefficients from 20eV to 10KeV", *Journal of Applied Physics* **52**, 11, (1981)
- [3.41] P. W. Wachulak, M. G. Capeluto, M. C. Marconi, C. S. Menoni, and J. J. Rocca, "Patterning of nano-scale arrays by table-top extreme ultraviolet laser interferometric lithography", *Optics Express* **15**, 6, 3465 (2007)
- [3.42] <http://www.microchem.com/> as in September 2005
- [3.43] I. Beak, J. Yang, W. Cho, C. Ahn, K. Im, S. Lee, "Electron beam lithography patterning of sub-10 nm line using hydrogen silsesquioxane for nanoscale device applications", *J. Vac. Sci. Technol. B* **23**, 6, 3120, (2005)
- [3.44] A. C. F. Hoole, M. E. Welland, A. N. Broers, "Negative PMMA as a high-resolution resist - the limits and possibilities", *Semicond. Sci. Technol.* **12**, 1166-1170 (1997)
- [3.45] K. Yamazaki, T. Yamaguchi, H. Namatsu, "Three-Dimensional Nanofabrication with 10-nm Resolution", *Jpn. J. Appl. Phys.* **43**, L1111-L1113 (2004)
- [3.46] <http://www.dowcorning.com> as in May 2007
- [3.47] B.R. Benware, C.D. Macchietto, C.H. Moreno, and J.J. Rocca, "Demonstration of a High Average Power Tabletop Soft X-Ray Laser," *Physical Review Letters* **81**, 5804, (1998)
- [3.48] P. W. Wachulak, M. G. Capeluto, M. C. Marconi, D. Patel, C. S. Menoni, J. J. Rocca, "Nanoscale patterning in high resolution HSQ photoresist by interferometric lithography with table top EVU lasers", *Journal of Vacuum Science & Technology B* **25**, 6, 2094 (2007)
- [3.49] P. W. Wachulak, M.G. Capeluto, C. S. Menoni, J. J. Rocca, M. C. Marconi, "Nanopatterning in a compact setup using table top extreme ultraviolet lasers", *Opto-Electronics Review* **16** (4), 444-450, (2008)

CHAPTER 4

4 Nanopatterning using Amplitude Division Interferometer (ADI)

In this section a compact interferometric nano-patterning tool based on the combination of an amplitude division interferometer (ADI) and a desk-top $\lambda=46.9$ nm capillary discharge laser will be presented. The ADI has significant advantages as compared with the wave-front division Lloyd's mirror configuration described in chapter 3. First, with the ADI interferometer it is possible to print larger areas due to its relaxed spatial coherence requirements. In the ADI the interference in the sample plane is obtained by the superposition of the two beams corresponding to the two branches which are replicas of the original wavefront impinging the beam-splitter diffraction grating. This is an important advantage, in particular when the interferometer is used in combination with reduced spatial coherence sources like laser-pumped table-top EUV lasers [4.1] for example. Secondly, the intensities of both beams are equalized and consequently produce a higher contrast interference pattern over the whole printed area.

The interferometer resembles in part a Mach-Zehnder configuration where the first beam splitter is a transmission diffraction grating. The concept of this interferometric tool is depicted in Figure 4.1.

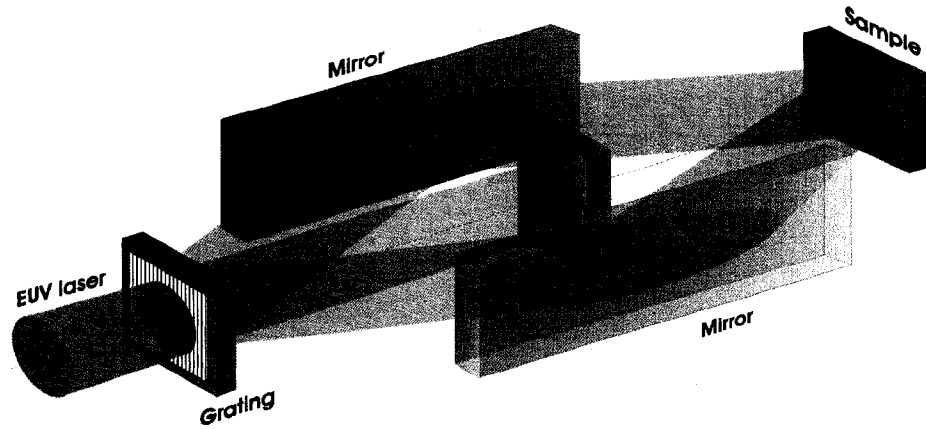


Figure 4.1. Schematic description of the amplitude division interferometer used for nanopatterning with transmission diffraction grating. Two equally intense diffraction orders are recombined at the sample plane using two mirrors. In the overlapping area interference intensity modulation exposes the photoresist.

4.1 Interferometer design

The 1st and -1st orders diffracted from a custom made transmission diffraction grating, are used to form the two arms of the interferometer. The diffraction angle α depends on the wavelength λ and the period of the diffraction grating d as $\alpha = \arcsin\left(\frac{\lambda}{d}\right)$. In the ADI implemented in this work the illumination wavelength was equal to $\lambda = 46.9nm$ and the grating period $d = 2\mu m$ resulting $\alpha = 1.34^\circ$. The zero order is blocked from reaching the sample plane. By tilting the mirrors it is possible to change the incidence angle of the beams at the sample plane. This is schematically depicted in Figure 4.2, where β describes the angle of the tilt from the axis of the interferometer. The size of the transmission diffraction grating was $2 \times 0.6mm^2$.

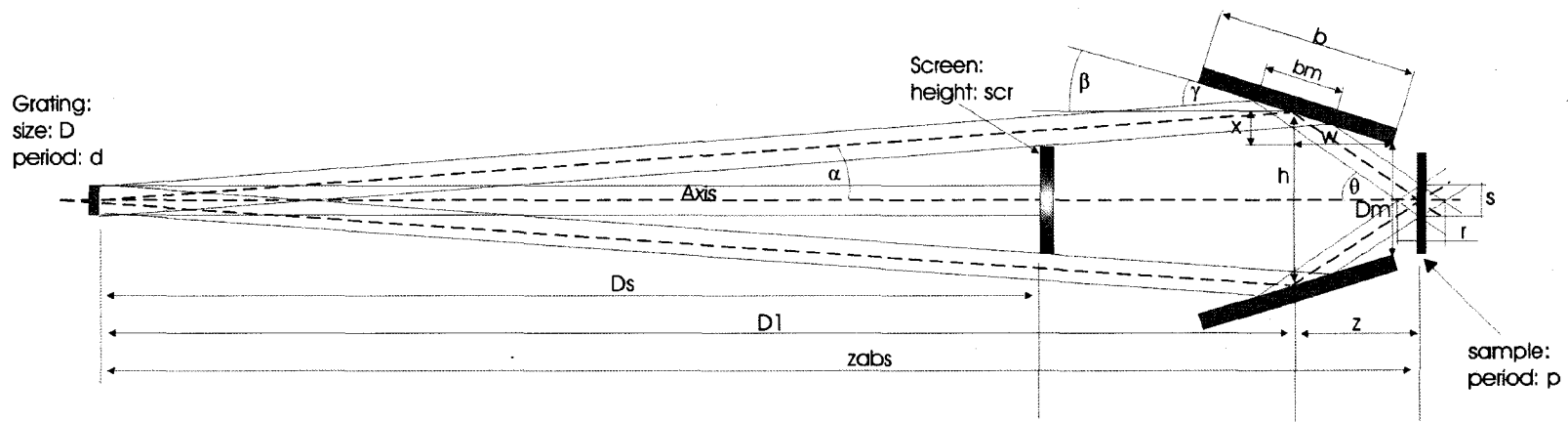


Figure 4.2. Schematic description of the interferometer used to calculate necessary parameters.

Assuming the period of the patterned structures p in the sample the two beams reflected from the mirrors need to overlap and interfere in the sample plane with incidence angles Θ equal to:

$$\Theta = \arcsin\left(\frac{\lambda}{2p}\right) \quad (4.1)$$

The mirror's grazing incidence angle for the illuminating beam γ can be then calculated using:

$$\gamma = \frac{1}{2}(\Theta + \alpha) \quad (4.2)$$

The distance between the sample and the center of the mirrors z depends on the assumed period as well as on the Θ angle and is equal to:

$$z = \frac{h}{2 \tan(\Theta)} = \frac{h}{2 \tan\left[\arcsin\left(\frac{\lambda}{2p}\right)\right]} \quad (4.3)$$

where h is the separation of the center of the mirrors.

At z position the overlap between two interfering beams should be maximal. However from geometrical point of view the pattern should be also visible at the sample locations

between $\left(z - \frac{r}{2}; z + \frac{r}{2}\right)$, where this range defines the overlap between two beams from

zero (no overlap) to maximum (s) to zero again:

$$s = \frac{D}{\cos(\Theta)} \quad (4.4)$$

and

$$r = \frac{s}{\tan(\Theta)} = \frac{D}{\sin(\Theta)} \quad (4.5)$$

r might be considered as the sample position accuracy in this case.

The quantities mentioned below considered during the design of the interferometer are depicted in Figure 4.2. The fabricated grating has a width $D = 0.6mm$. The separation between the centers of the mirrors was assumed to be $h = 15mm$. Each mirror was a square piece of a silicon wafer, $b = 1$ inch. The distance between the grating and the center of the mirrors was calculated to be $D1 = 31.97cm$. The 0th order beam block width was assumed to be $scr = 8mm$. Based on this assumption the distance of the beam block from the grating was calculated to be approximately $Ds = 18.3cm$. The period of the pattern in the sample was assumed to be $p = 100nm$ and the necessary incidence angle of the beams interfering at the sample plane generating the interference pattern with p period was calculated to be $\Theta = 13.56^\circ$. Mirror's grazing incidence angle for the illuminating beam for the period assumed previously will be equal to $\gamma = 7.45^\circ$ and the angle between the mirror's surface and the axis of the interferometer $\beta = 6.11^\circ$. The beam size on the mirror was then calculated resulting $bm = 4.63mm$ that is much smaller than the size of the mirror. The separation between the ends of two mirrors closest to the sample was equal to $Dm = 11.7mm$. The distance between the sample and the center of the mirrors for 100nm period was calculated to be $z = 31.1mm$. The total length of the interferometer was equal to $zabs = z + D1 = 35.1cm$. Placing the sample exactly at the z distance from the centers of the mirrors will produce the interference pattern with maximal width (maximal overlap of the beams) $s = 0.617mm$. The maximum displacement from the optimum z position allowed by this geometry will be $r/2 = 1.28mm$.

4.2 Spatial and temporal coherence requirements

If a perfectly collimated beam of light is used for the illumination, the required degree of spatial coherence is very small, because with proper alignment each fraction of the wavefront is made to interfere with itself. In practice, due to an imperfect collimated beam or the imperfect alignment of the instrument, a certain degree of spatial coherence is still required.

This interferometer is significantly less dependent on the spatial coherence of the source than a wavefront-division interferometer. The grating interferometer used in this work is based on the idea proposed by Weinberg and Wood [4.2]. Interferometric lithography was demonstrated with similar arrangements using low coherence sources by Yen et al. [4.3].

If a wave is superposed with a delayed copy of itself (as it is often done using any amplitude division interferometers) the delay over which they produce stable interference is known as the coherence time, Δt_c . If the delay between two copies of the same wavefront increases, then the interference pattern fringe visibility at the observation plane decreases. This time corresponds to the spatial dimension called coherence length which can be calculated: $l_c = c \cdot \Delta t_c$, where c is the speed of light.

The temporal coherence still plays a role in the modulation contrast, because in the ADI one wave is superposed with a delayed copy of itself generated by the transmission diffraction grating. If the delay between two interfering waves is more than

the coherence time τ_c , the stable interference will not occur and good modulation depth in the photoresist will not be possible. Thus the delay between two interfering beams (two arms of the interferometer) has to be minimized. The coherence length is related to the bandwidth of the source as $l_c = \lambda^2 / \Delta\lambda$. The interference will occur at the sample plane only if the optical path difference between two interferometer branches (arms) satisfies the equation below:

$$0 \leq OPD \leq l_c \quad (4.6)$$

To study the role of the temporal coherence on the modulation contrast let us consider the ADI interferometer perfectly aligned (symmetric), in which the $OPD = 0$ for two rays originating from the center of the transmission diffraction grating and overlapped at the sample plane. This is shown in Figure 4.3 in green rays.

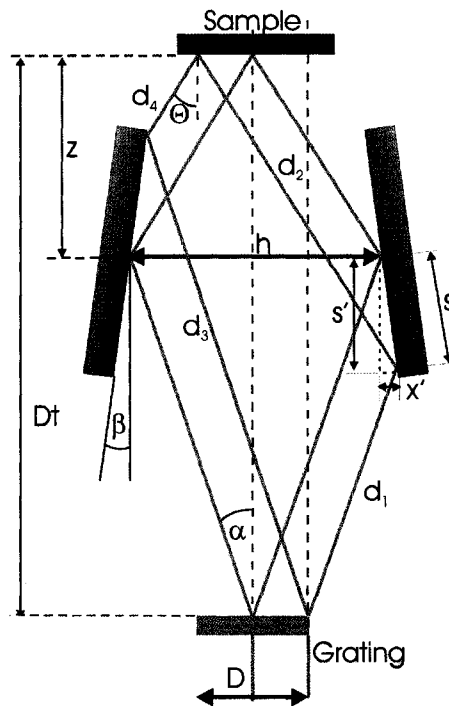


Figure 4.3. Scheme for OPD calculations in amplitude division interferometer.

Assuming uniform illumination of the grating, if the grating is displaced perpendicular to the interferometer axis (orange rays) the $OPD \neq 0$ and the modulation depth in the sample will be reduced.

Let us calculate the OPD for the displaced grating. s is the half of the beam size on the mirror and is equal to:

$$s = \frac{D}{\sin(\gamma)} = \frac{D}{\sin\left(\frac{\Theta + \alpha}{2}\right)} \quad (4.7)$$

It is also easy to notice that s' and x' are both dependent on the angle β :

$$\begin{aligned} x' &= s \cdot \sin(\beta) \\ s' &= s \cdot \cos(\beta) \end{aligned} \quad (4.8)$$

The paths of two beams originating from the grating and overlapped in the sample can be calculated using the equations below:

$$\frac{Dt - z - s'}{d_1} = \cos(\alpha) \Rightarrow d_1 = \frac{Dt - z - s'}{\cos(\alpha)} \quad (4.9)$$

$$\frac{z + s'}{d_2} = \cos(\Theta) \Rightarrow d_2 = \frac{z + s'}{\cos(\Theta)} \quad (4.10)$$

$$\frac{Dt - z + s'}{d_3} = \cos(\alpha) \Rightarrow d_3 = \frac{Dt - z + s'}{\cos(\alpha)} \quad (4.11)$$

$$\frac{z - s'}{d_4} = \cos(\Theta) \Rightarrow d_4 = \frac{z - s'}{\cos(\Theta)} \quad (4.12)$$

Since the interferometer is housed in the vacuum the index of refraction is equal to unity.

The path lengths in both arms are equal to:

$$d_1 + d_2 = \frac{Dt - z - s'}{\cos(\alpha)} + \frac{z + s'}{\cos(\Theta)} \quad (4.13)$$

$$d_3 + d_4 = \frac{Dt - z + s'}{\cos(\alpha)} + \frac{z - s'}{\cos(\Theta)} \quad (4.14)$$

The OPD has to satisfy the criterion $0 \leq (d_1 + d_2) - (d_3 + d_4) \leq l_c$ to be able to interfere in the photoresist:

$$0 \leq \frac{Dt - z - s'}{\cos(\alpha)} + \frac{z + s'}{\cos(\Theta)} - \frac{Dt - z + s'}{\cos(\alpha)} - \frac{z - s'}{\cos(\Theta)} \leq l_c \quad (4.15)$$

that can be expressed as:

$$0 \leq 2s' \left(\frac{1}{\cos(\Theta)} - \frac{1}{\cos(\alpha)} \right) \leq l_c \quad (4.16)$$

It is convenient to express the equation 4.16 in terms of the width of the transmission diffraction grating D used in the experiment. Substituting for s in the expression for s' one can obtain:

$$s' = \frac{D \cos(\beta)}{2 \sin\left(\frac{\Theta + \alpha}{2}\right)} = \frac{D \cos(\gamma - \alpha)}{2 \sin\left(\frac{\Theta + \alpha}{2}\right)} = \frac{D \cos\left(\frac{\Theta - \alpha}{2}\right)}{2 \sin\left(\frac{\Theta + \alpha}{2}\right)} \quad (4.17)$$

that will change the condition for the OPD to be expressed in terms of the grating width D instead of the intermediate variable s' :

$$0 \leq \frac{D \cos\left(\frac{\Theta - \alpha}{2}\right)}{\sin\left(\frac{\Theta + \alpha}{2}\right)} \left(\frac{1}{\cos(\Theta)} - \frac{1}{\cos(\alpha)} \right) \leq l_c \quad (4.18)$$

This equation can be simplified to:

$$0 \leq \frac{D \sin(\Theta - \alpha)}{\cos(\alpha) - \cos(\Theta)} \left(\frac{\cos(\alpha) - \cos(\Theta)}{\cos(\Theta) \cos(\alpha)} \right) \leq l_c \quad (4.19)$$

$$0 \leq \frac{D \sin(\Theta - \alpha)}{\cos(\Theta) \cos(\alpha)} \leq l_c \quad (4.20)$$

applying trigonometric identities a further simplification is possible:

$$0 \leq \frac{D[\sin(\Theta)\cos(\alpha) - \cos(\Theta)\sin(\alpha)]}{\cos(\Theta)\cos(\alpha)} \leq l_c \quad (4.21)$$

that finally can be reduced to:

$$0 \leq D[\tan(\Theta) - \tan(\alpha)] \leq l_c \quad (4.22)$$

It is also possible to express this condition in terms of the grating parameters: width and period - D, d respectively and the desired period of the patterned structure p .

Substituting $\Theta = \arcsin\left(\frac{\lambda}{2p}\right)$ and $\alpha = \arcsin\left(\frac{\lambda}{d}\right)$ for $0 \leq \Theta \leq \pi/2, 0 \leq \alpha \leq \pi/2$, equation

4.22 can take a form:

$$0 \leq D\lambda \left(\frac{1}{\sqrt{4p^2 - \lambda^2}} - \frac{1}{\sqrt{d^2 - \lambda^2}} \right) \leq l_c \quad (4.23)$$

A special case in this equation is when both mirrors are parallel to each other, then $\beta = 0$ and $\alpha = \Theta$. In this case the optical paths in both arms are always equal and $OPD = 0$. The temporal coherence will not affect the modulation of the intensity at the sample plane. But for this case the $p = d/2$, the period of the patterned structures is fixed to be always a half of the grating period. If $\Theta \neq \alpha$, the intensity modulation has period $p \ll d$ and use this intensity modulation to pattern the photoresist. Here we can consider two cases. First we can assume that the grating period is constant, thus $\alpha = const$. Then the maximum grating width will be a function of Θ angle and is limited by the upper limit $OPD = l_c$:

$$D_{\max}(\Theta) = \frac{l_c}{\tan(\Theta) - \tan(\alpha)} \quad (4.24)$$

In terms of patterned period p and fixed value of the grating period d :

$$D_{\max}(p) = \frac{l_c}{\lambda \left(\frac{1}{\sqrt{4p^2 - \lambda^2}} - \frac{1}{\sqrt{d^2 - \lambda^2}} \right)} \quad (4.25)$$

The second case assumes that the grating width is fixed ($D = \text{const.}$). Then the maximum Θ angle for the beams reflected from the mirrors is limited again by the condition $OPD = l_c$ to be equal to:

$$\Theta_{\max}(\alpha) = \alpha + \arctan\left(\frac{l_c}{D}\right) \quad (4.26)$$

The minimum value of the patterned period p_{\min} as a function of the grating period d is limited by the temporal coherence to be equal to:

$$p_{\min}(d) = \frac{\lambda d}{2 \left(\lambda + d \sin\left(\arctan\left(\frac{l_c}{D}\right)\right) \right)} \quad (4.27)$$

As an example, for the grating with $D = 0.6\text{mm}$, $l_c = 470\mu\text{m}$, and $d = 2\mu\text{m}$ gives $p_{\min} = 36.9\text{nm}$ that is the period limited by the temporal coherence. In fact the limitation is more severe since in these calculation we assumed that $OPD = l_c$. In practice to have a good quality interference pattern and good contrast in the photoresist the limitation should be $OPD < l_c$. OPD might be rewritten in slightly different way:

$$OPD = \eta \cdot l_c \quad (4.28)$$

where in principle $\eta \in \langle 0, 1 \rangle$, however from the practical point of view measurements presented later will show that in fact $\eta \in \langle 0, 0.3 \rangle$ to obtain a visible pattern in the photoresist surface.

4.3 Transmission diffraction grating fabrication

The transmission grating used to split the beam has 2 microns period with 50% duty cycle. It was fabricated in a $2 \times 0.6\text{mm}^2$ Si membrane approximately 100nm thick. Figure 4.4 shows schematically the sequence of steps in the grating fabrication process. A thin layer of Si was sputtered on top of a 100nm thick Si_3N_4 membrane fabricated in a $550\mu\text{m}$ thick Si wafer. Subsequently, a 350nm thick photoresist layer was deposited by spin coating on top of the sputtered Si.

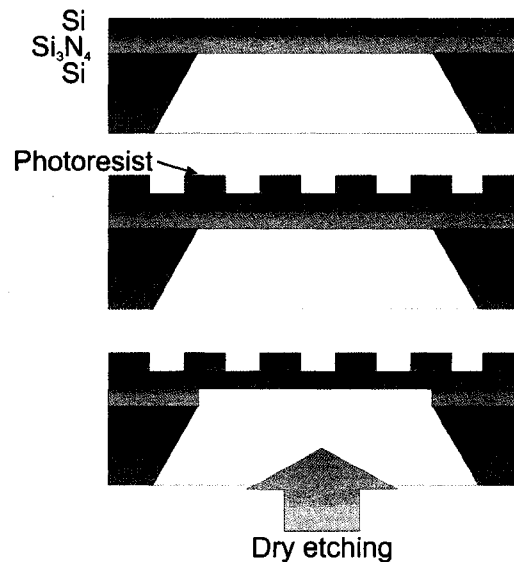


Figure 4.4. Sequence of steps for the fabrication of the transmission diffraction grating using electron beam lithography in a photoresist layer deposited on top of a 100nm Si membrane.

The grating was patterned in the photoresist by electron beam lithography. Finally, the Si_3N_4 layer was removed by chemically assisted ion beam etching (CAIBE) leaving a self standing 100nm thick Si membrane with the grating defined in the photoresist. The Si_3N_4 membrane was etched in 12 cycles each with duration of 15 seconds. The CAIBE parameters used in this step were: discharge current 280mA, beam

current 19mA, beam voltage 250V, acceleration voltage 500V, argon gas flow 2.5scm and chlorine gas flow 4scm. The etching rate was estimated before to be $\sim 7.4\text{\AA}/\text{s}$. The thin Si membrane provides theoretically $\sim 20\%$ transparency to the $\lambda = 46.9\text{nm}$ photons, while the photoresist that remains in the membrane act as perfectly absorbent regions, constituting an amplitude transmission diffraction grating.

The total transmission defined as a ratio between the intensity transmitted by the grating in the zero and all diffracted orders and the incident beam was measured in a subsequent test to be less than 10% at 46.9nm wavelength. The measured grating was illuminated by the laser beam and the laser light was diffracted by the grating on the detector placed $\sim 25\text{mm}$ behind the grating. Due to limited size of the detector ($\sim 6\text{mm}$ diameter) up to ± 5 diffracted orders were captured and considered in the grating transmission measurements. The error introduced by neglecting higher orders is not substantial due to the fact that only 0.83% intensity of the zero order is in the each $\pm 7^{\text{th}}$ diffraction order as shows in Appendix IV.

Figure 4.5 shows an atomic force microscope scan of the completed grating (Novascan 3D AFM in “tapping” mode), revealing a highly regular profile.

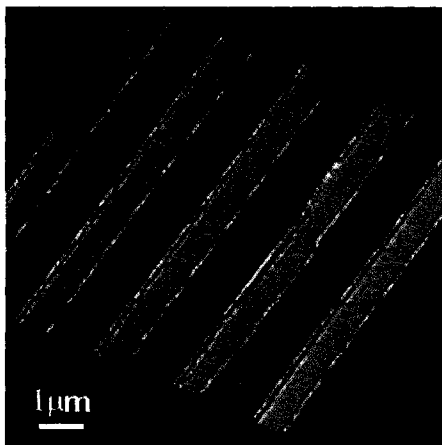


Figure 4.5. AFM image of the transmission diffraction grating.

The resulting open areas were measured to be 980nm wide, and to have the period 2.02 μ m. The simulations of the diffraction efficiency of the ideal 50% duty cycle grating and fabricated 48.5% duty cycle grating are presented in Appendix IV.

4.4 Desk Top Capillary Discharge Laser in nanopatterning

The ADI lithography tool was used in combination with an extremely compact, “desk-top” $\lambda=46.9$ nm Ne-like Ar capillary discharge laser configured to emit pulses with energy of approximately 10 μ J and about 1ns FWHM duration. The EUV laser can operate at repetition rates up to 12Hz producing pulses, corresponding to average powers up to 0.12mW. Due to its short capillary plasma column length - 21cm, its spatial coherence length is a fraction of a millimeter at the sample location. The laser temporal coherence length is approximately 470 μ m determined by its line width $\Delta\lambda/\lambda < 1 \times 10^{-4}$. The laser is extremely compact, it occupies a footprint of 0.8 \times 0.4m² including its turbomolecular pump, and has a small power supply that can fit under the optical table [4.4]. Figure 4.6a shows the “desk-top” capillary discharge laser connected through the vacuum manifold to the experimental chamber that houses the ADI interferometer. The side view of the laser is shown in Figure 4.6b. Although the energy per pulse (max ~13 μ J) is more than one order of magnitude smaller than the table top version of capillary discharge laser the source doesn’t require as high voltage as the previous version. In this unit the Marx generator generating 200kV for excitation was replaced by a much more compact pulser generating 90kV.

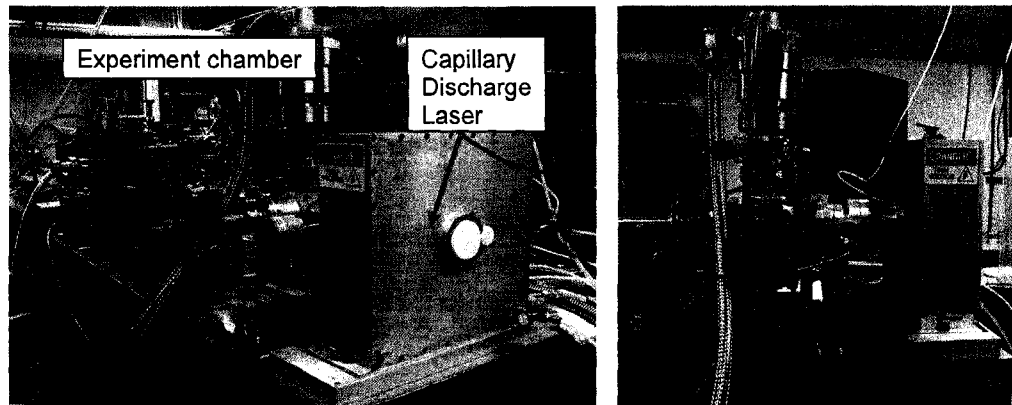


Figure 4.6. a) photograph of the “desk-top” capillary discharge laser (right) connected using vacuum manifold to the experimental chamber (left) housing the ADI interferometer. b) desk-top version of the capillary discharge laser. Much more compact source with energy per pulse up to $13\mu\text{J}$ and repetition rate up to 12Hz.

As a result the size of the source and mechanical stress on the capillary was drastically reduced with an improvement of the capillary lifetime up to 20-30 thousands laser pulses per capillary. The maximum peak excitation current is $\sim 22\text{kA}$.

4.5 Experimental details

Figure 4.7 is a photograph of the ADI interferometer showing all the major components. The folding mirrors were implemented using two Si wafers placed at an incidence angle between 5 and 8 degrees. Both mirrors are coupled with gears and driven by a single rack with a vacuum actuator to change the incidence angle in both mirrors simultaneously. This mechanism can be seen in detail in Figure 4.7b. The footprint of the interferometer is small, approximately $0.2 \times 0.4\text{m}^2$ and its overall light throughput is at maximum $\sim 1.94\%$.

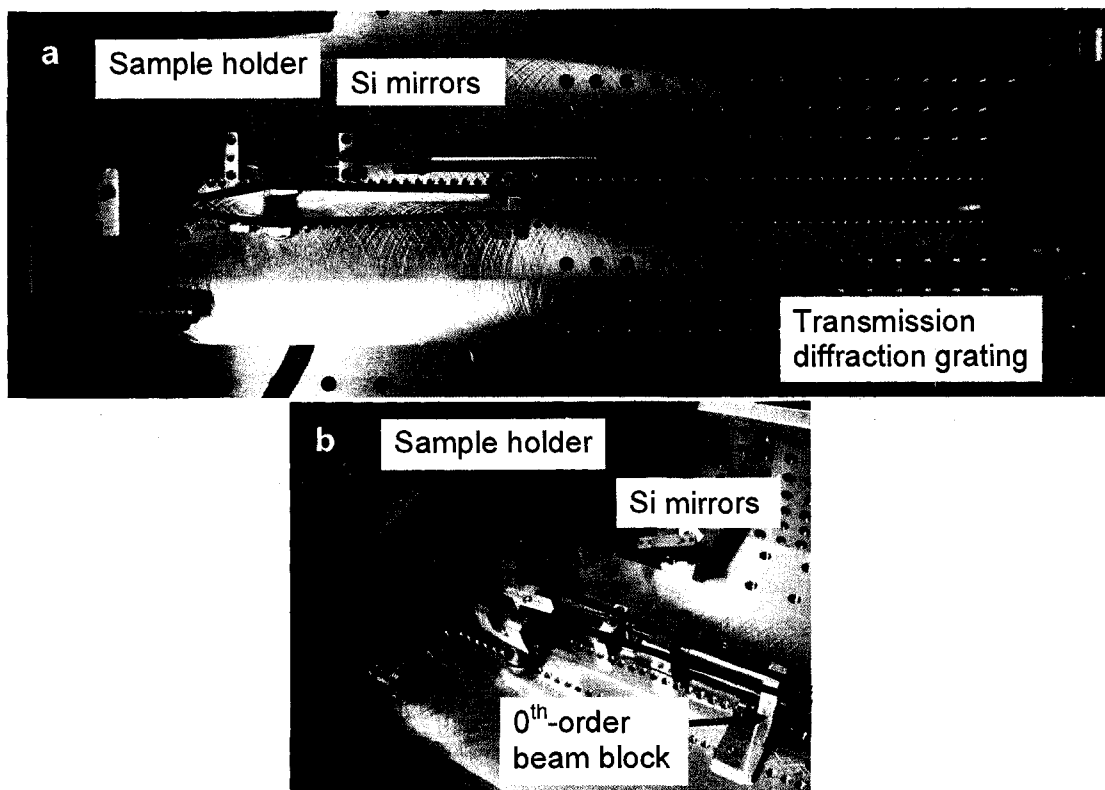


Figure 4.7. Photograph of the set up a). Purple lines illustrate the optical path of the two beams ($\pm 1^{\text{st}}$ diffraction orders from the beamsplitter – transmission diffraction grating). Laser beam – green line, 0^{th} diffraction order is blocked by beam block (light blue line). More detailed image of the interferometer showing mirror – sample assembly b).

The interference gives rise to a sinusoidal pattern with period p , defined by the wavelength of the light λ and the incidence angle Θ . The optical path difference between the two branches of the interferometer can be easily adjusted within a distance smaller than the longitudinal coherence of the laser source that for this capillary discharge laser is approximately $470\mu\text{m}$. The required accuracy in the overlapping of the two beams at the sample's surface is defined by the spatial coherence of the beams, which for the $\lambda=46.9\text{ nm}$ laser used in this experiment is a fraction of a millimeter at the location of the sample, which is also easily achievable. The alignment was performed using a He-Ne laser aligned to be coaxial with the path of the 46.9nm laser. A small slit

was positioned near the grating and the 0th diffraction order from the He-Ne laser was further diffracted on the variable width slit. The slit width was adjusted so the secondary diffraction lobes of the He-Ne laser propagated near by the beam block, thus reproducing the path of the EUV photons. The He-Ne light from the adjustable slit shined through a hole in the beam block. This setup produces three spots (the primary lobe of the diffracted He-Ne light on the slit through the hole in the beam block and two secondary lobes reflected from the mirrors) that are overlapped at the sample plane. During the patterning the aligning hole in the beam block was closed. The system is very robust, requiring only minor adjustments after its initial alignment.

4.6 Results

Figure 4.8a shows an AFM scan with a grating with period of 145nm (72.5nm thick lines). The pattern was recorded on ~80nm thick hydrogen silsesquioxane (HSQ, 6% solution, XR-1541 from Dow Corning) photoresist deposited on a Si wafer in standard spin coater. Samples were prebaked 1 minute at 115 °C using standard hot plate. After exposure the sample was postbaked for 1 minute at 115 °C. After cooling the samples were developed in 2.38% solution of TMAH (tetramethylammonium hydroxide) for 3 seconds, rinsed with DI water and dried with compressed nitrogen.

The printed area corresponds to the size of the grating, in this experiment $2 \times 0.6 \text{mm}^2$. The penetration length of the 46.9nm light in the photoresist is approximately 120nm. The images shown in Figure 4.8 are atomic force microscope (AFM) scans of a small section of the sample obtained with the AFM (Novascan 3D) working in “tapping”

mode. To print gratings with smaller period, the angle between the interference beams impinging in the sample was increased by changing the angle of incidence of the two Si mirrors and correcting the position of the sample. A grating with a period of $\sim 95\text{nm}$ period (47.5nm wide lines) was printed over same area, $2\times 0.6\text{mm}^2$. An AFM scan of this grating is shown in Figure 4.8b.

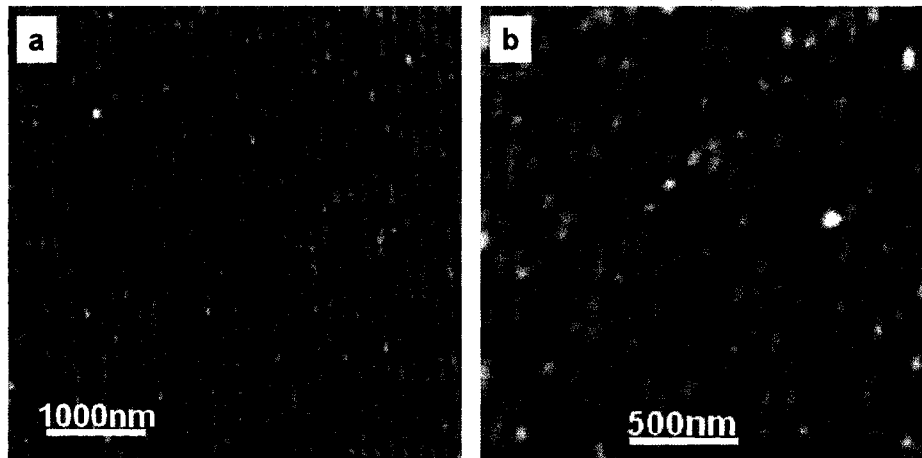


Figure 4.8. a) AFM image of a 145nm period grating printed by interferometric lithography using an EUV laser. b) AFM image of a 95nm period grating. Both images were obtained with the AFM working in “tapping” mode over a small section of the printed grating.

Since the laser was operated at a repetition rate of only 3Hz, exposures of more than 10 minutes were required (at least 2000 laser shots) [4.5]. The exposures can be reduced by more than one order of magnitude by combining this amplitude division interferometer with the table-top version of the capillary discharge laser, that is capable of producing mW average power [4.6, 4.7].

Larger areas are also possible by either utilizing a transmission grating beam splitter of larger dimensions, or by precise translating the sample and realizing multiple exposures. Free-standing grating instead of the grating suspended on the 100nm thick

silicon membrane might greatly improve the throughput of the device and decrease the exposure time significantly. Because of the limited size of the grating (grating smaller than the beam) a parasitic diffraction effects on the edges of the grating appeared in the patterned photoresist. The 95nm period lines show decreased pattern quality as compared with the larger pitch sample. One possible explanation for this lower quality printing is the influence of vibrations during the exposure, which are more severe for smaller pitch lines. In addition the print quality may be possibly affected by photo-resist scumming, that is particularly severe in 50% duty cycle lines with linewidths approaching 50nm in HSQ photoresist [4.8] or by the presence of scattering centers in the grating and mirrors that introduce a random noise background reducing the fringe visibility.

4.7 Influence of the OPD on the pattern quality

An additional experiment was performed to show the influence of the transmission diffraction grating position on the quality of the pattern in the photoresist surface. Displacing the grating perpendicularly to the interferometer's axis changes the optical paths in the two interferometer arms as described in section 4.2 . To move the grating, an additional translation stage was incorporated in the setup driven with micrometer screw. This can be seen in the Figure 4.9. The interferometer was adjusted to produce periodic 1-D patterns (lines) with $p = 125nm$ that corresponds to $\Theta = 10.81^\circ$ and $\alpha = 1.34^\circ$.

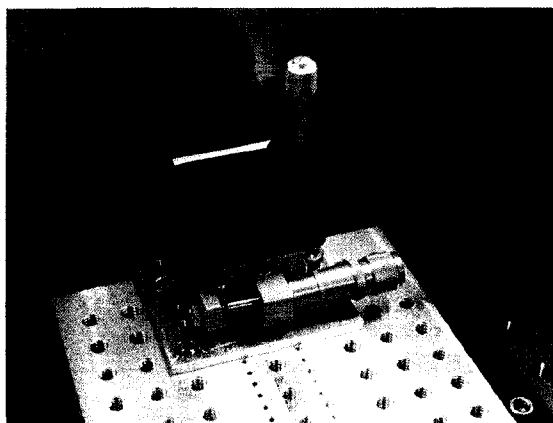


Figure 4.9. Translation stage was incorporated in the previous ADI setup to allow the grating displacement in the direction perpendicular to the interferometer's axis.

The grating used in this experiment was described in section 4.3 and Appendix IV. A lateral displacement of the grating by Δx distance will result optical path difference equal to $OPD = \Delta x [\tan(\Theta) - \tan(\alpha)]$ as discussed in section 4.2. After the interferometer was initially aligned with a He-Ne laser the grating position was assumed to be $\Delta x = 0$. Then a few samples were exposed displacing the grating. HSQ samples were used and processed as explained in section 4.6. Each sample was exposed with 600 laser pulses (10 minute exposure) from the table top version of the capillary discharge laser operated at 1Hz repetition rate and configured to emit $\sim 100\mu J$ per pulse. All the samples were scanned with an AFM with the same scanning parameters, the same tip and the same scan size $1.5 \times 1.5\mu m^2$ for good comparison. The results of this experiment are shown in Figure 4.10. The best result by inspection was obtained for $\Delta x = 200\mu m$ away from the initial alignment ($\sim 33.5\mu m$ change in OPD).

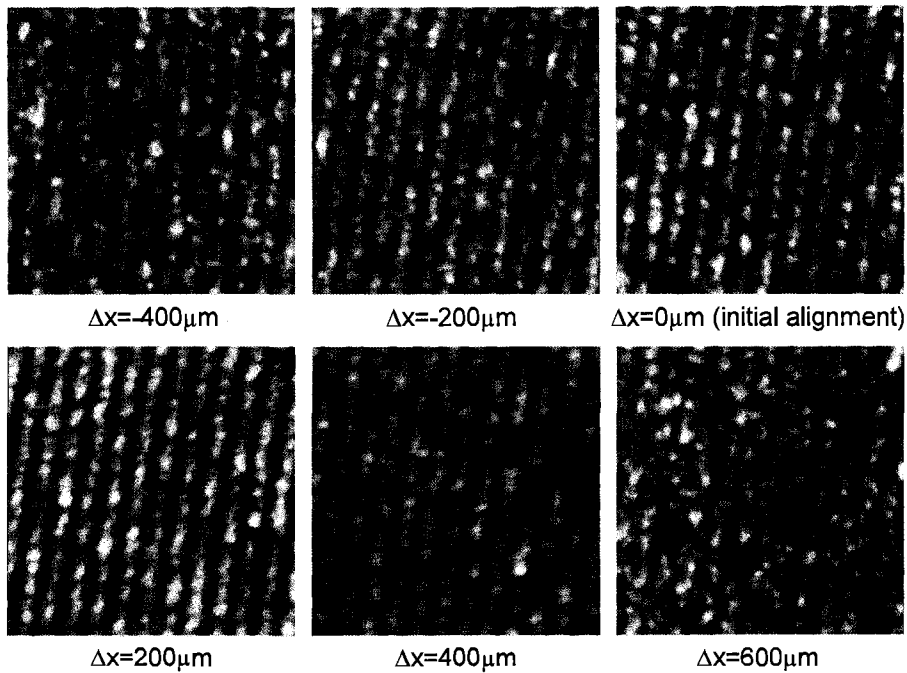


Figure 4.10. AFM scans of the patterned photoresist surface $1.5 \times 1.5 \mu\text{m}^2$ size for various displacements of the transmission diffraction grating. Lines are 125nm period. All samples were processed in the same way to provide good comparison.

Rotating the images to have perfectly vertical lines and by binning the image in the vertical direction a set of 1-D modulation plots were obtained. From these plots the visibility for each pattern was obtained and plotted as a function of the optical path difference in both interferometer arms. The visibility plot is depicted in Figure 4.11. The plot shows the visibility change of the pattern for different OPD in the interferometer. The plot also indicates that in practice the condition that the optical path difference should be equal to the longitudinal coherence length $OPD = l_c$ is an overestimation for good quality pattern. From the visibility plot, the maximum $\sim 83\%$ was obtained when the optical path difference was equal to zero. The best visual appearance for $OPD = 33.5 \mu\text{m}$ gives slightly smaller visibility $\sim 80\%$.

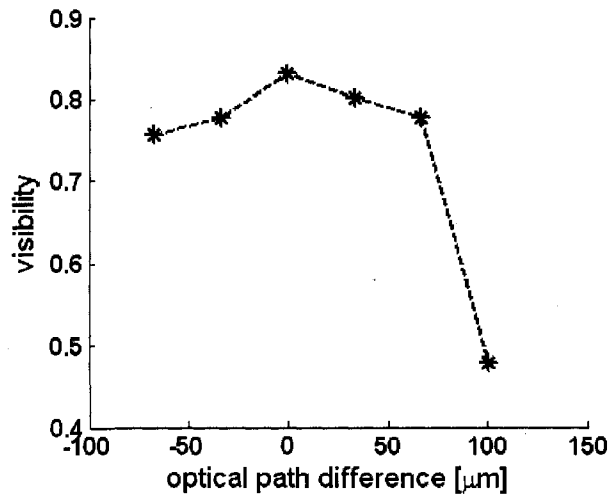


Figure 4.11. The visibility of the patterns obtained by rotating the image to have vertical lines and by binning the image vertically as a function of the optical path difference between both interferometer arms.

From this data one can conclude, that a total displacement of $\Delta x = 1\text{mm}$ corresponding to the optical path difference $OPD \sim 166\mu\text{m}$ changed the quality of the pattern dramatically from best quality possible from that set of data to very poor quality pattern. This experiment allows to evaluate the factor η described in section 4.2 as $\eta \in \langle 0, 0.3 \rangle$ for the patterning purpose.

4.8 Summary

A compact EUV interferometric lithography tool that combines an amplitude division interferometer with desk-top size EUV laser was demonstrated. In this experiment we printed gratings over areas of $\sim 1\text{mm}^2$, with periods down to 95nm. As the average power of shorter wavelength (for example 13.9nm) high repetition rate table-top

EUV lasers increases, their combination with this interferometer will allow the printing of arrays with feature size only limited by the photoresist resolution in a very compact table-top system [4.9].

-
- [4.1] Y. Liu, Y. Wang, M.A. Larotonda, B.M. Luther, J.J. Rocca, and D.T. Attwood, "Spatial coherence measurements of a 13.2 nm transient nickel-like cadmium soft X-ray laser pumped at grazing incidence", *Optics Express*, **14**, 12872 (2006)
- [4.2] F.J. Weinberg, N.B. Wood, "Interferometer based on four diffraction gratings", *Journal of Scientific Instruments* **36**, 227 (1959)
- [4.3] A. Yen, E.H. Anderson, R.A. Ghanbari, M.L. Schattenburg, and H.I. Smith, "Achromatic holographic configuration for 100-nm-period lithography", *Applied Optics* **31**, 4540 (1992)
- [4.4] S. Heinbuch, M. Grisham, D. Martz, J.J. Rocca, "Demonstration of a desk-top size high repetition rate soft x-ray laser", *Optics Express* **13**, 4050 (2005)
- [4.5] P. Wachulak, M. Grisham, S. Heinbuch, D. Martz, W. Rockward, D. Hill, J.J. Rocca, C.S. Menoni, E. Anderson, M. Marconi, "Interferometric lithography with an amplitude division interferometer and a desk-top extreme ultraviolet laser", *Journal of the Optical Society of America B* **25**, 7, B104-B107 (2008)
- [4.6] Benware, B.R., C.D. Macchietto, C.H. Moreno, and J.J. Rocca, "Demonstration of a high average power tabletop soft X-ray laser", *Physical Review Letters* **81**, 5804 (1998)
- [4.7] Macchietto, C.D., B.R. Benware, and J.J. Rocca, "Generation of millijoule-level soft-x-ray laser pulses at a 4-Hz repetition rate in a highly saturated tabletop capillary discharge amplifier", *Optics Letters* **24**, 1115 (1999)
- [4.8] D.P. Mancini, K.A. Gehoski, E. Ainley, K.J. Nordquist, D.J. Resnick, T.C. Bailey, S.V. Sreenivasan, J.G. Ekerdt, C.G. Willson, "Hydrogen silsesquioxane for direct electron-beam patterning of step and flash imprint lithography templates", *J. Vac. Sci. Technol. B* **20**, 2896-2901 (2002)
- [4.9] Y. Wang, M.A. Larotonda, B.M. Luther, D. Alessi, M. Berrill, V.N. Shlyaptsev, J.J. Rocca, "Demonstration of high-repetition-rate tabletop soft-x-ray lasers with saturated output at wavelengths down to 13.9 nm and gain down to 10.9 nm", *Physical Review A* **72**, 5 (2005)

CHAPTER 5

5 Extreme Ultraviolet Holography

5.1 Introduction

The word “hologram” (from the greek “*holos*”: whole, complete and “*graphos*”: writing, drawing) means “total recording”. Holography is a technique that allows to store both the amplitude and the phase of a given wavefront [5.1]. Gabor in 1948 proposed this two-steps technique of lensless imaging. He realized that the interference of two mutually coherent waves, one called the reference wave and the second one – the object wave, allows for the recording the information of both the amplitude and phase of the diffracted or scattered beam from an object. This coding of the amplitude and phase of the object beam into an interference pattern allowed him to demonstrate that from this complicated holographic pattern, ultimately the image of the original object can be obtained. Gabor was originally motivated by the potential applications of this technique to electron microscopy, however from practical reasons he was unable to realize his goal. Later improvements led to many other applications Gabor couldn’t even initially imagine.

In the 1960’s the invention of the laser greatly improved the holographic technique due to the advantages of using a highly coherent light source such as a laser. E. N. Leith and J. Upatnieks [5.2] improved Gabor’s original technique suggesting off-line holography that overcomes the twin image problem (mentioned later in section 5.3)

present in the Gabor's original scheme [5.3]. Holography coupled with highly coherent laser sources allowed for lensless three-dimensional imaging [5.4].

As in other imaging techniques, in holography the resolution of the recorded holograms improves with the use of shorter wavelengths. This idea was recognized early by Baez [5.5] in 1952, shortly after the introduction of in-line holography.

Different types of short wavelength sources were utilized in high resolution holography. Using an early X-ray laser pumped by two beams of the fusion-class NOVA laser at Lawrence Livermore National Laboratory Gabor holography was demonstrated with a spatial resolution of $5\mu\text{m}$ [5.6]. In 1987 the high resolution X-ray imaging was realized by use of 2.5–3.2nm soft x-ray radiation from the National Synchrotron Light Source (NSLS), where a spatial resolution of 40nm was demonstrated. Fourier transform holography at the NSLS achieved a spatial resolution of 60nm. Other experiments utilized synchrotron light to image biological samples, nano structures, and magnetic domains [5.7-5.9].

The practical demonstration of extreme ultraviolet (EUV) or soft X-ray (SXR) holography demonstrated to be difficult in particular due to the lack of sufficiently bright and coherent sources at short wavelengths. The widespread use of this technique has been further restricted because spatially and temporally coherent EUV and soft x-ray laser sources have historically been restricted to large user facilities.

The inconvenience of utilization of the large facilities such as synchrotrons or fusion class lasers was a motivation of using much more compact EUV and soft x-ray sources. The emergence of table-top sources of laser-like coherent EUV radiation [5.10, 5.11] opened the possibility of a wide-spread applicability of table-top coherent EUV

imaging [5.12-5.14]. In this approach, the first demonstration of coherent table-top imaging achieved 7 micron spatial resolution with a spatially-coherent high harmonic generation (HHG) source [5.15]; this resolution has been improved to a resolution of 0.8 μm in later experiments [5.16]. Time resolved holographic imaging was also implemented with HHG sources to study the ultra fast dynamics of surface deformation with a longitudinal resolution (depth) of less than 100nm and a lateral resolution of less than 80 microns [5.17]. Lens-less imaging with HHG sources has been recently demonstrated with 214nm spatial resolution [5.18]. The high temporal coherence of table-top EUV lasers is advantageous for high spatial resolution coherent imaging for example lens-less imaging with 70nm resolution using a highly coherent, table-top 46.9nm EUV laser [5.19].

The following sections of this dissertation will be devoted to the recent results in EUV holography using table-top EUV laser.

5.2 Holographic recording and reconstruction

Holography is a two step process that has a recording phase and a reconstruction phase. The holographic recording in Gabor's in-line configuration is depicted in Figure 5.1a. During the recording step the interference between two mutually coherent beams occurs and is stored in the recording medium. Two interfering beams are the reference beam (depicted in black dashed lines) and the object beam (green solid lines).

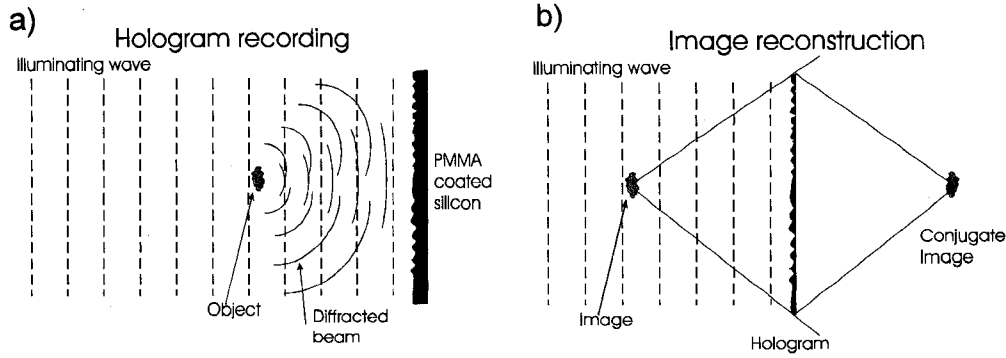


Figure 5.1. Holographic recording scheme a) using Gabor's in-line configuration. The interference pattern between flat wavefront reference beam and beam diffracted from the object – object beam is stored in the recording medium (PMMA photoresist). Optical reconstruction b), where the transmission hologram is illuminated by the reconstruction beam (the same as reference beam) and the image of the object appears where the object was located during the recording phase.

If the object and reference wavefronts are both expressed as a two complex fields having an amplitude and the phase:

$$o(x, y) = |o(x, y)| e^{j\phi(x, y)} \quad (5.1)$$

$$r(x, y) = |r(x, y)| e^{j\psi(x, y)} \quad (5.2)$$

The interference between these two complex fields occurring at the location of the recording medium can be expressed as the intensity of the sum of the two fields:

$$\begin{aligned} I(x, y) &= |r(x, y) + o(x, y)|^2 = \\ &= [r(x, y) + o(x, y)][r(x, y) + o(x, y)]^* = \\ &= |r(x, y)|^2 + |o(x, y)|^2 + r^*(x, y) \cdot o(x, y) + o^*(x, y) \cdot r(x, y) \end{aligned} \quad (5.3)$$

The first two terms are the intensities of both interfering beams, while the last terms depend also on their phases (cross terms). That is why the recording medium sensitive only to the intensity is capable of storing the information of the intensity and the phase.

The recording medium is a material used to record the interference pattern that can provide the linear mapping between the incident intensity during the recording step

and the medium change such as the reflection, transmission or height modulation for example. This linear mapping can be described as the transmission change of the recording medium (for example photographic film) as a function of the incident intensity:

$$t(x, y) = t_0 + \kappa \cdot I(x, y) \quad (5.4)$$

where t_0 is the uniform transmittance of the film introduced by the constant exposure and κ is a linear factor relating the transmission to the incident intensity $I(x, y)$. By substituting equation 5.3 into 5.4 the transmission of the recording medium can be thus expressed as:

$$t(x, y) = t_0 + \kappa \cdot \left[|r(x, y)|^2 + |o(x, y)|^2 + r^*(x, y) \cdot o(x, y) + o^*(x, y) \cdot r(x, y) \right] \quad (5.5)$$

This interference pattern stored in the recording medium during the reconstruction step acts as a complex diffraction grating. If the intensity of the interference pattern during the recording step is linearly translated into a recording medium transmission then the reconstruction step is similar to the one depicted in Figure 5.1b. The hologram is placed in the same geometry and illuminated by the same wavefront as in the recording step, now called reconstruction wavefront. This can be expressed as:

$$u(x, y) = r(x, y) \cdot t(x, y) = r(x, y) \cdot \left(t_0 + \kappa \cdot |r(x, y)|^2 \right) + \kappa \cdot r(x, y) \cdot |o(x, y)|^2 + \kappa \cdot o(x, y) \cdot |r(x, y)|^2 + \kappa \cdot o^*(x, y) \cdot |r(x, y)|^2 \quad (5.6)$$

The reconstructed intensity image is $U(x, y) = u(x, y) \cdot u^*(x, y)$. The first term is a background, the second is very small due to the Gabor holography requirement of the object with high transmission, thus the $|o(x, y)|^2 \rightarrow 0$. The wavefront diffracted from complex transmission diffraction grating (hologram) converges behind the hologram generating the real image (fourth term) while divergent wavefront generates the virtual

image in front of the hologram where the object was placed during the recording step (third term).

5.3 Twin image problem

From equation 5.6 it can be seen that the reconstructed wave will have two images one exact and one conjugate copy of the object wavefront. To visualize this lets consider the situation depicted in Figure 5.2. A Fresnel zone plate (FZP) pattern is illuminated by the flat wavefront. Acting similar to the diffraction grating, diffraction orders are generated (only 0^{th} , $+1^{\text{st}}$ and -1^{st} orders for continuous tone grating).

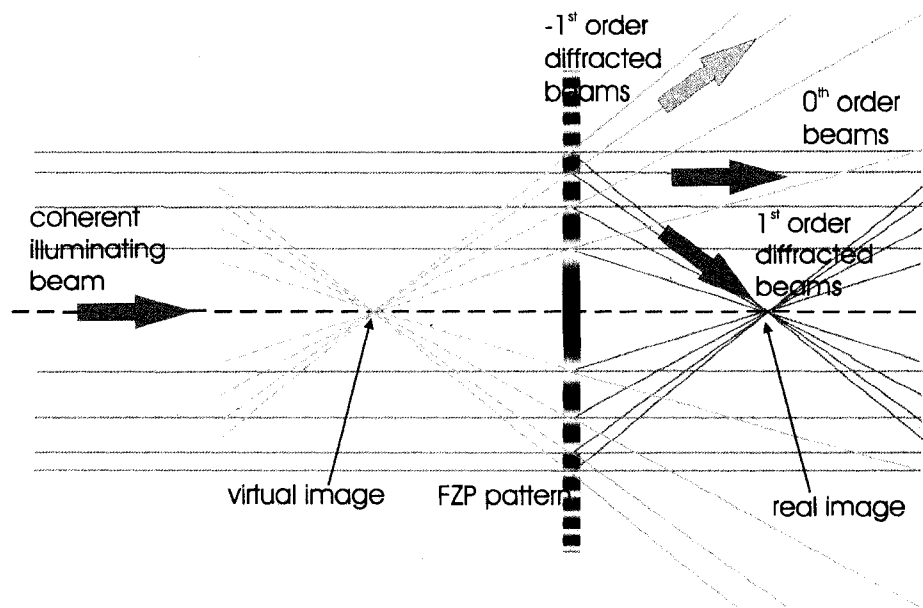


Figure 5.2. FZP pattern is illuminated by the flat wavefront. Generation of real and virtual images.

The FZP hologram illuminated by the reconstructing beam (blue) generates an image of a point in the intersection of 1^{st} diffracted orders, converging beam (green). This

is called “real image” and it is a conjugate copy of the object wavefront. -1^{st} diffracted orders are divergent (yellow) and they produce the image on the other side of the hologram, called “virtual image” that is the exact copy of the object wavefront.

In this simple case a point source will generate the hologram as a FZP pattern during the recording step and during the reconstruction image of this point will be obtained from recorded hologram. This situation can be seen in Figure 5.3. Gabor hologram generates simultaneously real and virtual images of the object (transmission variations of the object in fact). Both images are centered on the hologram axis. These two images are often called twin-images and are separated by the distance $2z_p$.

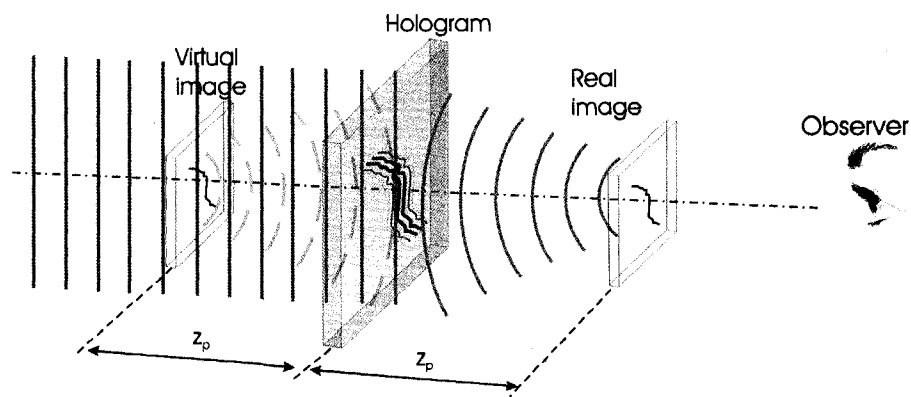


Figure 5.3. Formulation of twin image in Gabor holography.

This is actually one of the limitations in Gabor in-line scheme. The twin-image is perceived by an observer as a noisy background that distorts the reconstructed image. When the real image is brought to focus by precisely adjusting the z_p reconstruction distance, it is always accompanied by second image that is out of focus and vice versa. Thus even if the overall transmission of the object is high, the quality of the reconstructed

image is always affected by the twin-image effect. The way to avoid this problem is to apply the off-axis scheme proposed by Leith and Upatnieks [5.2, 5.4].

5.4 Spatial resolution limitations in high numerical aperture

Gabor holography

The hologram as an interference pattern is stored in the recording medium that changes its parameters linearly according to the intensity of the interference pattern. If a photoresist is used as a recording medium, the information about the object is converted into the height modulation after the developing process. To reconstruct this hologram the digitization process is necessary. Digitization (often done with AFM) converts the photoresist height modulation into a gray-scale image that can be processed numerically in order to obtain the reconstruction of the object.

In any imaging system, the resolution is dictated by the numerical aperture $NA = n \cdot \sin(\Theta)$, where Θ is the maximum half-angle of the cone of light that can enter the imaging system, n is the index of refraction of the medium.

In holography, the spatial resolution depends also on the resolution of the recording medium. The highest spatial frequency that can be recorded sets a limit to the NA of the recording. To minimize this influence the holograms were recorded in a high resolution photoresist. In this experiment PMMA photoresist was used that has a spatial resolution of $\sim 10\text{nm}$ [5.20, 5.21].

The spatial resolution of the hologram is also limited by the spatial and temporal coherence of the illumination source and by the digitization process. The spatial and

temporal coherence of the illumination source are the limitations to the hologram NA when the path difference between the radiation diffracted by the object and the reference beam exceeds either the longitudinal or transverse coherence lengths. The spatial resolution is given by:

$$\Delta = \frac{a \cdot \lambda}{NA} \quad (5.7)$$

where $a \in \langle 0.3, 1 \rangle$ depending on the method used to measure the resolution and coherence of the source, λ is the wavelength of the illumination [5.22].

The limitation to the resolution set by the spatial coherence can be understood by the scheme depicted in Figure 5.4.

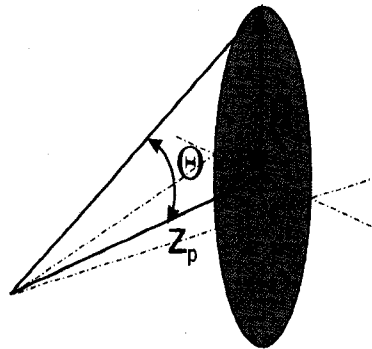


Figure 5.4. Schematic description of the spatial coherence limitation to the hologram resolution.

The interference fringes produced by the reference beam and the beam diffracted from the point object can be stored in the recording medium only within the coherence area depicted as a green oval, with coherence radius R_c . Beyond that region one can assume that the interference will not occur. If the angle between the two beams is Θ , then the numerical aperture is equal to:

$$NA_{sc} = \sin \left[\arctan \left(\frac{R_c}{z_p} \right) \right] \quad (5.8)$$

z_p defines the distance from the object to the recording medium. The resolution is limited to:

$$\Delta_{sc} = \frac{a\lambda}{\sin \left[\arctan \left(\frac{R_c}{z_p} \right) \right]} \quad (5.9)$$

The temporal coherence limits the numerical aperture as well. This can be seen in the scheme in Figure 5.5. The optical path difference δ between the reference and the diffracted beam has to be smaller than the coherence length of the illumination in order to observe the interference.

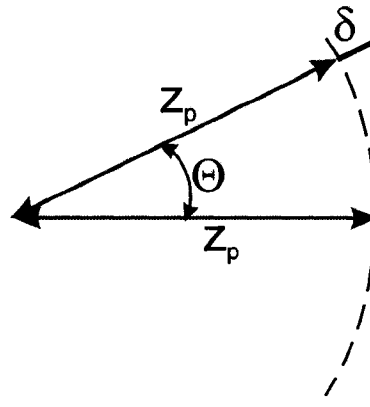


Figure 5.5. Schematic description of the temporal coherence limitation to the hologram resolution.

This limits the region where the interference takes place that can be defined by the angle Θ . The numerical aperture is thus restricted to:

$$NA_{tc} = \sqrt{1 - \left(\frac{z_p}{z_p + l_c} \right)^2} \quad (5.10)$$

and similarly the resolution:

$$\Delta_{lc} = \frac{a\lambda}{\sqrt{1 - \left(\frac{z_p}{z_p + l_c}\right)^2}} \quad (5.11)$$

An important limitation to the resolution is also the process of the digitization of the hologram stored in the recording medium – photoresist surface. The limitation to the numerical aperture during the digitization process is schematically shown in Figure 5.6.

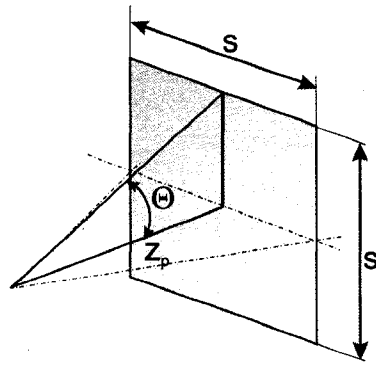


Figure 5.6. Schematic description of the scanning limitation to the hologram resolution

The resolution of the reconstructed image is affected by the scanning size because for an object located at the center of the scanning area, the higher spatial frequencies are located at the edges of the scanned area. This can be related to the numerical aperture of the digitization as:

$$NA_d = \sin \left[\arctan \left(\frac{s}{2z_p} \right) \right] \quad (5.12)$$

and similarly the resolution:

$$\Delta_d = \frac{a\lambda}{\sin \left[\arctan \left(\frac{s}{2z_p} \right) \right]} \quad (5.13)$$

5.5 Reconstruction algorithm for Gabor holography

5.5.1 Fresnel propagator

A spherical wave can be expressed in space and time as:

$$x^2 + y^2 + z^2 - c^2 t^2 = r^2 \quad (5.14)$$

From this $z^2 = r^2 - (x^2 + y^2) + c^2 t^2$. Considering z as the propagation axis:

$$z_{sph} = r \sqrt{1 - \frac{x^2 + y^2}{r^2} + \frac{c^2 t^2}{r^2}} \quad (5.15)$$

In paraxial approximation z_{sph} truncated to the second order in the Taylor series to:

$$z_{sph} = r \left(1 - \frac{x^2 + y^2}{2r^2} + \frac{c^2 t^2}{2r^2} \right) \quad (5.16)$$

Substituting equation 5.16 in the spherical wave equation:

$$A(x, y, z, t) = \frac{A_0 \exp(ikz_{sph})}{z_{sph}} = \exp \left[ikr \left(1 - \frac{x^2 + y^2}{2r^2} + \frac{c^2 t^2}{2r^2} \right) \right] \quad (5.17)$$

where $k = \frac{2\pi}{\lambda}$ is the wave number.

A plane wavefront propagating in z-direction can be expressed as:

$$z_{pl} = r - ct \quad (5.18)$$

$$B(x, y, z, t) = B_0 \exp(ikz_{pl}) = \exp[ik(r - ct)] = \exp[i(kr - \omega t)] \quad (5.19)$$

If we consider both wavefronts at a certain moment of time, the temporal dependence can be neglected leaving $A(x, y, z) \approx e^{ikz_{ph}} = \exp\left[ikr\left(1 - \frac{x^2 + y^2}{2r^2}\right)\right]$ and $B(x, y, z) \approx e^{ikz_{pl}} = \exp(ikr)$.

The hologram is generated by the interference between the object beam and the reference beam. The simplest case of a Gabor's hologram is a hologram of a single point-object. Two mutually coherent wavefronts are made to interfere, one – the object wavefront is a spherical wave that propagates outward from the origin (yellow), as schematically depicted in Figure 5.7 and the plane wavefront (green). Superposing the spherical wavefront with the plane wavefront, the phase difference at the location $z = r$ can be written as:

$$\Delta\varphi = kr - kr\left(1 - \frac{x^2 + y^2}{2r^2}\right) = k\frac{x^2 + y^2}{2r} = k\frac{R^2}{2r} \quad (5.20)$$

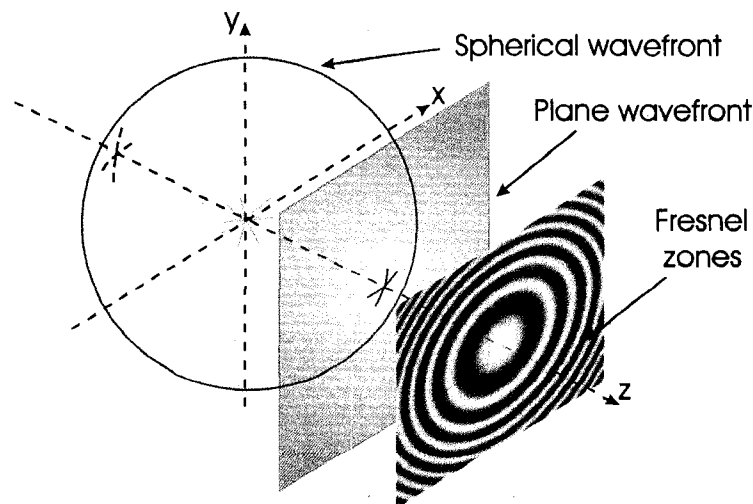


Figure 5.7. The hologram of a point object. The interference between the spherical wavefront and plane wavefront produces the Fresnel zones. The phase between two wavefronts changes producing constructive and destructive interference radially outwards the z-axis.

The interference between the spherical and the plane wave gives rise to a series of concentric rings with maxima and minima of intensity described by radii:

$$R_{\max} = \sqrt{\frac{4n\pi r}{k}} = \sqrt{2nr\lambda} \quad (5.21)$$

$$R_{\min} = \sqrt{\frac{2(2n+1)\pi r}{k}} = \sqrt{(2n+1)r\lambda} \quad (5.22)$$

This pattern of concentric of constructive and destructive interference circles of different radii is depicted in Figure 5.8a. It shows the Fresnel zones (FZ) that correspond to the Gabor hologram of a point source.

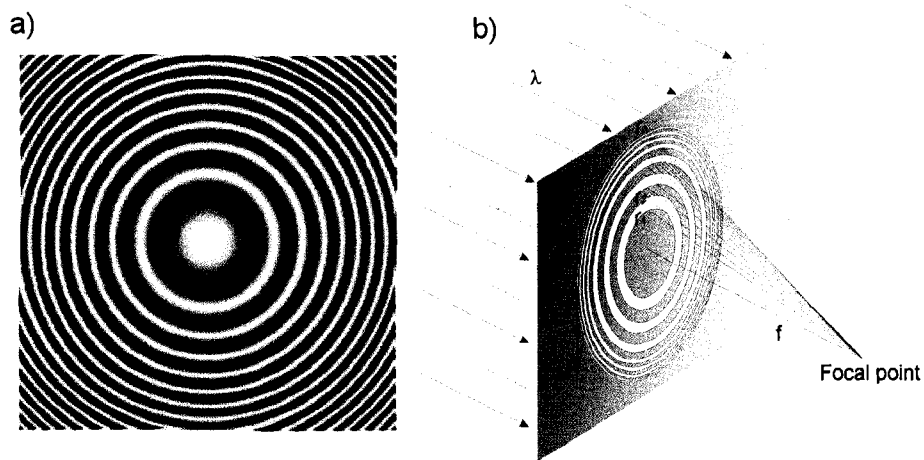


Figure 5.8. Fresnel zones pattern a), and the focusing property of this pattern b).

The generation of the hologram can be mathematically described using Fresnel propagator. The Fresnel propagator is a function that describes the phase difference between flat and spherical wavefronts. The propagator in the spatial domain can be expressed in the form of complex function:

$$F \sim \exp(i\Delta\varphi) \quad (5.23)$$

where $\Delta\varphi$ is the phase difference between the spherical wavefront and the plane wavefront. Substituting equation 5.20 that leads to the Fresnel propagator in spatial domain:

$$F \sim \exp\left(ik \frac{R^2}{2r}\right) = \exp\left(\frac{i\pi R^2}{\lambda r}\right) \quad (5.24)$$

5.5.2 Hologram as a lens

It was noted by G. L. Rogers [5.23] that the zone plate is a particular case of a hologram generated artificially by two on-axis point sources (the analysis above assumes that one of the point sources is located at infinity) and by illuminating this zone plate by a single point source, the image of a second point source will be generated, as depicted in Figure 5.9b. Thus the zone plate has the properties of a lens. Moreover it was also noticed, that any hologram can be considered as a superposition of many zone plates, in the same way as any object can be considered to be composed by many point sources. Thus the hologram can be regarded as a generalized zone plate with a focal length f . As the object is composed from the point sources, the hologram of complex object will be the two-dimensional convolution of the holograms of the point objects or in other way it will be a two-dimensional convolution between the object and the propagator. From the analysis in section 5.5.1 the propagator that relates the object and the hologram can be expressed as a complex function:

$$F \sim \exp(i\Delta\varphi) = \exp\left(ik \frac{x^2 + y^2}{2r}\right) = \exp\left(i\pi \frac{x^2 + y^2}{\lambda r}\right) \quad (5.25)$$

To derive the Fresnel propagator assuming that the hologram is a lens lets consider a situation schematically depicted in Figure 5.9a. A flat wavefront is focused by the lens to a single point at focal distance away, or in the case of hologram the reconstruction wavefront is affected by the hologram and as a result a sharp image of the recorded object is formed. Lens converts a flat wavefront into a converging wave to the focal point and this effect can be described by a Fresnel propagator.

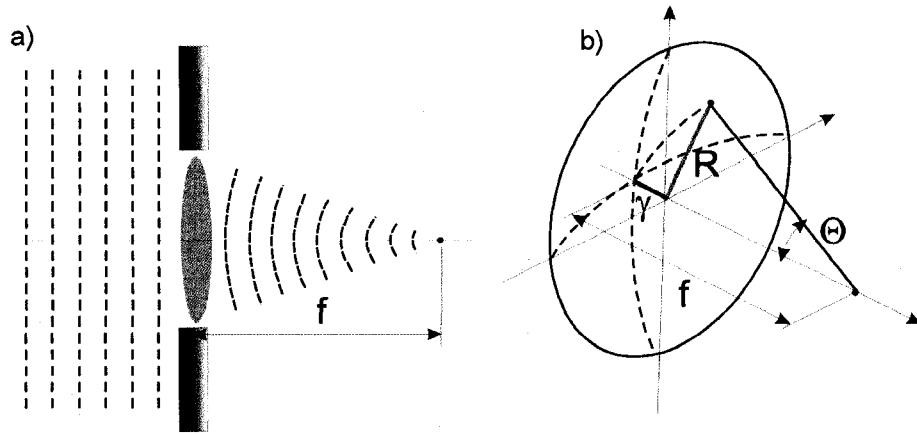


Figure 5.9. Fresnel propagator derivation in spatial domain. Flat wavefront is focused by the lens or other focusing system to a single point at focal distance away from the lens principle plane a). The optical path difference in the spherical wavefront created by focusing lens at the lens plane between the center point and the second point separated from the center of the lens b) is depicted as γ .

The propagator can be expressed in the form of complex function:

$$F \sim \exp(ik\gamma) \quad (5.26)$$

where $k = 2\pi/\lambda$ is a wave vector and γ is the optical path difference between the spherical wavefront created by focusing lens and the plane wavefront. In Figure 5.9b one can easily see that:

$$R^2 + (f - \gamma)^2 = f^2 \quad (5.27)$$

after simplification this will be:

$$\gamma^2 - 2\gamma f + R^2 = 0 \quad (5.28)$$

Square component of the phase difference will be insignificant, $\gamma^2 \rightarrow 0$ and the solution to this equation is:

$$\gamma \sim \frac{R^2}{2f} \quad (5.29)$$

Substituting to the equation 5.26 will lead to the lens propagator in spatial domain:

$$F \sim \exp\left(ik \frac{R^2}{2f}\right) = \exp\left(i \frac{\pi R^2}{\lambda f}\right) \quad (5.30)$$

that is equivalent to equation 5.24. Equivalence of equations 5.24 and 5.30 justifies the fact that the hologram may be considered as a lens.

5.5.3 Sampling considerations and the Fresnel propagator

In any numerical computation we have a discrete representation of the real system and we must consider the effects of the sampling. In any image the sharper the features are in the image the higher spatial frequencies the image will possess. Going further for the simple case of single point generating FZ pattern the higher spatial frequencies we want to consider, the smaller and farther Fresnel zones we include in the reconstruction process the reconstructed point corresponding to the point source will be smaller. Nyquist sampling theorem states that to be able to retrieve the band limited signal from its sampled version, the sampling frequency has to be at least twice the maximum frequency component of the band limited signal. Otherwise in the spatial frequency domain in the sampled signal the copies of the original band limited signal will overlap and the aliasing will occur [5.24]. To avoid an aliasing we have to sample the maximum frequency component in the image with at least two samples correspondingly in the simple case of

FZ hologram we need to sample the outer zone width with at least one pixel. The Fresnel propagator can be defined in the spatial domain, as was described in section 5.5.1, then it is called real space propagator and in the spatial frequency domain, called Fourier space propagator. Let's first consider real space propagator. The phase argument of the real space propagator is given by:

$$\Delta\varphi_r = k \cdot r \sim \pi \left(\frac{x_{\max}^2 + y_{\max}^2}{\lambda \cdot z} \right) \quad (5.31)$$

Thus the number of Fresnel zones (the number of π phase shifts occur in the phase of the propagator) is given by:

$$N_{F_real} = \frac{x_{\max}^2 + y_{\max}^2}{\lambda \cdot z} \quad (5.32)$$

If a point size in the image is equal to $\delta_x = \delta_y = \delta$ and the total number of samples along x and y is equal to N , then number of Fresnel zones in the real space propagator is equal to:

$$N_{F_real} = \frac{2 \left(\frac{N}{2} \delta \cdot \frac{N}{2} \delta \right)}{\lambda \cdot z} = \frac{2 \left(\frac{N}{2} \right)^2 \delta^2}{\lambda \cdot z} = \frac{(N\delta)^2}{2\lambda \cdot z} \quad (5.33)$$

On the other hand let us consider Fourier space propagator now. The phase argument of the Fourier space propagator is given by:

$$\varphi_F = k \cdot r \sim \pi \cdot \lambda \cdot z \left(f_{x_max}^2 + f_{y_max}^2 \right) \quad (5.34)$$

where f_{x_max} and f_{y_max} are maximum spatial frequencies in the frequency domain space.

Again the total number of Fresnel zones is:

$$N_{F_Fourier} = \lambda \cdot z \left(f_{x_max}^2 + f_{y_max}^2 \right) \quad (5.35)$$

Knowing that for a square image from Nyquist sampling criterion one has:

$$f_{x_max} = f_{y_max} = \frac{1}{2\delta} = \frac{1}{2} f_s \quad (5.36)$$

where f_s is the spatial frequency at which the image was sampled the maximum number of Fresnel zones is given by:

$$N_{F_Fourier} = \lambda \cdot z \left(\frac{1}{4\delta^2} + \frac{1}{4\delta^2} \right) = \frac{\lambda \cdot z}{2\delta^2} \quad (5.37)$$

Finally let us consider the sampling itself. If z is the propagation distance between the object and recording medium, there will be a particular distance at which number of Fresnel zones in the real domain is the same as number of Fresnel zones in the Fourier domain:

$$N_{F_real} = N_{F_Fourier} = \frac{(N\delta)^2}{2\lambda \cdot z_{mag}} = \frac{\lambda \cdot z_{mag}}{2\delta^2} \quad (5.38)$$

This distance is called “magic” and is equal to:

$$z_{mag} = \frac{N\delta^2}{\lambda} \quad (5.39)$$

When one chooses the number of pixels in the image to be N^2 with a pixel size δ , then the propagator has to be constructed either in the real spatial domain and transformed to the spatial frequency domain, or directly constructed in spatial frequency domain depending on whether the sampling conditions are better in the spatial domain or spatial frequency domain. If the focal length of the hologram $f > z_{mag}$ the real space propagator contains less Fresnel zones than the Fourier space propagator and for a given N or N^2 points the real space propagator is better sampled than the Fourier space propagator. Thus the propagator is calculated in spatial domain directly:

$$H_{F_real}(x, y) = e^{i \frac{\pi \cdot R(x, y)^2}{\lambda \cdot f}} \quad (5.40)$$

For $f < z_{mag}$ the Fourier space propagator has less Fresnel zones and is better sampled than the other one, and in this case the propagator is calculated directly in the spatial frequency domain:

$$H_{F_Fourier}(f_x, f_y) = e^{-i \pi \lambda f \cdot f_{Rs}(f_x, f_y)^2} \quad (5.41)$$

Because in the spatial domain the process of formation of the interference pattern from a complicated object can be considered as the superposition of FZs, the hologram can be calculated as a convolution. By the convolution theorem if:

$$h(x, y) = o(x, y) \otimes p(x, y) \quad (5.42)$$

where $h(x, y)$ defines the hologram, $o(x, y)$ defines the object and $p(x, y)$ defines the propagator in spatial domain and \otimes denotes the 2-D convolution operation, this hologram may be equivalently described as a multiplication in spatial frequency domain:

$$h(x, y) = \mathfrak{F}^{-1} \{ O(f_x, f_y) \cdot P(f_x, f_y) \} \quad (5.43)$$

In the spatial frequency domain the whole process can be simplified and it takes much less time to compute.

5.5.4 Hologram reconstruction code

The hologram reconstruction code is based on the Fresnel propagator. In our experiment the distance between the object and the recording medium z_p for the Gabor's

in-line scheme is much smaller (μm to mm range) than the distance from the source to the object z_m , in our case $\sim 2\text{m}$.

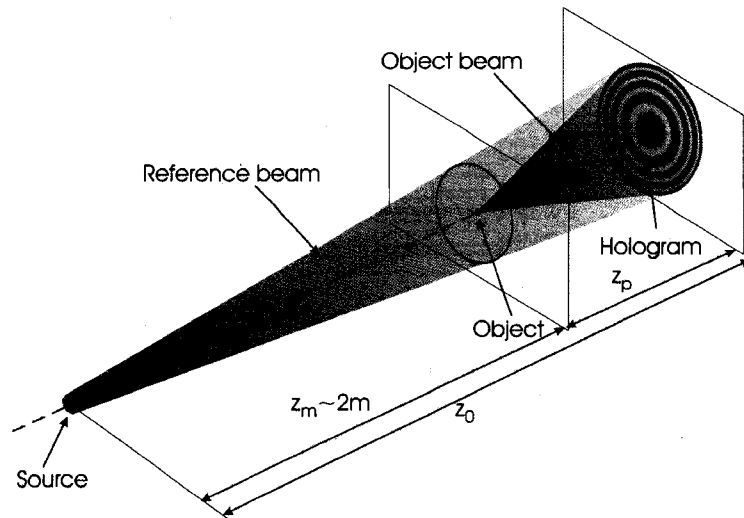


Figure 5.10. Setup for recording Gabor's in-line hologram of a point with distances z_m , z_p and z_0 indicated.

Consequently it can be safely assumed that the laser beam at the object plane has a plane wavefront. In that case the interference occurs between plane wavefront of the reference beam and the wavefront produced by the object.

The digital reconstruction of the hologram is based on a numerical Fresnel propagator [5.25-5.27]. To obtain the amplitude and the phase distribution of the field in the image plane, the simulated field emerging from the hologram illuminated by a plane wave is numerically back propagated with the Fresnel-Kirchhoff convolution integral. The integral was evaluated by the product of the spatial frequency representation of the hologram obtained through a two dimensional fast Fourier transformation and the quadratic phase free space Fresnel propagator in the spatial frequency domain as described in section 5.5.3. The back-propagation distance is determined by calculating

the Fresnel Zone Plate (FZP) focal distance for the specific hologram geometry [5.15]. For the specific geometry employed in this experiment, the FZP focal length is approximately the distance between the object and the recording medium.

The hologram was stored in the surface of the photoresist and chemically developed creating a relief pattern proportional to the intensity distribution during the recording step. The exposure dose was adjusted to work in the linear response region of the photoresist, thus it can be assumed that this is a linear dependence. The photoresist was scanned using an atomic force microscope and gray-level image of the scanned area was obtained. This image corresponds to a matrix with pixels location and intensity values. This is the input matrix for the code.

If necessary, the image is pre-filtered to eliminate the AFM instrumental noise. This noise is easy to detect, because it has a very distinctive frequency component in the spatial frequency domain as compared with the random noise and the typical hologram frequencies. In the spatial frequency domain it can be seen as two conjugate points which can be removed by masking. The filtered image is loaded to the reconstruction code. Then two parameters are specified: z_p – approximate distance from the object to the recording medium and z_m – distance from the laser to the object. The size of the input image is stored in to two separate constants (N_x, N_y , if the image is square, that is usually the case because of square scans from atomic force microscope, then $N = N_x = N_y$) and the AFM pixel size $D = D_x = D_y$ (the size of the pixel in the image) is also specified. The total distance from the source to the hologram is calculated $z_0 = z_p + z_m$. The flowchart of the hologram reconstruction code is depicted in Figure 5.11.

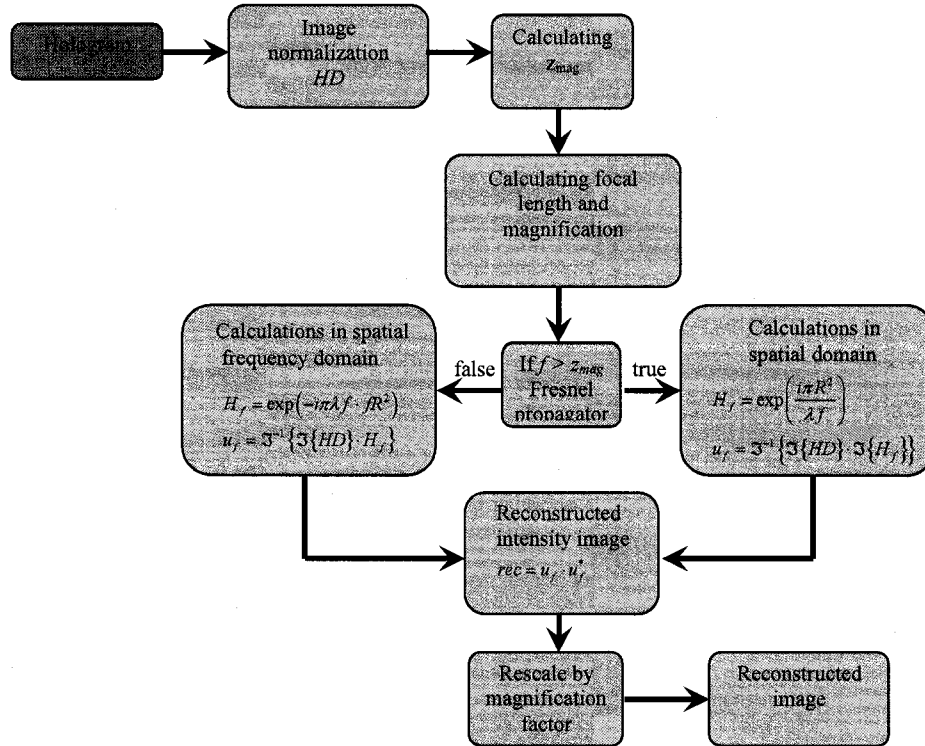


Figure 5.11. Flowchart representing the hologram reconstruction code based on Fresnel propagator.

Because the hologram can be considered as a generalized zone plate, then from the geometrical parameters its focal length and the system magnification can be found:

$$f = \frac{1}{\frac{1}{z_p} - \frac{1}{z_0}} \quad (5.44)$$

$$M = \frac{1}{1 - \frac{z_p}{z_0}} \quad (5.45)$$

Two vectors are created that define the location of the pixels in the image:

$$x = \left([1:N_x] - \frac{N_x}{2} \right) \cdot D_x \quad (5.46)$$

$$y = \left(\left[1 : N_y \right] - \frac{N_y}{2} \right) \cdot D_y \quad (5.47)$$

The distance from the center of the image to an arbitrary point is equal to $R = \sqrt{X^2 + Y^2}$. Similar calculations are made in the spatial frequency domain. Vectors in the spatial frequency domain can be expressed as:

$$\Delta f_x = \frac{1}{N_x D_x}, \Delta f_y = \frac{1}{N_y D_y} \quad (5.48)$$

$$f_x = \left(\left[1 : N_x \right] - \frac{N_x}{2} \right) \cdot \Delta f_x, f_y = \left(\left[1 : N_y \right] - \frac{N_y}{2} \right) \cdot \Delta f_y \quad (5.49)$$

Similarly a grid on the spatial frequency domain is created describing the distance from the origin in the spatial frequency domain $fR = \sqrt{fX^2 + fY^2}$ and is shifted to have the DC component ($f_x = f_y = 0$) in the center of the image. The z_{mag} distance is computed as:

$$z_{mag} = \frac{D^2 \cdot N}{\lambda} \quad (5.50)$$

The code calculates the propagator in the real space or in the Fourier space depending on the value of f and z_{mag} as discussed in section 5.5.3:

$$H_{F_real} = e^{\frac{i\pi R^2}{\lambda \cdot f}}, f > z_{mag} \quad (5.51)$$

$$H_{F_Fourier} = e^{-i\pi \lambda \cdot f \cdot fR^2}, f < z_{mag} \quad (5.52)$$

For $f > z_{mag}$ the code computes the FFT of the Fresnel propagator as well as the FFT of the original image and multiplies them component by component. The back propagated field is obtained by doing inverse FFT:

$$u_f = \mathfrak{F}^{-1} \left\{ \mathfrak{F}(H_{image}) \cdot \mathfrak{F}(H_{F_real}) \right\} \quad (5.53)$$

However for $f < z_{mag}$ the propagator was already calculated in spatial frequency domain so it simplifies further calculations to:

$$u_f = \mathfrak{F}^{-1} \left\{ \mathfrak{F}(H_{image}) \cdot H_{F_Fourier} \right\} \quad (5.54)$$

Then the vectors x and y are rescaled by the geometrical magnification factor M to resize the reconstructed image, because the object was projected onto a holographic medium during the recording step:

$$x_M = \frac{x}{M}, y_M = \frac{y}{M} \quad (5.55)$$

and the reconstructed intensity image rec is calculated

$$rec = u_f \cdot u_f^* \quad (5.56)$$

Using the rescaled parameters x_M, y_M , the matrix rec contains the reconstructed image at a distance z_p from the recording medium. The code has a few subroutines: loading the image, filtering the image in the spatial frequency domain and finally there is a reconstruction code in the loop that allows to change slightly the distance z_p for each reconstruction and to obtain more or less in focus images. Because the distance z_p is known with a limited precision, *a priori*, one can set the initial reconstruction distance and adjust the value of z_p in the code to obtain the best reconstruction. Different z_p will reconstruct slightly different images. This is equivalent to adjust the objective-sample distance in a regular microscope to see the images in and out of focus. An example of the reconstruction of the hologram can be seen in Figure 5.12. This is a hologram of an AFM tip with a triangular shape. Figure 5.12a is a hologram recorded in the surface of the

photoresist, Figure 5.12b is the reconstructed image obtained by processing the hologram with the reconstruction code at the object-recording medium distance $z_p \sim 120\mu m$.

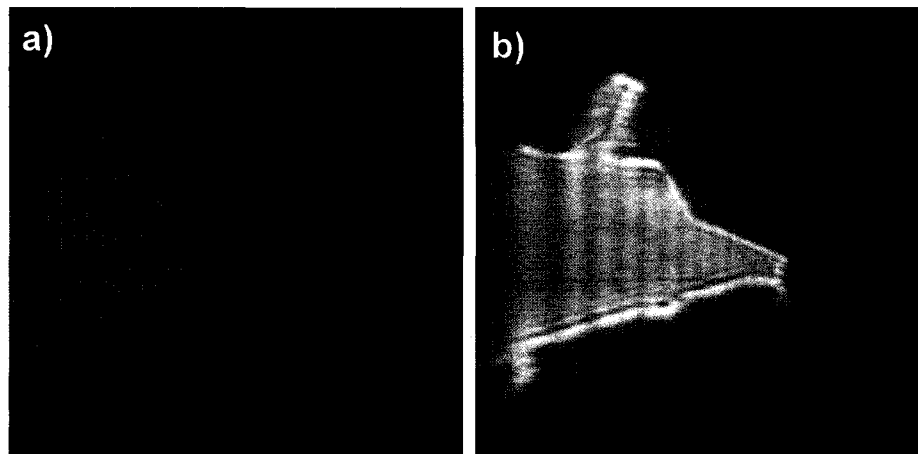


Figure 5.12. The example of the hologram scanned with AFM a), reconstructed image b) at the distance $z_p \sim 120\mu m$ that results in having a sharp image of the original object.

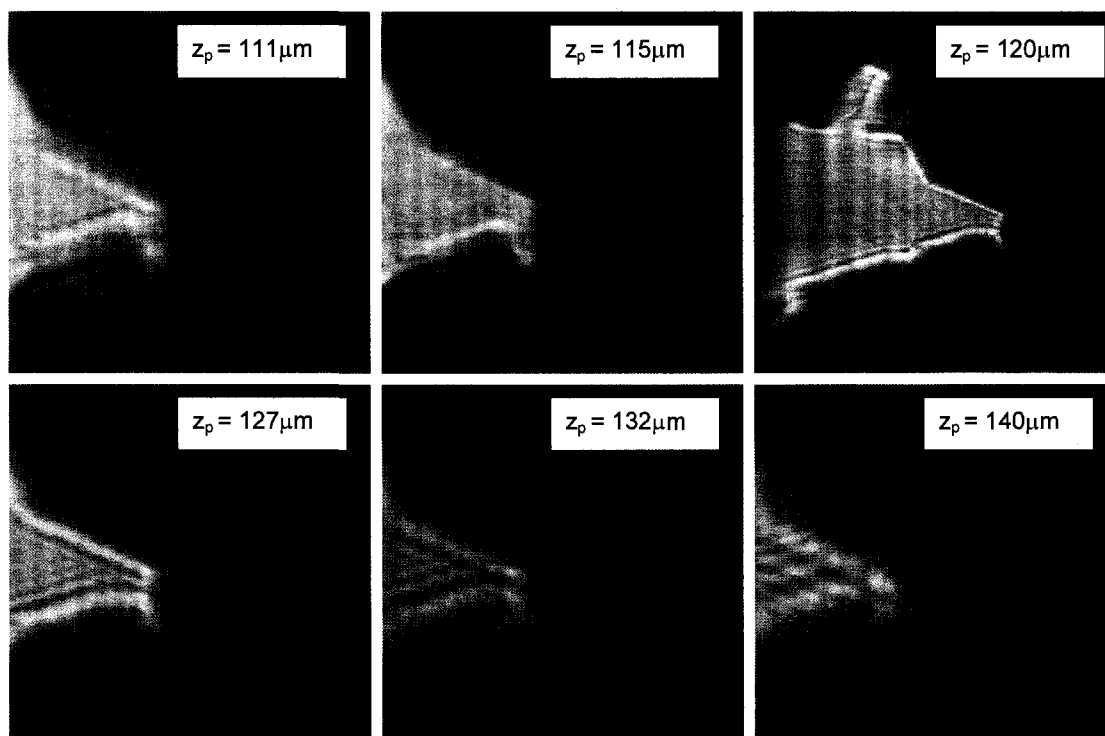


Figure 5.13. A few examples of results of running the code at different distances between the object and recording medium – z_p .

The image reconstructed in focus reveals sharp edges. If z_p is changed in the reconstruction code, the reconstructed image is clearly out of focus. A sequence of different reconstructions at different values of z_p is depicted in Figure 5.13.

5.6 Sampling considerations during the digitization process

The hologram is an interference pattern stored in the recording medium. The information about the highest spatial frequencies in the hologram has to be properly stored in the recording medium and subsequently retrieved to reconstruct the image of the object with the maximum possible resolution. To evaluate the influence of the digitization process with the AFM on the resolution that can be achieved in the reconstruction, let us consider the simplest possible hologram corresponding to a point source that as described in section 5.5.1 is a FZ pattern. For this simple hologram the maximum spatial frequency will be given by the outermost zone width Δr . Figure 5.14 is a representation of such a hologram with Δr indicated.

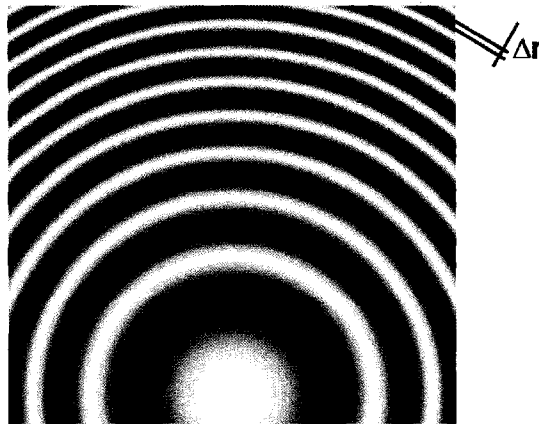


Figure 5.14, Synthesized hologram of a point object (FZP pattern) the outermost circular zone has to be sampled properly with AFM to reconstruct the object with maximal possible resolution.

The resolution of the recording medium has to be better than the highest spatial frequency component in the hologram $\Delta_{rec} \leq \Delta r$, in order to faithfully reproduce the object. Similarly the pixel size in the AFM that defines the resolution has to be equal or smaller than the highest spatial frequency component in the hologram $\Delta_{AFM} \leq \Delta r$. Given the relationship between the NA and outermost zone width Δr of an FZP [5.28], the minimum number of samples required for a given spatial resolution is:

$$N_{samples/line} = \frac{D}{\Delta r} \quad (5.57)$$

where D is the size of the digitized hologram. The numerical aperture defined by the outermost zone width can be expressed as:

$$NA = \frac{\lambda}{2\Delta r} \quad (5.58)$$

Substituting equation 5.7 yields:

$$\Delta = 2a\Delta r \quad (5.59)$$

On the other hand the numerical aperture is limited by the size of the digitized hologram and the distance to the object during the recording step or equivalently the reconstruction distance z_p :

$$NA = \frac{D/2}{\sqrt{(D/2)^2 + z_p^2}} = \sin \left[\arctan \left(\frac{D}{2z_p} \right) \right] \quad (5.60)$$

using equation 5.7 one can find that:

$$D = 2z_p \tan \left[\arcsin \left(\frac{a\lambda}{\Delta} \right) \right] \quad (5.61)$$

if $0 \leq \frac{a\lambda}{\Delta} \leq 1$. Finally the number of sample points obtained with AFM in single scan line

has to be equal to:

$$N_{samples/line} = \frac{2aD}{\Delta} = \frac{4az_p}{\Delta} \tan \left[\arcsin \left(\frac{a\lambda}{\Delta} \right) \right] \quad (5.62)$$

For the case of small angle approximation it will be equal to:

$$N_{samples/line} = \frac{4a^2 z_p \lambda}{\Delta^2} \quad (5.63)$$

For the Rayleigh criterion:

$$N_{samples/line} = \frac{1.488 z_p \lambda}{\Delta^2} \quad (5.64)$$

The total number of sampling points for the two dimensional interferogram can be expressed as:

$$N_{total} = (N_{sample/line})^2 = \frac{16a^4 z_p^2 \lambda^2}{\Delta^4} \quad (5.65)$$

This equation shows that the number of AFM points necessary to attain a given image resolution Δ scales as $N_{total} \sim \Delta^{-4}$. This imposes a practical limitation if the distance z_p is not kept small.

-
- [5.1] D. Gabor, "A new microscope principle", *Nature* **161**, 777 (1948)
- [5.2] E. N. Leith, J. Upatnieks, "Wavefront reconstruction and communication theory", *Journal of the Optical Society of America* **52**, 1123 (1962)
- [5.3] E. N. Leith, J. Upatnieks, "Wavefront reconstruction with continuous tone objects", *Journal of the Optical Society of America* **53**, 1377 (1963)
- [5.4] E. N. Leith, J. Upatnieks, "Wavefront reconstruction with diffused illumination and three-dimensional objects", *Journal of the Optical Society of America* **54**, 1295 (1964)
- [5.5] A. V. Baez, "A study in diffraction microscopy with special reference to X-Rays", *Journal of the Optical Society of America* **42**, 756 (1952)
- [5.6] J. E. Trebes, S.B. Brown, E.M. Campbell, D.L. Matthews, D.G. Nilson, G.F. Stone, D.A. Whelan, "Demonstration of X-ray holography with an X-ray laser", *Science* **238**, 517 (1987)
- [5.7] C. Jacobsen, M. Howells, J. Kirz, S. Rothman, "X-Ray Holographic Microscopy using Photoresists", *Journal of the Optical Society of America A-Optics Image Science And Vision* **7**, 1847 (1990)
- [5.8] S. Lindaas, H. Howells, C. Jacobsen, A. Kalinovsky, "X-ray holographic microscopy by means of photoresist recording and atomic-force microscope readout", *Journal of the Optical Society of America A-Optics Image Science and Vision* **13**, 1788 (1996)
- [5.9] I. McNulty, J. Kirz, C. Jacobsen, E.H. Anderson, M.R. Howells, D.P. Kern, "High Resolution Imaging by Fourier Transform X-ray Holography", *Science* **256**, 1009 (1992)
- [5.10] B. R. Benware, C.D. Macchietto, C.H. Moreno, J.J. Rocca, "Demonstration of a high average power tabletop soft X-ray laser", *Physical Review Letters* **81**, 5804 (1998)
- [5.11] Y. Wang, M.A. Larotonda, B.M. Luther, D. Alessi, M. Berrill, V.N. Shlyaptsev, J.J. Rocca, "Demonstration of high-repetition-rate tabletop soft-x-ray lasers with saturated output at wavelengths down to 13.9 nm and gain down to 10.9 nm", *Physical Review A* **72**, 5 (2005)
- [5.12] F. Brizuela, G. Vaschenko, C. Brewer, M. Grisham, C.S. Menoni, M.C. Marconi, J.J. Rocca, W. Chao, J.A. Liddle, E.H. Anderson, D.T. Attwood, A.V. Vinogradov, I.A. Artioukov, Y.P. Pershyn, V.V. Kondratenko, "Reflection mode imaging with nanoscale resolution using a compact extreme ultraviolet laser", *Optics Express* **13**, 3983 (2005)

-
- [5.13] G. Vaschenko, C. Brewer, E. Brizuela, Y. Wang, M.A. Larotonda, B.M. Luther, M.C. Marconi, J.J. Rocca, C.S. Menoni, "Sub-38 nm resolution tabletop microscopy with 13 nm wavelength laser light", *Optics Letters* **31**, 1214 (2006)
- [5.14] G. Vaschenko, F. Brizuela, C. Brewer, M. Grisham, H. Mancini, C.S. Menoni, M.C. Marconi, J.J. Rocca, W. Chao, J.A. Liddle, E.H. Anderson, D.T. Attwood, A.V. Vinogradov, I.A. Artioukov, Y.P. Pershyn, V.V. Kondratenko, "Nanoimaging with a compact extreme-ultraviolet laser", *Optics Letters* **30**, 2095 (2005)
- [5.15] R. A. Bartels, A. Paul, H. Green, H.C. Kapteyn, M.M. Murnane, S. Backus, I.P. Christov, Y.W. Liu, D. Attwood, C. Jacobsen, "Generation of spatially coherent light at extreme ultraviolet wavelengths", *Science* **297**, 376 (2002)
- [5.16] A. S. Morlens, J. Gautier, G. Rey, P. Zeitoun, J.P. Caumes, M. Kos-Rosset, H. Merdji, S. Kazamias, K. Casson, M. Fajardo, "Submicrometer digital in-line holographic microscopy at 32 nm with high-order harmonics", *Optics Letters* **31**, 3095 (2006)
- [5.17] R. I. Tobey, M.E. Siemens, O. Cohen, M.M. Murnane, H.C. Kapteyn, K.A. Nelson, "Ultrafast extreme ultraviolet holography: dynamic monitoring of surface deformation", *Optics Letters* **32**, 286 (2007)
- [5.18] R. L. Sandberg, A. Paul, D.A. Raymondson, S. Hadrich, D.M. Gaudiosi, J. Holtsnider, R.I. Tobey, O. Cohen, M.M. Murnane, H.C. Kapteyn, "Lensless diffractive imaging using tabletop coherent high-harmonic soft-x-ray beams", *Physical Review Letters* **99**, 098103 (2007)
- [5.19] R. L. Sandberg, C. Song, P. W. Wachulak, D. A. Raymondson, A. Paul, B. Amirbekian, E. Lee, A. Sakdinawat, C. L. Vorakiat, M. C. Marconi, C. S. Menoni, M. M. Murnane, J. J. Rocca, H. C. Kapteyn, J. Miao, "High numerical aperture tabletop soft X-ray diffraction microscopy with 70 nm resolution", *Proceedings of the National Academy of Science* **105**, 24 (2008)
- [5.20] A. C. F. Hoole, M. E. Welland, A. N. Broers, "Negative PMMA as a high-resolution resist - the limits and possibilities", *Semicond. Sci. Technol.* **12**, 1166-1170 (1997)
- [5.21] K. Yamazaki, T. Yamaguchi, H. Namatsu, "Three-Dimensional Nanofabrication with 10-nm Resolution", *Jpn. J. Appl. Phys.* **43**, L1111-L1113 (2004)
- [5.22] J. M. Heck, D. T. Attwood, W. Meyer-Ilse, E. H. Anderson, "Resolution determination in X-ray microscopy: an analysis of the effects of partial coherence and illumination spectrum", *Journal of X-Ray Science and Technology* **8**, 95 (1998)
- [5.23] G. L. Rogers, "Gabor diffraction microscope: the hologram as a generalized zone plate", *Nature* **166**, 237 (1950)

[5.24] H. Nyquist, "Certain topics in telegraph transmission theory", Trans. AIEE, vol. **47**, 617 (1928)

[5.25] U. Schnars, P.O. Jüptner, "Digital recording and reconstruction of holograms in hologram interferometry and shearography", Appl. Opt **33**, 4373 (1994)

[5.26] U. Schnars, P.O. Jüptner, "Digital recording and numerical reconstruction of holograms", Meas. Sci. Technol **13**, R85 (2002)

[5.27] J.W. Goodman, *Introduction to Fourier Optics* (Roberts & Company Publishers, 2005, p. 45)

[5.28] D. Attwood, *Soft X-ray and extreme ultraviolet radiation*, (Cambridge University Press. 1999)

CHAPTER 6

6 High spatial resolution holography

In this chapter the application of the EUV compact laser sources in high resolution holographic imaging will be presented. The key idea behind this technique is the improved resolution attainable with the short EUV illumination.

The resolution of the optical system is described by the Rayleigh criterion. This criterion states that the image of two point sources of quasi monochromatic radiation with equal intensities in a noise free background will produce two Airy intensity patterns in the image plane. If the points are separated enough, then the image will be formed by two distinct Airy patterns, one for each source. The point sources are said in this case to be resolved. If the sources are closer, then their Airy patterns will start to overlap. If the two sources are mutually incoherent, the superposition of the two Airy patterns is an intensity addition. By bringing the two sources closer together the intensity between them increases and it makes more difficult to distinguish the individual source images. According to the Rayleigh criterion, the separation between the sources where two point sources are said to be just resolved corresponds to the superposition of the first null of the Airy intensity pattern from the first source with the maximum of the Airy intensity

pattern from the second source. This distance defines the resolution of the optical system in the straightforward way and is equal to:

$$\Delta_r = \frac{0.61\lambda}{NA} \quad (6.1)$$

where λ is the illumination wavelength and NA is a numerical aperture of the system. This equation assumes incoherent illumination. More generally, the value 0.61 can be changed by a constant k :

$$\Delta_r = \frac{k\lambda}{NA} \quad (6.2)$$

According to Heck et al. [6.1] the value of k may change from ~ 0.34 up to 1 depending on the degree of coherence of the illumination, the illumination spectrum, and the type of the resolution test.

Equation 6.2 shows that one way to improve the spatial resolution of the imaging system is by reducing the illumination wavelength. This was the motivation to employ short-wavelength illumination source such as the capillary discharge laser emitting at $\lambda = 46.9nm$ described in Chapter 2. This wavelength is $\sim 10x$ shorter than the visible light and allows to significantly improve the imaging resolution.

Another avenue to improve the resolution is by increasing the numerical aperture. The goal of the experiment described in this chapter was to obtain the ultimate imaging resolution in the holographic recording. The approach was both to use shorter illumination wavelength and to increase the NA of the recording. The results of the experiments shown in this chapter were reported in recent publications [6.2-6.4].

6.1 Holographic imaging of AFM tips

6.1.1 Introduction

Two holograms of an atomic force microscope tip were obtained using a table top EUV laser in a Gabor's in-line configuration. This configuration requires no optics or critical beam alignment. The hologram recording scheme is very simple and doesn't need special sample preparation.

The hologram was recorded as a relief pattern in a high resolution photoresist. The holograms recorded in the photoresist cannot be reconstructed in the conventional way by illuminating with a replica of the reference beam. Instead, following the approach by Bartolini [6.5]. The hologram was digitized by scanning the surface of the photoresist with an atomic force microscope and numerically reconstructed with the code described in chapter 5. Two independent techniques were used to assess the spatial resolution of the image, the 10-90% slope knife-edge resolution test and a wavelet decomposition and correlation algorithm.

6.1.2 Experimental details

The experimental set up is schematically illustrated in Figure 6.1. The source was a compact $\lambda = 46.9\text{nm}$ table top discharge pumped capillary Ne-like Ar laser. The laser source was described in detail in chapter 2. In this experiment the laser was operated with

18.4cm long capillaries and produced pulses with energy $\sim 100\mu\text{J}$ at a repetition rate of 1 Hz [6.6].

The Gabor (in-line) configuration was used to record the hologram. The object was placed at the distance z_p away from the recording medium, as schematically depicted in Figure 6.1. The object illuminated by the laser diffracts the light (indicated in the figure with a darker cone shaped beam). The diffracted beam and the remaining illumination beam that passes unperturbed around the object interfere in the hologram plane. The interference pattern created in this way is recorded in the photoresist as a hologram of the object.

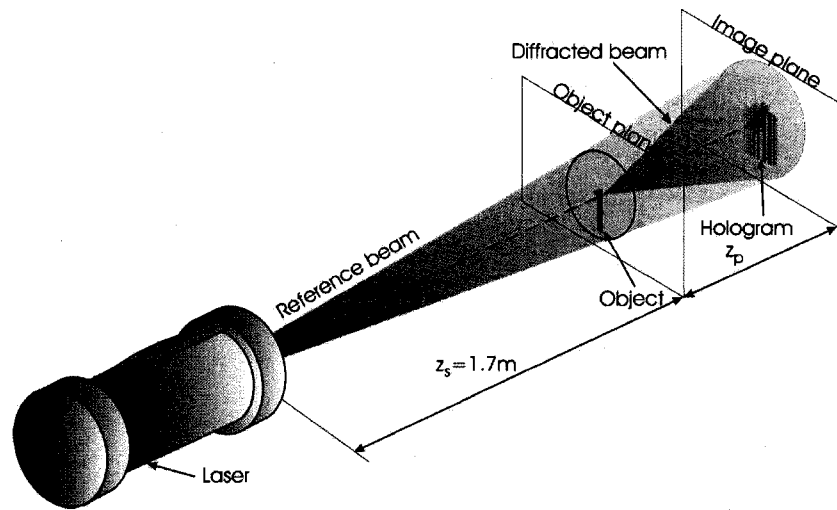


Figure 6.1. Schematic description of the Gabor's in-line holographic scheme for hologram recording.

The laser and the experimental setup are depicted in Figure 6.2. The laser is connected through the vacuum manifold to the experimental chamber that houses the holographic setup.

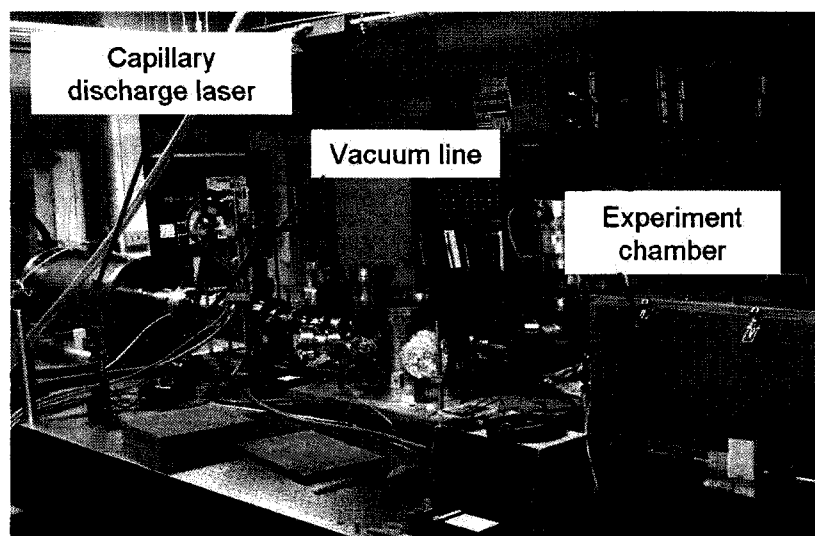
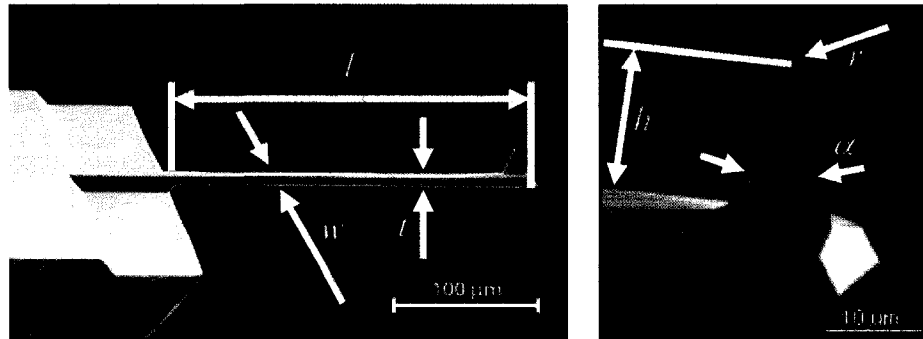


Figure 6.2. Photograph of the laser system used to make the holograms.

The object and photoresist assembly were illuminated by the laser beam and the exposure was adjusted to work in the linear region of the photoresist response curve. After the exposure the photoresist was developed and the modulation in the photoresist surface was digitized with an AFM. The digitized image was processed with the reconstruction code described in chapter 5 and the image of the object was reconstructed.

Two holograms with $z_p \sim 4mm$ and $z_p \sim 120\mu m$ were obtained. The recording was done in a 120nm thick layer of PMMA (MicroChem 950'000 molecular weight) spin-coated on a silicon wafer. The object used was an AFM tip. An electron microscope image of the tip is shown in Figure 6.3. The AFM cantilever has the following physical characteristics: cantilever length $l = 230\mu m$, width $w = 40\mu m$, thickness $t = 7\mu m$, full tip cone angle $\alpha = 30^\circ$, tip height $h = 20 \div 25\mu m$, typical tip curvature radius of the tip $r < 10nm$. The triangular profile of the tip provides an adequate object with continuously varying dimensions suitable for image resolution estimation.



<http://www.spmtips.com/nsc16/al-bs>

Figure 6.3. An example of AFM tip used as the object for Gabor holography.

Exposures of approximately 100 laser shots (100 seconds) were made with this experimental setup. After the exposure, the photoresist was developed using the standard procedure. The sample was immersed in a solution of MIBK-methyl isobutyl ketone (4-Methyl-2-Pentanone) with IPA (isopropyl alcohol) 1:3 for 30 seconds and rinsed with IPA for 30 seconds. Finally the sample was dried using compressed nitrogen.

6.1.3 Results

For the first exposure where $z_p \sim 4mm$ a Veeco Nanoscope III model NS3a AFM operated in tapping mode was used for the digitization. The maximum scan area allowed by this instrument was $100 \times 100 \mu m^2$. However, in the hologram, the interference fringes were visible over large areas, several hundreds of microns away from the central image of the tip and in excess to the maximum scan allowed by the AFM. To achieve the large NA needed to reconstruct the image with high resolution, several scans of partially superposed regions of the hologram were obtained and the different images were stitched

together to cover a larger surface. The final digitized interferogram image covering a total area of $270 \times 290 \mu\text{m}^2$ composed by 9 sub-scans is shown in Figure 6.4a. In this image the AFM pixel size is $\sim 270 \text{nm}$.

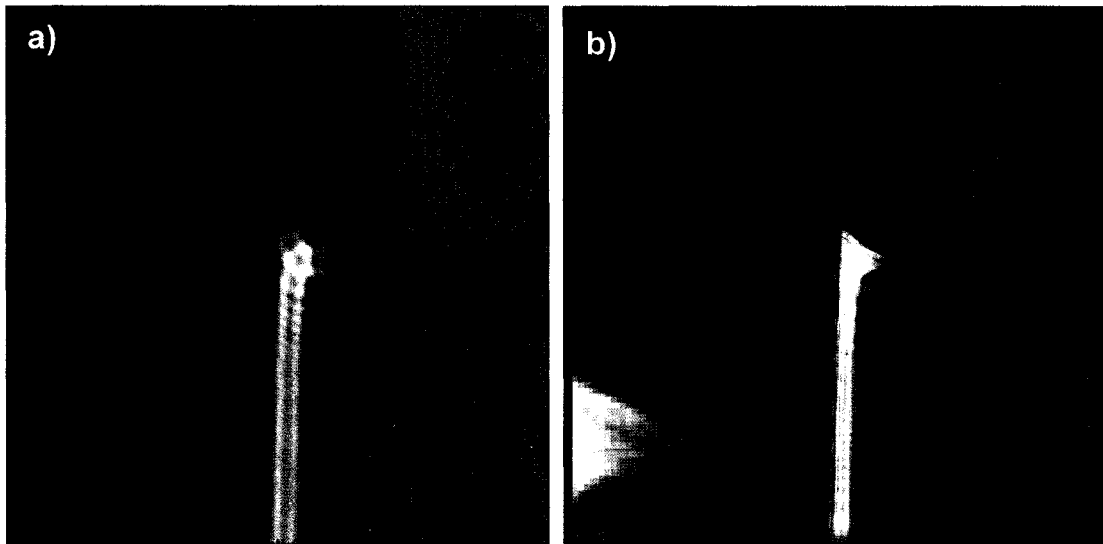


Figure 6.4. a) Hologram scanned with AFM at $z_p \sim 4 \text{mm}$. The image is composed by 9 sub scans to cover a total area $270 \times 290 \mu\text{m}^2$, b) numerical reconstruction of the hologram obtained with the Fresnel propagator with zoomed area of the end of the reconstructed tip.

In a second experiment where $z_p \sim 120 \mu\text{m}$ the hologram was digitized using a Novascan 3D AFM operated in “tapping” mode with a maximum scan area $42 \times 42 \mu\text{m}^2$. In this exposure, the AFM pixel size was $\sim 41 \text{nm}$. The hologram digitized with the AFM is depicted in Figure 6.5a.

In the reconstructions (Figure 6.4b and Figure 6.5b) the triangular shape of the tip is clearly revealed. In Figure 6.5b only the tip is imaged without the cantilever. The reconstruction also revealed that the tip was broken and also contaminated as shown by the protrusion on the upper side of the image.

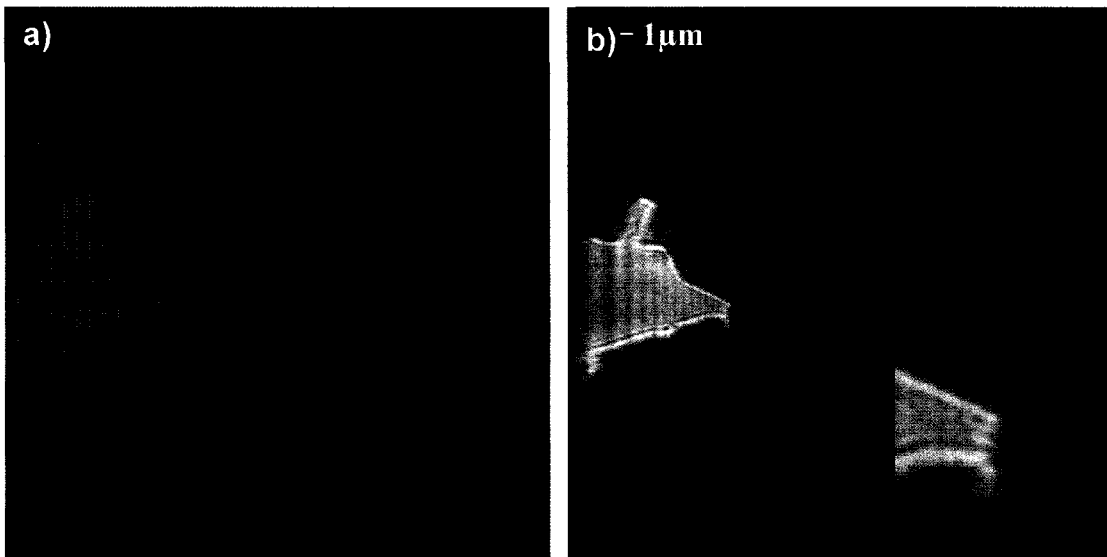


Figure 6.5. a) Hologram scanned with AFM at $z_p \sim 120\mu\text{m}$. Single scan image to cover a total area $42 \times 42\mu\text{m}^2$, b) numerical reconstruction of the hologram obtained with the Fresnel propagator with zoomed area of the end of the reconstructed tip.

One can also notice that in the reconstructed images there is still additional fringing effect due to the twin image discussed in chapter 5.

To roughly evaluate the resolution one can do a line section of the reconstructed image, as shown in Figure 6.6.

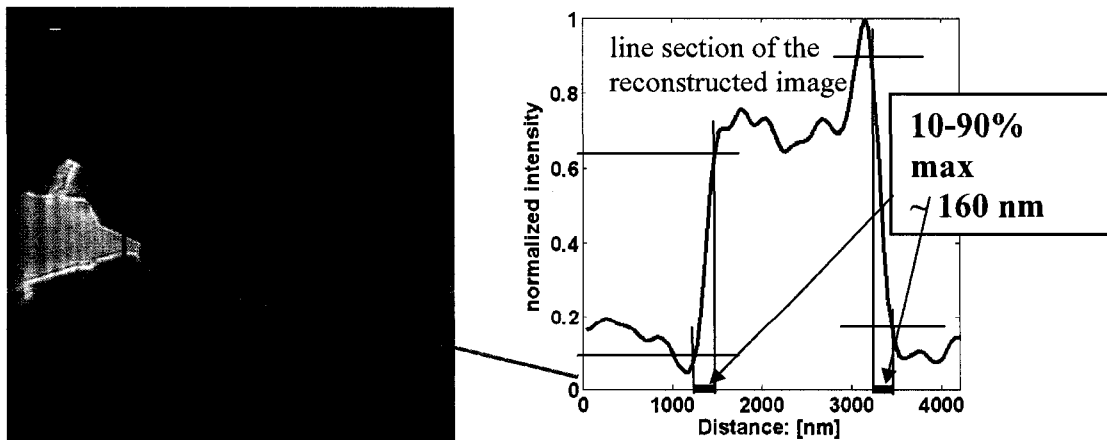


Figure 6.6. Line section through the example of reconstructed image showing sharp edges and roughly 160-170nm resolution.

From this lineout, using the 10-90% slope criterion a resolution of 160-170nm is obtained. The next section will show that using a more rigorous analysis to evaluate the resolution, based on the wavelet decomposition and image correlation, values consistent with this simple analysis were obtained.

The longitudinal coherence length of the table-top capillary discharge laser was estimated to be equal to $\sim 470\mu\text{m}$ ($\Delta\lambda/\lambda \sim 10^{-4}$). For the 46.9nm laser and Rayleigh resolution criterion $k = 0.61$ the temporal coherence limits the NA to approximately 0.446, limiting the image spatial resolution to $\Delta = 64.1\text{nm}$ for $z_p = 4\text{mm}$ and $NA \sim 0.97$, $\Delta = 29.2\text{nm}$ for $z_p = 120\mu\text{m}$. Similarly, the source's spatial coherence limits the numerical aperture of the hologram to be about 0.084 and resolution to 337.8nm for larger separation between the object and the recording medium (4mm) and to $NA \sim 0.94$, $\Delta = 30.4\text{nm}$ for smaller separation. The coherence radius of the discharge pumped 46.9nm laser equipped with 18.4cm long capillary, as used in this experiment was approximately $R_c \sim 340\mu\text{m}$ at the object plane located at $z_s = 1.7\text{m}$ from the laser.

6.1.4 Resolution evaluation

To estimate the resolution of the reconstructed images a wavelet decomposition and correlation algorithm was developed. The method presented in this section is based on the correlation between the image and a set of templates with variable and calibrated resolution. The two dimensional correlation between the data image and the template is capable to recognize the similarities in both images thus it may be considered as an

objective way to decide which template is most similar to the data image and decide what is the resolution of the data image. The key element of this analysis is the wavelet decomposition algorithm having dyadic characteristics. This means that the resolution in each decomposition step is reduced by a constant factor, in this case two. The set of calibrated templates generated in this way was correlated with the image. The maximum correlation coefficient obtained indicates which template is most similar to the reconstructed image and what is its resolution.

6.1.4.1 Wavelet analysis

To generate the set of templates with reduced resolution a wavelet decomposition scheme was employed. A wavelet is a mathematical function that is used to decompose another given function or continuous in time signal into many different frequency components. That allows to study each component separately with a resolution that matches the wavelet scale. Wavelet analysis decomposes the signal into components of logarithmically decreasing frequency intervals and sample rates. Usually it is implemented using filters that decompose a broadband signal into a set of successively more band limited components. At the output of each successive level of decomposition the signal bandwidth is reduced twice by appropriate filtering and down sampling and the resolution is reduced by the same factor. This is equivalent to smoothing the sharp edges in the image. The wavelet synthesis reconstructs a signal, which was decomposed by the wavelet analysis filter bank. The synthesis or reconstruction process is the inverse of the analysis process. It restores the original signal in successive steps by increasing the

sampling rate (up sampling) and applying appropriate filters. Wavelet transforms have the advantage over the traditional Fourier transform that it can represent the functions with discontinuities and sharp peaks, also it can accurately decompose and reconstruct finite, non-periodic and non-stationary signals.

6.1.4.2 Binary template generation

To generate the set of templates with decreasing resolution, a master template is required. By decomposition of this template a lower resolution template is generated in each step of the decomposition. The shape of the object was to be known *a priori* from the manufacturer specifications. That allowed to manually generate the first template shown in Figure 6.7.

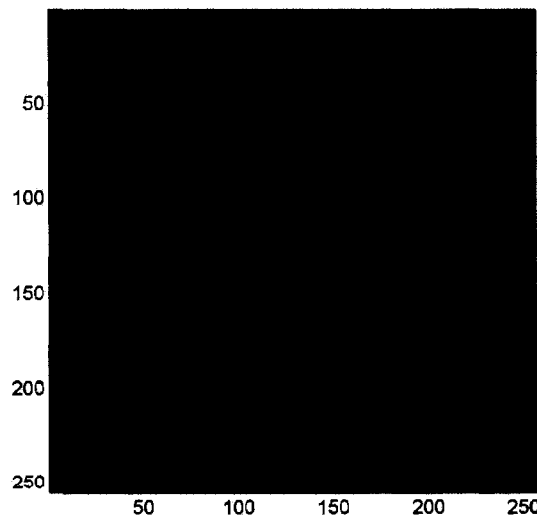


Figure 6.7. The 0th order template generated for resolution estimation. This binary image resembles the size and shape of the object and has resolution equal to one pixel.

The template consists of a binary (zeros and ones) image of the AFM tip. Its size matches exactly the size of reconstructed sub-images. This first template called 0th order template is binary and by definition the 0th order template has the best possible resolution equal to one pixel, because the transition in the lineout made in that image is across one pixel. The 0th order template resembles the size and shape of the object used in the experiment.

6.1.4.3 Secondary template generation

To estimate the resolution of the reconstructed images a multiresolution analysis was implemented based on wavelets [6.7]. The advantage of using the wavelet approach is the dyadic decomposition scheme, which allows an immediate correspondence between the scale of the decomposition and the resolution. This is a consequence of the properties of the wavelets. In each decomposition step a new template is generated with a relative resolution to the 0th order template given by $Y = 2^X$, where Y is the relative resolution between the 0th order template and the considered template in the wavelet decomposition and X is the wavelet order (the level of decomposition). The relation between X and Y shows that in each decomposition step the resolution of the resulting template is reduced by a factor two (dyadic decomposition scheme) [6.7]. Also each template is reduced in size by a factor two in each coordinate in each decomposition step. The first four wavelet components obtained from the 0th order template are shown in Figure 6.8.

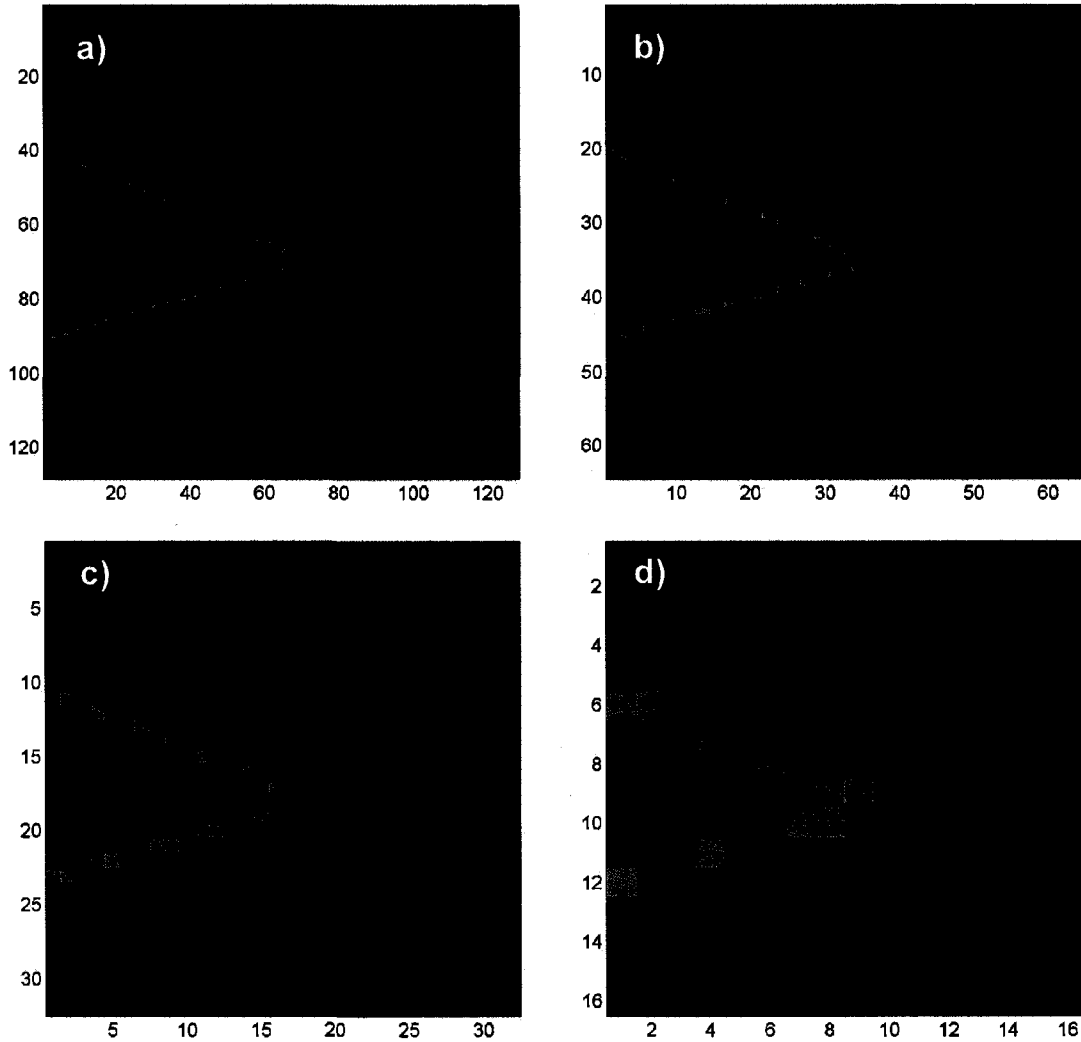


Figure 6.8. Wavelet decomposition: templates with reduced resolution obtained from the 0th order template. a) 1st order, resolution reduced 2x, b) 2nd order, resolution reduced 4x, c) 3rd order, resolution reduced 8x, d) 4th order, resolution reduced 16x.

6.1.4.4 Correlation analysis

The final step in the algorithm performs the correlation between each of the templates obtained by wavelet decomposition with the reconstructed image. The 2-D correlation is capable to measure the similarity between two images. If A, B are two

images represented by two $M \times N$ matrices, then the correlation coefficient can be expressed as:

$$r = \frac{\sum_{m \in M} \sum_{n \in N} (A(m, n) - \bar{A})(B(m, n) - \bar{B})}{\sqrt{\left(\sum_{m \in M} \sum_{n \in N} (A(m, n) - \bar{A})^2 \right) \left(\sum_{m \in M} \sum_{n \in N} (B(m, n) - \bar{B})^2 \right)}} \quad (6.3)$$

where \bar{A}, \bar{B} are mean values of the two matrices calculated as:

$$\bar{A} = \frac{1}{M \cdot N} \sum_{m \in M} \sum_{n \in N} A(m, n), \bar{B} = \frac{1}{M \cdot N} \sum_{m \in M} \sum_{n \in N} B(m, n) \quad (6.4)$$

If the two images are identical, then the correlation coefficient will be equal to $r = 1$. If the images are completely uncorrelated, the correlation coefficient $r = 0$. If two images are identical, but inverted in gray scale, then $r = -1$. The values between 0 and 1 or 0 and -1 are quantitative measure of the similarity between two images.

6.1.4.5 Wavelet decomposition and correlation algorithm

The general flowchart for the EUV holography reconstruction and resolution estimation code is depicted in Figure 6.9. The AFM image after removing artifacts and filtering the noise is reconstructed with the reconstruction algorithm described in chapter 5. 256x256 size images reconstructed at different z_p stored by the reconstruction algorithm were loaded to the wavelet decomposition and correlation algorithm.

The 0th order template of the image is generated and subsequently decomposed using wavelet analysis to produce a set of templates. Because the 0th order template in this experiment synthesized manually it might be slightly displaced compared with the

reconstructed image. A set of different 0th order templates with a relative shift ± 2 pixels in each direction of the tip position were made to obtain the best superposition with the image.

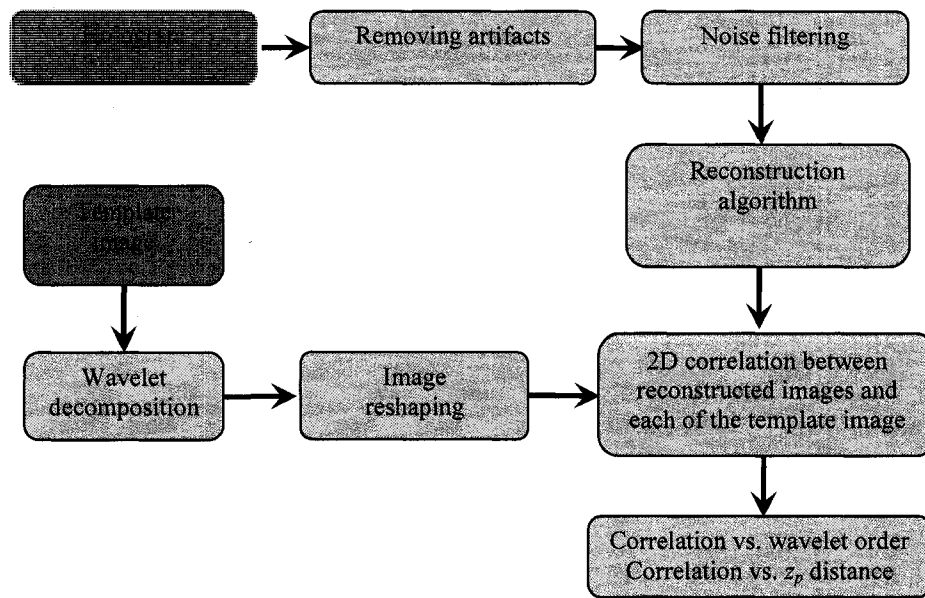


Figure 6.9. Flowchart representing the EUV holography reconstruction and resolution estimation code. AFM image after removing artifacts and noise is reconstructed with the reconstruction algorithm mentioned in previous section. Template of the image is generated and subsequently decomposed using wavelet analysis to produce a set of templates. Then to estimate the resolution each reconstruction image is correlated with set of templates and the results are plotted.

In each decomposition the image size is reduced twice as depicted in Figure 6.8. However the correlation step requires that all the images have the same size, thus the images were resized to 256x256 pixels by a linear extrapolation.

The wavelet used was a “*db1*”– daubechi wavelet of 1st order (often called “*haar*” wavelet). Using the image processing toolbox in MATLAB a subset of templates, based on the 0th order master template with decreased resolution was generated by wavelet decomposition of the image in Figure 6.7. The pixel size in each template is the

same as in the data image and is equal to 41nm for the case of the hologram recorded at $z_p \sim 0.12mm$ and 270nm for the holograms recorded at $z_p \sim 4mm$.

To estimate the resolution each reconstructed image is correlated with the set of wavelet components, a correlation coefficient is obtained for each wavelet component and the result of the correlation coefficient vs. the wavelet order is plotted. To reduce the error between positions of the template image and reconstructed one, the algorithm was executed a few times for a few shifted templates to maximize the correlation coefficients.

6.1.4.6 Resolution estimation results

The wavelet decomposition and correlation method was applied to the two holograms shown in section 6.1. Firstly the reconstructed images from the hologram with $z_p \sim 4mm$ and lower numerical aperture were analyzed. Figure 6.10 is the plot of the calculated correlation coefficients for different images reconstructed with different distances z_p as a function of the wavelet order X . By slightly changing the reconstruction distance one can see, that the correlation coefficient changes slightly but the shape of the curve remains the same. The largest value of the correlation coefficient for all z_p values corresponds to the wavelet order $X=0$ and does not change significantly between $X=0$ and $X=1$, decreasing faster for higher wavelet decomposition levels. As a conservative assumption it was considered that the best correlation value corresponds to $X \sim 0.5$. With this assumption this analysis indicates a

resolution $2^{0.5} \sim 1.41$ relative to the reference image equivalent to 1.41 pixels or $\Delta \sim 380nm$.

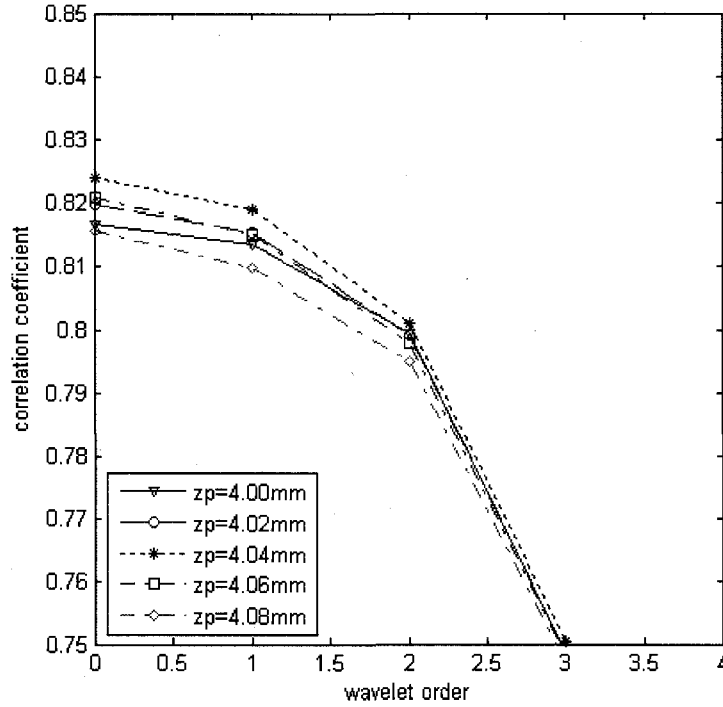


Figure 6.10. Image correlation between reconstructed images at different distances between the object and recording medium z_p and wavelet decomposition levels for $z_p \sim 4mm$ separation.

The second reconstruction analyzed was the hologram recorded at $z_p \sim 120\mu m$ thus having higher recording numerical aperture. Figure 6.11 shows clearly a maximum in the correlation plot for $X = 2$, for all reconstruction distances z_p ranging from 118 to 132 μm . This plot indicates that the maximum correlation values correspond to $X = 2$ for all z_p , thus setting the spatial resolution to 4 pixels. The pixel size corresponds to 41nm, this indicates that the spatial resolution in the image is $\Delta = 164nm$. Based on the NA of the recording set up, the limit to the spatial resolution is set by the Rayleigh criterion to $\Delta = 0.61\lambda / NA$, which gives for this set up 166nm that compares very well with the

wavelet analysis result. This value was calculated knowing the size of the square scan D (hologram size) and the approximate value of the z_p according to the equation

$$NA = \sin \left[\arctan \left(\frac{D}{2z_p} \right) \right].$$

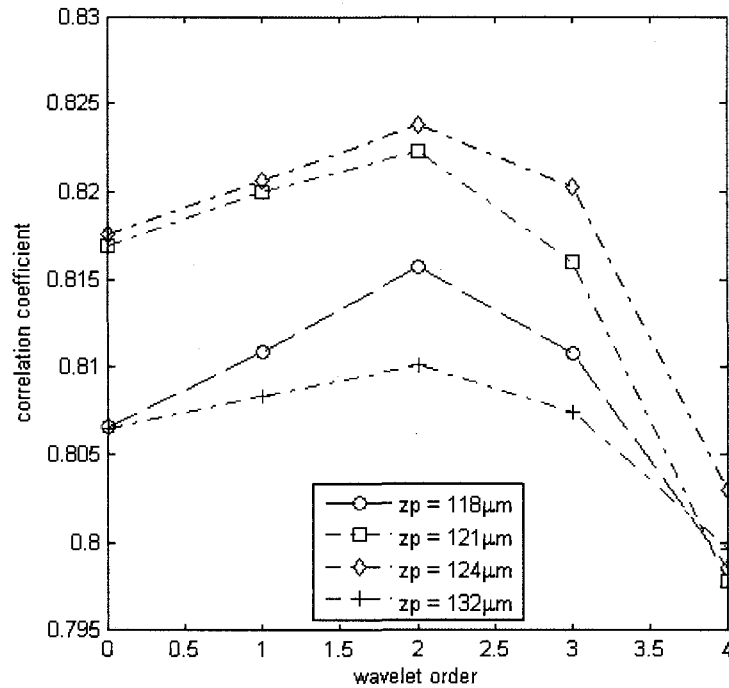


Figure 6.11. Image correlation between reconstructed images at different distances between the object and recording medium z_p and wavelet decomposition levels for $z_p \sim 120 \mu\text{m}$ separation.

This result compares well with the resolution measured using knife-edge analysis mentioned in section 6.1.3. The analysis suggested 160-170nm resolution.

The wavelet decomposition and correlation algorithm presented in this chapter allows also for the selection of the optimum z_p . Figure 6.12 shows the results of applying the wavelet decomposition and correlation code to the reconstructed images for

slightly different z_p starting from 3.8mm up to 4.3mm in the case of lower numerical aperture hologram depicted in Figure 6.4.

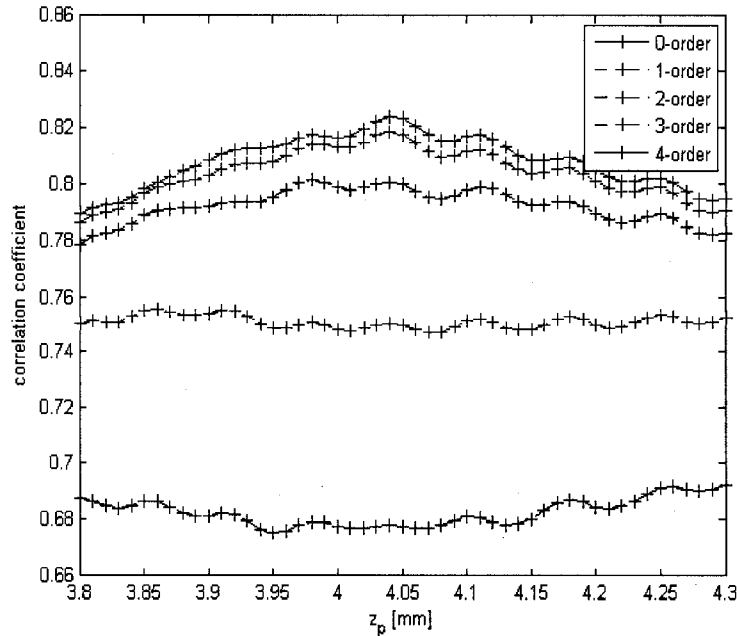


Figure 6.12. Correlation coefficients as a function of z_p distance for different wavelet decomposition levels for $z_p \sim 4mm$ separation.

Because z_p was known only approximately, this plot allows to find out z_p more precisely. The optimum reconstruction distance in that case can be found as the distance at which the correlation coefficient has the highest global value. One can see that it actually happens for 0th level wavelet decomposition (red curve), but 1st level has almost the same profile and slightly lower correlation values (green curve). The other levels of decomposition give much smaller correlation coefficients and they do not have a global maximum as obvious as the plots for 0th and 1st orders. Based on that plot the optimum z_p distance was estimated to be $z_p = 4.04mm$, which gives a global maximum of correlation coefficient to be ~ 0.82 , high enough to be considered as a high similarity between two images.

For the case of the higher numerical aperture hologram shown in Figure 6.5, the approximate distance was $z_p \sim 120\mu m$. Figure 6.13 shows the correlation coefficient for each wavelet decomposition level versus the reconstruction distance. In this case the separation was changed from $\sim 110\mu m$ to $140\mu m$ with $1\mu m$ steps. Comparing with Figure 6.11 one can also see, that the maximum correlation coefficient was obtained for 2nd wavelet order that corresponds to a resolution equal to 4 pixels that is 164nm. The other curves give smaller correlation values.

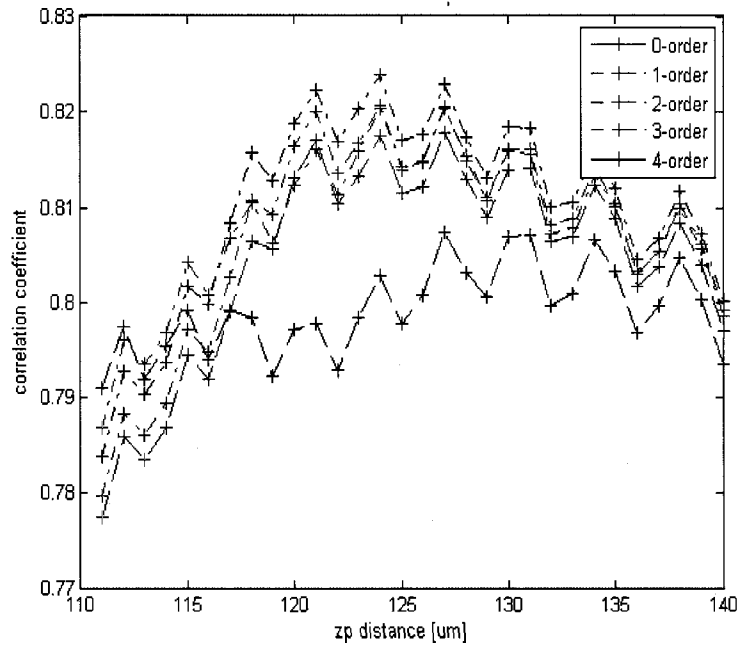


Figure 6.13. Correlation coefficients as a function of z_p distance for different wavelet decomposition levels for $z_p \sim 120\mu m$ separation.

Based on these data the optimum reconstruction distance for the higher numerical aperture hologram was estimated to be $z_p = 124\mu m$. The correlation coefficient is ~ 0.825 and the reconstruction at that distance has the resolution $\sim 164nm$ that is ~ 3.5 wavelengths.

The correlation and convolution method gave good results for the reconstructed images from two different holograms. The results are in good agreement with the theoretical calculations and coherence limitations mentioned in chapter 5 and in section 6.1.3. The results of these two experiments are summarized in the Table 6.1.

Table 6.1. Coherence limitation to the resolution, AFM sampling limitations and the experimentally obtained resolutions estimated based on correlation analysis.

Rayleigh criterion based $k = 0.61$	Spatial coherence $\Delta = \frac{k\lambda}{\sin\left(\arctan\left(\frac{R_c}{z_p}\right)\right)}$	Temporal coherence $\Delta = \frac{k\lambda}{\sqrt{1 - \left(\frac{z_p}{z_p + l_c}\right)^2}}$	AFM pixel size $\Delta_{AFM} = \Delta r$	AFM sampling limit $\Delta = 2k\Delta r$	Experimental resolution
$z_p = 4 \text{ mm}$	337.8 nm	64.1 nm	270 nm	329.4 nm	380 nm
$z_p = 120 \text{ }\mu\text{m}$	30.4 nm	29.2 nm	41 nm	50 nm	164 nm

The calculated limitations due to the coherence of the source indicate that this is not a limiting factor and as the separation between the object and the recording medium decreases these limitations became less important. The technique shown here was extended to reach the resolutions in EUV holography below 50nm (approximately wavelength resolution). The results for wavelength resolution EUV holography will be presented in section 6.2.

6.1.4.7 The influence of the wavelet type on the algorithm results

The same resolution analysis was repeated for different type of wavelet. As an example “db3” wavelet (daubechi 3rd order wavelet) was used. “haar” or “db1” are the

lowest order wavelets and to represent them in terms of the response function the least number of coefficients is necessary. However, there are other wavelets, more complicated and to check the influence of the other wavelets on the algorithm results was a motivation to repeat this analysis.

The combined results of the analysis are presented in Figure 6.14. For $z_p \sim 4mm$ separation between the object and the recording medium (low numerical aperture case) the correlation coefficient as a function of the wavelet order for different reconstruction distances is presented in Figure 6.14a. The correlation coefficient curves behave similarly to the ones in Figure 6.10 however the correlation coefficient drops more rapidly for higher order wavelets than in the previous case. Here also one can assume similar resolution $2^{0.5} \sim 1.41$ of the pixel size.

To find the optimum reconstruction distance, the correlation coefficients for different reconstruction distances were plotted for the different decomposition levels as depicted in Figure 6.14b. The results are also very similar to Figure 6.12 indicating that the optimal reconstruction distance is $z_p = 4.04mm$ similarly to the case with “*db1*” wavelet. For $z_p \sim 120\mu m$ (higher numerical aperture case and better resolution) the correlation coefficient as a function of the wavelet order for different reconstruction distances is presented in Figure 6.14c. The correlation curves changed slightly, but the maximum correlation coefficient is still for the second order wavelet indicating 4 pixels resolution (164nm) and the optimal reconstruction distance is equal to $z_p = 124\mu m$ as indicated in Figure 6.14d.

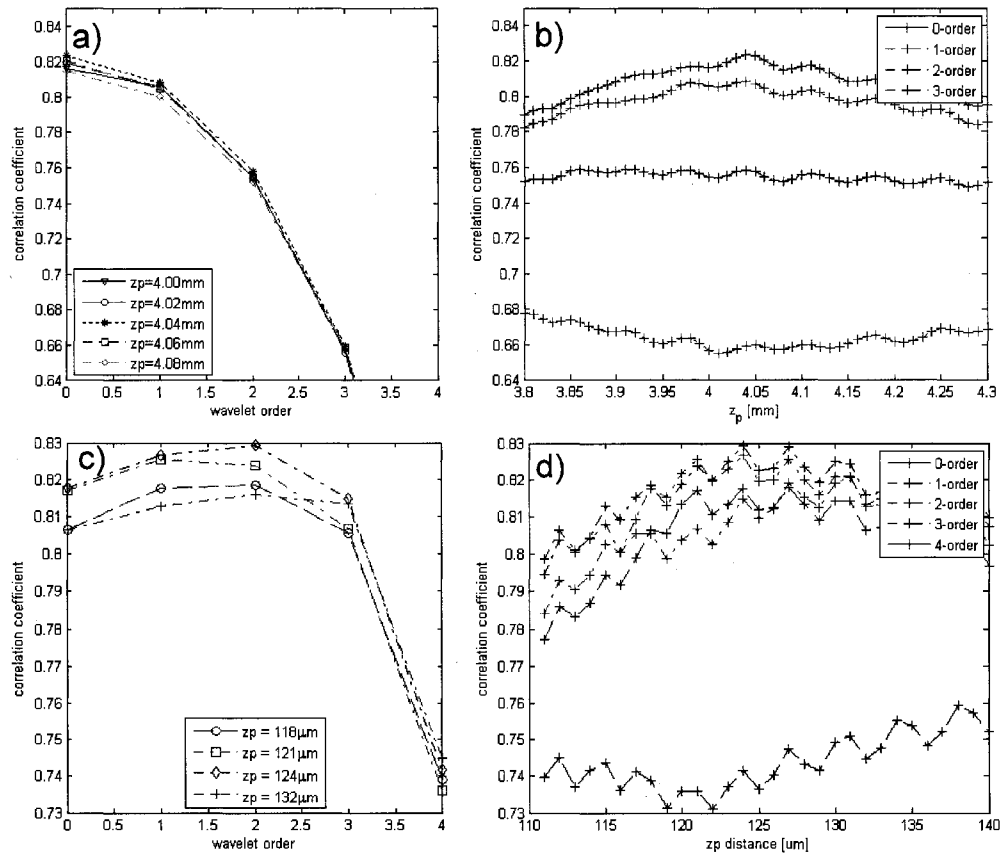


Figure 6.14. Image correlation between reconstructed images at different distances between the object and recording medium z_p and wavelet decomposition levels for $z_p \sim 4\text{mm}$ separation (a) and for $z_p \sim 120\mu\text{m}$ separation (c) decomposed using “*db3*” wavelet. Correlation coefficients as a function of z_p distance for different wavelet decomposition levels for $z_p \sim 4\text{mm}$ separation (b) and for $z_p \sim 120\mu\text{m}$ separation (d) decomposed using “*db3*” wavelet.

The results obtained with “*db3*” wavelet are similar to the results obtained with “*db1*” wavelet. The curves are slightly changed, but the resolution and the optimum reconstruction distance remain invariant.

6.2 Wavelength resolution holography

6.2.1 Introduction

Imaging tools for nanoscience involving sub-100nm scale objects have been dominated by atomic force microscopy (AFM), scanning tunneling microscopy (STM), and electron microscopy. These imaging techniques have contributed substantially to the development of nanoscience, providing a very powerful diagnostic tool capable of atomic resolution or as a subsidiary mechanism to arrange or modify surfaces also at the atomic scale [6.8,6.9]. However, some important problems have resisted traditional nanoscale imaging techniques. For example when scanning a nanometer size object that is not attached rigidly to the surface, the interaction with the tip will significantly perturb the specimen precluding the image acquisition. Electron microscopy often requires surface preparation, consisting of metallization of the sample to avoid surface charging. Additionally the metallization of the sample may alter its characteristics and also limit the resolution. In both cases, if the sample is large (millimeter size) due to the limited field of view, the image obtained with these conventional methods is only representative of a very small portion of the object.

In this section holographic microscopy with ultimate sub-50nm resolution, corresponding to wavelength resolution, using a table-top 46.9nm EUV laser will be presented [6.10]. A sample composed of carbon nanotubes placed on a thin semi-transparent silicon membrane was imaged using a table top EUV laser in a Gabor's in-line configuration. This approach requires no optics or critical beam alignment; thus the

hologram recording scheme is very simple and doesn't need special sample preparation. In holography, image contrast requires absorption to provide scattering by the illuminating beam. The EUV laser wavelength employed in this experiment is advantageous because carbon based materials typically exhibit very small attenuation lengths, around 25nm. The high absorption provokes that even small object volumes will produce high optical contrasts. The short attenuation length thus enables nearly full contrast for most objects without applying forces to the imaged objects, without charge buildup, and without the need for complicated sample preparation.

The hologram was recorded and reconstructed as explained previously in chapter 5. Two independent techniques were used to assess the spatial resolution of the image, the 10-90% slope knife-edge resolution test and a correlation and convolution method. Both evaluations yielded a resolution of around 46nm, which is approximately equal to the wavelength $\lambda=46.9\text{nm}$ utilized in the recording step. The simple and versatile method opens new possibilities for high resolution imaging of arbitrary shaped objects and might find practical application in biology or material science. Uniquely, the holograms recorded in this fashion have the ultimate wavelength resolution in the entire surface. Due to the short wavelength and high coherence of the table top EUV laser, this recording allows for hologram recording over several millimeters square with high resolution, equivalent to a data storage density of approximately 0.3Tbit/in^2 .

6.2.2 Experimental details

The spatial resolution in holography is determined by the numerical aperture (NA) of the recorded holographic interferogram. The hologram described in section 6.1

has a spatial resolution approaching 160nm. The AFM sampling was a practical limitation due to the unfavorable scaling of the required scanned points with the resolution. Thus the simpler approach to achieve the ultimate resolution is to decrease the recording-reconstruction distance z_p . The recording distance in this experiment was reduced to $z_p \sim 2.5\mu\text{m}$.

The sample was a dispersion of multiple wall carbon nanotubes (CNT) deposited on a thin semi-transparent silicon membrane. The CNT had an outer diameter between 50 and 80nm and a length of 10-20 μm . The sample was prepared by depositing a drop of water/CNT mix on the surface of a 100nm thick Si membrane as show in profile in Figure 6.15. The membrane was fabricated by sputtering a 100nm thick layer of Si on the surface of a $2\times 0.6\text{mm}^2$ silicon-nitride (Si_3N_4) window previously defined in a Si wafer. The Si_3N_4 layer was subsequently removed by chemically assisted ion etching leaving only approximately 100nm thick silicon membrane. The CNT remained attached to this membrane by van der Waals forces after the water evaporated. This is schematically depicted in Figure 6.15b.

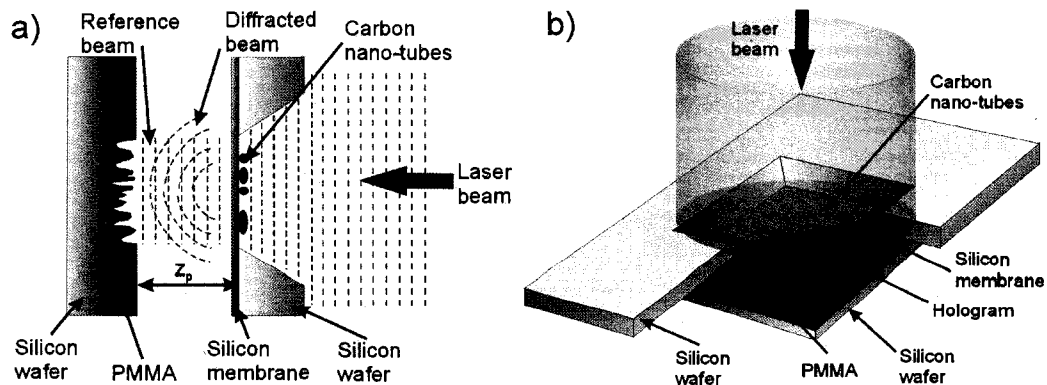


Figure 6.15. Gabor's in-line configuration for high resolution hologram recording (a). The EUV laser beam illuminates the object composed of carbon nanotubes deposited in a Si membrane. The recording medium is a high resolution photoresist. On the other side of the membrane a high resolution photoresist was placed almost in contact with the membrane ($z_p \sim$ a few micrometers). Three dimensional view of the scheme (b).

The membrane provides a convenient support for the sample with a transparency approximately 25% at $\lambda = 46.9\text{nm}$ wavelength. Figure 6.16 is a scanning electron microscope image of the nanotubes.

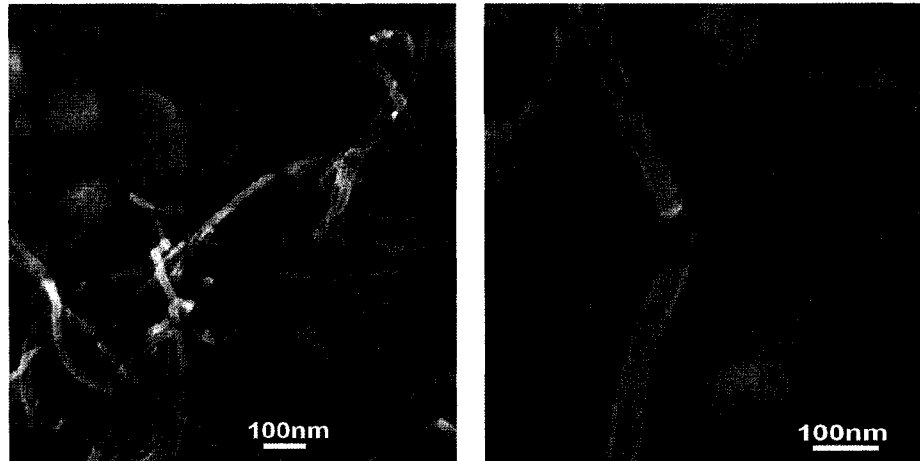


Figure 6.16. SEM images of 50-80nm diameter carbon nanotubes. The tubes were deposited on top of a thin Si membrane and used as the object in holographic imaging.

The Si membrane containing the nanotube sample was placed at a few microns ($z_p = 2.5 \div 3\mu\text{m}$) away from a Si wafer spin-coated with a 120nm thick layer of polymethyl methacrylate – PMMA photoresist. The in-line hologram was recorded directly in the photoresist. Mounting the sample in a mechanically rigid sample holder, shown in Figure 6.17, provides a robust and stable way for mounting object samples a few microns away from the photoresist. That enables high NA hologram recording permitting high spatial resolution imaging.

The CNTs were illuminated by a compact $\lambda = 46.9\text{nm}$ discharge-pumped capillary Ne-like Ar EUV capillary discharge laser described in detail in chapter 2. Sufficient doses for exposure were achieved in this experimental set up with

approximately 150 laser shots, equivalent to $53\text{mJ}/\text{cm}^2$. The exposure was kept low enough so that a linear response regime of the photoresist is maintained. In this way the holographic pattern was converted after resist developing to a height modulation in the surface of the photoresist proportional to the intensity.

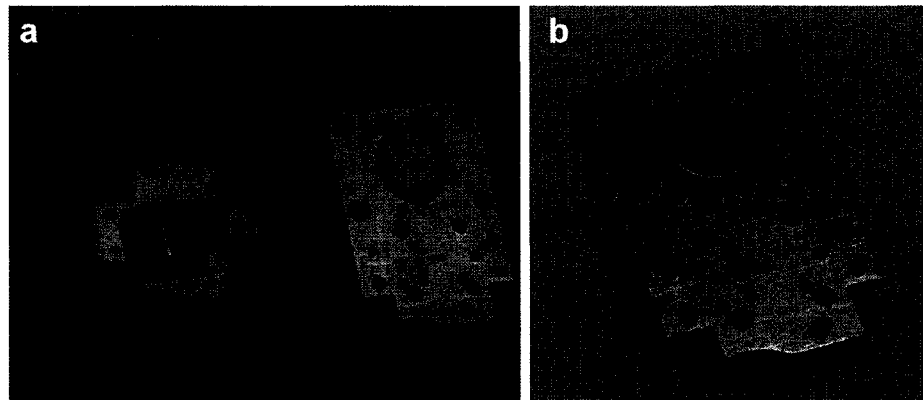


Figure 6.17. Sample holder assembly for high resolution holographic imaging. a) holder disassembled showing all the parts, b) holder assembled.

After recording the PMMA photoresist was developed using standard developing procedure mentioned in section 6.1. The hologram was digitized by scanning the surface of the photoresist with an atomic force microscope (Novascan 3D) operated in “tapping” mode. The holograms were digitized into 1024×1024 matrix with a pixel size of 9.7nm and thus a spatial extent of ~ 10 microns. The optical micrograph of the recorded hologram is shown in Figure 6.18. While in the optical micrographs it is impossible to see the hologram of the nanotubes, the higher resolution atomic force microscope readout shows clearly the complicated interference pattern. The high absorption of the EUV light in the carbon structures enabled high contrast in the interference pattern and opened the possibility to use the photoresist as a recording medium. Figure 6.19(a-c) shows several

holograms digitized with the AFM. Interference pattern is clearly visible in all the images.



Figure 6.18. Optical micrograph of the hologram recorded in the surface of the photoresist after developing procedure. Only big clusters are visible, while single nanotube holograms are impossible to see.

6.2.3 Reconstruction results

The digitized holograms are reconstructed by numerically recreating the illumination with a EUV readout wave. The digital image of the hologram processed with the Fresnel propagation code, described in detail in chapter 5, generated the reconstructed images shown in Figure 6.19(d-f).

The reconstructed in-line holograms shown in Figure 6.19 (d-f) show clearly the nanotubes. An initial assessment of the image resolution may be obtained by line-cuts through the image.

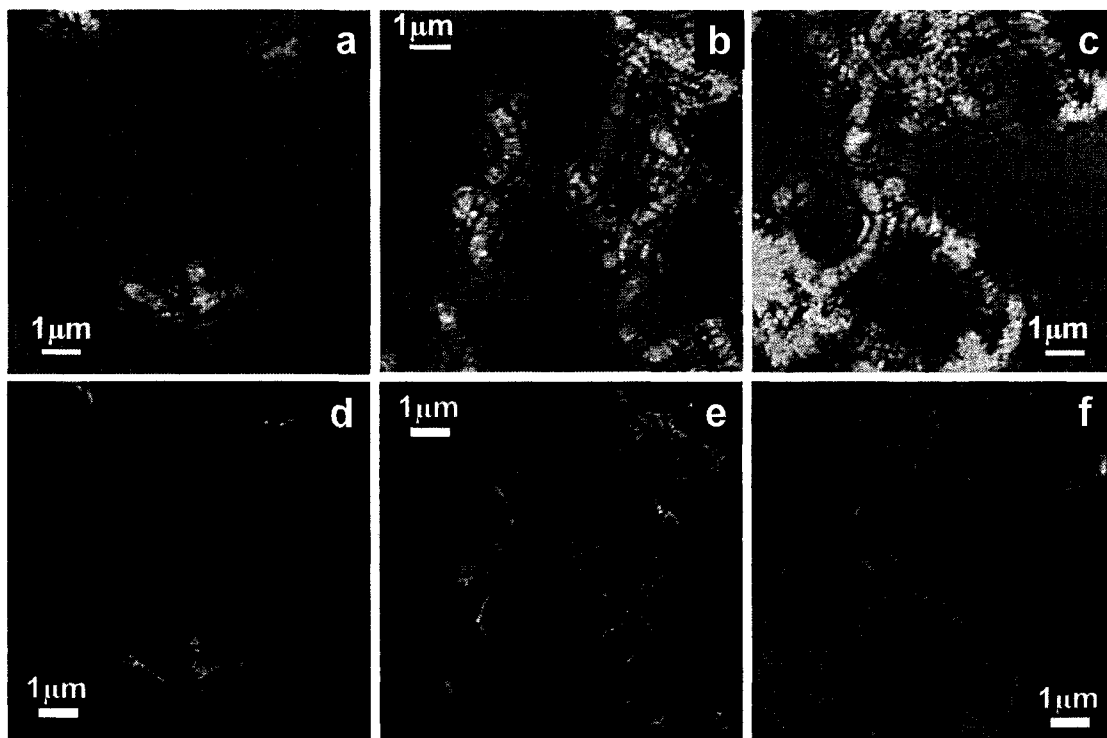


Figure 6.19. Holograms (a to c) and reconstructed images (d to f) of 50-80nm diameter carbon nanotubes. The holograms were obtained by digitizing of the small area of the photoresist with AFM showing the complicated interference pattern stored in the photoresist surface. In the reconstructed images, single nanotubes and clusters of nanotubes are depicted.

An example of such a line-cut indicated in Figure 6.20a is shown in Figure 6.20b. This cut was realized in a region where a “plateau” in the maximum and minimum intensities was clearly reached to recreate the knife edge resolution test. Taking the 10-90% rise of the intensity along an edge of the line-cut image yields an estimate of the spatial resolution approximately 46nm. Other cuts realized in different points of the image indicated a resolution 45.8 ± 1.9 nm where the error was determined by the spread of the different measurements.

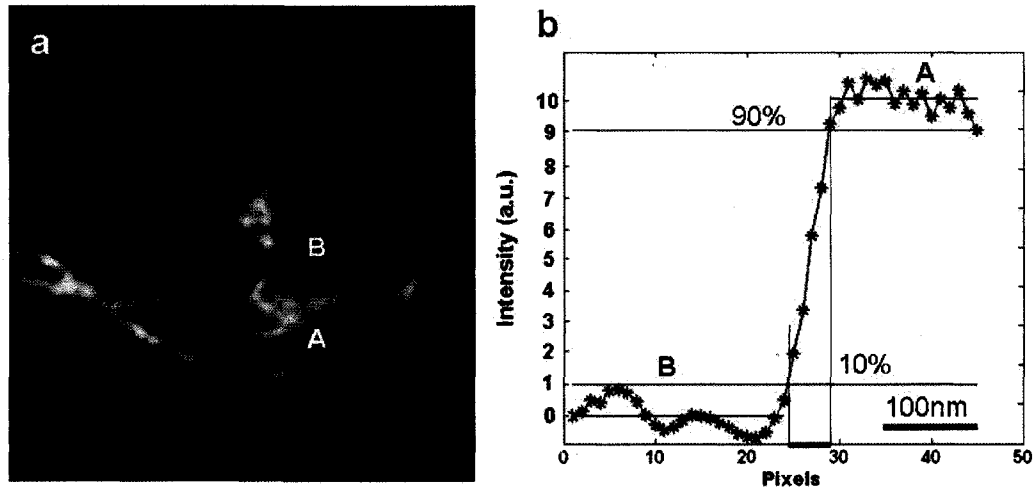


Figure 6.20. Knife edge test applied to estimate the resolution of the image a). The intensity lineout through the image from A to B is shown in b) indicating a 10-90% intensity modulation over approximately 4.5 pixels, corresponding to 45.8nm.

6.2.4 Resolution limitations in wavelength resolution holography

The relative bandwidth of the EUV laser is approximately $\Delta\lambda/\lambda \approx 10^{-4}$, resulting longitudinal coherence length of the laser equal to $l_c = 470\mu m$. This limits the Rayleigh resolution to 28.6nm, because $z_p \ll l_c$. The spatial coherence defined by the coherence radius of the capillary discharge laser, measures at 75cm away from the capillary exit, was equal to $R_c = 340\mu m$, [6.11, 6.12] and because it is also much larger than z_p the spatial coherence also limits the Rayleigh resolution to 28.6nm.

If one assume, that the reasonable scanning size for the AFM digitization of the hologram will be $D = 10\mu m$ with 1024 points per scan line then the numerical aperture limited by the digitization will equal to $NA = 0.894$. This will limit the Rayleigh resolution to be $\sim 32\text{nm}$. The AFM pixel size defined as a ratio between the scan width

and number of pixels per line will be equal to 9.7nm. Another AFM limiting factor is the probe diameter of 20nm. The recording medium – photoresist has resolution defined by the narrowest possible line written in the photoresist with photons to be approximately 19nm [6.13]. This resolution is comparable to the AFM pixel size and is much better than the resolution limited by the coherence of the source and the digitization process.

6.2.5 Simultaneous estimation of resolution and feature size

To obtain a more rigorous and global assessment of the imaging spatial resolution and simultaneously to estimate the feature size, a correlation analysis of the reconstructed holograms was developed [6.14]. This method is based on the correlation between the image and a template generated from a “master binary” image (pixels with values zero and one). The method described in this section allows for simultaneous determination of the image resolution and the feature size in the images where the feature size has a constant value. Similar in concept to the method described in section 6.1.4 it is based on the correlation between the data image and the set of templates with various resolutions. Three major differences however were made: the way the resolution of the images was adjusted by continuously variable Gaussian filter width, the subroutine to find the feature size and finally the way the master template is generated.

Previously the resolution of the secondary templates was adjusted in controllable way by applying the wavelet decomposition method. In each decomposition step the resolution was changed by a factor of two. That created a sparse sequence of the templates with the resolutions decreasing by a factor 2^X where X is the wavelet order.

This scaling didn't allow to set the resolution of the template precisely. In this method the wavelet decomposition was replaced by the Gaussian filter with a variable width. This approach allows to change the resolution of the secondary templates more precisely than the wavelet decomposition algorithm.

The binary master template was generated based on the reconstructed image of the object. By applying a skeletonizing algorithm [6.16], a representation of the object one pixel wide was obtained. In the previous method described in section 6.1.4.5 the master template was generated manually based on the previous knowledge of the object. In this algorithm the master binary template was generated using the skeletonizing algorithm followed by a convolution, thus the previous knowledge about the object is not required and the process of the template generation is automatic.

Finally the subroutine to find the feature size was added by employing the convolution between the skeleton image and circular templates with variable radii. This allowed to change the second parameter in the set of templates that is the feature size. Previously one dimensional set of templates now is 2-D (resolution vs. feature size) thus after the 2-D correlation is performed allows to assess both the resolution and the feature size in the image.

6.2.5.1 Gaussian filtering process

A sub set of templates with decreasing resolution was obtained by applying a Gaussian filter of increasing width. Filtering the binary image causes a blurring that increases the size of the features in the image and reduces the resolution by a factor

inversely proportional to the filter width w_f . In the spatial frequency domain this is equivalent to reduction of the image spectrum by the same factor. The full width at half maximum (FWHM) of the Gaussian filter necessary to apply to the image with pixel size w_0 in order to obtain a given resolution δ is [6.14]:

$$w_f(\delta) = w_0 \sqrt{\left(\frac{\delta}{w_0}\right)^2 - 1} \quad (6.5)$$

A detailed description of this derivation is in Appendix II.

6.2.5.2 Correlation methods tests

Different tests were designed to characterize the developed algorithm. In the first test the capability of the 2D correlation to compare and find the best match between the images was tested. The flowchart of the test is depicted in Figure 6.21.

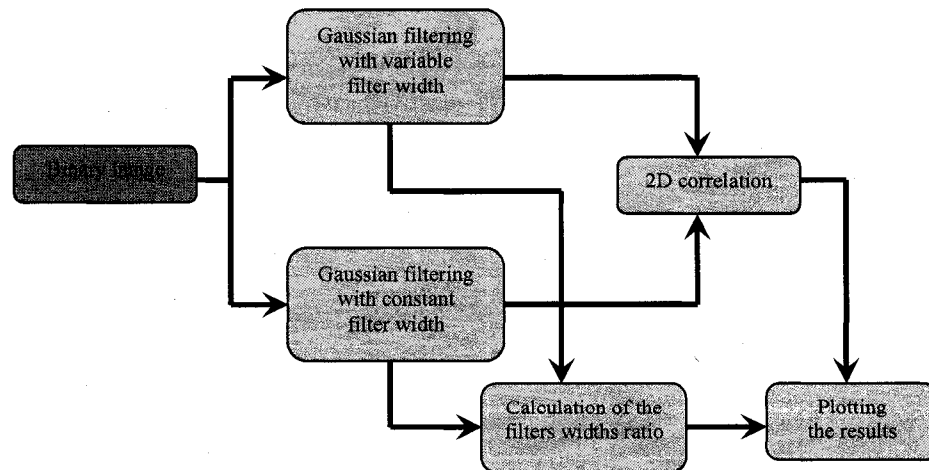


Figure 6.21. Testing the capability of the 2D correlation to compare and find best match between the images.

The approach is very simple. An arbitrary binary image was filtered by a Gaussian filter with constant width Δ to set one arbitrary resolution. The same image was also filtered by Gaussian filters with different widths. The filter width ratio was then calculated between variable Gaussian filter and Δ . The image filtered with the Gaussian filter with constant width Δ was 2-D correlated with the set of images obtained from the variable filters. The correlation coefficient was plot as a function of the filter widths ratio. Different binary images were used to test this part of the algorithm, as shown in Figure 6.22(a-d) to see if the correlation is capable to find the similarity in the images. Applying the Gaussian filter reduces the resolution of the image.

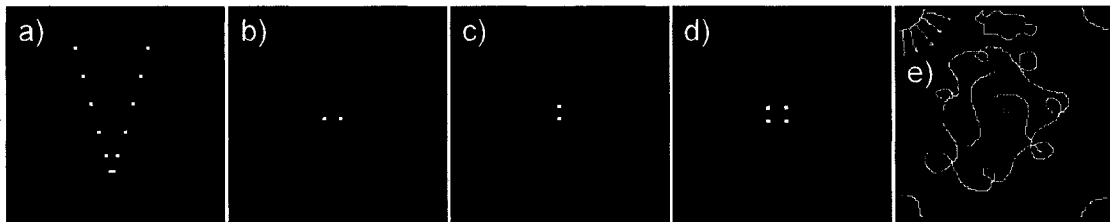


Figure 6.22. Different binary images used for testing the correlation part of the code. Images a-d are magnified for better appearance. All dots are 1 pixel. a) variable dot separation, b) horizontal dots, c) vertical dots, d) four dots, e) arbitrary image with four dots in the center.

Figure 6.23a shows an arbitrary shaped binary image with one pixel width and consequently one pixel resolution. By applying the Gaussian filter this image is degraded in resolution to 50nm (Figure 6.23b) and to 100nm (Figure 6.23c).

Figure 6.24 shows the plot of the correlation coefficients as a function of the filter width ratio. As expected the correlation maximum is equal to one for all input images in the case of filter width ratio equal to one.

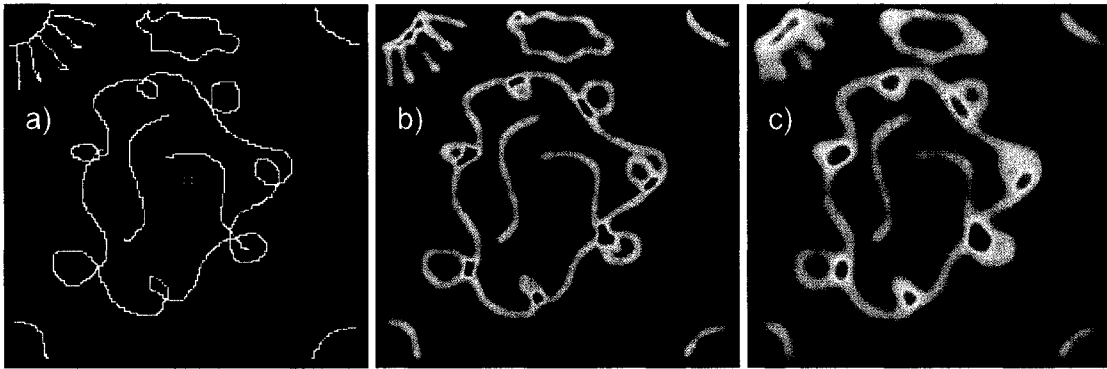


Figure 6.23. Applying the Gaussian filter with various widths to decrease the resolution of the binary image. a) binary arbitrary shape image, b) resolution set to 50nm, c) resolution set to 100nm, when one pixel is 10nm.

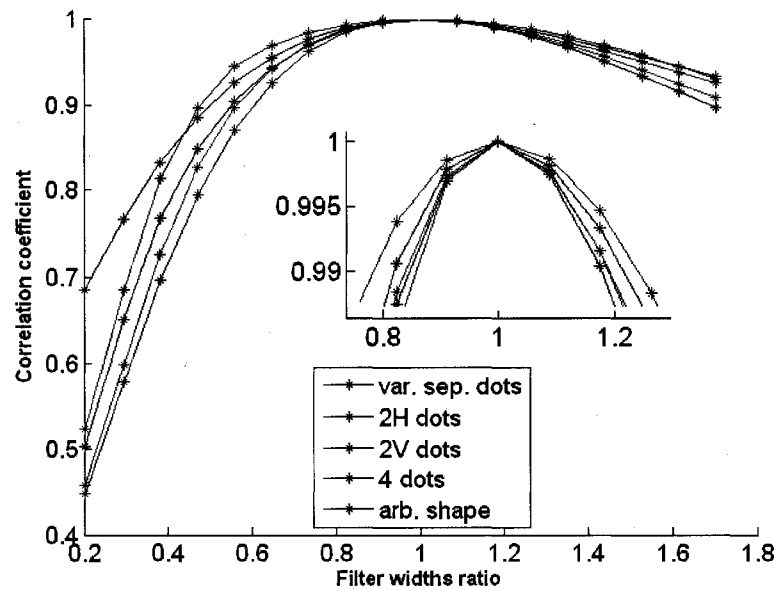


Figure 6.24. Correlation coefficient as a function of the filter width ratio for different binary test images. The maximum of the correlation coefficient is equal to one for all tested input images and, as expected, for filter width ratio equal to one.

The second test was design to investigate if the correlation algorithm is capable to distinguish between different resolutions in the same image. The flowchart for this test is depicted in Figure 6.25. The procedure is very similar to the first test, however instead of applying a single Gaussian filter, two Gaussian filters with constant widths w_1 and w_2

are applied to two parts of the binary image. These two parts are recombined to make a single template image. The test image used is depicted in Figure 6.26a. This is also a binary image with the resolution set by the pixel size that in this example is 10nm. The results of applying the Gaussian filter with different widths to different parts of the test image are depicted in Figure 6.26b. The resolution of the left part of the image was set to be approximately 32nm while the resolution of the right part was set by changing the Gaussian filter width appropriately to be 87nm. The binary image used to make this template (Figure 6.26a) was also filtered by the Gaussian filter with variable width resulting in the resolution decrease from 12 to 97nm. A few examples of the filtering process are depicted in Figure 6.27. The progressive lost of details in the images is observable. These images were in turn correlated with the template image shown in Figure 6.26b and the correlation coefficient as a function of the resolution set by the Gaussian filter width was obtained. This is presented in Figure 6.28.

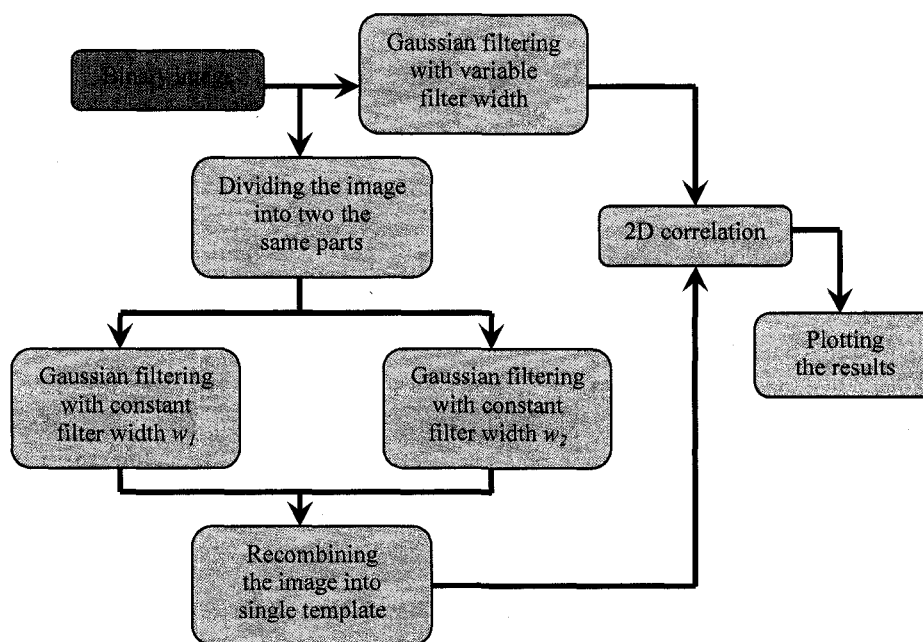


Figure 6.25. Testing the capability of the correlation code to distinguish between different resolutions in the processed image.

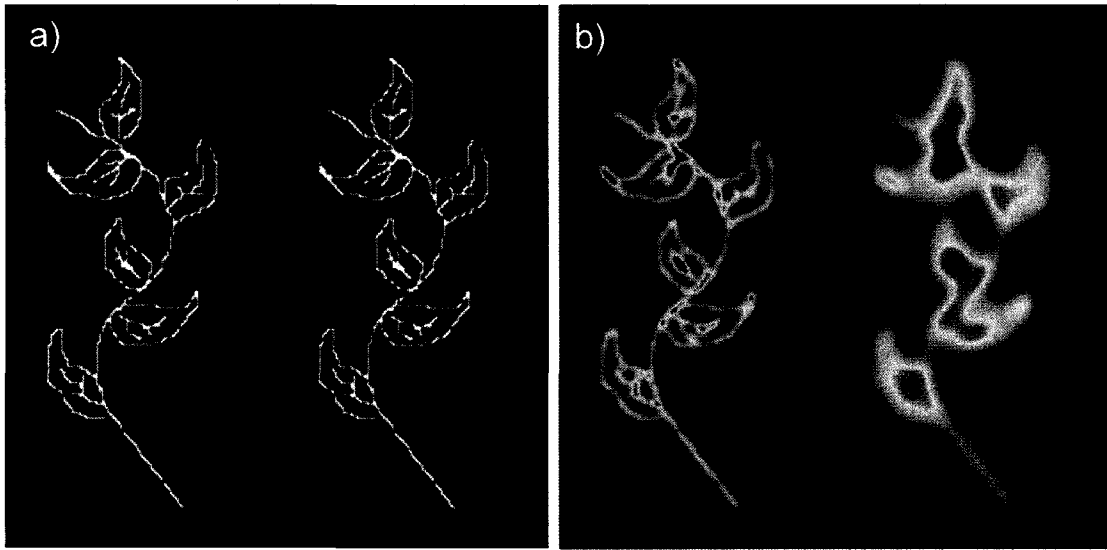


Figure 6.26. Template image for the multiresolution test a) and the result of applying Gaussian filter with two different widths to the different part of the test image b). Left image resolution was set to be 32nm and right has 87nm resolution.

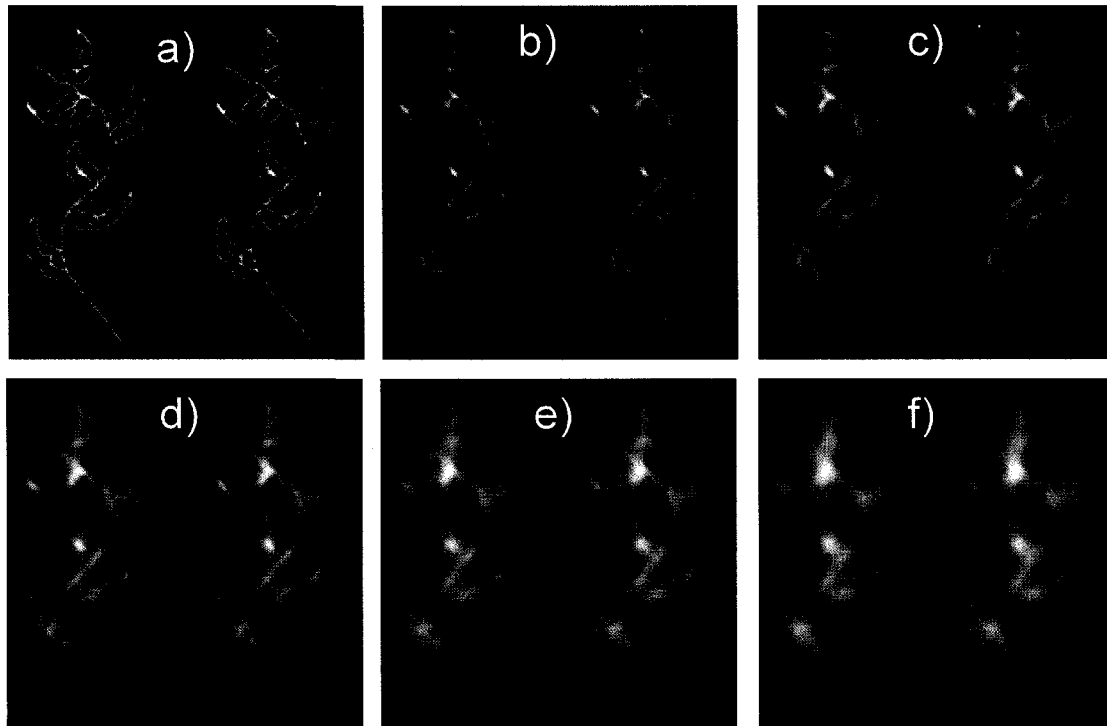


Figure 6.27. The results of applying Gaussian filter with variable width to the test image, Figure 6.26a) resulting in resolution decreasing. Resolution was set to be 12nm – a), 27nm – b), 42nm – c), 57nm – d), 72nm – e) and 87nm – f).

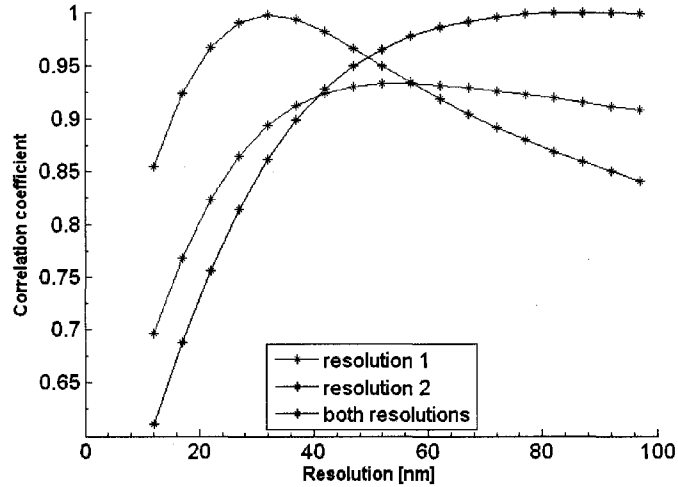


Figure 6.28. Correlation coefficient as a function of the resolution showing the averaging effect of the correlation algorithm.

When the template image has both resolutions simultaneously (32nm and 87nm), as depicted in Figure 6.26b the correlation coefficient never reaches unity, having a maximum at resolution 57nm showing that the resolution of this template is between the values of true resolutions. This is like averaging property of the correlation algorithm and means, that the algorithm always considers the image as a whole and assesses the global value of the resolution.

6.2.5.3 Correlation and convolution algorithm

The simplified flowchart of the algorithm is depicted in Figure 6.29. To explain how the algorithm works the reconstructed image of the single carbon nanotubes was used. The algorithm executes by applying the following procedures.

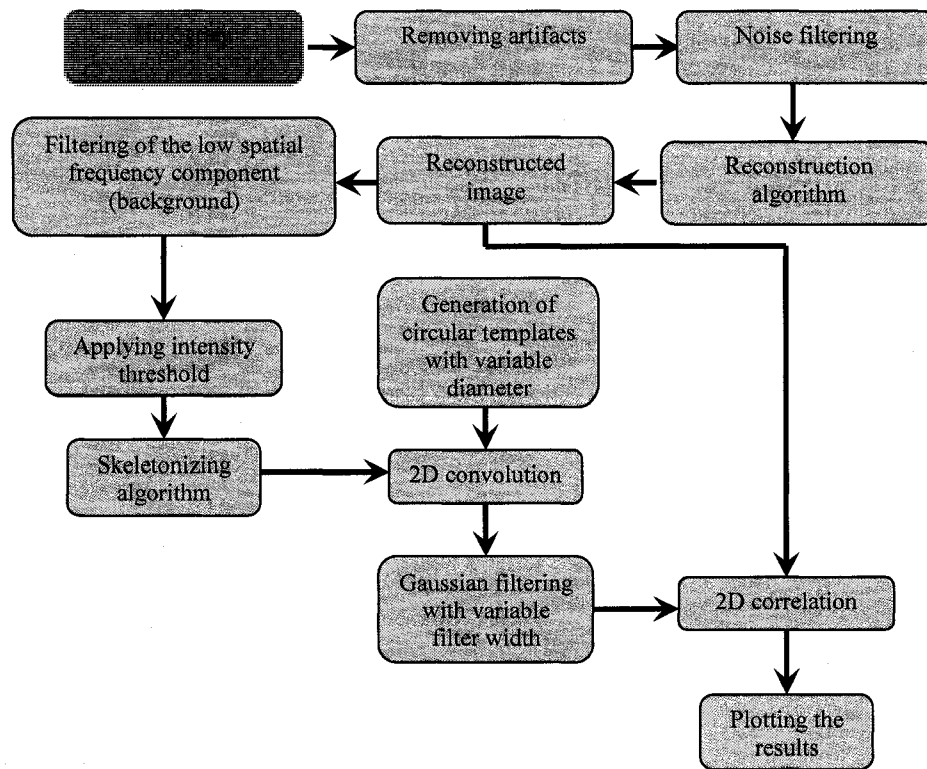


Figure 6.29. Algorithm designed for resolution and feature size estimation from reconstructed images in EUV holographic imaging of carbon nanotubes.

First the reconstructed image is filtered in the frequency domain to remove the low spatial frequency components. Figure 6.30a is the filtered image of a nanotube. Second an intensity threshold is applied to the image to obtain a homogeneous background. The value of the applied threshold is arbitrarily adjusted to eliminate the fluctuations in the background and simultaneously to keep the object profile unchanged. The threshold value does not change the ultimate result of the algorithm because this step is only used for the construction of the reference template. Third, the image is “skeletonized” using the algorithm described in [6.15, 6.16]. The skeletonizing algorithm produces a 1 pixel wide contour that follows the nanotube shape and is shown in Figure 6.30b. Fourth, the skeleton is convolved with K different circular templates with different

radii. The set of circular templates is shown in Figure 6.30c. The convolution of the circular templates with the skeleton generates a set of K templates that resembled the image of the nanotube, each one with different thickness. All the templates generated in this manner are also “binary” images, with pixel values equal to zero or one. Figure 6.30d shows one of these binary templates obtained by convolution of the skeleton with one of the circular template. Fifth, the K templates are degraded in resolution by applying L Gaussian filters with different FWHM and generate from each of the K binary templates, another sub-set of L templates with different resolutions.

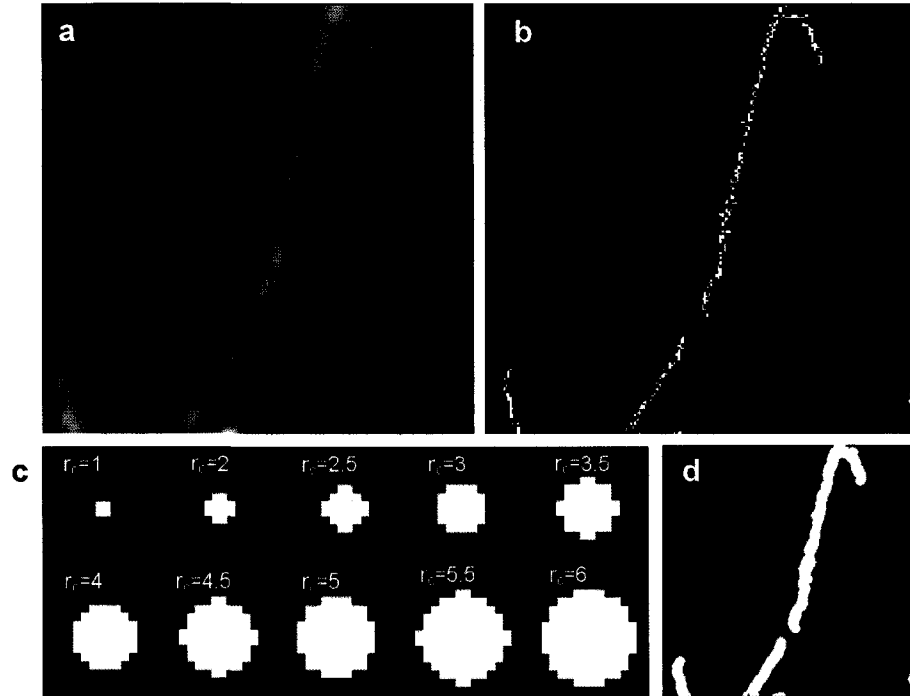


Figure 6.30. Description of the convolution procedure responsible for making the templates with various thicknesses. a) The image is filtered to remove the low frequency background fluctuations. b) With a skeletonizing algorithm the position of the nanotube is found. c) Various radii circles are convolved with the skeleton image to simulate the change of the tube diameter. d) High resolution template of the nanotubes (binary image) with given tube diameter $D_t=2r_c$.

The whole procedure produced a $K \times L$ set of templates of the nanotube image. Figure 6.31a shows one of the binary templates, that after the convolution with the

Gaussian filter generated a degraded resolution template as the one shown in Figure 6.31b. Finally the $K \times L$ templates were individually correlated with the original image shown in Figure 6.30a and $K \times L$ correlation coefficients were obtained.

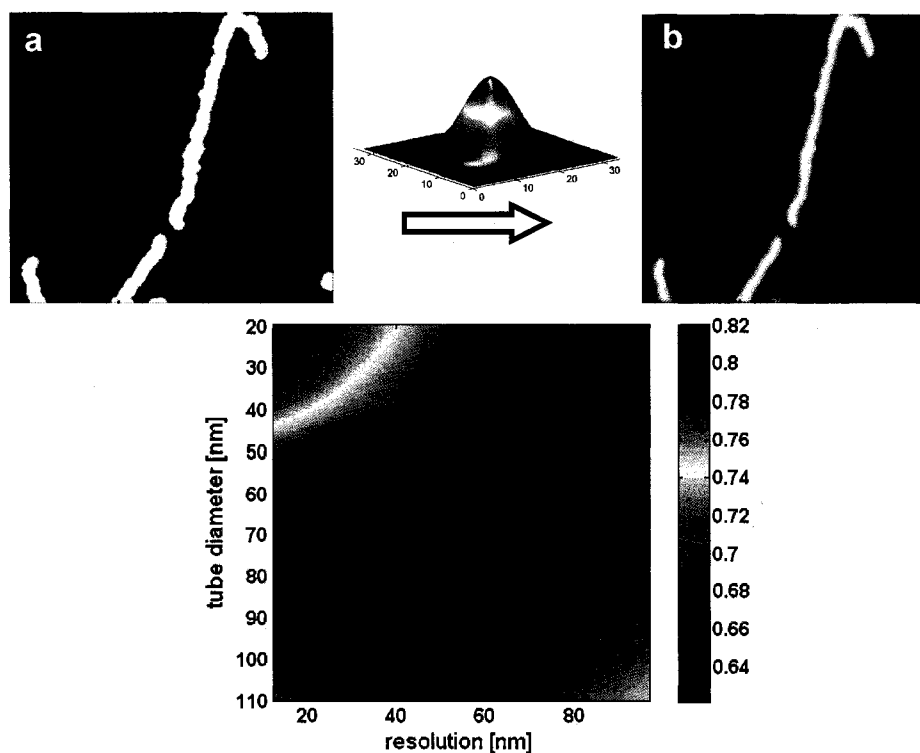


Figure 6.31. Description of the correlation code used to obtain the correlation coefficient to assess the image resolution and feature size. a) Template with a given thickness is convolved with a 2D Gaussian filter to obtain a degraded resolution template b). This template is correlated with original data image to construct a 2D plot in the resolution/tube diameter space shown in c). Both the resolution and tube diameter are found by localizing a global maximum in this plot.

The linewidth of the nanotubes was ranging from 1 to 6 pixels, that corresponds to tube diameters from 19.4 to 116.4nm and the resolution was ranging from 12 to 100nm. Figure 6.31c is a plot of the correlation coefficients in the $K \times L$ dimensional space corresponding to the K different template thicknesses and the L different resolutions. This plot has a global maximum that determines the feature size (the

nanotube diameter) and the resolution of the image: the nanotube diameter equals to 70.6nm and the spatial resolution equals to 45.5nm. The values obtained from this analysis compare very well with the expected diameter of the nanotubes used as the object (50-80nm, normal distribution) and also with the measured diameters obtained from the SEM images. The resolution also compares very well with the value obtained by the direct knife edge test 45.8nm.

6.2.5.4 Correlation and convolution algorithm results

The correlation and convolution algorithm was also used to estimate the resolution and the tube diameter for a smaller reconstructed image obtained as a sub image of the image in Figure 6.30a. The results of the calculations are depicted in Figure 6.32:

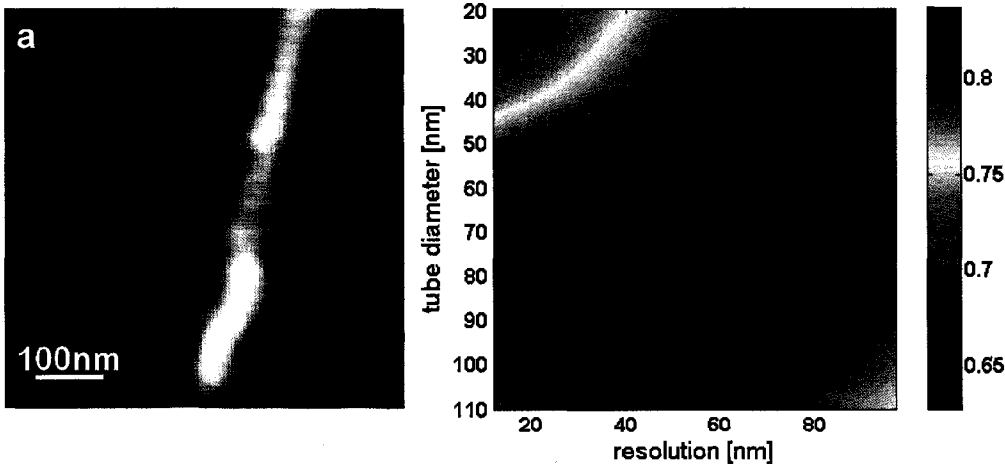


Figure 6.32. Resolution and feature size estimation using the correlation algorithm for sub image a) obtained from Figure 6.31c), the localization of the global maximum in the correlation coefficient plot b).

The sub image obtained from Figure 6.30a is depicted in Figure 6.32a. This is the central portion of the previous figure. The localization of the global maximum in the correlation coefficient is depicted in Figure 6.32b and shows that the nanotube diameter was found to be equal to 70.6nm and the spatial resolution equal to 47.5nm. As one can expect from analyzing the same image, only smaller portion of it, the results are not far off. The tube diameter was found to be exactly the same while the resolution value is different by 2nm.

Different hologram was also analyzed to check the consistency of the results. The small section of the reconstructed hologram is depicted in Figure 6.33a.

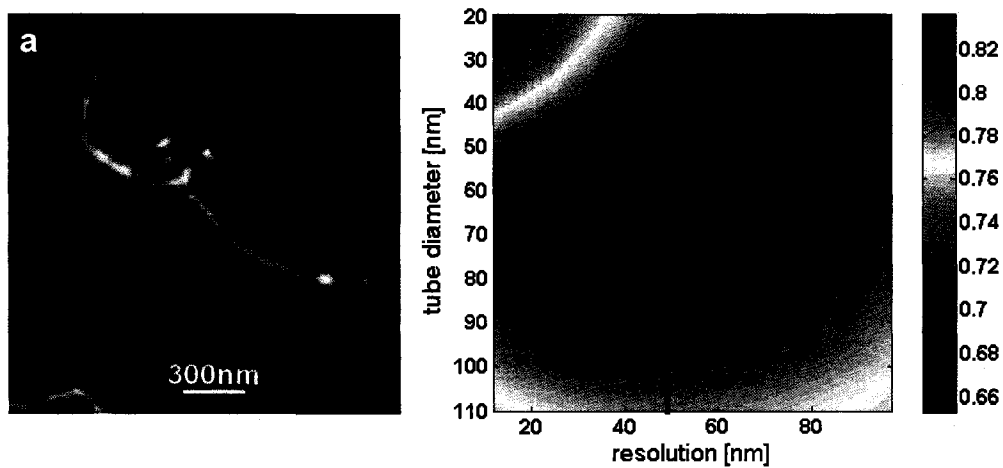


Figure 6.33. Resolution and feature size estimation using the correlation algorithm for different reconstructed image a), the localization of the global maximum in the correlation coefficient plot b).

Figure 6.33b shows the localization of the global maximum of the correlation coefficient. The nanotubes diameter was found to be 56.1nm and the image resolution 48.8nm. As a remainder the tubes used for imaging were in the diameter range $50 \div 80nm$ and the resolution obtained is also very close to the expected value and compares well with the

previous estimations. Table 6.2 summarizes the resolution and feature sizes estimated using Gaussian filtering and correlation analysis.

Table 6.2. Summary of the results for high resolution EUV holographic imaging using carbon nanotubes as the object for three different reconstructions.

Parameter	Reconstruction 1 (Figure 6.31)	Reconstruction 2 (Figure 6.32)	Reconstruction 3 (Figure 6.33)
Nanotube width [nm]	70.6	70.6	56.1
Resolution from the algorithm [nm]	45.5	47.5	48.8

A detailed explanation of the relation between the resolution and the FWHM of the Gaussian filter can be found in Appendix II.

6.3 Summary

Two holograms were recorded in the surface of PMMA at different separations (~4mm and ~0.12mm) to compare the results. The spatial resolution of the image obtained by numerical reconstruction was estimated utilizing the wavelet image decomposition and image correlation. Calculations were done for different reconstruction distances and for different wavelet orders to estimate the resolution of both holograms and to find the optimum reconstruction distances in each case. Also different wavelets used for wavelet decomposition were studied indicating the robustness of the algorithm at low wavelet orders.

Holographic imaging with spatial resolution comparable to the illumination wavelength was also presented in detail. Combining the advantages of short wavelength

EUV lasers with high resolution recording medium such as a photoresist enables holographic imaging maintaining sub-50nm resolution. The field of view is limited by the AFM scan size and consequently can be increased while the resolution in our case was limited by the wavelength of illumination. The assessment of the resolution of the reconstructed images and the nanotubes diameter was done by employing convolution and correlation algorithm based on the extensive comparison between the reconstructed image and the set of template images. This algorithm can be applied to any images providing the reference value as in most cases can be the pixel size of the investigated image or the field of view.

The method to assess the resolution and the feature size in the digital image was demonstrated. A property of the algorithm is that it considers the image as a whole and averages all the fluctuations in both parameters. For some applications this might be an obvious advantage.

-
- [6.1] J. M. Heck, D. T. Attwood, W. Meyer-Ilse, E. H. Anderson, "Resolution determination in X-ray microscopy: an analysis of the effects of partial coherence and illumination spectrum", *Journal of X-Ray Science and Technology* **8**, 95 (1998)
- [6.2] P. W. Wachulak, R. A. Bartels, M. C. Marconi, C. S. Menoni, J. J. Rocca, Y. Lu, B. Parkinson, "Sub 400 nm spatial resolution extreme ultraviolet holography with a table top laser", *Optics Express* **14**, 21, 9636 (2006)
- [6.3] P. W. Wachulak, M.C. Marconi, R. A. Bartels, C. S. Menoni, J.J. Rocca, "Volume extreme ultraviolet holographic imaging with numerical optical sectioning", *Optics Express* **15**, 17, 10622 (2007)
- [6.4] P. W. Wachulak, M. C. Marconi, R. A. Bartels, C. S. Menoni and J. J. Rocca, "Numerical Optical Sectioning for 3D Holographic Images with EUV Lasers", *Optics & Photonic News* 2007, special issue *Optics in 2007* **18**, 12 (2007)
- [6.5] R. A. Bartolini, "Characteristics of relief phase holograms recorded in photoresist", *Applied Optics* **13**, 129 (1974)
- [6.6] B. R. Benware, C.D. Macchietto, C.H. Moreno, J.J. Rocca, "Demonstration of a high average power tabletop soft X-ray laser", *Physical Review Letters* **81**, 5804 (1998)
- [6.7] J. Nunez, X. Otazu, M.T. Merino, "A multiresolution-based method for the determination of the relative resolution between images: First application to remote sensing and medical images", *International Journal of Imaging Systems and Technology* **15**, 225 (2005)
- [6.8] M. F. Crommie, C.P. Lutz, D.M. Eigler, "Confinement of Electrons to Quantum Corrals on a Metal Surface", *Science* **262**, 218 (1993)
- [6.9] N. L. Abbott, J.P. Folkers, G.M. Whitesides, "Manipulation of the Wettability of Surfaces in the 0.1 micrometer to 1 micrometer Scale Through Micromachining and Molecular Self Assembly", *Science* **257**, 1380 (1992)
- [6.10] P. W. Wachulak, M.C. Marconi, R. A. Bartels, C. S. Menoni, J.J. Rocca, "Soft x-ray laser holography with wavelength resolution", *J. Opt. Soc. Am. B*, **25**, 11, 1811 (2008)
- [6.11] Y. Liu, M. Seminario, F.G. Tomasel, C. Chang, J.J. Rocca, D.T. Attwood, "Achievement of essentially full spatial coherence in a high-average-power soft-x-ray laser", *Physical Review A* **6303**, 033802 (2001)

-
- [6.12] Y. Liu, M. Seminario, F.G. Tomasel, C. Chang, J.J. Rocca, D.T. Attwood, "Spatial coherence measurement of a high average power table-top soft X-ray laser", *Journal de Physique Iv.* **11**, 123 (2001)
- [6.13] H. H. Solak, D. He, W. Li, S. Singh-Gasson, F. Cerrina, B. H. Sohn, X. M. Yang, P. Nealey, "Exposure of 38 nm period grating patterns with extreme ultraviolet interferometric lithography", *Applied Physics Letters* **75**, 15, 2328 (1999)
- [6.14] P.W. Wachulak, C.A. Brewer, F. Brizuela, C.S. Menoni, W. Chao, E.H. Anderson, R. A. Bartels, J.J. Rocca, M.C. Marconi, "Analysis of extreme ultraviolet microscopy images of patterned nanostructures based on a correlation method", *J. Opt. Soc. Am. B* **25**, 7, B20 (2008)
- [6.15] T. Yatagai, M. Idesawa, Y. Yamaashi, M. Suzuki, "Interactive Fringe Analysis system- Applications to Moire Contourogram and interferogram", *Optical Engineering* **21**, 901 (1982)
- [6.16] T. Yatagai, S. Nakadate, M. Idesawa, H. Saito, "Automatic fringe analysis using digital image processing techniques", *Optical Engineering*, **21**, 432 (1982)

CHAPTER 7

7 3D reconstruction by numerical sectioning

7.1 Introduction

In this section a proof of principle experiment in which three dimensional imaging in a volume was obtained from a single high numerical aperture (NA) hologram will be discussed. The three dimensional images were obtained from Gabor holograms recorded in a photoresist after exposure with a table-top EUV laser. Digitized holograms were numerically reconstructed over a range of image planes by numerically sweeping the reconstruction distance, resulting in the numerical optical sectioning of the object.

7.2 Experimental details

The experimental set up is schematically illustrated in Figure 7.1. A compact $\lambda = 46.9\text{nm}$ table top discharge-pumped capillary Ne-like Ar laser was used for recording the hologram. The laser source was described in detail in chapter 2.

The test object used in the holographic volume imaging experiment consisted of a tilted metallic surface covered with opaque spherical markers. This test object was

fabricated placing a 100nm thick aluminum foil covering a hole 1.5mm in diameter made in a 80 μ m thick Mylar sheet.

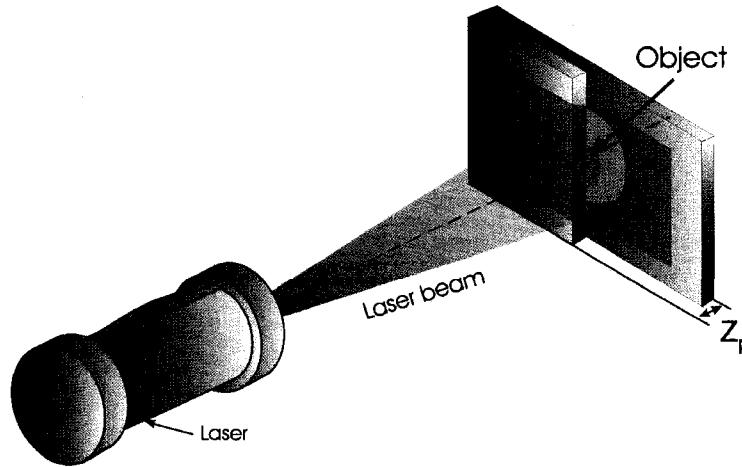


Figure 7.1. Scheme of the experimental set up.

The hole was partially covered with a second Mylar sheet 80 μ m thick, as schematically indicated in Figure 7.2. The aluminum foil contours over the semicircular aperture to produce a variable height surface with the desirable characteristics for this test.

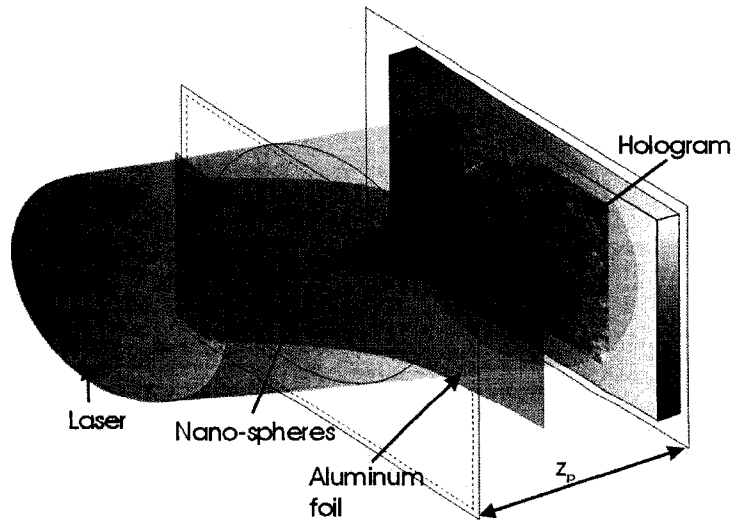


Figure 7.2. Detailed scheme of the test object used in volume holographic imaging.

The 100nm aluminum foil has a theoretical transmission of approximately 80% at $\lambda = 46.9nm$ but due to the layer of native oxide [7.1] the transmission was reduced to ~35%. The Al filter also suppresses the lower photon energy plasma emission (i.e., long wavelength background) from the Ar discharge in the laser source. In Figure 7.3 the transmission of a 100nm thick aluminum film is plotted as a function of the wavelength. Wavelengths above $\lambda = 70 \div 80nm$ (UV and visible light from plasma emission) are efficiently attenuated by the aluminum filter.

The object was prepared by placing a drop of water with a suspension of latex spheres, 465nm in diameter [7.2] on the aluminum foil membrane. Evaporation of the water left a random distribution of latex spheres deposited over the partially transparent tilted Al foil membrane. These spheres are completely opaque to the 46.9nm EUV laser radiation. With this procedure, these markers are distributed at locations yielding a range of distances from the photoresist where the holograms are subsequently recorded.

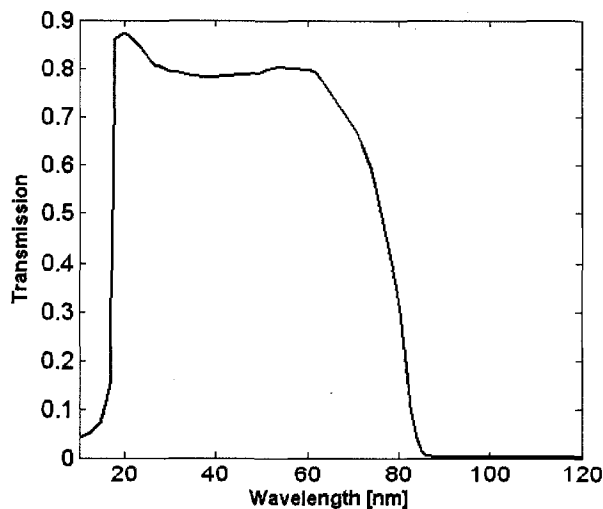


Figure 7.3. Transmission of the 100nm thick pure aluminum foil (based on calculations from [7.1]).

The holograms were recorded by exposing a 120nm thick layer of PMMA spin-coated on a silicon wafer to the Gabor hologram interference pattern produced by the illuminating EUV laser beam. To activate PMMA with 46.9nm radiation exposure required is in the range of $\sim 2 \times 10^7$ photons/ μm^2 . With the energy $\sim 130\mu\text{J}$ per pulse exposure required approximately 240 laser shots, equivalent to a 4 minutes exposure time at the repetition rate employed in this experiment. After exposure, the photoresist was developed using standard developing procedure.

7.3 Results

During the recording phase of the Gabor holography, the exposure was carefully adjusted so that the photoresist operated in a linear response regime. This is important since a nonlinearity of the recording medium may lead to artifacts in the reconstructed images. The holographic interference pattern generated by the reference and the object beams was recorded in the photoresist and converted to a surface modulation after the developing procedure similarly as in the experiment described in chapter 6. In order to numerically reconstruct the holograms, the surface modulation was digitized with a Novascan 3D AFM operated in “tapping” mode. A hologram digitized in this manner is displayed in Figure 7.4a.

The reconstruction of the hologram is based on a numerical Fresnel propagator [7.3-7.5]. The Fresnel propagator reconstruction algorithm was discussed in detail in section 5.5.

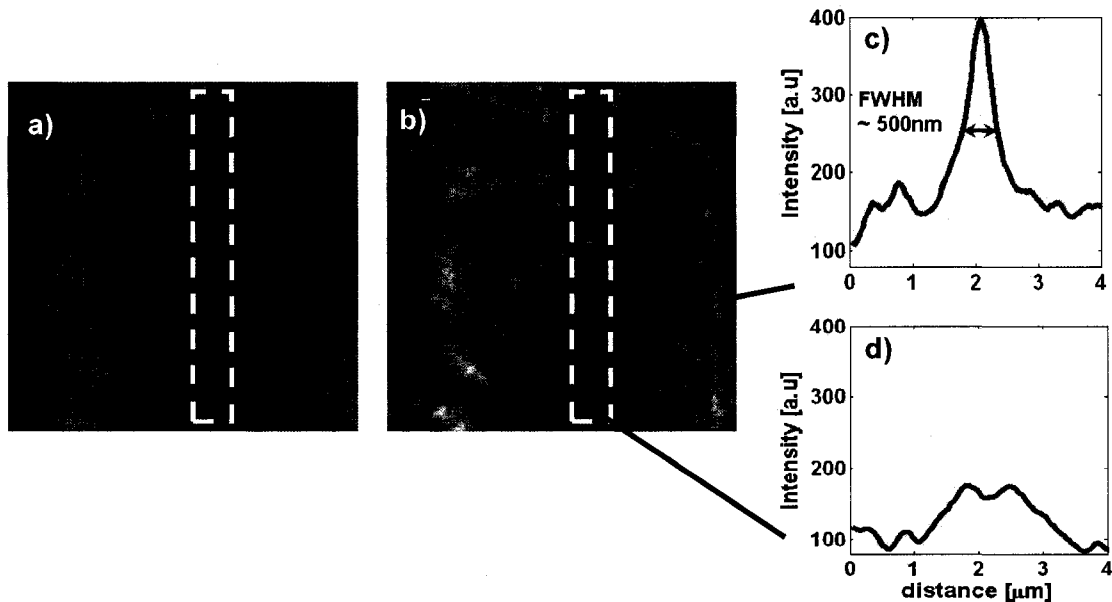


Figure 7.4. a) Hologram of the 3-D object with a random distribution of 465nm diameter latex spheres (markers) over the tilted surface of an Al foil recorded in the photoresist surface and digitized with an atomic force microscope. b) Digital reconstruction of the hologram. Intensity cuts in the vertical direction of one “in focus” marker c) and one “out of focus” marker d). The white dotted lines indicate the region in the reconstruction that is “in focus”.

Figure 7.4a shows a small section of the hologram with an area $42 \times 42 \mu\text{m}^2$. The numerical reconstruction of the hologram using a Fresnel propagator provided images of the object described above and schematically shown in Figure 7.2. One of the critical parameters in the reconstruction code is the distance between the recording medium and the object, indicated in the diagram of Figure 7.2 as z_p . Small changes in z_p reconstructs slightly different images. To determine the value of z_p corresponding to the optimum reconstruction, an image correlation technique was utilized similar to the algorithm used for resolution estimation for the imaging of the AFM tips discussed in chapter 6.

To demonstrate the retrieval of the depth information from the hologram the reconstruction code was executed with the digitized image of the hologram shown in Figure 7.4a for different values of the distance z_p . The different runs produced different

reconstructed images in which the latex spheres markers located at the correct z_p generated a sharper image than those markers “out of focus”. Figure 7.4b shows one of these reconstructed images. In this case the reconstruction is optimum for a distance z_p that matches the height of the central part of the hologram, indicated in the figure by a white dotted box. In this box the height is such that the markers located in this region reconstruct “in focus”, while the latex spheres above and below this level are reconstructed blurred. This can be observed in Figure 7.4(c, d) where the intensity profiles obtained in a vertical cut of one “in focus” marker (c) and one “out of focus” marker (d) are plotted. By changing z_p in the reconstruction code only the latex sphere markers located at a height equal to z_p produced sharper images as compared to those markers out of focus. This is also depicted in more detail in Figure 7.5a, where a small region of the hologram was reconstructed at different distances z_p between $160\mu\text{m}$ and $174\mu\text{m}$.

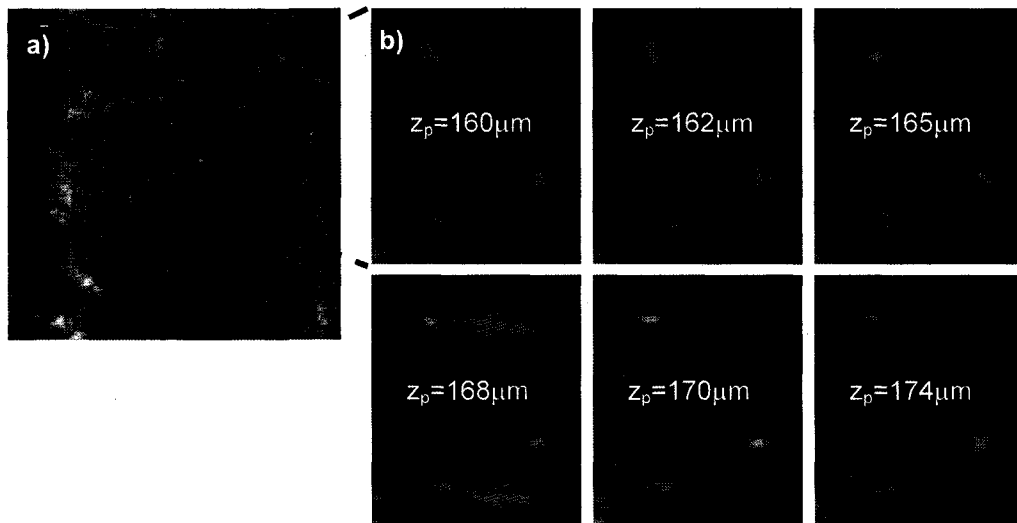


Figure 7.5. Reconstruction of the small portion of the hologram of the tilted surface with markers on the top a). Magnified regions of the reconstructed image at different reconstruction distances b). Arrows indicate markers close to the sharpest image, in focus.

One can see in Figure 7.5b that by changing the reconstruction distance the image of two markers is sharp close to $168\mu\text{m}$ (orange arrows) while a third one (indicated by green arrow) produces the sharpest image at approximately $170\mu\text{m}$. This is similar effect to an optical sectioning but performed on a digitally reconstructed image [7.6, 7].

In order to retrieve the depth information coded in the hologram in a systematic way, another algorithm was developed to help track all the markers and their three dimensional positions.

7.4 Retrieving 3-D information from a single high NA hologram

The depth information in the hologram can be retrieved varying the reconstruction parameter z_p . To determine the value of z_p at which the best reconstruction is obtained the reconstructed image was correlated with a template of the marker consisting of a circular mask with the size and shape of the latex sphere. The algorithm flow chart is presented in Figure 7.6.

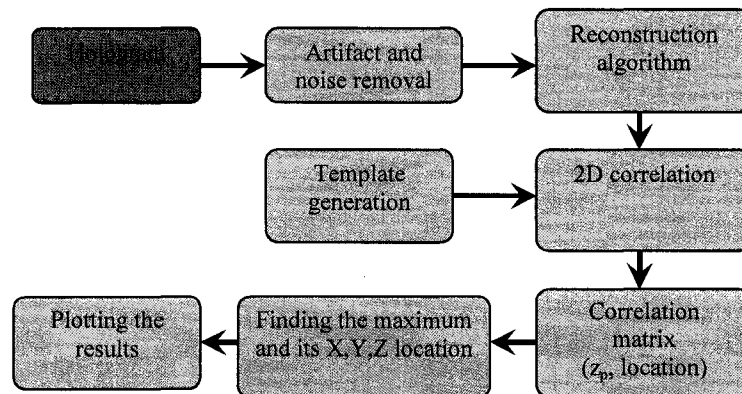


Figure 7.6. Simplified flowchart describing the algorithm used to retrieve 3D information from a single EUV high resolution hologram. The algorithm is based on 2D correlation between reconstructed images at different planes and template generated based on previous knowledge about the markers used.

The hologram scanned with the AFM was preprocessed to remove the artifacts and the AFM noise present in the image. Then a set of reconstructed images was generated for various reconstruction distances z_p . Next markers were chosen manually from the image and their X and Y locations were stored. The markers considered in this analysis are depicted in Figure 7.7a. A template image was generated based on the previous knowledge about the size and shape of the markers. Then each marker at each reconstruction distance was correlated with the template image of the marker and a correlation coefficient was obtained. This constructs a correlation matrix. The correlation matrix has the information about the x - y position of each marker, the reconstruction distance z_p and the correlation coefficients resulting from the 2D correlation operation. The correlation coefficients for each marker as the reconstruction distance z_p was swept in the algorithm carry the information about the z -position of the marker. To find the z -position of the marker one has to find the reconstruction distance at which the correlation coefficient has the maximum value.

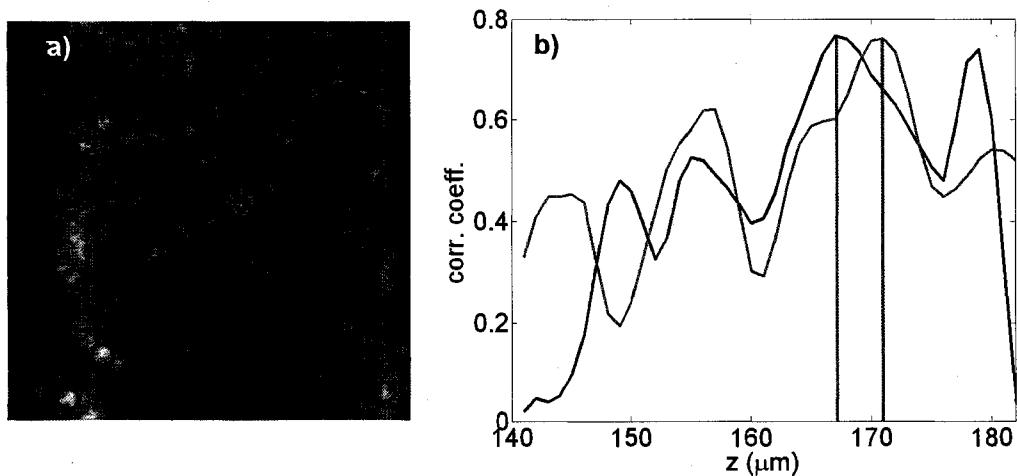


Figure 7.7. Reconstructed image with all considered markers indicated with blue circles a) and correlation coefficients for only two indicated spheres (orange and violet) as a function of the reconstruction distance z_p showing the global maximum indicated with gray lines b).

Figure 7.7b shows the correlation coefficients as a function of z_p for two arbitrary markers selected from the reconstructed image. These markers are indicated by purple and orange circles in Figure 7.7a. For the marker indicated by an orange circle the optimum z -position indicated by the maximum value of the correlation coefficient is equal to $171\mu\text{m}$. For the marker indicated by the violet circle this optimum distance is equal to $168\mu\text{m}$. The algorithm tracks the correlation value for each marker (approximately 30 markers were selected) and finds the maximum correlation coefficient and optimal z -position of the marker for every selected marker. Combining this information with the x - y coordinates of each marker allowed for a complete determination of the marker position in 3D space and a reconstruction of the surface of the test object with depth resolution by a surface fitting to the data from each marker.

7.5 Surface reconstruction

The calculations were done for two sets of data corresponding to two different locations of the markers. Because the aluminum foil slope span across $\sim 1\text{mm}$ it was impossible using the AFM to scan the whole area with the necessary resolution to properly resolve the markers. Our AFM allowed for scanning only $\sim 42 \times 42 \mu\text{m}^2$. However by considering two different locations small areas of the aluminum foil were reconstructed. All the results are depicted in Figure 7.8 and Figure 7.9.

The first region considered was the region of the test object close to the edge of the Mylar spacer, where the slope of the aluminum foil is expected to be high. This region is indicated by the purple square in Figure 7.8a. The locations of the chosen

markers are depicted in Figure 7.8b showing clearly the slope in one direction. The surface was fitted to the data showing the surface of the aluminum foil at this particular region, Figure 7.8d.

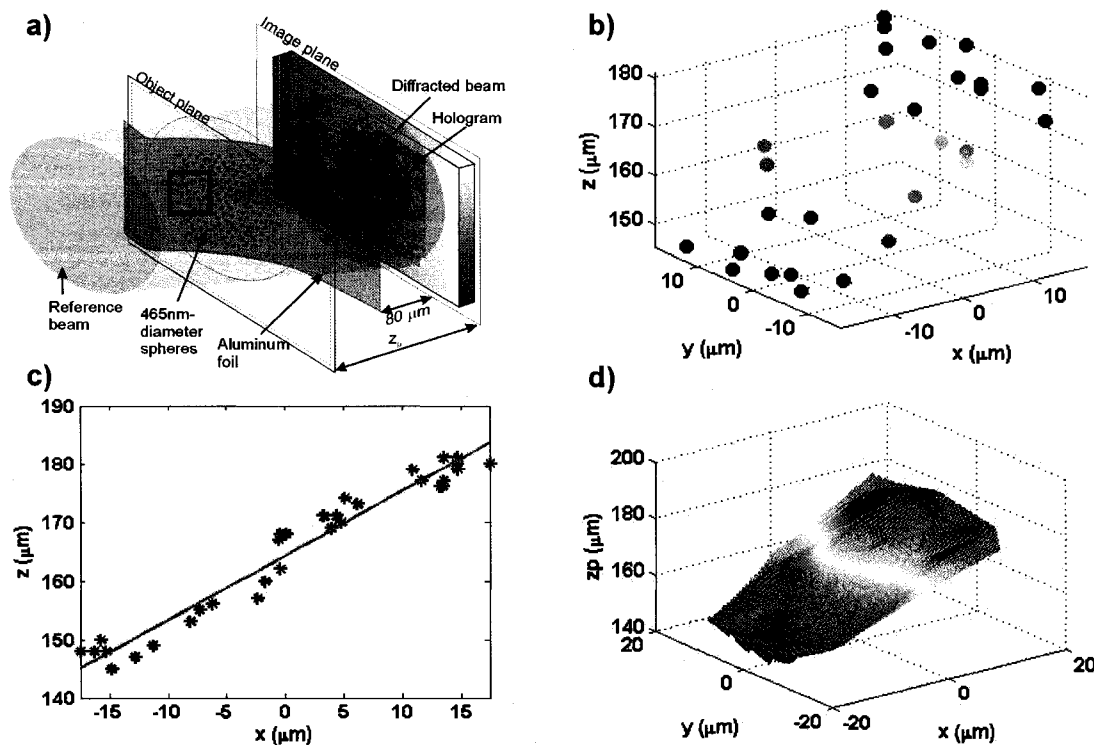


Figure 7.8. Al foil surface reconstruction for the region close to the edge of the spacer where a high slope is revealed a), position of each marker in 3D space obtained from the correlation algorithm b), projection of all markers on a x-z plane emphasizing the Al foil higher slope in one direction and line fitted to the data c), surface topography obtained from (b) using surface fitting algorithm d).

A similar AFM scan performed at a distance approximately 200μm away from the edge of the spacer shown Figure 7.9a, produced an image indicated in Figure 7.9b. The surface was fitted to the data showing the surface of the aluminum foil at different region revealing a smaller slope, Figure 7.9d. Figure 7.8c and Figure 7.9c show the calculated heights for all markers as a function of the transversal coordinate x in the same two regions of the object plotted Figure 7.8b and Figure 7.9b respectively.

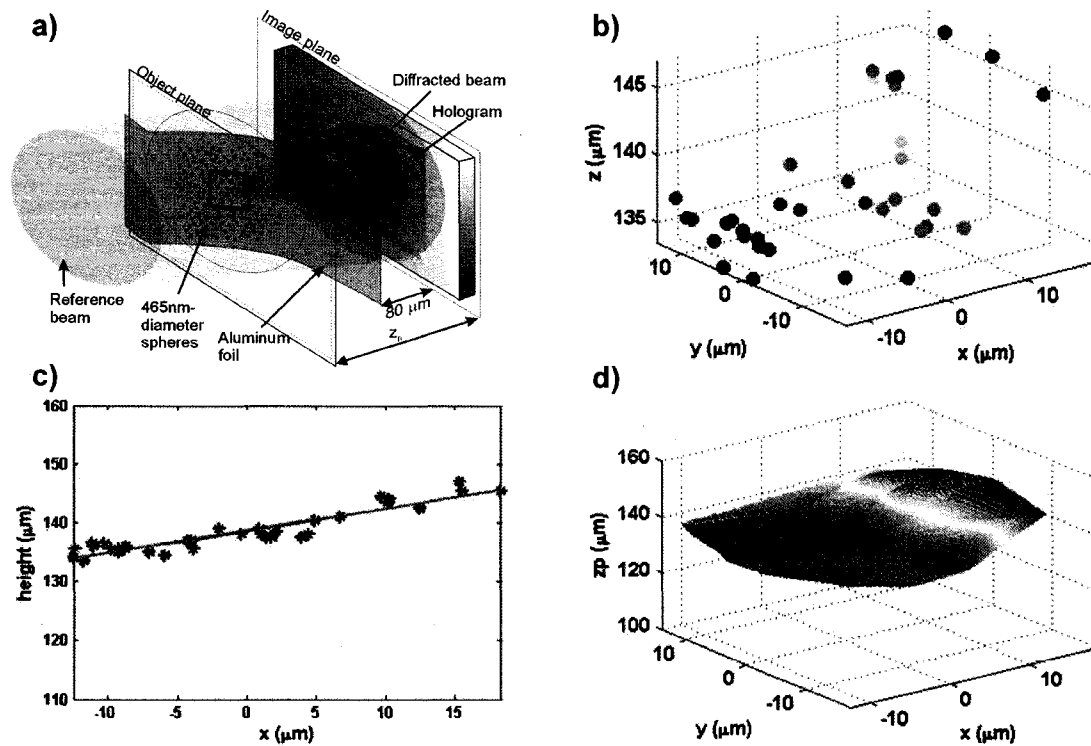


Figure 7.9. Al foil surface reconstruction for the region approximately $200\mu\text{m}$ away from the edge of the spacer where a low slope is revealed a), position of each marker in 3D space obtained from the correlation algorithm b), projection of all markers on a x - z plane emphasizing the Al foil lower slope in one direction and line fitted to the data c), surface topography obtained from (b) using surface fitting algorithm d).

In the plots all markers are represented regardless of its y coordinate. These plots give a measure of the spread of the calculated heights for all the markers and also show, as indicated by the best linear fit, the different slopes in the two regions. The statistical dispersion of the data points relative to the best linear fit are $\Delta z = 2.64\mu\text{m}$ for the region with high slope (Figure 7.8c) and $\Delta z = 1.32\mu\text{m}$ for the region with lower slope (Figure 7.9c). This spread in the measured heights of the markers compares well with the expected accuracy in the z direction determined by the NA utilized recording the hologram. As pointed out by Rogers, if one assumes the hologram as a superposition of

FZPs [7.8], the resolution in the z coordinate can be related to its depth of focus. For a FZP the depth of focus is given by [7.9]:

$$\delta z = \frac{\lambda}{NA^2} \quad (7.1)$$

The NA corresponding to the higher slope region where $z_p \sim 160\mu m$ is $NA = 0.13$, yielding a depth of focus $\delta z = 2.77\mu m$. In the region where the Al foil has a lower slope, the latex markers were closer to the hologram, at a distance $z_p \sim 140\mu m$. For this reconstruction the expected vertical resolution is $\delta z = 2.12\mu m$.

7.6 Summary

Through detailed processing of the reconstructed holographic images, performed by changing the object-hologram distance in the reconstruction algorithm and correlation between the marker template and each marker on the considered surface, it was possible to retrieve the depth information of the object stored in high numerical aperture EUV hologram. Using a specially fabricated object composed of spherical markers 465nm in diameter spread on a tilted transparent surface, the reconstruction and analysis of the hologram allowed to map the surface topography with a depth resolution close to $2\mu m$, depending on the particular NA of the exposure. The surface of the aluminum foil was reconstructed over an area $\sim 40 \times 40 \mu m^2$ and was limited by the AFM scan size. Two different locations were considered showing the different aluminum foil slopes, as was expected. The separation between the foil and the recording medium was chosen

appropriately to be able to resolve the markers laterally (in x-y plane) resulting the lateral resolution $\sim 200\text{nm}$ [7.6, 7.7].

-
- [7.1] Center for X-Ray Optics: <http://www-cxro.lbl.gov> as in June 2007
- [7.2] Suspension 2.62% in water of latex spheres from Polysciences Inc., diameter 465 nm.
- [7.3] U. Schnars, P.O. Jüptner, "Digital recording and reconstruction of holograms in hologram interferometry and shearography", *Appl. Opt* **33**, 4373 (1994)
- [7.4] U. Schnars, P.O. Jüptner, "Digital recording and numerical reconstruction of holograms", *Meas. Sci. Technol* **13**, R85 (2002)
- [7.5] J.W. Goodman, *Introduction to Fourier Optics* (McGraw Hill, 1996, p. 66)
- [7.6] P. W. Wachulak, M.C. Marconi, R. A. Bartels, C. S. Menoni, J.J. Rocca, "Volume extreme ultraviolet holographic imaging with numerical optical sectioning", *Optics Express* **15**, 17, 10622-10628 (2007)
- [7.7] P. W. Wachulak, M. C. Marconi, R. A. Bartels, C. S. Menoni and J. J. Rocca, "Numerical Optical Sectioning for 3D Holographic Images with EUV Lasers", *Optics & Photonic News* 2007, special issue Optics in 2007, **18**, 12, 22 (2007)
- [7.8] G. L. Rogers, "Gabor diffraction microscope: the hologram as a generalized zone plate", *Nature* **166**, 237 (1950)
- [7.9] D. Attwood, *Soft X-ray and extreme ultraviolet radiation*, (Cambridge University Press. 1999)

CHAPTER 8

8 Gaussian filtering and correlation analysis in EUV microscopy

8.1 Introduction

The method based on the convolution and 2-D correlation described in detail in section 6.2 was used with EUV microscope image for the simultaneous determination of the resolution and the feature size. Images obtained with a EUV microscope were analyzed using the algorithm showing a good agreement with measurements performed with alternative methods.

The spatial resolution of an optical system can be expressed in terms of the Rayleigh criterion as $R = \frac{k\lambda}{NA}$, where λ is the wavelength of the illumination, NA is the numerical aperture of the optical system and k is a constant that depends on the coherence of the illumination and the applied test [8.1]. In practice, the spatial resolution of a microscope can be assessed by analyzing images of specifically designed objects with well-established tests, such as the knife-edge or grating tests [8.2]. Under perfect focusing conditions, the image resolution coincides with the resolution of the imaging

system. If the feature size of the imaged object is significantly larger than the resolution of the instrument, its dimensions can be readily determined from the image. However, when the size of the object approaches the resolution or when the image is not perfectly focused, it is difficult to extract the size of the object's features from the image.

Analytical methods can improve the quality of the image, especially in situations when noise is a dominant component [8.3-8.5]. These techniques have been successfully employed to enhance contrast in images obtained with a soft X-ray microscope [8.5]. Image analysis can also be used to map the location of markers, such as gold nanoparticles [8.6], or to determine the position of latex nanospheres in three dimensions as described in chapter 7 of this dissertation [8.7]. In section 6.1 an image analysis was presented that allows the determination of the image resolution by means of a correlation between the image and the calibrated set of templates obtained by the wavelet decomposition. The approach discussed below is based on continuous size Gaussian filters and allows for a more precise determination of the correlation coefficient compared to the wavelet decomposition method described in chapter 6 [8.8, 8.9].

The correlation method with Gaussian filtering was used to assess the spatial resolution of CNT holograms presented in section 6.2. Here the same algorithm will be applied to images obtained with a EUV microscope. A series of calibrated gratings with well defined dimensions were imaged using the EUV microscope [8.10]. The resolution and linewidth of these gratings were assessed by performing the analysis with the Gaussian filter algorithm and compared with the resolution obtained from the grating modulation and SEM linewidth measurements. This experiment, described in detail in the next section, was performed to validate the method.

8.2 Microscopy of nano-scale periodic patterns at $\lambda=13.2$ nm

The EUV images used to test the correlation method, were acquired with a full-field microscope operating in transmission mode at a wavelength of $\lambda=13.2$ nm [8.12]. Briefly, the EUV microscope uses Fresnel Zone plates (FZP) condenser and objective with numerical aperture $NA_c = 0.07$ and $NA_o = 0.132$ respectively. The condenser zone plate collects the laser light and focuses it onto the test pattern. The objective zone plate forms the image of the test pattern onto a back-illuminated charge coupled detector (CCD). The scheme of the microscope is depicted in Figure 8.1.

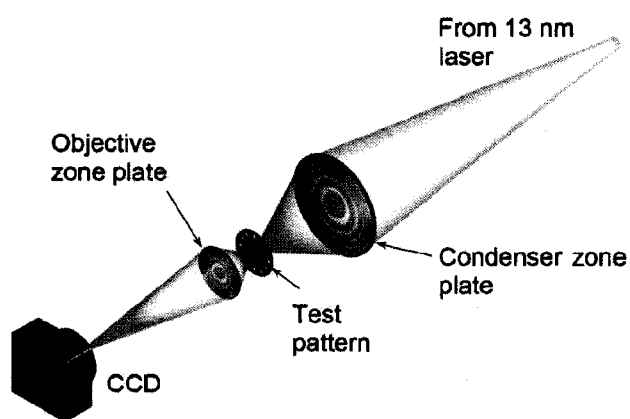


Figure 8.1. Schematic diagram of the 13nm wavelength imaging system. A condenser zone plate collects the laser light and focuses it onto the test pattern. An objective zone plate forms the image of the test pattern onto a back-illuminated charge coupled detector (CCD). Picture was taken from [8.10].

The microscope is illuminated by the highly directional output from a $\lambda = 13.2$ nm Ni-like cadmium laser operating at a repetition rate of 5Hz [8.11, 8.12]. Gratings and periodic elbow patterns fabricated by electron beam lithography on a 100nm thick metalized silicon nitride membrane, of various shapes and dimensions were used as test objects [8.13, 8.14]. The images were recorded using a 2048×2048 back illuminated CCD

camera with 13.5 μm pixel size. Images of dense line gratings with 100 and 200nm period and an elbow shaped grating with 100nm period were obtained with a magnification of 1080x. At this magnification, the pixel size in the image plane corresponds to 12.5nm at the object plane, which ensures that the image resolution is not limited by the detection system. The spatial resolution of the $\lambda = 13.2\text{nm}$ microscope was obtained from the analysis of EUV images of gratings with periods down to 76nm and linewidths down to 38nm [8.12]. Figure 8.2 shows the EUV images used to test the correlation method described herein, and compares them with scanning electron microscope (SEM) from which the linewidths of the test patterns were independently assessed.

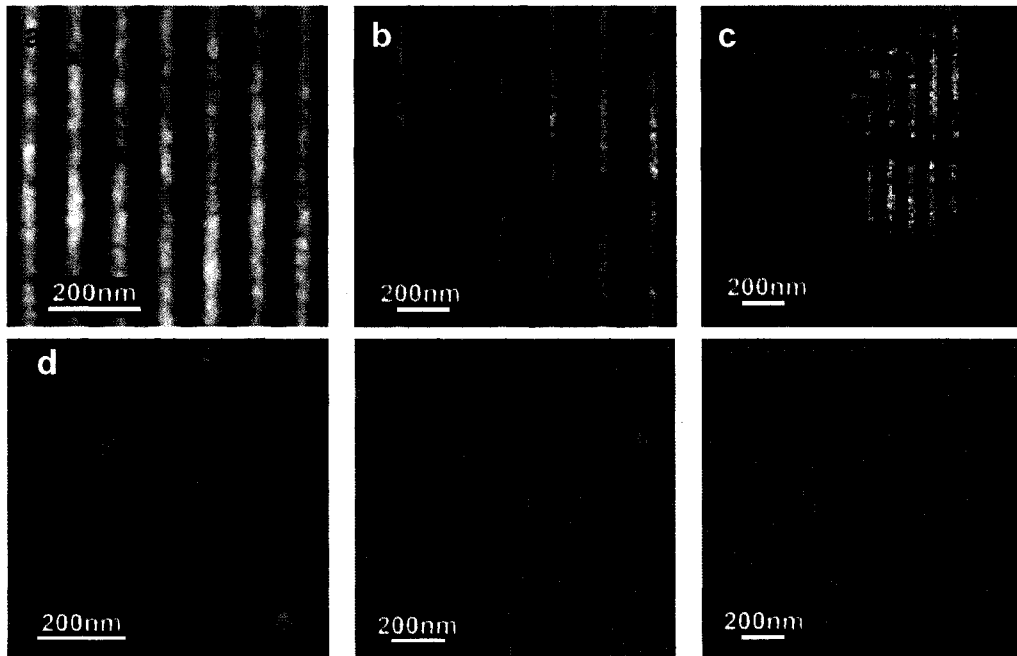


Figure 8.2. EUV microscope image of a) a 100nm full period grating, b) 200nm full period grating, and c) 100nm full period elbow-shaped grating obtained with 13.2nm wavelength laser illumination. d), e) and f) are the corresponding SEM images of the test objects.

8.3 Algorithm for the simultaneous determination of feature size and resolution

In this paragraph the sequence of steps involved in the algorithm will be described. The test image is a EUV microscope image of a 200nm period grating shown in Figure 8.3a. First an intensity threshold is applied to the EUV image to homogenize the background. The threshold level is adjusted to maintain the features of the image while generating a new image with improved contrast for the next processing step. The thresholded image is shown in Figure 8.3b. In a second step a skeletonizing algorithm is applied to the thresholded image [8.15] to produce a template with one pixel wide contours that follow shape of the original image.

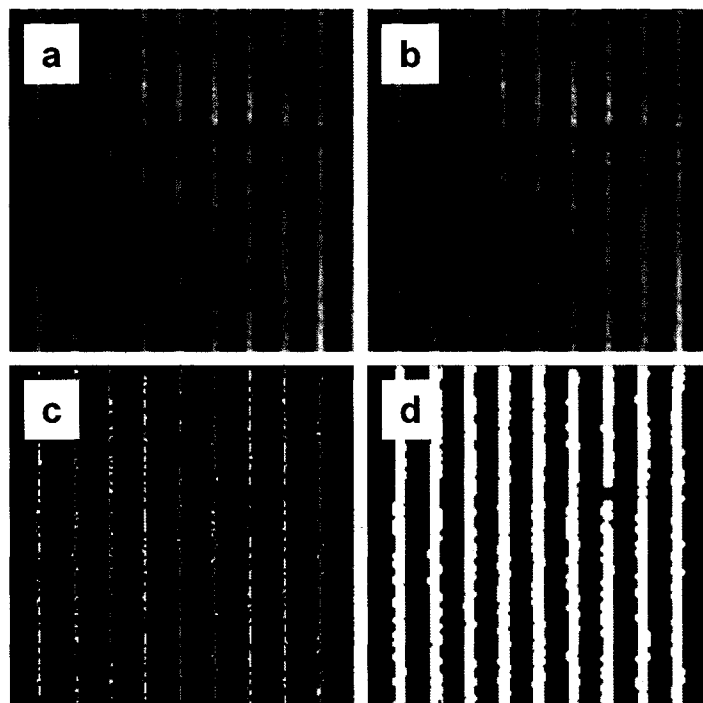


Figure 8.3. a) EUV image of the 200 nm full period grating. b) Image of the 200nm period grating with the threshold applied. c) Skeleton obtained from the image shown in (b). d) Binary template generated by convolution of the skeleton image with a circle with diameter $D=50nm$.

The skeleton of the grating of Figure 8.3b is shown in Figure 8.3c. Third, the skeleton is convolved with K different circular templates of diameters ranging in this particular example from 5nm to 100nm. The convolution between the skeleton and the K different circular templates generates a set of K binary templates, each one with a different linewidth, that resemble the original grating image. One of these K binary templates is shown in Figure 8.3d. Fourth, the K templates are degraded in resolution by applying L different Gaussian filters with selected full width at half maximum (FWHM). A description of the Gaussian filter design and their relationship to the image resolution is provided in Appendix II. Figure 8.4 shows a set of degraded resolution templates obtained from the binary image of Figure 8.3d after the convolution with Gaussian filters of different FWHM.

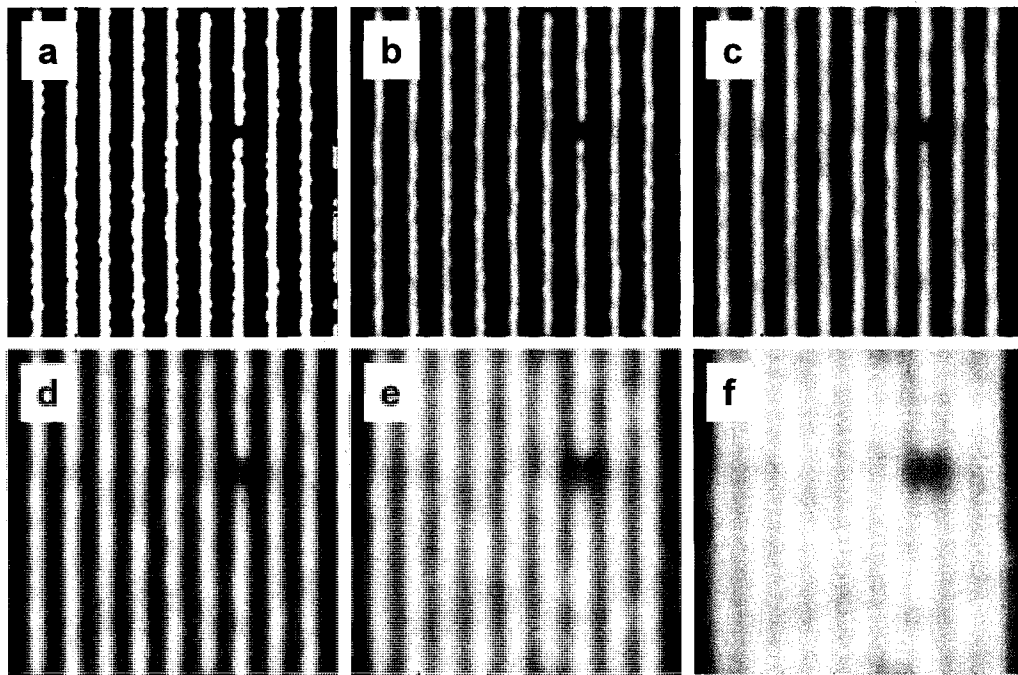


Figure 8.4. Set of templates obtained applying Gaussian filters of different FWHM yielding different resolutions δ . a) $\delta = 15$ nm, b) $\delta = 45$ nm, c) $\delta = 75$ nm, d) $\delta = 105$ nm, e) $\delta = 135$ nm and f) $\delta = 165$ nm.

In these templates the image resolution varies from 15nm to 165nm in 30nm steps. Applying the L Gaussian filters to each one of the K binary templates produces a set of $K \times L$ templates. These $K \times L$ templates are individually correlated with the original image. The correlation coefficients plotted in the $K \times L$ dimensional space generate a surface which global maximum that identifies the template that best resembles the original EUV image. The width of the template (K) and the FWHM of the Gaussian filter (L) correspond to the size of the feature and the resolution δ of the image respectively.

8.3.1 Relation to the incoherent Rayleigh criterion

The relationship between the width of the Gaussian filter that maximizes the correlation coefficient (the resolution given by the algorithm) and the Rayleigh resolution criterion was determined by applying the algorithm to a set of synthesized images composed of two Airy disks separated by different distances. These synthesized images correspond to the images that should be expected from two point sources. According to the Rayleigh criterion, two point sources are resolved if the minimum intensity in the cross section along the line relating the centers of the Airy disks is below 73.5% of the maximum intensity. The distance R between the two Airy disks at which the intensity modulation equals this value is defined as the Rayleigh resolution. The images of the Airy disks were synthesized changing the separation between Airy disks and its width in such a way to have always the intensity drop to $\sim 73.5\%$ of the maximum intensity thus reproducing the case for the incoherent Rayleigh resolution criterion. The images of the

two point sources in this set of templates called here Set#1 by definition are exactly resolved according to Rayleigh criterion.

A second set of templates was generated called Set#2. This set of templates was obtained starting with two pixels with values equal to unity (in otherwise zeroed matrix) separated by different distances R equal to the distances between two maxima of the Airy disks in the first set of templates. A Gaussian filter with variable width corresponding to a resolution r was applied to each of these two-point templates from Set#2, thus generating set of $R \times r$ templates. Finally, for each value of R the template from Set#1 was 2-D correlated with the set of variable resolution templates from Set#2. For each value of R the maximum correlation coefficient was found. The resolution according to the correlation algorithm (r) was plotted as a function of the resolution according to the Rayleigh incoherent criterion (R). Figure 8.5 is this plot.

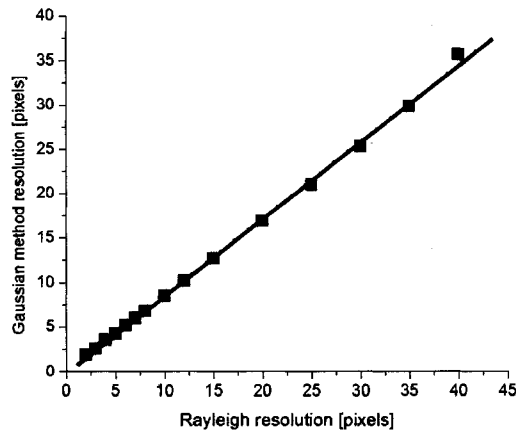


Figure 8.5. Resolution estimated from the optimum Gaussian filter size as a function of the Rayleigh resolution. Dotted line is a linear fit to the calculated points marked with squares.

The linear dependence indicates that both magnitudes are equivalent, and the slope $\beta = 0.786$ is the factor that relates the resolution derived from a Gaussian filter and

correlation algorithm to the Rayleigh resolution. Therefore the image resolution according to Rayleigh incoherent criterion can be obtained by dividing the resolution derived from the Gaussian filter algorithm by the factor β . A detailed explanation of the relation between the resolution and the FWHM of the Gaussian filter can be found in Appendix II.

8.4 Algorithm results

Figure 8.6 shows the correlation plots resulting from applying the algorithm to the three images in Figure 8.2 (a-c).

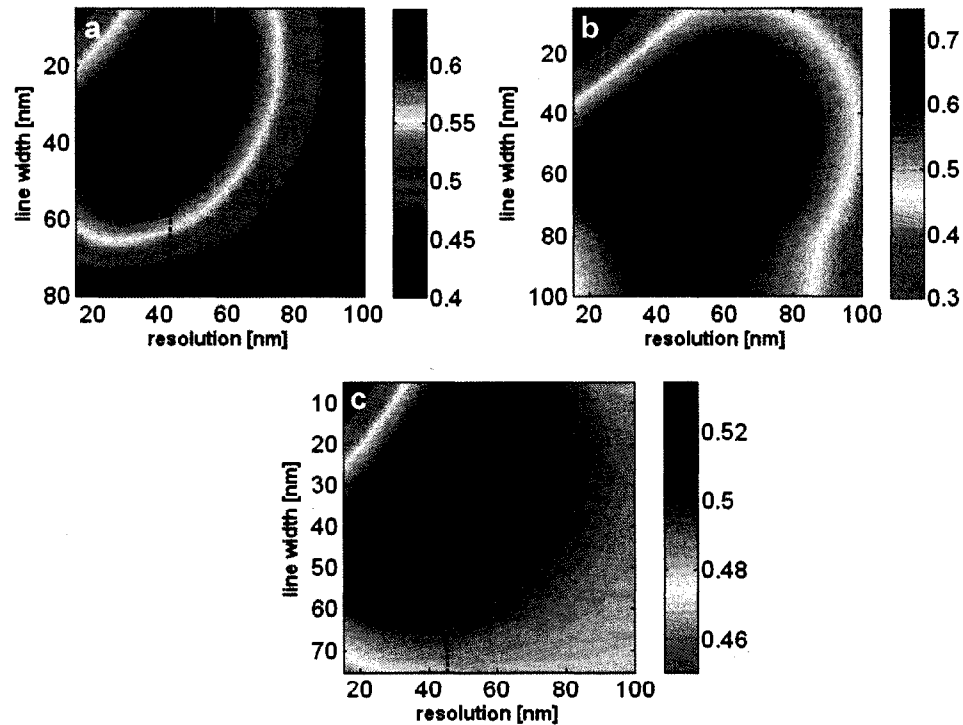


Figure 8.6. Correlation coefficients plotted in the feature size-resolution space showing a global maximum for each of the three different images of Figure 8.2. The dashed lines indicate the coordinates of the global maxima for each of the data sets: a) 100nm full period grating linewidth 31 ± 5 nm, and Rayleigh resolution 54.8 ± 5 nm. b) 200nm full period grating, linewidth 53.6 ± 5 nm and 59.2 ± 5 nm resolution c) 100nm full period elbow-shaped grating, linewidth 29 ± 5 nm and 58.3 ± 5 nm resolution.

The minimum step size in both resolution and linewidth was set in the algorithm to be 5nm which corresponds to the step size in the calculations. The surface was fitted to the correlation map using bi-cubic interpolation and from the interpolated plots the feature size and the image resolution δ for each pattern was estimated. Table 8.1 summarizes the results.

Table 8.1. Comparison of linewidth size and image resolution determined by the correlation algorithm with measurements from the SEM images and grating test respectively for three different test images obtained with the EUV microscope at 13.2nm illumination.

	Test Image		
	100nm period gratings	200nm period gratings	100nm period elbow shaped gratings
Grating linewidth from the SEM measurements	$31 \pm 2.6nm$	$53.8 \pm 1.8nm$	$31.3 \pm 2.4nm$
Grating linewidth from the algorithm	$31 \pm 5nm$	$53.6 \pm 5nm$	$29 \pm 5nm$
Image resolution determined by algorithm δ	$43.1nm$	$46.5nm$	$45.8nm$
Image resolution according to Rayleigh criterion (δ / β), $\beta = 0.786$	$54.8 \pm 5nm$	$59.2 \pm 5nm$	$58.3 \pm 5nm$
Instrument resolution from grating test measurement	$< 76nm$	$< 76nm$	$< 76nm$

The grating linewidths obtained for all three patterns are in very good agreement with those obtained independently from the SEM images. The error in the image resolution was conservatively assigned to one step in the algorithm, in this case 5nm. The error bars in linewidth obtained from the SEM images correspond to the standard deviation of the values measured at ten different locations. Other images containing patterns with different shapes were also analyzed, resulting in similar degree of

agreement. The Rayleigh resolution obtained from the image analysis is in agreement with the spatial resolution of the $\lambda = 13.2\text{nm}$ microscope measured by imaging gratings of decreasing periods, that yielded a resolution of better than 76nm (38nm half period resolution) - the period of the smallest grating in the test [8.10]. The results of this experiment were published in [8.16].

8.5 Summary

A correlation method capable of simultaneous determination of the size of the imaged features and the resolution of the image was used in this section to analyze the EUV microscope images. Its global approach makes the method robust and tolerant of local variations in image contrast. The method was applied to determine the size of nanoscale patterns from images of patterned nanostructures acquired with 13.2nm light zone plate microscope. The results obtained are in very good agreement with independent measurements, which further validate developed algorithm presented in this section. Image analysis algorithms that evaluate the image resolution, such as the one described here, have the capability to enable the optimization of the EUV/SXR microscope during image acquisition. This is especially critical for the acquisition of EUV images with high magnification, where depth of focus are limited to $\sim 100\text{nm}$ or less and where subjective human judgment might not be optimal.

-
- [8.1] D. Attwood, *Soft X-ray and extreme ultraviolet radiation*, (Cambridge University Press. 1999)
- [8.2] J. Heck, D. T. Attwood, W. Meyer-Ilse, E. H. Anderson, "Resolution determination in X-ray microscopy: an analysis of the effects of partial coherence and illumination spectrum", *Journal of X-Ray Science and Technology* **8**, 95 (1998)
- [8.3] Q. Kemao, "Two-dimensional windowed Fourier transform for fringe pattern analysis: Principles, applications and implementations", *Optics and Lasers in Engineering* **45**, 304 (2007)
- [8.4] M. S. Pattichis, A.C. Bovik, "Analyzing image structure by multidimensional frequency modulation", *IEEE Transactions on Pattern Analysis and Machine Intelligence* **29**, 753 (2007)
- [8.5] H. Stollberg, J.B. de Monvel, A. Holmberg, H.M. Hertz, "Wavelet-based image restoration for compact X-ray microscopy", *Journal of Microscopy-Oxford* **211**, 154 (2003)
- [8.6] H. Stollberg, P. Guttmann, P.A.C. Takman, H.M. Hertz, "Size-selective colloidal-gold localization in transmission X-ray microscopy", *Journal of Microscopy-Oxford* **225**, 80 (2007)
- [8.7] P. Wachulak, M. C. Marconi, R. Bartels C. S. Menoni, J. J. Rocca, "Volume extreme ultraviolet holographic imaging with numerical optical sectioning", *Optics Express* **15**, 10622 (2007)
- [8.8] P. Wachulak, R. Bartels, M. C. Marconi, C. S. Menoni, J. J. Rocca, Y. Lu, B. Parkinson, "Sub 400 nm spatial resolution extreme ultraviolet holography with a table top laser", *Optics Express* **14**, 9636 (2006)
- [8.9] J. Nunez, X. Otazu, M.T. Merino, "A multiresolution-based method for the determination of the relative resolution between images: First application to remote sensing and medical images", *International Journal of Imaging Systems and Technology* **15**, 225 (2005)
- [8.10] G. Vaschenko, C. Brewer, E. Brizuela, Y. Wang, M.A. Larotonda, B.M. Luther, M.C. Marconi, J.J. Rocca, C.S. Menoni, "Sub-38 nm resolution tabletop microscopy with 13 nm wavelength laser light", *Optics Letters* **31**, 1214 (2006)
- [8.11] Y. Wang, M.A. Larotonda, B.M. Luther, D. Alessi, M. Berrill, V.N. Shlyaptsev, J.J. Rocca, "Demonstration of high-repetition-rate tabletop soft-x-ray lasers with

saturated output at wavelengths down to 13.9 nm and gain down to 10.9 nm”, *Physical Review A* **72**, 5 (2005)

[8.12] J. J. Rocca, Y. Wang, M.A. Larotonda, B.M. Luther, M. Berrill, D. Alessi, “Saturated 13.2 nm high-repetition-rate laser in nickellike cadmium”, *Optics Letters* **30**, 2581 (2005)

[8.13] E. H. Anderson, “Specialized electron beam nanolithography for EUV and X-ray diffractive optics”, *IEEE Journal of Quantum Electronics* **42**, 27 (2006)

[8.14] E. H. Anderson, D.L. Olynick, B. Harteneck, E. Veklerov, G. Denbeaux, W.L. Chao, A. Lucero, L. Johnson, D. Attwood, “Nanofabrication and diffractive optics for high-resolution x-ray applications”, *Journal of Vacuum Science & Technology B* **18**, 2970 (2000)

[8.15] T. Yatagai, S. Nakadate, M. Idesawa, H. Saito, “Automatic fringe analysis using digital image processing techniques”, *Optical Engineering*. **21**, 432 (1982)

[8.16] P.W. Wachulak, C.A. Brewer, F. Brizuela, W. Chao, E. Anderson, R. A. Bartels, C.S. Menoni, J.J. Rocca, M.C. Marconi, “Analysis of extreme ultraviolet microscopy images of patterned nanostructures based on a correlation method”, *Journal of the Optical Society of America B*, **25**, B20, (2008), this article was also published in *The Virtual Journal for Biomedical Optics*, **3**, 8, (2008)

SUMMARY

9 Summary and final thoughts

Two applications of EUV light were presented in this dissertation: EUV nanopatterning and EUV holography. These applications take advantage of unique properties of the capillary discharge laser such as high temporal and spatial coherence, high photon flux and short wavelength. High spatial and temporal coherence enables high contrast interference patterns over relatively large areas desirable in nanopatterning and holography. High flux allows for short exposures and high throughput. Finally ten times shorter wavelength than visible light opens possibility of patterning and holographic imaging with sub-50nm spatial resolution.

In both applications the recording medium was a high resolution photoresist. In the case of nanopatterning the photoresist was used as a mask to subsequently transfer the pattern down to the underlying substrate while in the case of holography it was used as a high resolution recording medium to store the interference pattern, the hologram, in its surface. The spatial resolution of the photoresist is in the nanometer range permitting high resolution patterning and imaging, however the photoresist requires much larger flux than other recording media such as CCD cameras.

EUV nanopatterning using much shorter wavelength enables to pattern the surface of the materials in nano-meter scale. Application of EUV light to this field is very

important since a lot of effort is currently made to develop new techniques that will allow in the future to increase the information storage density and computation speed of the processors. Shorter wavelength might be one of the ways to accomplish this difficult task. The goal of the work is to show the advantages of using EUV light and explore new possibilities associated with this approach. Interferometric lithography (IL) was chosen as a main technique due to the relatively high coherence of the laser source used in this work. Although IL was limited to printing one and two dimensional periodic patterns it is one of the techniques (in the author's opinion) that will have a lot of potential in information storage media fabrication due to the possibility of fabrication of large areas with uniform features, sub-100nm in size. Two types of interferometers were studied, a wavefront division Lloyd's mirror configuration and an amplitude division interferometer and the fabrication results for both interferometers were presented. The Lloyd's mirror interferometer allowed for patterning surfaces up to $\sim 0.5 \times 0.5 \text{mm}^2$ with feature sizes down to sub-50nm (45nm pillars and 47 nm lines) in different types of photoresists such as PMMA and HSQ, while with the use of the amplitude division interferometer it was possible to pattern up to $\sim 2 \times 0.6 \text{mm}^2$ surfaces with sub-50nm feature sizes (lines 47nm width) in HSQ photoresist.

The second application discussed in this work was EUV holography. Holographic imaging doesn't require any optics which is very convenient especially at EUV wavelengths where lack of good quality and high throughput optics is a major problem. Different objects were used in the experiments presented (AFM probes, latex nanospheres and carbon nanotubes) leading to successful two and three dimensional imaging with spatial resolution approaching the illumination wavelength. This technique

has a lot of potential and can be considered as a complimentary technique to optical imaging, AFM and SEM. As compared with scanning microscopy or electron microscopy holographic imaging at EUV wavelength doesn't require any sample preparation such a metallization and is free of sample-tip interactions.

The work presented in this dissertation can and will evolve even further to reach the sub-10 nanometer scale. With the development of new shorter wavelength sources, similar approaches to the ones presented here might be extended further to study the matter on nanometer scales. The new developments in this exciting field will continue and might lead to a lot of excitement in this field for many years ahead.

APPENDICES

10.1 Appendix I: Reflectivity calculations for the Cr mirror for compact nanopatterning tool using atomic scattering factors

In this appendix the detailed analysis of the reflection from the metallic surface will be presented. This analysis is based on [10.1]. The interface of two materials and the coordinate system and symbols used in this analysis is shown in Figure 10.1.1. The media above and below the plane $z = 0$ have permeabilities and permittivities μ', ϵ' and μ, ϵ , respectively. The indices of refraction are defined by $n' = \sqrt{\mu'\epsilon' / \mu_0\epsilon_0}$ and $n = \sqrt{\mu\epsilon / \mu_0\epsilon_0}$. A plane wave with vector \vec{k} and frequency ω is incident from medium with parameters μ, ϵ and creates the reflected and refracted waves with wave vectors \vec{k}' and \vec{k}'' , respectively. Unit normal vector \vec{n} is directed from medium μ, ϵ to μ', ϵ' .

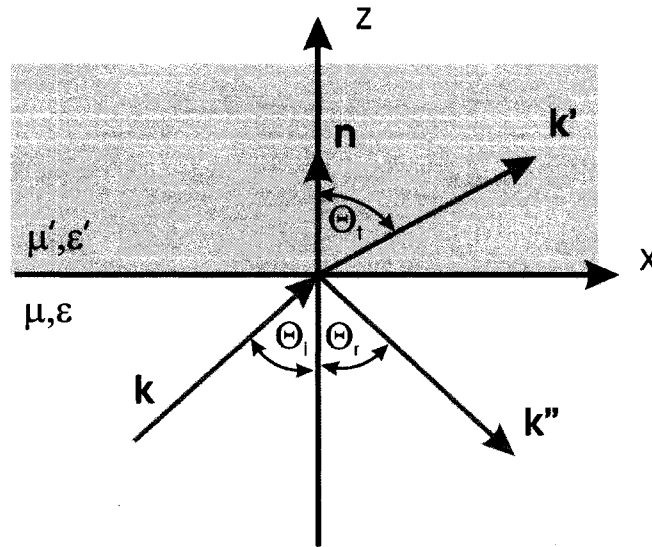


Figure 10.1.1. The coordinate system and the symbols used in the analysis of the reflection coefficient from the Cr mirror. The incident wave k strikes plane interface separating two media and gives rise to the reflected k'' and refracted k' wave.

The incident, refracted and reflected waves can be expressed as the plane waves. Both electric field and magnetic induction components for incident wave are shown below:

$$\vec{E} = \vec{E}_0 e^{i(\vec{k} \cdot \vec{x} - \omega t)}, \vec{B} = \sqrt{\mu \varepsilon} \frac{\vec{k} \times \vec{E}}{k} \quad (10.1.1)$$

For the refracted wave:

$$\vec{E}' = \vec{E}'_0 e^{i(\vec{k}' \cdot \vec{x} - \omega t)}, \vec{B}' = \sqrt{\mu' \varepsilon'} \frac{\vec{k}' \times \vec{E}'}{k'} \quad (10.1.2)$$

And for the reflected wave:

$$\vec{E}'' = \vec{E}''_0 e^{i(\vec{k}'' \cdot \vec{x} - \omega t)}, \vec{B}'' = \sqrt{\mu \varepsilon} \frac{\vec{k}'' \times \vec{E}''}{k} \quad (10.1.3)$$

The magnitudes of the wave vectors for incident and reflected waves are equal.

$$|\vec{k}| = |\vec{k}''| = k = \omega \sqrt{\mu \varepsilon} \quad (10.1.4)$$

And for refracted wave vector

$$|\vec{k}'| = k' = \omega \sqrt{\mu' \varepsilon'} \quad (10.1.5)$$

The boundary conditions at the $z = 0$ plane must be satisfied for all points on the plane and at all times. That means that the spatial and temporal variations of both fields must be the same at $z = 0$.

$$(\vec{k} \cdot \vec{x})_{z=0} = (\vec{k}' \cdot \vec{x})_{z=0} = (\vec{k}'' \cdot \vec{x})_{z=0} \quad (10.1.6)$$

Three wave vectors are in the same plane and by applying the dot product to the above equation one can see that:

$$|\vec{k}| |\vec{x}| \cos\left(\frac{\pi}{2} - \Theta_i\right) = |\vec{k}'| |\vec{x}| \cos\left(\frac{\pi}{2} - \Theta_i\right) = |\vec{k}''| |\vec{x}| \cos\left(\frac{\pi}{2} - \Theta_r\right) \quad (10.1.7)$$

Simplifying above equation

$$k \sin(\Theta_i) = k' \sin(\Theta_i) = k'' \sin(\Theta_r) \quad (10.1.8)$$

Because $k'' = k$, angles $\Theta_i = \Theta_r$ have to be equal as well. That is well known Snell's law:

$$\frac{\sin(\Theta_i)}{\sin(\Theta_r)} = \frac{k'}{k} = \sqrt{\frac{\mu' \varepsilon'}{\mu \varepsilon}} = \frac{n'}{n} \quad (10.1.9)$$

The boundary conditions for this simple interface state that normal components of displacement vector \vec{D} and magnetic induction \vec{B} are continuous, also the tangential components of the electric field vector \vec{E} and magnetic field vector \vec{H} are continuous as well at the boundary $z = 0$. Let's consider the normal component of \vec{D} vector.

$$\vec{D} \cdot \vec{n} = 0 \quad (10.1.10)$$

By substituting for \vec{D} we have:

$$(\varepsilon \vec{E} + \varepsilon \vec{E}'' - \varepsilon' \vec{E}') \cdot \vec{n} = 0 \quad (10.1.11)$$

$$\left(\varepsilon \vec{E}_0 e^{i(\vec{k} \cdot \vec{x} - \omega t)} + \varepsilon \vec{E}''_0 e^{i(\vec{k}'' \cdot \vec{x} - \omega t)} - \varepsilon' \vec{E}'_0 e^{i(\vec{k}' \cdot \vec{x} - \omega t)} \right) \cdot \vec{n} = 0 \quad (10.1.12)$$

We can extract the repeating terms:

$$e^{i[(\vec{k} + \vec{k}'' + \vec{k}') \cdot \vec{x} - \omega t]} \left(\varepsilon \vec{E}_0 + \varepsilon \vec{E}''_0 - \varepsilon' \vec{E}'_0 \right) \cdot \vec{n} = 0 \quad (10.1.13)$$

Finally we have:

$$(\varepsilon \vec{E}_0 + \varepsilon \vec{E}'' - \varepsilon' \vec{E}') \cdot \vec{n} = 0 \quad (10.1.14)$$

The normal component of the magnetic induction has to be continuous at the boundary and can be expressed as:

$$\vec{B} \cdot \vec{n} = 0 \quad (10.1.15)$$

For all vectors considered in this problem:

$$\vec{B} \cdot \vec{n} + \vec{B}'' \cdot \vec{n} - \vec{B}' \cdot \vec{n} = 0 \quad (10.1.16)$$

After substitution:

$$\sqrt{\mu \varepsilon} \frac{\vec{k} \times \vec{E}}{k} \cdot \vec{n} + \sqrt{\mu \varepsilon} \frac{\vec{k}'' \times \vec{E}''}{k} \cdot \vec{n} - \sqrt{\mu' \varepsilon'} \frac{\vec{k}' \times \vec{E}'}{k'} \cdot \vec{n} = 0 \quad (10.1.17)$$

From Snell's law given equality holds:

$$\frac{\sqrt{\mu \varepsilon}}{k} = \frac{\sqrt{\mu' \varepsilon'}}{k'} \quad (10.1.18)$$

That leads to the simpler form

$$(\vec{k} \times \vec{E}) \cdot \vec{n} + (\vec{k}'' \times \vec{E}'') \cdot \vec{n} - (\vec{k}' \times \vec{E}') \cdot \vec{n} = 0 \quad (10.1.19)$$

By substituting for the vectors once more the full expression and rearranging the terms leads to:

$$(\vec{k} \times \vec{E}_0 e^{i(\vec{k} \cdot \vec{x} - \omega t)} + \vec{k}'' \times \vec{E}_0'' e^{i(\vec{k}'' \cdot \vec{x} - \omega t)} - \vec{k}' \times \vec{E}_0' e^{i(\vec{k}' \cdot \vec{x} - \omega t)}) \cdot \vec{n} = 0 \quad (10.1.20)$$

$$e^{i[(\vec{k} + \vec{k}'' + \vec{k}') \cdot \vec{x} - \omega t]} (\vec{k} \times \vec{E}_0 + \vec{k}'' \times \vec{E}_0'' - \vec{k}' \times \vec{E}_0') \cdot \vec{n} = 0 \quad (10.1.21)$$

Finally the condition for normal component of the magnetic induction

$$(\vec{k} \times \vec{E}_0 + \vec{k}'' \times \vec{E}_0'' - \vec{k}' \times \vec{E}_0') \cdot \vec{n} = 0 \quad (10.1.22)$$

Now let's focus on the tangential components. For the tangential component of \vec{E}

$$\vec{E} \times \vec{n} = 0 \quad (10.1.23)$$

For the three considered waves

$$(\vec{E} + \vec{E}'' - \vec{E}') \times \vec{n} = 0 \quad (10.1.24)$$

$$(\vec{E}_0 e^{i(\vec{k} \cdot \vec{x} - \omega t)} + \vec{E}_0'' e^{i(\vec{k}'' \cdot \vec{x} - \omega t)} - \vec{E}_0' e^{i(\vec{k}' \cdot \vec{x} - \omega t)}) \times \vec{n} = 0 \quad (10.1.25)$$

$$e^{i[(\vec{k} + \vec{k}'' + \vec{k}') \cdot \vec{x} - \omega t]} (\vec{E}_0 + \vec{E}_0'' - \vec{E}_0') \times \vec{n} = 0 \quad (10.1.26)$$

That leads to final equation

$$(\vec{E}_0 + \vec{E}_0'' - \vec{E}_0') \times \vec{n} = 0 \quad (10.1.27)$$

For the tangential component of the magnetic field \vec{H} ,

$$\vec{H} \times \vec{n} = 0 \quad (10.1.28)$$

$$(\vec{H} + \vec{H}'' - \vec{H}') \times \vec{n} = 0 \quad (10.1.29)$$

Knowing the magnetic induction vectors, obtaining the magnetic field vectors in magnetically isotropic medium is straightforward:

$$\vec{H} = \frac{\vec{B}}{\mu} = \sqrt{\mu\epsilon} \frac{\vec{k} \times \vec{E}}{\mu k} \quad (10.1.30)$$

$$\vec{H}' = \frac{\vec{B}'}{\mu'} = \sqrt{\mu'\epsilon'} \frac{\vec{k}' \times \vec{E}'}{\mu' k'} \quad (10.1.31)$$

$$\vec{H}'' = \frac{\vec{B}''}{\mu} = \sqrt{\mu\epsilon} \frac{\vec{k}'' \times \vec{E}''}{\mu k''} \quad (10.1.32)$$

Plugging it back to the equation for the tangential \vec{H} component:

$$\left(\sqrt{\mu\epsilon} \frac{\vec{k} \times \vec{E}}{\mu k} + \sqrt{\mu\epsilon} \frac{\vec{k}'' \times \vec{E}''}{\mu k''} - \sqrt{\mu'\epsilon'} \frac{\vec{k}' \times \vec{E}'}{\mu' k'} \right) \times \vec{n} = 0 \quad (10.1.33)$$

Using $\frac{\sqrt{\mu\epsilon}}{k} = \frac{\sqrt{\mu'\epsilon'}}{k'}$ we have:

$$\frac{\sqrt{\mu\epsilon}}{k} \left(\frac{\vec{k} \times \vec{E}}{\mu} + \frac{\vec{k}'' \times \vec{E}''}{\mu} - \frac{\vec{k}' \times \vec{E}'}{\mu'} \right) \times \vec{n} = 0 \quad (10.1.34)$$

By rearranging the terms we have:

$$\left[\frac{1}{\mu} (\vec{k} \times \vec{E} + \vec{k}'' \times \vec{E}'') - \frac{1}{\mu'} (\vec{k}' \times \vec{E}') \right] \times \vec{n} = 0 \quad (10.1.35)$$

Substituting the expressions for each vector leads to:

$$e^{i[(\vec{k} + \vec{k}'' + \vec{k}') \cdot \vec{x} - \omega t]} \left[\frac{1}{\mu} (\vec{k} \times \vec{E}_0 + \vec{k}'' \times \vec{E}_0'') - \frac{1}{\mu'} (\vec{k}' \times \vec{E}_0') \right] \times \vec{n} = 0 \quad (10.1.36)$$

Finally we have:

$$\left[\frac{1}{\mu} (\vec{k} \times \vec{E}_0 + \vec{k}'' \times \vec{E}_0'') - \frac{1}{\mu'} (\vec{k}' \times \vec{E}_0') \right] \times \vec{n} = 0 \quad (10.1.37)$$

Those four equations shown below are the boundary conditions that need to be satisfied for each wave vector for all spatial coordinates and for all times:

$$(\epsilon \vec{E}_0 + \epsilon \vec{E}_0'' - \epsilon' \vec{E}_0') \cdot \vec{n} = 0 \quad (10.1.38)$$

$$(\vec{k} \times \vec{E}_0 + \vec{k}'' \times \vec{E}_0'' - \vec{k}' \times \vec{E}_0') \cdot \vec{n} = 0 \quad (10.1.39)$$

$$(\vec{E}_0 + \vec{E}_0'' - \vec{E}_0') \times \vec{n} = 0 \quad (10.1.40)$$

$$\left[\frac{1}{\mu} (\vec{k} \times \vec{E}_0 + \vec{k}'' \times \vec{E}_0'') - \frac{1}{\mu'} (\vec{k}' \times \vec{E}_0') \right] \times \vec{n} = 0 \quad (10.1.41)$$

In applying these boundary conditions usually two separate situations are considered. One is in which the incident plane wave is linearly polarized with its polarization vector perpendicular to the plane of incidence defined by \vec{k} and \vec{n} . The second situation is when the polarization vector is parallel to the plane of incidence. For an arbitrary elliptic polarization the general case can be obtained by appropriate linear combination of these two cases.

For \vec{E} perpendicular to the plane of incidence also called (TE-transverse electric) or s-polarization, the general description of the problem is depicted in Figure 10.1.2. All the electric fields vectors are shown with direction away from the viewer, while the

directions of \vec{B} vectors were chosen to give the energy flow in the direction of the wave vectors which has a positive sign. The electric fields in each of the waves are parallel to the interface, thus

$$\vec{E} \cdot \vec{n} = |\vec{E}| |\vec{n}| \cos(\Theta_{E,n}) = |\vec{E}| |\vec{n}| \cos\left(\frac{\pi}{2}\right) = 0 \quad (10.1.42)$$

The third equation after applying the dot product gives:

$$|\vec{E}_0| |\vec{n}| \sin\left(\frac{\pi}{2}\right) + |\vec{E}_0''| |\vec{n}| \sin\left(\frac{\pi}{2}\right) - |\vec{E}_0'| |\vec{n}| \sin\left(\frac{\pi}{2}\right) = 0 \quad (10.1.43)$$

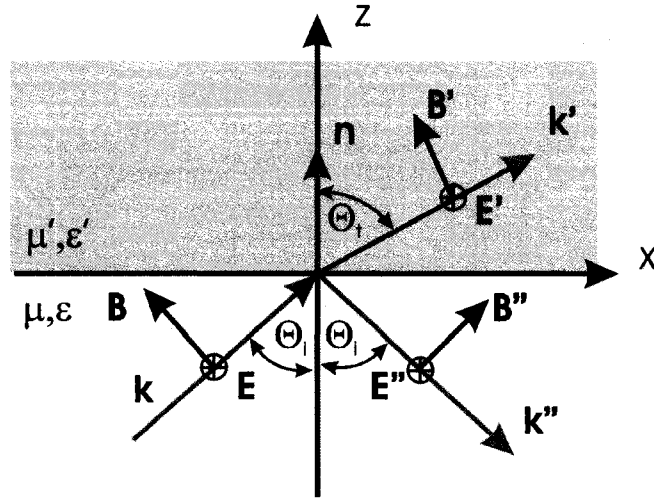


Figure 10.1.2. Reflection and refraction with polarization perpendicular to the plane of incidence (TE)

Because \vec{n} is the unit normal vector, then $|\vec{n}| = 1$. That gives:

$$E_0 + E_0'' - E_0' = 0 \quad (10.1.44)$$

Using equation 10.1.41 and the cross product rules for each of the waves it is easy to see that:

$$\frac{1}{\mu} \left[(\vec{k} \times \vec{E}_0) \times \vec{n} + (\vec{k}'' \times \vec{E}_0'') \times \vec{n} \right] - \frac{1}{\mu'} \left[(\vec{k}' \times \vec{E}_0') \times \vec{n} \right] = 0 \quad (10.1.45)$$

Using the cross product vector identity $(\vec{k} \times \vec{E}) \times \vec{n} = -\vec{n} \times (\vec{k} \times \vec{E})$

$$-\frac{1}{\mu} \left[\vec{n} \times (\vec{k} \times \vec{E}_0) + \vec{n} \times (\vec{k}'' \times \vec{E}_0'') \right] + \frac{1}{\mu'} \left[\vec{n} \times (\vec{k}' \times \vec{E}_0') \right] = 0 \quad (10.1.46)$$

$$\begin{aligned} -\frac{1}{\mu} \left[(\vec{k} (\vec{n} \cdot \vec{E}_0) - \vec{E}_0 (\vec{n} \cdot \vec{k})) + (\vec{k}'' (\vec{n} \cdot \vec{E}_0'') - \vec{E}_0'' (\vec{n} \cdot \vec{k}'')) \right] \\ + \frac{1}{\mu'} \left[(\vec{k}' (\vec{n} \cdot \vec{E}_0') - \vec{E}_0' (\vec{n} \cdot \vec{k}')) \right] = 0 \end{aligned} \quad (10.1.47)$$

Each component after applying the dot product rule is now dependent on the angles between the vectors:

$$\begin{aligned}
-\frac{1}{\mu} \left[\vec{k} (\vec{n} \cdot \vec{E}_0) - \vec{E}_0 (\vec{n} \cdot \vec{k}) \right] &= -\frac{1}{\mu} \left[\vec{k} |\vec{n}| |\vec{E}_0| \cos\left(\frac{\pi}{2}\right) - \vec{E}_0 |\vec{n}| |\vec{k}| \cos(\Theta_i) \right] = \\
&= -\frac{1}{\mu} \left[0 - \vec{E}_0 k \cos(\Theta_i) \right] = \frac{k}{\mu} \vec{E}_0 \cos(\Theta_i) = \omega \sqrt{\frac{\varepsilon}{\mu}} \vec{E}_0 \cos(\Theta_i)
\end{aligned} \tag{10.1.48}$$

$$\begin{aligned}
-\frac{1}{\mu} \left[\vec{k}'' (\vec{n} \cdot \vec{E}_0'') - \vec{E}_0'' (\vec{n} \cdot \vec{k}'') \right] &= -\frac{1}{\mu} \left[\vec{k}'' |\vec{n}| |\vec{E}_0''| \cos\left(\frac{\pi}{2}\right) - \vec{E}_0'' |\vec{n}| |\vec{k}''| \cos(\pi - \Theta_i) \right] = \\
&= -\frac{1}{\mu} \left[-\vec{E}_0'' k (-\cos(\Theta_i)) \right] = -\omega \sqrt{\frac{\varepsilon}{\mu}} \vec{E}_0'' \cos(\Theta_i)
\end{aligned} \tag{10.1.49}$$

$$\begin{aligned}
\frac{1}{\mu'} \left[\vec{k}' (\vec{n} \cdot \vec{E}_0') - \vec{E}_0' (\vec{n} \cdot \vec{k}') \right] &= \frac{1}{\mu'} \left[\vec{k}' |\vec{n}| |\vec{E}_0'| \cos\left(\frac{\pi}{2}\right) - \vec{E}_0' |\vec{n}| |\vec{k}'| \cos(\Theta_i) \right] = \\
&= -\frac{k'}{\mu'} \left[\vec{E}_0' k \cos(\Theta_i) \right] = -\omega \sqrt{\frac{\varepsilon'}{\mu'}} \vec{E}_0' \cos(\Theta_i)
\end{aligned} \tag{10.1.50}$$

Combining all the terms leads to:

$$\omega \sqrt{\frac{\varepsilon}{\mu}} \vec{E}_0 \cos(\Theta_i) - \omega \sqrt{\frac{\varepsilon}{\mu}} \vec{E}_0'' \cos(\Theta_i) - \omega \sqrt{\frac{\varepsilon'}{\mu'}} \vec{E}_0' \cos(\Theta_i) = 0 \tag{10.1.51}$$

$$\sqrt{\frac{\varepsilon}{\mu}} (\vec{E}_0 - \vec{E}_0'') \cos(\Theta_i) - \sqrt{\frac{\varepsilon'}{\mu'}} \vec{E}_0' \cos(\Theta_i) = 0 \tag{10.1.52}$$

All the electric field vectors have the same direction and can be replaced by their magnitudes only

$$\sqrt{\frac{\varepsilon}{\mu}} (E_0 - E_0'') \cos(\Theta_i) - \sqrt{\frac{\varepsilon'}{\mu'}} E_0' \cos(\Theta_i) = 0 \tag{10.1.53}$$

Combining the above equations with $E_0 + E_0'' - E_0' = 0$ there are three unknowns (the electric field amplitudes) and two equations so it is possible to find the ratios of the unknowns:

$$E_0'' = E_0' - E_0 \tag{10.1.54}$$

$$\sqrt{\frac{\varepsilon}{\mu}} (2E_0 - E_0') \cos(\Theta_i) - \sqrt{\frac{\varepsilon'}{\mu'}} E_0' \cos(\Theta_i) = 0 \tag{10.1.55}$$

and after some manipulations

$$\frac{E_0'}{E_0} = \frac{2\sqrt{\frac{\varepsilon}{\mu}} \cos(\Theta_i)}{\sqrt{\frac{\varepsilon}{\mu}} \cos(\Theta_i) + \sqrt{\frac{\varepsilon'}{\mu'}} \cos(\Theta_i)} \tag{10.1.56}$$

Trigonometric identity says that $\cos(\alpha) = \sqrt{1 - \sin^2(\alpha)}$ and from the Snell's law we got also $\sin(\Theta_t) = \frac{n}{n'} \sin(\Theta_i)$. Using those equation one can find the electric fields ratio:

$$\frac{E'_0}{E_0} = \frac{2\sqrt{\varepsilon} \cos(\Theta_i)}{\sqrt{\varepsilon} \cos(\Theta_i) + \sqrt{\varepsilon'} \sqrt{\frac{\mu}{\mu'}} \sqrt{1 - \frac{n^2}{n'^2} \sin^2(\Theta_i)}} \quad (10.1.57)$$

In terms of indices of refraction $n = \sqrt{\mu\varepsilon / \mu_0\varepsilon_0}$ and $n' = \sqrt{\mu'\varepsilon' / \mu_0\varepsilon_0}$ it can be finally rewritten as:

$$t_s = \frac{E'_0}{E_0} = \frac{2n \cos(\Theta_i)}{n \cos(\Theta_i) + \frac{\mu}{\mu'} \sqrt{n'^2 - n^2 \sin^2(\Theta_i)}} \quad (10.1.58)$$

This is the expression for an amplitude transmission coefficient for *s*-polarization (TE). The amplitude reflection coefficient now can be found as a ratio between the reflected and incident electric field:

$$E'_0 = E''_0 + E_0 \quad (10.1.59)$$

$$\sqrt{\frac{\varepsilon}{\mu}} (E_0 - E''_0) \cos(\Theta_i) - \sqrt{\frac{\varepsilon'}{\mu'}} (E''_0 + E_0) \cos(\Theta_i) = 0 \quad (10.1.60)$$

$$E_0 \left[\sqrt{\frac{\varepsilon}{\mu}} \cos(\Theta_i) - \sqrt{\frac{\varepsilon'}{\mu'}} \cos(\Theta_i) \right] - E''_0 \left[\sqrt{\frac{\varepsilon}{\mu}} \cos(\Theta_i) + \sqrt{\frac{\varepsilon'}{\mu'}} \cos(\Theta_i) \right] = 0 \quad (10.1.61)$$

$$\frac{E''_0}{E_0} = \frac{\sqrt{\frac{\varepsilon}{\mu}} \cos(\Theta_i) - \sqrt{\frac{\varepsilon'}{\mu'}} \cos(\Theta_i)}{\sqrt{\frac{\varepsilon}{\mu}} \cos(\Theta_i) + \sqrt{\frac{\varepsilon'}{\mu'}} \cos(\Theta_i)} \quad (10.1.62)$$

Expressing this relation in terms of the incident angle only we have:

$$\frac{E''_0}{E_0} = \frac{\sqrt{\frac{\varepsilon}{\mu}} \cos(\Theta_i) - \sqrt{\frac{\varepsilon'}{\mu'}} \sqrt{1 - \frac{n^2}{n'^2} \sin^2(\Theta_i)}}{\sqrt{\frac{\varepsilon}{\mu}} \cos(\Theta_i) + \sqrt{\frac{\varepsilon'}{\mu'}} \sqrt{1 - \frac{n^2}{n'^2} \sin^2(\Theta_i)}} \quad (10.1.63)$$

Finally in terms of indices of refraction the expression for an amplitude reflection coefficient for *s*-polarization is equal to

$$r_s = \frac{E''_0}{E_0} = \frac{n \cos(\Theta_i) - \frac{\mu}{\mu'} \sqrt{n'^2 - n^2 \sin^2(\Theta_i)}}{n \cos(\Theta_i) + \frac{\mu}{\mu'} \sqrt{n'^2 - n^2 \sin^2(\Theta_i)}} \quad (10.1.64)$$

For the optical frequencies it is often permitted to substitute $\mu / \mu' = 1$.

If the electric field is parallel to the plane of incidence, as in Figure 10.1.3, the boundary conditions that needs to be considered are continuity of normal \vec{D} , tangential

\vec{E} and \vec{H} . This polarization is also called TM (transverse magnetic) or simply *p*-polarization in respect to the interface plane.

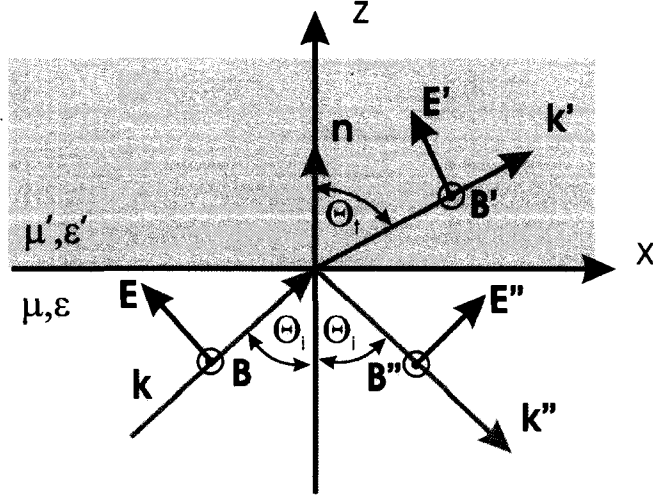


Figure 10.1.3. Reflection and refraction with polarization parallel to the plane of incidence (TM)

Considering firstly the tangential component of electric field \vec{E} and using the cross product rule we have:

$$(\vec{E}_0 + \vec{E}'' - \vec{E}') \times \vec{n} = 0 \quad (10.1.65)$$

$$(\vec{E}_0 + \vec{E}'' - \vec{E}') \times \vec{n} = 0 \quad (10.1.66)$$

Knowing that $\vec{a} \times \vec{b} = |\vec{a}| |\vec{b}| \sin(\Theta_{ab})$ and considering the angles one can write:

$$|\vec{E}_0| |\vec{n}| \sin\left(\frac{\pi}{2} - \Theta_i\right) + |\vec{E}''| |\vec{n}| \sin\left(\frac{3}{2}\pi - \Theta_i\right) - |\vec{E}'| |\vec{n}| \sin\left(\frac{\pi}{2} - \Theta_t\right) = 0 \quad (10.1.67)$$

$$E_0 \cos(\Theta_i) + E''(-\cos(\Theta_i)) - E' \cos(\Theta_t) = 0 \quad (10.1.68)$$

By rearranging the terms it is easy to see that:

$$(E_0 - E'') \cos(\Theta_i) - E' \cos(\Theta_t) = 0 \quad (10.1.69)$$

Now for the normal component of displacement field \vec{D} :

$$(\epsilon \vec{E}_0 + \epsilon \vec{E}'' - \epsilon' \vec{E}') \cdot \vec{n} = 0 \quad (10.1.70)$$

$$\epsilon \vec{E}_0 \cdot \vec{n} + \epsilon \vec{E}'' \cdot \vec{n} - \epsilon' \vec{E}' \cdot \vec{n} = 0 \quad (10.1.71)$$

Using the dot product rule and the Snell's law:

$$\epsilon |\vec{E}_0| |\vec{n}| \cos\left(\frac{\pi}{2} - \Theta_i\right) + \epsilon |\vec{E}''| |\vec{n}| \cos\left(\frac{3}{2}\pi + \Theta_i\right) - \epsilon' |\vec{E}'| |\vec{n}| \cos\left(\frac{\pi}{2} - \Theta_t\right) = 0 \quad (10.1.72)$$

$$\epsilon E_0 \sin(\Theta_i) + \epsilon E'' \sin(\Theta_i) - \epsilon' E' \sin(\Theta_t) = 0 \quad (10.1.73)$$

Snell's law can be written in terms of wave vectors as:

$$\frac{\sin(\Theta_t)}{\sin(\Theta_i)} = \frac{k'}{k} \Rightarrow \sin(\Theta_t) = \sin(\Theta_i) \frac{k'}{k} \quad (10.1.74)$$

Substituting this to the previous equation we have:

$$\frac{\varepsilon}{k} E_0 + \frac{\varepsilon}{k} E_0'' - \frac{\varepsilon'}{k'} E_0' = 0 \quad (10.1.75)$$

$$\sqrt{\frac{\varepsilon}{\mu}} (E_0 + E_0'') - \sqrt{\frac{\varepsilon'}{\mu'}} E_0' = 0 \quad (10.1.76)$$

Similarly using 10.1.69 and 10.1.76 we again can derive the expressions for the amplitude reflection and refraction coefficients.

$$E_0'' = \frac{\sqrt{\frac{\varepsilon'}{\mu'}} E_0' - \sqrt{\frac{\varepsilon}{\mu}} E_0}{\sqrt{\frac{\varepsilon}{\mu}}} \quad (10.1.77)$$

$$\left(E_0 - \frac{\sqrt{\frac{\varepsilon'}{\mu'}} E_0' - \sqrt{\frac{\varepsilon}{\mu}} E_0}{\sqrt{\frac{\varepsilon}{\mu}}} \right) \cos(\Theta_i) - E_0' \cos(\Theta_i) = 0 \quad (10.1.78)$$

$$2\sqrt{\frac{\varepsilon}{\mu}} E_0 \cos(\Theta_i) - E_0' \left(\sqrt{\frac{\varepsilon'}{\mu'}} \cos(\Theta_i) + \sqrt{\frac{\varepsilon}{\mu}} \cos(\Theta_i) \right) = 0 \quad (10.1.79)$$

$$\frac{E_0'}{E_0} = \frac{2\sqrt{\frac{\varepsilon}{\mu}} \cos(\Theta_i)}{\sqrt{\frac{\varepsilon'}{\mu'}} \cos(\Theta_i) + \sqrt{\frac{\varepsilon}{\mu}} \cos(\Theta_i)} \quad (10.1.80)$$

In terms only of the incident angle

$$\frac{E_0'}{E_0} = \frac{2\sqrt{\frac{\varepsilon}{\mu}} \cos(\Theta_i)}{\sqrt{\frac{\varepsilon'}{\mu'}} \cos(\Theta_i) + \sqrt{\frac{\varepsilon}{\mu}} \sqrt{1 - \frac{n^2}{n'^2} \sin^2(\Theta_i)}} \quad (10.1.81)$$

Plugging back the indices of refraction for each region

$$t_p = \frac{E_0'}{E_0} = \frac{2nn' \cos(\Theta_i)}{\frac{\mu}{\mu'} n'^2 \cos(\Theta_i) + n \sqrt{n'^2 - n^2 \sin^2(\Theta_i)}} \quad (10.1.82)$$

This is the amplitude transmission coefficient for *p*-polarization. Using the same approach we can find that:

$$E_0' = \frac{\sqrt{\frac{\varepsilon}{\mu}} (E_0'' + E_0)}{\sqrt{\frac{\varepsilon'}{\mu'}}} \quad (10.1.83)$$

$$(E_0 - E_0'') \cos(\Theta_i) - \frac{\sqrt{\frac{\epsilon}{\mu}} (E_0'' + E_0)}{\sqrt{\frac{\epsilon'}{\mu'}}} \cos(\Theta_i) = 0 \quad (10.1.84)$$

$$\sqrt{\frac{\epsilon'}{\mu'}} (E_0 - E_0'') \cos(\Theta_i) - \sqrt{\frac{\epsilon}{\mu}} (E_0'' + E_0) \cos(\Theta_i) = 0 \quad (10.1.85)$$

$$E_0 \left[\sqrt{\frac{\epsilon'}{\mu'}} \cos(\Theta_i) - \sqrt{\frac{\epsilon}{\mu}} \cos(\Theta_i) \right] - E_0'' \left[\sqrt{\frac{\epsilon'}{\mu'}} \cos(\Theta_i) + \sqrt{\frac{\epsilon}{\mu}} \cos(\Theta_i) \right] = 0 \quad (10.1.86)$$

$$\frac{E_0''}{E_0} = \frac{\sqrt{\frac{\epsilon'}{\mu'}} \cos(\Theta_i) - \sqrt{\frac{\epsilon}{\mu}} \cos(\Theta_i)}{\sqrt{\frac{\epsilon'}{\mu'}} \cos(\Theta_i) + \sqrt{\frac{\epsilon}{\mu}} \cos(\Theta_i)} \quad (10.1.87)$$

In terms of the incidence angle only:

$$\frac{E_0''}{E_0} = \frac{\sqrt{\frac{\epsilon'}{\mu'}} \cos(\Theta_i) - \sqrt{\frac{\epsilon}{\mu}} \sqrt{1 - \frac{n^2}{n'^2} \sin^2(\Theta_i)}}{\sqrt{\frac{\epsilon'}{\mu'}} \cos(\Theta_i) + \sqrt{\frac{\epsilon}{\mu}} \sqrt{1 - \frac{n^2}{n'^2} \sin^2(\Theta_i)}} \quad (10.1.88)$$

Finally replacing permittivity and permeability by index of refraction one can have:

$$r_p = \frac{E_0''}{E_0} = \frac{\frac{\mu}{\mu'} n'^2 \cos(\Theta_i) - n \sqrt{n'^2 - n^2 \sin^2(\Theta_i)}}{\frac{\mu}{\mu'} n'^2 \cos(\Theta_i) + n \sqrt{n'^2 - n^2 \sin^2(\Theta_i)}} \quad (10.1.89)$$

This is the amplitude reflection coefficient for p -polarization.

The equations for r_s, r_p, t_s, t_p are the well known Fresnel equations. In the case of Lloyd mirror interferometer, one medium was a vacuum while the other was a thin layer of chromium evaporated on the silicon wafer. The index of refraction of vacuum is equal to $n=1$, while for the metal layer the index of refraction is a complex quantity $n=1-\delta+i\beta$. According to the theory of atomic scattering factors and the extensive data tables [10.2] this index of refraction can be written in terms of atomic scattering factors $f_1^0(\omega)$ and $f_2^0(\omega)$. Scattering by multiple electrons atom can be described with semi-classical model that assumes point electrons each with its own resonant frequency, excited by a continuous electromagnetic wave [10.3]. At very short wavelengths (X-ray region of e-m spectrum) the assumption of the same coordinates for each electron doesn't hold any more, since the wavelength is comparable to the size of the atom. The general idea of the scattering of light by multi electron atom is depicted in Figure 10.1.4.

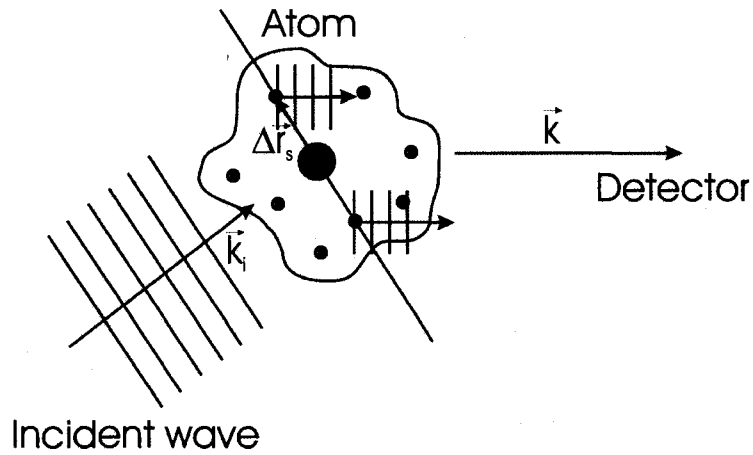


Figure 10.1.4. Scattering diagram for atom that contains many electrons.

Assuming that each electron's motion can be described by an oscillatory motion excited by the incident electric field:

$$m \frac{d^2 \bar{x}_s}{dt^2} + m\gamma \frac{d\bar{x}_s}{dt} + m\omega_s^2 \bar{x}_s = -eE_i \quad (10.1.90)$$

The complex atomic scattering factor $f(\Delta\vec{k}, \omega)$ can be expressed as:

$$f(\Delta\vec{k}, \omega) = \sum_{s=1}^Z \frac{\omega^2 e^{-i\Delta\vec{k} \cdot \Delta\vec{r}_s}}{\omega^2 - \omega_s^2 + i\gamma\omega} \quad (10.1.91)$$

$\Delta\vec{r}_s$ is the vector displacement of the electron from the nucleus, Z is the total number of electrons in the atom, ω is the frequency of the incident wave, ω_s is the resonant frequency for each electron, $\Delta\vec{k} = \vec{k} - \vec{k}_i$ is the vector periodicity associated with the inhomogeneity of the medium, that results in a scattering of the propagation vector \vec{k}_i in a direction characterized by a vector \vec{k} as schematically depicted in Figure 10.1.5. Since both \vec{k}_i and \vec{k} propagate in vacuum and the scattering is stationary the vector diagram is isosceles and $|\Delta\vec{k}| = 2\vec{k}_i \sin \Theta$

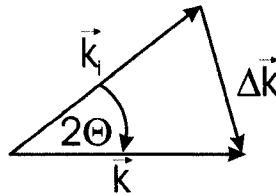


Figure 10.1.5. A vector scattering diagram for incident wave vector \vec{k}_i and scattered wave vector \vec{k} .

In general $\Delta\vec{k} \cdot \Delta\vec{r}$ phase terms do not simplify. That makes the analysis of complex atomic scattering factors difficult. There are however two special cases when this phase terms do simplify. Knowing that $\vec{k}_i = 2\pi / \lambda$, then

$$\Delta k = \frac{4\pi}{\lambda} \sin \Theta \quad (10.1.92)$$

Charge distribution within the atom is mostly contained in the dimensions in orders of the Bohr radius:

$$a_0 = \frac{4\pi\epsilon_0\hbar^2}{me^2} = 0.529 \text{ \AA} \quad (10.1.93)$$

With this assumption the phase expression is equal to $|\Delta\vec{k} \cdot \Delta\vec{r}| \leq \frac{4\pi a_0}{\lambda} \sin \Theta$. Two special cases can be considered. The first case is for $|\Delta\vec{k} \cdot \Delta\vec{r}| \rightarrow 0$ when the illumination wavelength is much longer than the Bohr radius $a_0/\lambda \ll 1$. This is called long wavelength limit. The second case is $|\Delta\vec{k} \cdot \Delta\vec{r}| \rightarrow 0$ if $\Theta \rightarrow 0$, for the case of forward scattering only. In each of these two cases the $f(\Delta\vec{k}, \omega)$ reduces to:

$$f^0(\omega) = \sum_{s=1}^Z \frac{\omega^2}{\omega^2 - \omega_s^2 + i\gamma\omega} \quad (10.1.94)$$

Zero in superscript denotes those special cases. Clearly at the EUV laser wavelength $\lambda = 46.9 \text{ nm}$ long wavelength limit approximation holds. The atomic scattering factor is a complex quantity and can be expressed in terms of its real and imaginary parts. The sign of the imaginary part of complex atomic scattering factor may be different depending on the data source. In this analysis CXRO database approach will be used to be consistent with the CXRO data.

$$f^0(\omega) = f_1^0(\omega) + if_2^0(\omega) \quad (10.1.95)$$

Now the complex index of refraction of the material can be expressed in terms of the atomic scattering factors:

$$n(\omega) = 1 - \delta + i\beta = 1 - \frac{n_a r_e \lambda^2}{2\pi} [f_1^0(\omega) + if_2^0(\omega)] \quad (10.1.96)$$

n_a is the number of atoms per unit volume in the material, r_e is a classical electron radius, $r_e = 2.818 \cdot 10^{-15} \text{ m}$.

To compare the reflectivity of the Cr mirror for different polarizations obtained from CXRO database at 30eV, 41.3nm wavelength, with the values calculated based on the atomic scattering factors, the complex index of refraction for Cr material was calculated based on the values of atomic scattering factors obtained at photon energy $E = 29.77 \text{ eV}$, $f_1^0 = 5.9291$, $f_2^0 = 2.9049$. The density of chromium is $7140 \frac{\text{kg}}{\text{m}^3}$ and the

atomic mass of chromium $m_{at_Cr} = 51.996$, that gives $n_a = 8.27 \cdot 10^{28} \frac{1}{\text{m}^3}$ atoms per cubic meter. Finally the complex index of refraction for chromium at that energy is equal to $n_{Cr} = n' = 0.6186 - i0.1869$. This index of refraction value was plugged back into the Fresnel equations derived previously to calculate the reflectivity of the mirror for both s and p -polarizations. The reflectivity coefficients were calculated $R_s = |r_s|^2$ and $R_p = |r_p|^2$

considering the intensities, not the amplitudes of the fields. Figure 10.1.6 compares the calculated reflectivity and the values obtained from the CXRO website [10.4] as a function of the grazing incidence angle $\Theta = \frac{\pi}{2} - \Theta_i$.

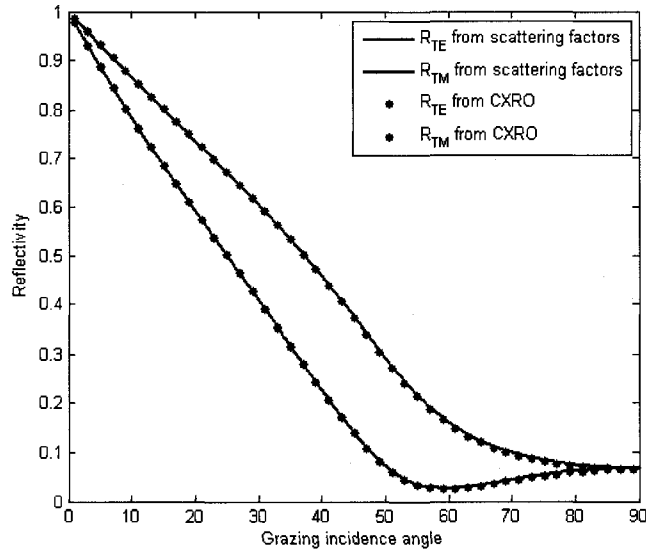


Figure 10.1.6. Comparison plot for the reflectivity of the chromium mirror between the data obtained from CXRO database and calculated using complex atomic scattering factors for various polarizations.

One can see very good agreement between both data. That means, that using the reflectivity data from CXRO database for visibility calculations or calculating it from atomic scattering factors leads to the same results discussed in previous chapters.

10.2 Appendix II: Description of the design of the Gaussian filters and their relation to the image resolution

The method used to estimate the image resolution is based on the correlation between the raw image and a series of synthesized templates of known feature size and resolution that are generated by appropriate processing of the original image as described in the experiments with the carbon nanotubes and the EUV microscope images.

The images and templates are digital in nature and therefore pixilated. These images can be considered as a discrete version of a continuous image $c(x,y)$ sampled in a matrix. A grid of $M \times N$ pixels of size w_x and w_y was assumed. The sampled image $c(x_m, y_n)$ is obtained by multiplication of $c(x,y)$ with an array of delta functions located in every pixel:

$$c(x_m, y_n) = \sum_{m \in M} \sum_{n \in N} \delta(x - x_m, y - y_n) \cdot c(x, y) \quad (10.2.1)$$

where $x_m = w_x \cdot m$ and $y_n = w_y \cdot n$ are the coordinates of the pixel (m,n) .

The pixelated image can be represented as a convolution between the sampled image $c(x_m, y_n)$ with a 2D rectangular function $p(w_x, w_y)$ that represents the pixel.

The first of the reference templates is “binary”, i.e. the function $c(x, y)$ has only two possible values, zero or one. With this assumption the binary template can be expressed:

$$\begin{aligned} i_b(x, y) &= c_b(x_m, y_n) \otimes p(w_x, w_y) \\ &= \left[\sum_{m \in M} \sum_{n \in N} \delta(x - x_m, y - y_n) \cdot c_b(x, y) \right] \otimes p(w_x, w_y) \end{aligned} \quad (10.2.2)$$

where $c_b(x_m, y_n)$ is a binary function that represents the sampled binary image. In the spatial frequency domain the function $p(w_x, w_y)$ can be expressed in terms of a 2-D *sinc* function:

$$\begin{aligned} I_b(f_x, f_y) &= \left[\sum_{m \in M} \sum_{n \in N} \exp(-j2\pi(f_x x_m + f_y y_n)) \otimes C_b(f_x, f_y) \right] \cdot \\ &\quad \frac{\sin(\pi f_x w_x)}{\pi f_x w_x} \cdot \frac{\sin(\pi f_y w_y)}{\pi f_y w_y} \end{aligned} \quad (10.2.3)$$

where f_x and f_y are the coordinates corresponding to x and y in the Fourier spatial frequency domain and $C_b(f_x, f_y)$ is the Fourier transform of the binary function $c_b(x_m, y_n)$. Notice that the scaling factors were neglected. The exponential terms in 10.2.3 account for the phase accumulation dependent on the shift of each pixel relative to the (0, 0) reference position.

The binary image has a resolution of one pixel by construction (the transition from maximum to minimum intensity takes place over the distance of one pixel). In order to modify the resolution and generate the set of templates that are used to correlate with the image under analysis, we implemented a Gaussian filter with a FWHM equal to w_f . These Gaussian filters are used to generate the set of templates with known resolution. In the spatial frequency domain the Gaussian filter is represented by:

$$F(f_x, f_y, w_f) = \exp\left(-\frac{\pi^2 w_f^2}{4 \ln 2} (f_x^2 + f_y^2)\right) \quad (10.2.4)$$

The effect of reducing the spatial resolution in an image is equivalent to decreasing the range of the spatial frequencies in its Fourier domain. In order to generate a series of templates with different spatial resolutions, the filter defined in 10.2.4 was initially applied to each one of the pixels in the binary template described by equation 10.2.3. This corresponds in the spatial domain to a convolution while in the spatial frequency domain can be described as the product of the two functions:

$$T(f_x, f_y) = I_b(f_x, f_y) \cdot F(f_x, f_y, w_f) \quad (10.2.5)$$

where $T(f_x, f_y)$ describes the template after applying a filter of width w_f represented in the Fourier domain. We assume that the pixels are squares, this is $w_x = w_y = w_0$. Furthermore we also replace each square pixel by a “Gaussian pixel” defined as a Gaussian profile with FWHM equal to w_0 . This substitution modifies the binary template and generates an error that is at the most 6% and that can be easily evaluated comparing

the integral of a two dimensional square function (representing the real square pixel) with the integral of a 2D Gaussian function (representing the approximate Gaussian pixel). The Gaussian pixel provides a convenient way to easily establish an analytical relationship between the Gaussian filter width and the spatial resolution. The substitution of the square pixels by the Gaussian pixels results in changing the image function defined in 10.2.3 to:

$$I_b(f_x, f_y) = \left[\sum_{m \in M} \sum_{n \in N} \exp(-j2\pi(f_x x_m + f_y y_n)) \otimes C_b(f_x, f_y) \right] \cdot \exp\left(-\pi^2 \frac{w_0^2}{4 \ln 2} (f_x^2 + f_y^2)\right) \quad (10.2.6)$$

With this substitution equation 10.2.5 becomes:

$$T(f_x, f_y) = \left[\sum_{m \in M} \sum_{n \in N} \exp(-j2\pi(f_x m \cdot w_0 + f_y n \cdot w_0)) \otimes C_b(f_x, f_y) \right] \cdot \exp\left(-\pi^2 \frac{w_0^2}{4 \ln 2} (f_x^2 + f_y^2)\right) \cdot \exp\left(-\pi^2 \frac{w_f^2}{4 \ln 2} (f_x^2 + f_y^2)\right) \quad (10.2.7)$$

This expression in the spatial domain corresponds to a convolution expressed as:

$$t(x, y) = \left[\sum_{m \in M} \sum_{n \in N} \delta(x - m \cdot w_0, y - n \cdot w_0) \cdot C_b(x, y) \right] \otimes \exp\left(-\frac{4 \ln 2}{w_0^2} (x^2 + y^2)\right) \otimes \exp\left(-\frac{4 \ln 2}{w_f^2} (x^2 + y^2)\right) \quad (10.2.8)$$

The first two terms in this expression are the approximated image function $i_b(x_m, y_n)$ where the rectangular pixels were replaced by the Gaussian pixels of width w_0 .

To evaluate the effect of the Gaussian filtering in the Gaussian pixels, the simplest case of an image composed by only one pixel with value 1 in the position $m = n = 0$ was considered. In this simplified example the convolution with a Gaussian filter of width w_f can be expressed by:

$$T(f_x, f_y, w_0, w_f) = \exp\left(-\pi^2 \frac{w_0^2 + w_f^2}{4 \ln 2} (f_x^2 + f_y^2)\right) = \exp\left(-\pi^2 \frac{\delta^2}{4 \ln 2} (f_x^2 + f_y^2)\right) \quad (10.2.9)$$

where $\delta = \sqrt{w_0^2 + w_f^2}$ is the FWHM of the image obtained after a Gaussian filter of width w_f is applied to a Gaussian pixel of width w_0 . This relation shows that applying the Gaussian filter with width w_f causes the image features to be larger by a factor $\eta = \delta / w_0$. In the spatial frequency domain this is equivalent to reduce the spectrum width by the same factor. The resolution of the filtered image can thus be related to the factor δ . The width of the filter necessary to apply to reduce the spectrum by a factor η may now be expressed as:

$$w_f(\delta) = w_0 \sqrt{\left(\frac{\delta}{w_0}\right)^2 - 1} = w_0 \sqrt{\eta^2 - 1} \quad (10.2.10)$$

To improve the sampling in the definition of the filter, in particular when the filter's FWHM becomes comparable to pixel size, the initial pixel was divided by an integer factor r . This division increases the size of the array containing the image by a factor $r \times r$. The new image represented with the smaller pixels is obtained by extrapolation using the nearest neighborhood method. The extrapolation also changes the size of the image. The pixel in the expanded scale will have a width $w'_0 = w_0/r$. The Gaussian pixel with original width w_0 will be represented by a Gaussian pixel with width $r \cdot w'_0$. All the formalism presented above applies now to the image with the smaller pixels and the filter width can be expressed as:

$$w'_f(\delta) = w_0 \sqrt{\left(\frac{\delta}{w_0/r}\right)^2 - 1} = (w'_0 \cdot r) \sqrt{(\eta \cdot r)^2 - 1} \quad (10.2.11)$$

Equation 10.2.11 was used to calculate the width of the Gaussian filter that it is necessary to apply to obtain a spectral reduction of a factor η in the filtered image. Although in all this formalism we are approximating the real image that originally has square pixels by an image with Gaussian pixels, the approximation gives very good results as it was shown in the analysis of the images processed with this algorithm. In the case of EUV microscope images for all the images analyzed the pixel size was $w_0 = 12.5nm$. Using an extrapolation factor $r = 5$ in the data processing, the resulting pixel size is $w'_0 = 2.5nm$. In the case of carbon nanotubes holographic imaging the pixel size was always $w_0 = 9.7nm$ and the extrapolation factor used in data processing was equal to $r = 3$ resulting pixel size equal to $w'_0 = 3.23nm$.

10.3 Appendix III: Codes and algorithms used in EUV holography experiments

Holography codes presented here were necessary for numerical data processing of the holograms, after the digitization with atomic force microscope (AFM). The result of this digitization can be either *.jpg file or *.csv file and both types of files were processed. Hologram reconstruction code was adopted from previous work of Prof. Randy Bartels and used with his approval (kernel reconstruction code for AFM tips, spherical markers and carbon nanotubes). The remaining codes shown in this Appendix were developed by the author who admits that he put all his efforts to honestly debug the codes.

10.3.1 Reconstruction algorithm for the Gabor holography

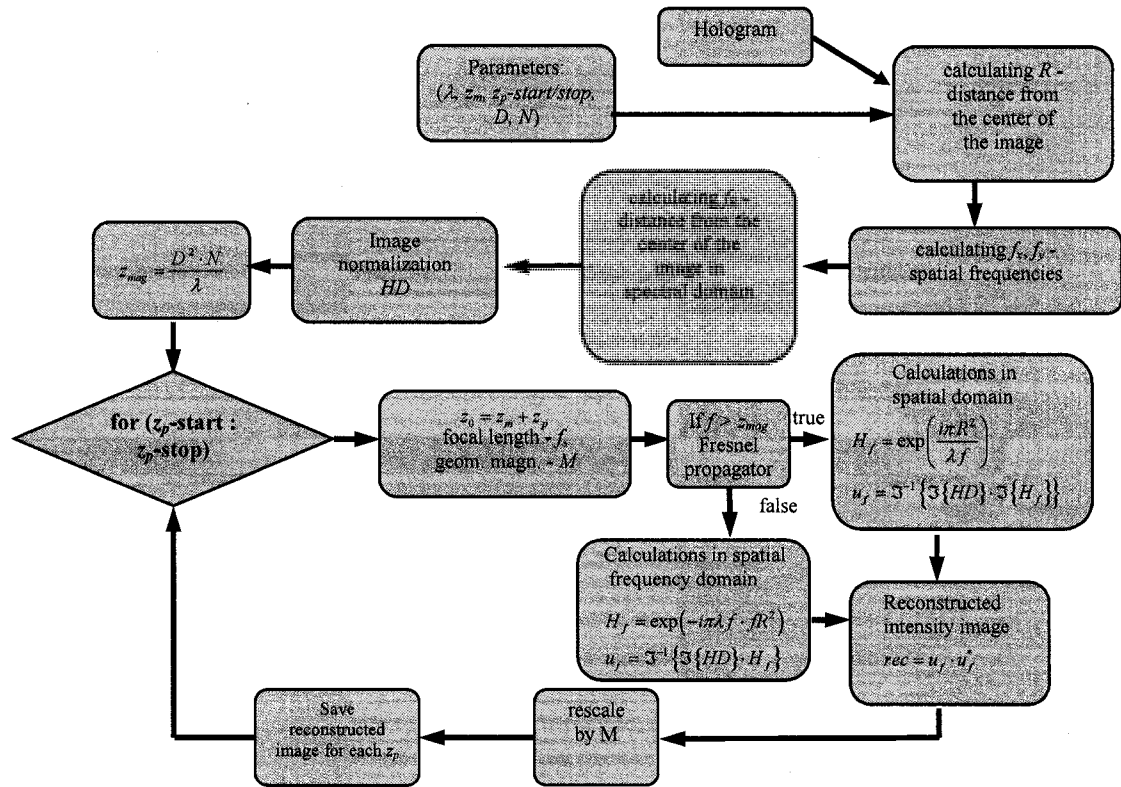


Figure 10.3.1. Detailed flowchart of the reconstruction code

```
% Kernel of the reconstruction algorithm in Gabor
holography
```

```
% Part 1
% Holography of AFM tips (reconstruction distance zp~4mm)
```

```
% units
clear all; clc;
um=1e-6;
nm=1e-9;
mm=1e-3;
```

```
file_num=1;
```

```
switch file_num
case 1
```

```

    file_name='rec8.JPG';

    % Read in Data File
    HD = imread(file_name, 'JPG');
    HD = rgb2gray(HD);
    HD = im2double(HD);

    % plot hologram
    figure(1)
    subplot(2,3,1)
    imagesc(HD);
    title('Loaded image')
    axis square

    S=size(HD);

    % get size of the hologram
    Nx=S(2);
    Ny=S(1);

    % hologram pixel size
    Dx=270*nm;      % 270nm for sep. 4mm
                   % 195.3nm for sep. 0.8mm 100um/512pix

    Dy=Dx; % square image
    otherwise
        file_name='error.asc';
end

% Main loop begins
% set reconstruction distanfes from 3.8mm to 4.3mm in 10um
step

for num=3.80:0.01:4.30
    zp=num*mm; % propagation distance from the hologram to the
    recording plane (recording-reconstruction distance
    % distance from source to hologram
    zm=1.5;
    % wavelength of illumination
    lambda=47*nm;

    % reconstruction location
    zo=zm+zp;
    % hologram focal distance
    f=1/(1/zp-1/zo);

```

```

% geometrical magnification factor
Mc=1/(1-zp/zo);

% Create the x,y grid;
x=( [1:Nx]-Nx/2)*Dx;
y=( [1:Ny]-Ny/2)*Dy;
[X,Y]=meshgrid(x,y);
R=sqrt(X.^2+Y.^2);

% calculate spatial frequencies
dfx=1/Nx/Dx;
fx=( [1:Nx]-Nx/2)*dfx;
fxs=fftshift(fx);

% do the same in spatial frequency domain
dfy=1/Ny/Dx;
fy=( [1:Ny]-Ny/2)*dfy;
fys=fftshift(fy);

[fX,fY]=meshgrid(fx,fy);
fR=sqrt(fX.^2+fY.^2);
fRs=fftshift(fR);

% calculate the Magic Distance
zmagic=Dx^2*Nx/lambda;

% normalize the hologram

HDp=HD/max(max(HD));

% plot the normalized hologram
subplot(2,3,2)
imagesc(x*1e3,y*1e3,HDp,[0 .8])
xlabel('x (mm)')
ylabel('y (mm)')
title('Gabor Hologram Data - normalized')
axis square
colormap gray

% transform to spatial frequency domain
% and plot the hologram in spatial frequency domain
Uf=fft2(sqrt(HD));
subplot(2,3,3)
imagesc(fx/1e3,fy/1e3,fftshift(log10(abs(Uf))))

```

```

axis square
xlabel('fx (mm-1)')
ylabel('fy (mm-1)')
title('Hologram Spatial Frequency Spectrum')

% reconstruct the hologram (with a plane wave)
if f>zmagic
    Hf=fft2(exp(-i*pi*R.^2/lambda/(-f)));
    uf=ifft2(fft2(HD).*Hf);
    uf=fftshift(uf);
else
    Hf=exp(i*pi*lambda*(-f)*fRs.^2);
    uf=ifft2(fft2(HD).*Hf);
end

% rescale axes by the geometrical magnification factor
x=x/Mc;
y=y/Mc;

% plot the reconstructed image
subplot(2,3,4)
Rec=uf.*conj(uf);
Rec=Rec/max(max(Rec));
imagesc(Rec);
title('Reconstructed Gabor Hologram');

% take small sub-image of interest from the reconstructed
image
Wave=Rec(405:532,636:763);

% and save it as a mat file
name=strcat('wave',int2str(zp/mm*100),'.mat');
save (name, 'Wave');
sprintf('calculating for zp= %f',zp);

end

```

```

% Part 2
% Holography of carbon nanotubes (CNT holography,
reconstruction distance zp~2.7um)

clear all; clc;
% units
um=1e-6;
nm=1e-9;
mm=1e-3;

zm=0.75; % distance from source to mask
lambda=47*nm; % wavelength

file_name='1 - 10x10um 1024_1.csv'; % filename to load from
Excel file
HD=csvread(file_name);

S=size(HD);
Nx=S(2);
Ny=S(1);
Dx=10*um/1024; % size of the pixel in the image
% (10micrometers scan divided by 1024 points per line
Dy=Dx; % square image

xx=(1:1024)*Dx/um;
figure(2), imagesc(xx,xx,HD)
title(['Hologram:'])
xlabel('Distance [\mum]'); ylabel('Distance [\mum]');
axis square
colormap gray
pause(2)
save ('HD.mat','HD');

%number of reconstructions
dx=20;
% start reconstruction distance in [um]
start=2.5;
% stop reconstruction distance in [um]
stop=3.0;
% save reconstruction data
save ('rec_cond.mat', 'start', 'stop', 'dx');

% ***** Precalculations: *****

% Create the x,y grid;
x=( [1:Nx]-Nx/2)*Dx;
y=( [1:Ny]-Ny/2)*Dy;

```

```

[X,Y]=meshgrid(x,y);
R=sqrt(X.^2+Y.^2);

% calculate spatial frequencies
dfx=1/Nx/Dx;
fx=( [1:Nx]-Nx/2)*dfx;
fxs=fftshift(fx);

dfy=1/Ny/Dx;
fy=( [1:Ny]-Ny/2)*dfy;
fys=fftshift(fy);

[fX,fY]=meshgrid(fx,fy);
fR=sqrt(fX.^2+fY.^2);
fRs=fftshift(fR);

% Magic Distance
zmagic=Dx^2*Nx/lambda;

% normalization
HDp=HD/max(max(HD));

% Main LOOP begins
for b=1:dx;
    dist=start+b*(stop-start)/dx;
    sprintf('Distance= %f um',dist)
% propagation distance from the mask to the recording plane
zp=(dist)*um;

% reconstruction location
% distance from the laser to the sample plane
zo=zm+zp;
% hologram focal length
f=1/(1/zp-1/zo);
% geometrical magnification
Mc=1/(1-zp/zo);

% reconstruct the hologram (with a plane wave)
if f>zmagic
    Hf=fft2(exp(-i*pi*R.^2/lambda/(-f)));
    uf=ifft2(fft2(HD).*Hf);
    uf=fftshift(uf);
else
    Hf=exp(i*pi*lambda*(-f)*fRs.^2);
    uf=ifft2(fft2(HD).*Hf);
end
end

```

```

% rescale by the geometrical magnification factor
x=x/Mc;
y=y/Mc;

% reconstruction image
Rec=uf.*conj(uf);
% normalized reconstruction image
Rec=Rec/max(max(Rec));

% save each image as a separate *.jpg file
name1=strcat('Rec',num2str(zp/um),'.jpg');
imwrite(Rec,name1);

end

% save reconstructed image
save ('Rec.mat','Rec');

```

10.3.2 Wavelet decomposition and correlation algorithm for resolution estimation

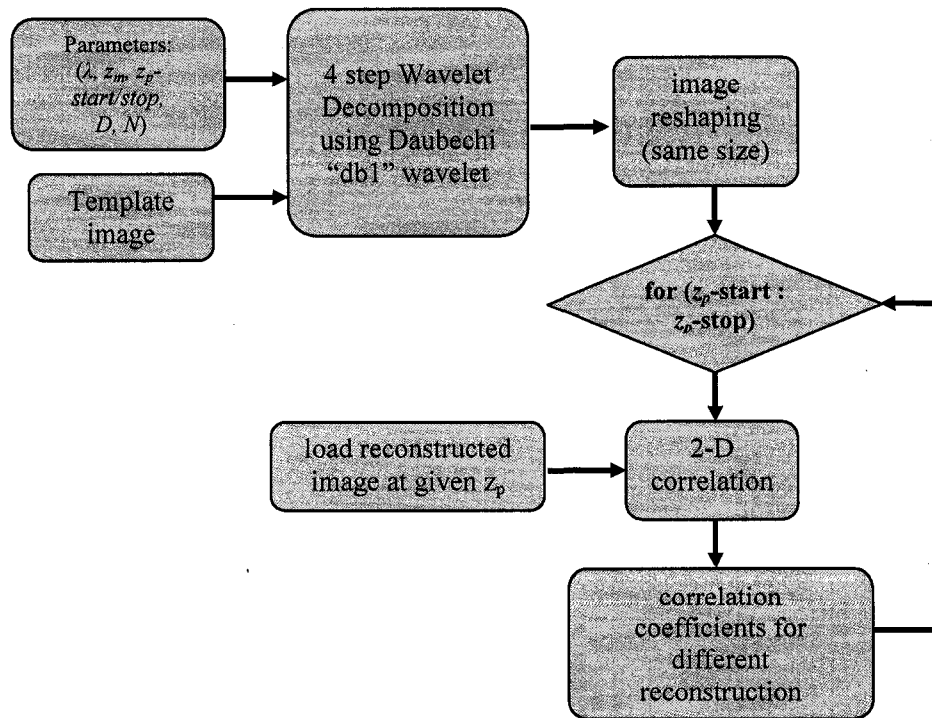


Figure 10.3.2. Detailed flowchart of the wavelet decomposition and correlation algorithm for resolution estimation

```

% Wavelets decomposition
clear all; clc;
load rec_cond.mat;
um=1e-6;

% Load original image.
Perf=imread('template.bmp');
HD = im2double(rgb2gray(Perf));

% Wavelet perfect image decomposition
cA0=HD;
[cA1,cH1,cV1,cD1] = dwt2(cA0,'db1');
cAr1=cA1+cH1+cV1+cD1;
[cA2,cH2,cV2,cD2] = dwt2(cAr1,'db1');
cAr2=cA2+cH2+cV2+cD2;
[cA3,cH3,cV3,cD3] = dwt2(cAr2,'db1');
cAr3=cA3+cH3+cV3+cD3;
[cA4,cH4,cV4,cD4] = dwt2(cAr3,'db1');
cAr4=cA4+cH4+cV4+cD4;

% resizing the matrices
resA0 = cA0;
resA1 = imresize(cAr1,size(cA0,1)/size(cAr1,1));
resA2 = imresize(cAr2,size(cA0,1)/size(cAr2,1));
resA3 = imresize(cAr3,size(cA0,1)/size(cAr3,1));
resA4 = imresize(cAr4,size(cA0,1)/size(cAr4,1));

% for different distances
for b=1:dx
    dist(b)=start+b*(stop-start)/dx;
    zp=(dist(b))*um; % propagation distance from the mask
    to the recording plane
    % load each reconstructed image at each reconstruction
    % distance zp.
    name=strcat('wave',num2str(zp/um),'.mat');
    load (name); Wavel(:, :, b)=Wave;
    % calculating the correlation coefficients
    % between each order and the data image
    % (reconstruction)
    W=Wavel(:, :, b);
    rc(1,b)= corr2(resA0, W);
end

```

```

        rc(2,b)= corr2(resA1, W);
        rc(3,b)= corr2(resA2, W);
        rc(4,b)= corr2(resA3, W);
        rc(5,b)= corr2(resA4, W);
end

ord=[0,1,2,3,4];

% plotting the results (correlation coefficients vs.
% wavelet order)
figure(3)
plot(ord,rc(:,6),'k*-',ord,rc(:,8),'ko--',ord,rc(:,11),'ks-
.',ord,rc(:,14),'kd-.',ord,rc(:,22),'k+-');
plot(ord,rc(:,8),'ro--',ord,rc(:,11),'gs-
.',ord,rc(:,14),'bd-.',ord,rc(:,22),'m+-'),axis square;
title(strcat('Wavelet decomposition at different zp'))
xlabel('wavelet order')
ylabel('correlation coefficient')
legend('zp = 116\mum','zp = 118\mum','zp = 121\mum','zp =
124\mum','zp = 132\mum','Location','NorthEastOutside');
legend('zp = 118\mum','zp = 121\mum','zp = 124\mum','zp =
132\mum','Location','South');

% plotting the results (correlation coefficients vs.
% reconstruction distance zp)
figure(4)
plot(dist,rc(1,:), 'k*-',dist,rc(2,:), 'ko--
',dist,rc(3,:), 'ks-.',dist,rc(4,:), 'kd-.',dist,rc(5,:), 'k+-
-');
plot(dist,rc(1,:), 'r+--',dist,rc(2,:), 'g+-
.',dist,rc(3,:), 'b+-.',dist,rc(4,:), 'm+-
.',dist,rc(5,:), 'k+--');
title(strcat('Correlation coeff. vs. zp distance'))
xlabel('zp distance [um]')
ylabel('correlation coefficient')
legend('0-order','1-order','2-order','3-order','4-order');

```

10.3.3 Three dimensional numerical holographic reconstruction from a single high numerical aperture hologram

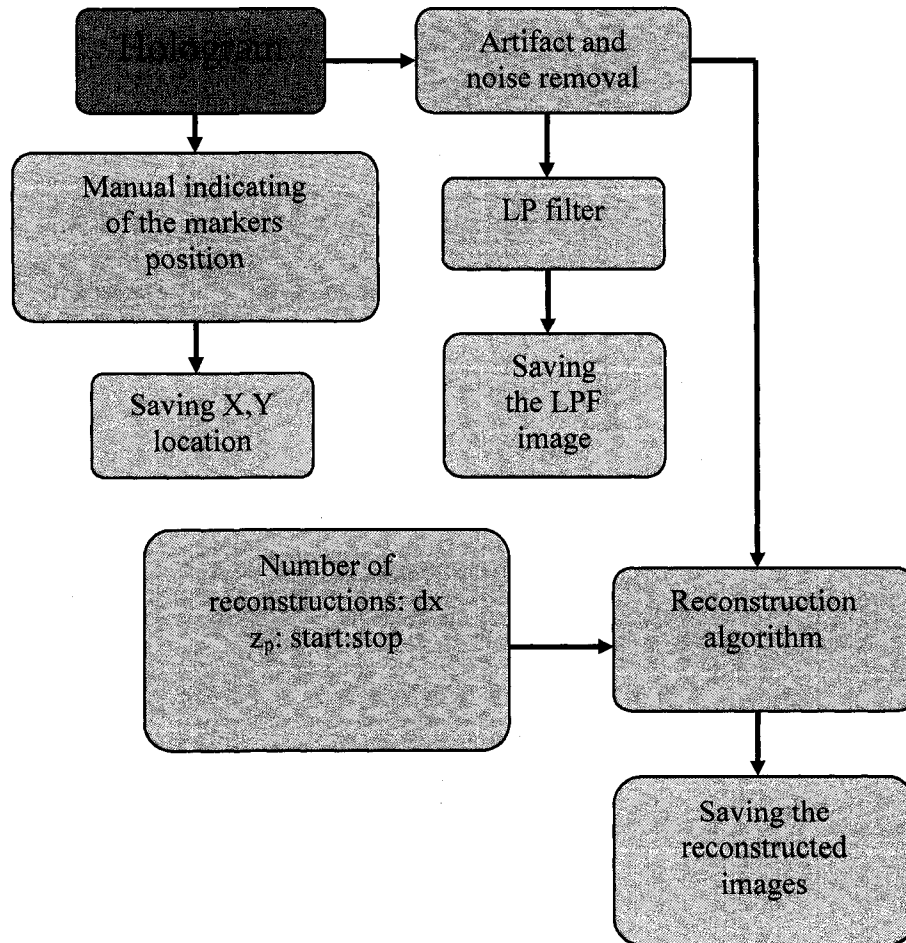


Figure 10.3.3. Detailed flowchart of the 3D holographic imaging algorithm (part 1)

```

% Part 1
% Loading the hologram from AFM microscope (*.csv file)
% units
clear all; clc;
um=1e-6;
nm=1e-9;
mm=1e-3;

file_num=1;
switch file_num
  case 1

```

```

        file_name='hologram.csv';
HD=csvread(file_name);
    zm=2.1; % distance from source to mask
    % calculation the hologram size
    S=size(HD);
    Nx=S(2);
    Ny=S(1);
    % calculating the AFM pixel size
    % 42um scan size and 1024 pixels per line
    Dx=42*um/1024;
    Dy=Dx;
    otherwise
        file_name='error.asc';
end

% wavelength of illumination
lambda=47*nm;

% save the hologram as a *.bmp file
imwrite(HD,'hologram.bmp')

% plot the hologram
figure(2), imagesc(HD)
title(['Hologram removed spots: ',file_name,])
axis square
colormap gray
pause(2)
close Figure 2

% Part 2
% Noise removal (filtering in spatial frequency domain)
% this part of the code is optional, sometimes filtering is
% necessary, sometimes not. It all depends on the hologram
% quality and a reasonable filtering is advised.

% units
clear all; clc;
um=1e-6;
nm=1e-9;
mm=1e-3;
lambda=47*nm; % wavelength of illumination

% loading the hologram image
HD = imread('hologram.bmp');
HD = im2double(HD);

```

```

% plotting the unfiltered hologram
figure(1), imagesc(HD)
title(['Hologram unfiltered: '])
axis square
colormap gray
pause(2)
close Figure 1

% image filtering in spatial frequency domain
FFTm=fft2(HD);
FFTsh=fftshift(FFTm);
figure(3)
imagesc(log(abs(FFTsh)))
title('FFT')
axis square
colormap gray

[x,y] = ginput;
close Figure 3
x=floor(x);
y=floor(y);

% defining the size of cleared domain in spatial frequency
% domain
rad=30;

% filtering in spatial frequency domain
for m=1:length(x)
    FFTsh(y(m)-rad/2:y(m)+rad/2,x(m)-rad/2:x(m)+rad/2)=0;
end

% plotting the filtering results in spatial frequency
% domain
figure(4)
imagesc(log(abs(FFTsh)))
title('FFT - removed components')
axis square
colormap gray

% transforming back to spatial domain
HDfilt=abs(ifft2(FFTsh));

% plotting the filtered hologram in spatial domain
figure(5), imagesc(HDfilt)
title(['Hologram filtered: '])

```

```

axis square
colormap gray

% saving the filtered hologram
name=['hologram_filt.bmp'];
imwrite(HDfilt,name)

% Part 3
% Making LPF mask, choosing the markers,

% units
clear all; clc;
um=1e-6;
nm=1e-9;
mm=1e-3;
lambda=47*nm;    % wavelength of illumination

% read the filtered hologram
HD = imread('hologram_filt.bmp');
HD = im2double(HD);

% generating Low Spatial Freq image
LPF=medfilt2(HD,[50,50]);

% saving the LPF image
save ('LPF.mat', 'LPF');
name=['LPF.bmp'];
imwrite(LPF,name)

% finding the dot's coordinates
% put coordinates or use a mouse

% for mouse use:
%[xd,yd] = ginput;
%xd=floor(xd);
%yd=floor(yd);
%

% manual coordinates
xd=[151,86,115,501,513,590,834,794,870,867,936,839,662,637,
360,498,454,470,140,237,237,129,201,314,333,592,606,617,501
,841,869,840,777,628];

```

```

yd=[345,223,694,361,509,469,154,910,106,790,384,569,308,533
,771,360,114,83,533,726,726,634,321,300,461,469,799,786,710
,340,107,569,548,661];

% saving the coordinates
save ('xd.mat', 'xd');
save ('yd.mat', 'yd');

% generating the Mask for intensity evaluations
Mask=zeros(1024);
dia=10; %pix 10
for m=1:length(xd)
    Mask(yd(m)-dia/2:yd(m)+dia/2,xd(m)-
dia/2:xd(m)+dia/2)=1;
end

% saving the Mask
save ('Mask.mat', 'Mask');
name=['Mask.bmp'];
imwrite(Mask,name)
imagesc(Mask);

% Part 4
% 3-D hologram reconstruction
% units
clear all; clc;
um=1e-6;
nm=1e-9;
mm=1e-3;

% distance from source to object in meters
zm=2.1;

% wavelength of illumination
lambda=47*nm;

% loading the filtered hologram
HD = imread('hologram_filt.bmp');
HD = im2double(HD);
% calculation the hologram size
S=size(HD);
Nx=S(2);
Ny=S(1);

```

```

% calculation the AFM pixel size 42um scan divided by 1024
% pixels per scan
Dx=42*um/1024;
Dy=Dx;

% plotting the filtered hologram
figure(1), imagesc(HD)
title(['Hologram filtered: '])
axis square
colormap gray
pause(2)
close Figure 1

% saving it as *.mat file
save ('HD.mat','HD');

% load previously saved data files
load LPF.mat
load Mask.mat
load xd.mat
load yd.mat

% setting the reconstruction parameters
%number of reconstructions
dx=50;

% start / stop reconstruction distance in micrometers [um]
start=140; stop=190;

% saving the reconstruction parameters
save ('rec_cond.mat', 'start', 'stop', 'dx');

% ***** Precalculations: *****

% Create the x,y grid;
x=([1:Nx]-Nx/2)*Dx;
y=([1:Ny]-Ny/2)*Dy;
[X,Y]=meshgrid(x,y);
R=sqrt(X.^2+Y.^2);

% calculate spatial frequencies
dfx=1/Nx/Dx;
fx=([1:Nx]-Nx/2)*dfx;
fxs=fftshift(fx);

dfy=1/Ny/Dx;
fy=([1:Ny]-Ny/2)*dfy;

```

```

fys=fftshift(fy);

% doing the same in spatial frequency domain
[fX,fY]=meshgrid(fx,fy);
fR=sqrt(fX.^2+fY.^2);
fRs=fftshift(fR);

% Magic Distance
zmagic=Dx^2*Nx/lambda;

% normalizing the hologram
HDp=HD/max(max(HD));

% Main LOOP begins here
for b=1:dx;
    % calculating the reconstruction distance in [um]
    dist=start+b*(stop-start)/dx;
    sprintf('Distance= %f um',dist)
    zp=(dist)*um;

% reconstruction location
zo=zm+zp;

% calculating the focal length of the hologram
f=1/(1/zp-1/zo);

% calculating the geometrical magnification
Mc=1/(1-zp/zo);

% reconstruct the hologram (with a plane wave)
if f>zmagic
    Hf=fft2(exp(-i*pi*R.^2/lambda/(-f)));
    uf=ifft2(fft2(HD).*Hf);
    uf=fftshift(uf);
else
    Hf=exp(i*pi*lambda*(-f)*fRs.^2);
    uf=ifft2(fft2(HD).*Hf);
end

% geometrical rescaling
x=x/Mc;
y=y/Mc;
% reconstructed image
Rec=uf.*conj(uf);
Rec=Rec/max(max(Rec));

% put a lum marker in the image

```

```

mark=ceil(1*um/Dx);
Rec(50:54,100:100+mark)=1;

Masked=(Rec-LPF).*Mask;

% saving each reconstructed image as a *.mat file
name=['Hol',int2str(b),'.mat'];
save(name,'Rec');

end

% Part 5
% Correlation between the reconstructed images and the
% marker template at each marker position defined manually
% previously

```

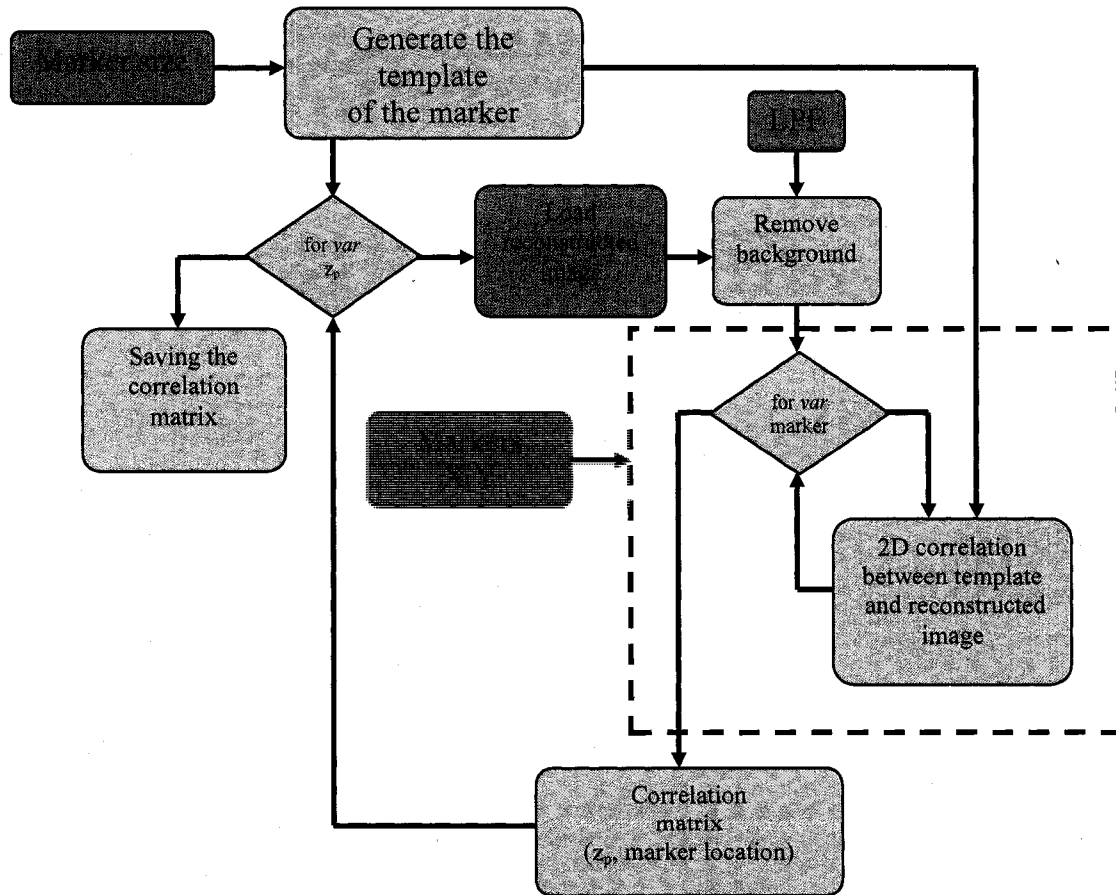


Figure 10.3.4. Detailed flowchart of the 3D holographic imaging algorithm (part 2)

```

% units
clear all; clc;
um=1e-6;
nm=1e-9;
mm=1e-3;

% distance from source to object in meters
zm=2.1;

% wavelength of illumination
lambda=47*nm;

% loading previously saved data files
load LPF.mat;
load Mask.mat;
load xd.mat;
load yd.mat;
load rec_cond.mat;

% calculating the AFM pixel size
Dx=42*um/1024;
Dy=Dx;

% setting the diameter of the marker
SSize=465*nm;
pix=Dx;

% Creating Template of the Marker (Latex Sphere)
rad=floor(SSize/2/pix);
SSize=floor(SSize/pix);
xsh=-SSize/2:SSize/2;
ysh=xsh;

TempS=zeros(21);
TempSM(:, :, 9)=zeros(21);

% Templates generation
for m=1:length(ysh) % Y
    for n=1:length(xsh) % X
        Dot(m,n)=sqrt(rad^2-xsh(n)^2-ysh(m)^2);
        Ra=sqrt(xsh(n)^2+ysh(m)^2);
        if Ra>rad
            Dot(m,n)=0;
        end
    end
end
end
end

```

```

% Embed the sphere in a larger size template
%      Y      X
TempS(5:16,6:17)=Dot; %21x21 size;
inity1=6; inity2=17; initx1=6; initx2=17;

% Make 9 templates of each marker +/-1 pixel displaced from
% it's original position to maximize the correlation
% coefficient
tok=1;
for xx=-1:1
    for yy=-1:1

TempSM(inity1+yy:inity2+yy,initx1+xx:initx2+xx,tok)=Dot;
%21x21 size original;
        tok=tok+1;
    end
end
tok=1;

% Preview the templates if necessary
%{
for g=1:size(TempSM,3)
    imagesc(TempSM(:, :,g))
    hold on
    pause(0.5)
end
hold off
%}

% creating Intensity matrix and Correlation Matrix
delta=(size(TempS,1)-1)/2;
radi=6; %pix 6

% sweeping for different zp reconstruction distances
for b=1:dx;
    % load each reconstructed image at different zp
    % distance
    name=['Hol',int2str(b),'.mat'];
    load (name);

    % remove the background and multiply by the mask image
    % for the intensity matrix calculations
    Masked=(Rec-LPF).*Mask;

    % remove the background for the correlation matrix

```

```

% calculations
Corred=(Rec-LPF);

% save images for code check
name=['Masked',int2str(b),'.jpg'];
imwrite(Rec-LPF,name)

% sweeping for every chosen marker
for m=1:length(xd)
    % intensity matrix (not explained in the text,
    % used as an alternative approach, although less
    % physical
    I(b,m)=sum(sum(Masked(yd(m)-
    radi/2:yd(m)+radi/2,xd(m)-radi/2:xd(m)+radi/2)));

    % correlation matrix for single not displaced
    % marker (on this the algorithm is
    % based, see description in the text)
    Cor(b,m)=corr2(TempS,Corred(yd(m)-
    delta:yd(m)+delta,xd(m)-delta:xd(m)+delta));

    % sleeping for each +/- 1 pixel displaced marker
    % generated before
    for bb=1:size(TempSM,3)
        % generating the same correlation
        % coefficient matrix as before additionally
        % for each displaced template too.
        Cortemp(bb)=corr2(TempSM(:,:,bb),Corred(yd(m)-
        delta:yd(m)+delta,xd(m)-delta:xd(m)+delta));
    end
    % finding the max. correlation coefficient
    % indicating the optimal marker position
    CorM(b,m)=max(Cortemp); % multicorrelation coeff.
end
end

% save all matrices

% intensity matrix (the optimum marker position is when the
% marker is in focus, thus the intensity in small masked
% region should be maximal)
save ('I.mat','I');

% correlation matrix (the optimum marker position is when
% the correlation between the fixed template and the data
% image-reconstruction is maximal)
save ('Cor.mat','Cor');

```

```

% multi-correlation matrix (the optimum marker position is
% when the correlation between the moving +/-1 pixel in
% each direction template and the data image-reconstruction
% is maximal)
save ('CorM.mat','CorM');

% multicorrelation and correlation approaches (last two)
% give almost the same results as far as the tests
% performed show

```

```

% Part 6
% Surface reconstruction and plotting the results

```

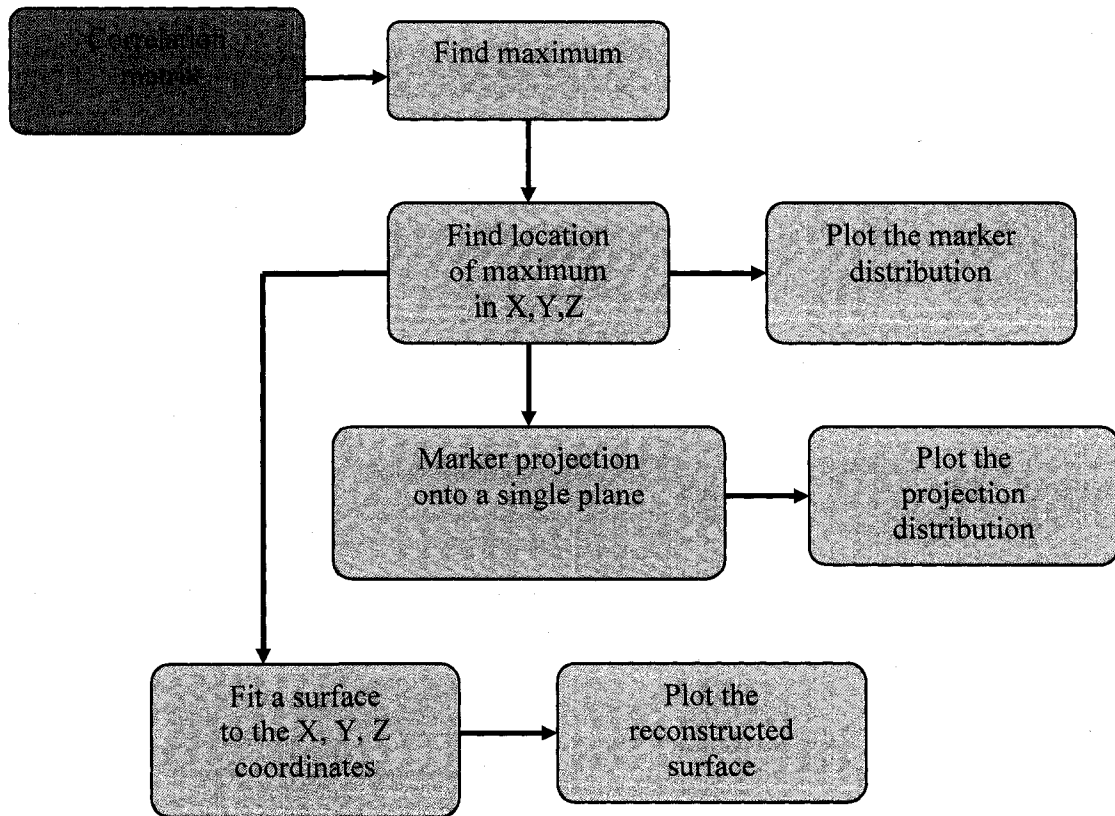


Figure 10.3.5. Detailed flowchart of the 3D holographic imaging algorithm (part 3)

```

clc; clear all;

% load previously saved data files
load I.mat;

```

```

load Cor.mat;
load CorM.mat;
load xd.mat;
load yd.mat;
load rec_cond.mat;
load HD.mat;
load Rec.mat;
load LPF.mat;
load Mask.mat;
um=1E-6;

% intensity method

% finding the maximum values in:
% intensity matrix I
% C: max values, Ind: indices of max values
[C,Ind] = max(I, [], 1); C=C-min(C);
C=C/max(C);

% simple correlation method
% C: max values, Ind: indices of max values
[C2,Ind2] = max(Cor, [], 1); C2=C2-min(C2);
C2=C2/max(C2);

% multicorrelation method
% C: max values, Ind: indices of max values
[C3,Ind3] = max(CorM, [], 1); C3=C3-min(C3);
C3=C3/max(C3);

% preparing the marker position vectors X, Y, Z
Xdist=(-42*um/2+xd*42*um/1024);
Ydist=-(-42*um/2+yd*42*um/1024);
Zdist=start+Ind*(stop-start)/dx; %um
Zdist2=start+Ind2*(stop-start)/dx;
Zdist3=start+Ind3*(stop-start)/dx;
Xtemp=(-42*um/2+(1:1024)*42*um/1024);
Ytemp=-(-42*um/2+(1:1024)*42*um/1024);

% plotting the hologram
figure(234)
subplot(2,2,1), imagesc(Xtemp/um,Ytemp/um,HD), axis
square,colormap gray,
title(['Processed hologram'])
xlabel('x (\mum)')
ylabel('y (\mum)')

```

```

% plotting the reconstructed image with
% background removed
subplot(2,2,2), imagesc(Xtemp/um,Ytemp/um,Rec-LPF),axis
square,colormap gray,
title(['Reconstructed image'])
xlabel('x (\mum)')
ylabel('y (\mum)')

% plotting the marker distribution in 2-D space
% color indicates the height, or the optimum reconstruction
% distance
subplot(2,2,3),
scatter(Xdist/um,Ydist/um,10,C,'filled'),axis
square,colormap gray,
title(['2D map of the distribution of the spheres in
intensity'])
xlabel('x (\mum)')
ylabel('y (\mum)')

% plotting the mask applied in intensity method
subplot(2,2,4), imagesc(Mask),axis square,colormap gray,
title(['Applied mask to the hologram'])
xlabel('x (\mum)')
ylabel('y (\mum)')

% comparison between the intensity and correlation method
colormap jet
figure(678) % second quad plot
subplot (2,2,1)
scatter(Xdist/um,Ydist/um,40,Zdist,'filled')
title(['2D map of the distribution of the spheres (int.
method)'])
xlabel('x (\mum)')
ylabel('y (\mum)')

subplot (2,2,2)
scatter(Xdist/um,Ydist/um,40,Zdist2,'filled')
title(['2D map of the distribution of the spheres (corr.
method)'])
xlabel('x (\mum)')
ylabel('y (\mum)')

subplot (2,2,3)
scatter(xd,yd,40,Zdist,'filled')
title(['2D map of the distribution (int. method)'])

```

```

xlabel('x points')
ylabel('y points')

subplot (2,2,4)
scatter(xd,yd,40,Zdist2,'filled')
title(['2D map of the distribution (corr. method)'])
xlabel('x points')
ylabel('y points')

Zdist=Zdist*um;
Zdist2=Zdist2*um;
Zdist3=Zdist3*um;

% 3D comparison plot between the intensity and the
% correlation method
figure(679) % second quad plot
subplot (2,2,1)
scatter3(Xdist/um,Ydist/um,Zdist/um,60,Zdist/um,'filled')
title(['3D map of the distribution (int. method)'])
xlabel('x (\mum)')
ylabel('y (\mum)')
zlabel('z (\mum)')
colorbar
axis([min(Xdist)/um max(Xdist)/um min(Ydist)/um
max(Ydist)/um min(Zdist)/um max(Zdist)/um])

subplot (2,2,2)
scatter3(Xdist/um,Ydist/um,Zdist2/um,60,Zdist2/um,'filled')
title(['3D map of the distribution (corr. method)'])
xlabel('x (\mum)')
ylabel('y (\mum)')
zlabel('z (\mum)')
colorbar
axis([min(Xdist)/um max(Xdist)/um min(Ydist)/um
max(Ydist)/um min(Zdist)/um max(Zdist)/um])

% curve fitting to the intensity data
ord=1;
p = polyfit(Xdist,Zdist,ord);
Xpol=(-20:1:20)*um;
f = polyval(p,Xpol);

% plotting the fitted data
%figure(34)
subplot (2,2,3)
plot(Xdist/um, Zdist/um, '*')

```

```

hold on
plot(Xpol/um, f/um, 'm')

xlabel('x (\mum)')
ylabel('f(estimateds,xdata)')
title('Fitting to data (intensity data)');
legend('data', ['fit using ',int2str(ord),' order
polynomial'],'Location','SouthEast')
axis([min(Xdist/um) max(Xdist/um) 140 185])
hold off

% curve fitting to the correlation data

ord=1;
p2 = polyfit(Xdist,Zdist2,ord);
Xpol=(-20:1:20)*um;
f2 = polyval(p2,Xpol);

% plotting the fitted data
%figure(35)
subplot (2,2,4)
plot(Xdist/um, Zdist2/um, '*')
hold on
plot(Xpol/um, f2/um, 'm')

xlabel('x (\mum)')
ylabel('f(estimateds,xdata)')
title('Fitting to data (correlation data) ');
legend('data', ['fit using ',int2str(ord),' order
polynomial'],'Location','SouthEast')
axis([min(Xdist/um) max(Xdist/um) 140 185])
hold off

% multicorrelation method results, plotting 2-D and 3-D map
% distribution of the markers, and surface fitting to the
% scattered data
figure(680)
subplot (2,2,1)
scatter(Xdist/um,Ydist/um,40,Zdist3,'filled')
scatter(xd,yd,40,Zdist3,'filled')
title(['2D map of the distribution of the spheres
(multicorr. method)'])
xlabel('x (\mum)')
ylabel('y (\mum)')

subplot (2,2,2)
scatter3(Xdist/um,Ydist/um,Zdist3/um,60,Zdist3/um,'filled')

```

```

title(['3D map of the distribution (multicorr. method)'])
xlabel('x (\mum)')
ylabel('y (\mum)')
zlabel('z (\mum)')
colorbar
axis([min(Xdist)/um max(Xdist)/um min(Ydist)/um
max(Ydist)/um min(Zdist3)/um max(Zdist3)/um])

subplot(2,2,3)
% curve fitting to the correlation data
ord=1;
p3 = polyfit(Xdist,Zdist3,ord);
Xpol=(-20:1:20)*um;
f3 = polyval(p3,Xpol);
plot(Xdist/um, Zdist3/um, '*')
hold on
plot(Xpol/um, f3/um, 'm')

xlabel('x (\mum)')
ylabel('z (\mum)')
title('Fitting to data (multicorrelation data) ');
legend('data', ['fit using ',int2str(ord),' order
polynomial'],'Location','SouthEast')
axis([min(Xdist/um) max(Xdist/um) 140 190])
hold off

for ss=1:length(xd)
    dify1(ss)=(Zdist(ss)-polyval(p,-
21*um+xd(ss)*42*um/1024));
    dify2(ss)=(Zdist2(ss)-polyval(p2,-
21*um+xd(ss)*42*um/1024));
    dify3(ss)=(Zdist3(ss)-polyval(p3,-
21*um+xd(ss)*42*um/1024));
end
s1 = std(dify1)/um;
s2 = std(dify2)/um;
s3 = std(dify3)/um;
sprintf(['Std. dev: int. m.=',num2str(s1),' um',',', corr.
m.=',num2str(s2),' um',',', multi corr. m.=',num2str(s3),'
um'])

% surface fitting
subplot(2,2,4)
[x y] = meshgrid(linspace(min(Xdist),max(Xdist),128),
linspace(min(Ydist),max(Ydist),128));
z = griddata(Xdist, Ydist, Zdist3, x, y, 'cubic');
mesh(x/um,y/um,z/um)

```

```

xlabel('x (\mum)')
ylabel('y (\mum)')
zlabel('zp (\mum)')
title(['Surface fitted into the data'])

% saving whole workspace
save wkspc_name;

```

10.3.4 Carbon nano-tubes holography, resolution and feature size estimation based on Gaussian filtering and correlation code

```

% Part 1
% Loading the image to *.bmp from *.csv
% units
clear all; clc;
um=1e-6;
nm=1e-9;
mm=1e-3;

file_num=1;
switch file_num
    case 1

        file_name='hologram.csv';
        HD=csvread(file_name);
        zm=2.1; % distance from source to object

        % take the hologram size
        S=size(HD);
        Nx=S(2);
        Ny=S(1);

        % calculate AFM pixel size
        Dx=42*um/1024;
        Dy=Dx;
    otherwise
        file_name='error.asc';
end

% illumination wavelength
lambda=47*nm;

imwrite(HD,'hologram.bmp')

```

```

% plotting the hologram to check
figure(2), imagesc(HD)
title(['Hologram removed spots: ',file_name,])
axis square
colormap gray
pause(2)
close Figure 2

% Part 2
% Hologram filtering (optional)

% units
clear all; clc;
um=1e-6;
nm=1e-9;
mm=1e-3;

% illumination wavelength
lambda=47*nm;

% artifacts can be removed manually from hologram.bmp
% making hologram_ret.bmp
HD = imread('hologram_ret.bmp');
HD = im2double(HD);

% plotting the unfiltered hologram
figure(1), imagesc(HD)
title(['Hologram unfiltered: '])
axis square
colormap gray
pause(2)
close Figure 1

% image filtering in spatial frequency domain
FFTm=fft2(HD);
FFTsh=fftshift(FFTm);
figure(3)
imagesc(log(abs(FFTsh)))
title('FFT')
axis square
colormap gray

[x,y] = ginput;
close Figure 3
x=floor(x);
y=floor(y);

```

```

rad=30; % setting how much to filter
for m=1:length(x)
    FFTsh(y(m)-rad/2:y(m)+rad/2,x(m)-rad/2:x(m)+rad/2)=0;
end

% plotting the removed components
figure(4)
imagesc(log(abs(FFTsh)))
title('FFT - removed components')
axis square
colormap gray

% retransforming back to the spatial domain
HDfilt=abs(iff2(FFTsh));
figure(5), imagesc(HDfilt)
title(['Hologram filtered: '])
axis square
colormap gray
%close Figure 4

% saving filtered hologram
name=['hologram_filt.bmp'];
imwrite(HDfilt,name)

% Part 3
% Hologram reconstruction
% units
clear all; clc;
um=1e-6;
nm=1e-9;
mm=1e-3;

% distance from source to object
zm=0.75;
% illumination wavelength
lambda=47*nm;

% load filtered hologram
HD = imread('hologram_filt.bmp');
HD = rgb2gray(HD);
HD = im2double(HD);

% computing size of the hologram and the AFM pixel size
S=size(HD);
Nx=S(2);

```

```

Ny=S(1);
Dx=10*um/1024;
Dy=Dx;

% to put a lum marker in the image
% mark=ceil(1*um/Dx);
% HD(1024-54:1024-50,100:100+mark)=max(max(HD));

% plotting the hologram
xx=(1:1024)*Dx/um;
figure(2), imagesc(xx,xx,HD)
title(['Hologram:'])
xlabel('Distance [\um]'); ylabel('Distance [\um]');
axis square
colormap gray
pause(2)

% saving the hologram as a *.mat file
save ('HD.mat','HD');

% setting the reconstruction parameters
%number of reconstructions
dx=20;

% reconstruction distance range in [um]
start=2.5;
stop=3.0;

% save reconstruction parameters
save ('rec_cond.mat', 'start', 'stop', 'dx');

% ***** Precalculations: *****

% Create the x,y grid;
x=([1:Nx]-Nx/2)*Dx;
y=([1:Ny]-Ny/2)*Dy;
[X,Y]=meshgrid(x,y);
R=sqrt(X.^2+Y.^2);

% calculate spatial frequencies
dfx=1/Nx/Dx;
fx=([1:Nx]-Nx/2)*dfx;
fxs=fftshift(fx);

dfy=1/Ny/Dx;

```

```

fy=([1:Ny]-Ny/2)*dfy;
fys=fftshift(fy);

[fX,fY]=meshgrid(fx,fy);
fR=sqrt(fX.^2+fY.^2);
fRs=fftshift(fR);

% Magic Distance
zmagic=Dx^2*Nx/lambda;

% use the hologram variable HD
HDp=HD/max(max(HD));

% Main LOOP begins
for b=1:dx;
    dist=start+b*(stop-start)/dx;
    sprintf('Distance= %f um',dist);

    % propagation distance from the mask to the recording
    % plane
    zp=(dist)*um;
    % reconstruction location
    zo=zm+zp;

    % focal length of the hologram
    f=1/(1/zp-1/zo);

    % geometrical magnification factor
    Mc=1/(1-zp/zo);

    % reconstruct the hologram (with a plane wave)
    if f>zmagic
        Hf=fft2(exp(-i*pi*R.^2/lambda/(-f)));
        uf=ifft2(fft2(HD).*Hf);
        uf=fftshift(uf);
    else
        Hf=exp(i*pi*lambda*(-f)*fRs.^2);
        uf=ifft2(fft2(HD).*Hf);
    end

    % rescaling by the geometrical magnification
    x=x/Mc;
    y=y/Mc;

    % generating the reconstructed image
    Rec=uf.*conj(uf);
    Rec=Rec/max(max(Rec));

```

```

        % save the reconstructions for different zp distances
        name1=strcat('Rec',num2str(zp/um),'.jpg');
        imwrite(Rec,name1);
end

% save as *.mat file
save ('Rec.mat','Rec');

% Part 4
% choosing the small portion of the whole reconstructed
% image for further processing
% units
clear all; clc;
um=1e-6;
nm=1e-9;
mm=1e-3;

% choosing „in focus“ reconstructed image
filename = 'hologram 3/Rec2.5167.jpg';
Rec=imread (filename);

% plot this reconstruction
subplot(2,2,3),
imagesc(Rec)
title(['Reconstruction:'])
xlabel('Pixels'); ylabel('Pixels');
axis square
colormap gray

% choose using mouse the small section of the hologram
[x,y] = ginput(1); x=floor(x); y=floor(y);
siz=101;
smRec=Rec(y-siz:y+siz-1,x-siz:x+siz-1);
smRec=double(smRec);

% plot the small image
subplot(2,2,4),
imagesc(smRec)
title(['Small Reconstruction:'])
xlabel('Pixels'); ylabel('Pixels');
axis square
colormap gray

% save it as a *.mat file
save ('small_recoH3_S5.mat','smRec');

```

```

% Part 5
% Resolution and feature size estimation using Gaussian
% filter algorithm with correlation technique

clear all; clc;

% load the *mat file containing small piece of
% reconstructed image
load small_reco_H3_S5.mat;

% choose threshold
th=0.3; qq=3;

% units
um=1E-6; nm=1E-9;

% AFM pixel size ~10um scan/1024 pixels/line
pix=9.7*nm;

% extrapolation factor to improve the filter sampling at
% low filter widths and extrapolated pixel width
r=3; pix=pix/r;

M=smRec;

% Filtering background (optional, same scheme as before)
F=fftshift(fft2(M));
X=103;Y=102;si=1;
F(Y-si:Y+si,X-si:X+si)=0;
imagesc(log10(abs(F)));axis square;
F=ifftshift(F);
M=abs(ifft2(F));

% normalizing
W=M;
W=W(2:size(M,1)-1,2:size(M,2)-1);
W=W-min(min(W));
W=W/max(max(W));
M=M-min(min(M));
M=M/max(max(M));

% Thresholding necessary for skeletonizing algorithm

for a=1:size(M,1)
    for b=1:size(M,2)
        if M(a,b)<th
            M(a,b)=0;
        end
    end
end

```

```

        end
    end
end

% Filtering "salt&pepper", optional, apply if necessary
Mf=M;
M=medfilt2(M,[4 4]);
% use small domain to not affect the image resolution

% Skeletonizing algorithm (reference in text)
s=0;
for a=3:size(M,1)-2
    for b=3:size(M,2)-2
        s=0;
        % X direction
        if (M(a,b)+M(a+1,b)+M(a-1,b))>(M(a-1,b-2)+M(a,b-2)+M(a+1,b-2))&...
            (M(a,b)+M(a+1,b)+M(a-1,b))>(M(a-1,b+2)+M(a,b+2)+M(a+1,b+2))
            s=s+1;
        end
        % Y direction
        if (M(a,b)+M(a,b-1)+M(a,b+1))>(M(a-2,b-1)+M(a-2,b)+M(a-2,b+1))&...
            (M(a,b)+M(a,b-1)+M(a,b+1))>(M(a+2,b-1)+M(a+2,b)+M(a+2,b+1))
            s=s+1;
        end
        % XY direction
        if (M(a,b)+M(a+1,b-1)+M(a-1,b+1))>(M(a-2,b-2)+M(a-1,b-2)+M(a-2,b-1))&...
            (M(a,b)+M(a+1,b-1)+M(a-1,b+1))>(M(a+2,b+2)+M(a+1,b+2)+M(a+2,b+1))
            s=s+1;
        end
        % -XY direction
        if (M(a,b)+M(a-1,b-1)+M(a+1,b+1))>(M(a-2,b+2)+M(a-2,b+1)+M(a-1,b+2))&...
            (M(a,b)+M(a-1,b-1)+M(a+1,b+1))>(M(a+2,b-2)+M(a+2,b-1)+M(a+1,b-2))
            s=s+1;
        end
    end

    if s==2 % can be 1, 2 or 3, one has to plot to see
        % if skeleton looks as it should
        % originally (Yatagai paper) s==2.
    end
end

```

```

        S(a,b)=1;
    else
        S(a,b)=0;
    end
end
end
end

figure(1)
% plot the reconstructed image
subplot(2,2,1), imagesc(W), title('Reconstruction'), axis
square, colormap gray;
xlabel('Pixels'); ylabel('Pixels');

% plot the thresholded image
subplot(2,2,2), imagesc(M), title('Reconstruction with
threshold'), axis square;
xlabel('Pixels'); ylabel('Pixels');

% plot the skeleton of the reconstructed image
subplot(2,2,3), imagesc(S), title('Skeleton'), axis square;
xlabel('Pixels'); ylabel('Pixels');

%*****
% defining the radius of the circles used to convolve with
% the skeleton
R=[1,2,2.55,3,3.55,4,4.55,5,5.55,6];
% 2.55 was chosen instead of 2.5 because for R=2 and R=2.5
% the both circles are the same (sampling issues)

% calculating the circles diameter
Dx=2*R*pix*r;

% sweeping all the radii
for rr=1:length(R)
% Convolution operation

% Template of the circle
siz=21; % size of the template in pixels has to be odd
% radius in pixels defined above
for a=1:siz+1
    x=-siz/2+a-1;
    for b=1:siz+1
        y=-siz/2+b-1;
        if (sqrt(x^2+y^2)<R(rr))

```

```

        Sph(a,b)=1;
    else
        Sph(a,b)=0;
    end
end
end

% part of the code excluded here used to plot all the
% circles in single plot (for diagnostics)
%{
% Circles
RR=[1,2,2.55,3,3.55,4,4.55,5,5.55,6];
%RR=[1,2,2.5,3,3.5,4,4.5,5,5.5,6];
for we=1:length(RR)
    siz=15; % size of the template in pixels has to be odd
% radius in pixels defined above
figure(45)
for a=1:siz+1
    x=-siz/2+a-1;
    for b=1:siz+1
        y=-siz/2+b-1;
        if (sqrt(x^2+y^2)<RR(we))
            Sphe(a,b,we)=1;
        else
            Sphe(a,b,we)=0;
        end
    end
end
end
subplot(3,4,we), imagesc(Sphe(:,:,we)); axis square, colormap
gray, hold on,
end
hold off
%}

% Image extrapolation
% nearest neighborhood extrapolation

% of the skeleton
Sex=imresize(S,r);

% of the marker
Sphe=imresize(Sph,r);

% of the data image - reconstructed image
Wex=imresize(W,r);

% convolution operation, skeleton thickening

```

```

Scon=conv2 (Sex, Spdex);

% resizing (convolution makes m+n+1 size larger in
% each direction
Scont=Scon(ceil(size(Spdex,1)/2):size(Scon,1)-
ceil(size(Spdex,1)/2),ceil(size(Spdex,2)/2):size(Scon,2)-
ceil(size(Spdex,2)/2));

% normalizing to max=1
for a=1:size(Scont,1)
    for b=1:size(Scont,2)
        if Scont(a,b)>1
            Scont(a,b)=1;
        end
    end
end

% plot the convolution result (code check)
figure(67), subplot (2,2,1), imagesc(Scont), axis square, colormap
gray,
xlabel('Pixels'); ylabel('Pixels');

    B=Scont;
    B=B/sum(sum(B));

xx=-size(B,1)/2+1:size(B,1)/2;
[XX,YY] = meshgrid(xx*r,xx*r);
RR=sqrt(XX.^2+YY.^2);

%*****
% setting the resolution limits
res=(12:5:100)*nm; % resolution
w0=1;

% Generate the filter widths (equation derived in
% Appendix II)
for c=1:length(res)
    wG(c)=sqrt((res(c)/(pix))^2-1)*(w0*r);
end
figure(234), imagesc(Wex);

% code check
%B=zeros(512); B(256,256)=1;
Fimg=fft2(B); % FFT of the object image

```

```

for c=1:length(res)
    % compute the filter
    % creating the Gaussian filter
    F=exp(-4*log(2)*RR.^2/wG(c)^2);

    % convolve in spectral domain (orders)
    % to reduce the resolution
    T=ifftshift(ifft2(fft2(F).*Fimg));
    % correct for ifft
    T = circshift(T,[1 1]);
    % plot the result (code check)
    %figure(235),hold on,subplot(2,3,c),imagesc(T),
    colormap gray, axis square, title(sprintf('%3.2f
nm',res(c)/nm)),hold off,pause(0.1);
    %figure(235),imagesc(T), title(sprintf('%3.2f
nm',res(c)/nm)),pause(0.1);

    % 2-D correlation between the lower resolution
    % template and the extrapolated data image
    rc(c,rr)= corr2(T, Wex);
    disp(sprintf(' resolution= %3.2f nm',res(c)/nm));
end

% finding the maximum in the correlation coefficients
[row,col] = find(rc==max(rc(:,rr)));
res_val=res(row);

%{
% plot the results
figure(3)
subplot(2,2,1), imagesc(W), axis square,
title('reconstructed image'), colormap gray;
subplot(2,2,2), imagesc(temp), axis square,
title('template image'), colormap gray;
subplot(2,2,3), plot(res/nm,rc,'b-
*');% ,resx,y2,'g',res_val,(500:800)/1000,'k-'),
%axis([28 63 0.78 0.82]);
xlabel('resolution [nm]'); ylabel('corr coeff');
title('correlation curve');
title(sprintf('Shift V1= %d, V2= %d, k= %d',V1(k),
V2(k),k));
%legend('data points','fitted curve','Location','South!');
%text(res_val,max(max(y2)),sprintf(' <==== res= %d nm',
res_val),...
% 'HorizontalAlignment','left')

```

```

subplot(2,2,4), plot(res/nm,rc,'g-
*');% ,resx,y2,'c','Linewidth',2,'MarkerSize',8);% ,resx,y2,'
g',res_val,(500:800)/1000,'k-'),
axis([15 110 max(max(rc))-0.035 max(max(rc))+0.007]);
xlabel('resolution [nm]'); ylabel('corr coeff');
title('correlation curve');
title(sprintf('Shift V1= %d, V2= %d, k= %d',V1(k),
V2(k),k));
%text(res_val+10,max(max(y2)),sprintf(' <===== res= %d
nm', res_val),...
% 'HorizontalAlignment','left')
%legend('data points','fitted curve','Location','South');
%}

end

% displaying the intermediate results for diagnostic
% purposes
disp(sprintf('max value of corr coeff=%f, and resolution =
%3.2f nm, Tube Dia=%3.2f nm at th=%3.2f, r=%d, f=%d
pix',...
max(rc(:,rr)),res_val/nm, Dx(rr)/nm, th, r, si))

% save data for further use
save ('rc1.mat','rc');
save ('R1.mat','R');
save ('pix1.mat','pix');
save ('res1.mat','res');
save ('int1.mat','r');

% plot the resolution/feature size map (code check)
figure(7)
imagesc(1:length(R),res/nm,rc), title('2D reconstruction
space'),
xlabel('Feature size [nm]'),ylabel('Resolution [nm]');

% Part 6
% Plotting the results, surface reconstruction

clear all; clc;

% loading previously saved data files
load rc1.mat
load res1.mat
load R1.mat

```

```

load pix1.mat
load int1.mat

um=1E-6; nm=1E-9;
res=res/nm;

Dx=2*R*pix*r/nm;
ord=res/(pix*r/nm);
rd=rc';

% plotting the results
figure(5)

% plotting 2D reconstruction space
subplot(2,2,1),
imagesc(rd), title('2D reconstruction space'),
xlabel('resol (index)')
ylabel('rc (index)')
axis square

% surface reconstruction
subplot(2,2,2),
[x y] = meshgrid(linspace(min(ord),max(ord),128),
linspace(min(R),max(R),128));
z = griddata(ord, R, rd, x, y, 'cubic');
imagesc(x(1,:)*(pix*r/nm),y(:,1)*2*pix*r/nm,z)
xlabel('resolution [nm]')
ylabel('tube diameter [nm]')
title(['Surface fitted into the data'])
axis square
axis([x(1,1)*(pix*r/nm) max(res) y(1,1)*2*pix*r/nm 110]);

% plotting fitted surface in 3D
subplot(2,2,3),
for a=1:length(res)
    for b=1:length(Dx)

scatter3(Dx(b),res(a),rc(a,b),50,rc(a,b),'filled'),hold on,
        end
    end
hold off,
xlabel('tube diameter [nm]'), ylabel('resolution [nm]');
title('3D plot'),

% plotting fitted surface in 3D as a mesh

```

```

subplot(2,2,4),
mesh(x(1,:)*(pix*r/nm),y(:,1)*2*pix*r/nm,z)
xlabel('resolution [nm]')
ylabel('tube diameter [nm]')
title(['Surface fitted into the data'])

```

Similar code was used in analysis of the EUV microscope images. All the steps performed were exactly the same with only small details that were different (threshold values, skeleton threshold, processed image size, filtering etc. might be adjusted for different processed images.

10.4 Appendix IV: Transmission diffraction grating analysis of the diffraction efficiency

The grating diffraction efficiency was calculated based on the diffraction theory. To calculate the diffraction efficiency of the grating the analysis from M. Born and E. Wolf [10.5] was adopted. The interference function is equal to:

$$H(p) = \left[\frac{\sin(Nkdp/2)}{N \sin(kdp/2)} \right]^2 \quad (10.4.1)$$

where N is the number of interfering sources, in this case the number of grooves in the grating. Although in our grating $N \sim 300$ ($0.6\text{mm}/2\mu\text{m}$) to improve the visual appearance of this function, only $N = 20$ sources (grooves) will be assumed in the Figure 10.4.1. $k = 2\pi/\lambda$ is the wavevector, $d = 2\mu\text{m}$ is the grating period, and $p = n\lambda/d, n \in \langle 0, 10 \rangle$ is scaled argument used to plot this function. The results are depicted in Figure 10.4.1a. The normalized intensity function of the slit, assuming the slit to have rectangular profile, can be expressed as shown below:

$$S(p) = \left[\frac{\sin(ksp/2)}{ksp/2} \right]^2 \quad (10.4.2)$$

where s is a width of the slit (grating groove), in our case 50% duty cycle was simulated, thus it was assumed that $s = d/2$. This is typical $\text{sinc}^2(x)$ function plotted in Figure 10.4.1b. The normalized intensity function of a grating consisting of N similar, equally spaced and parallel slits is a product of these two previously mentioned functions:

$$I(p) = H(p) \cdot S(p) = \left[\frac{\sin(Nkdp/2)}{N \sin(kdp/2)} \right]^2 \left[\frac{\sin(ksp/2)}{ksp/2} \right]^2 \quad (10.4.3)$$

and is depicted in Figure 10.4.1c (red curve) with the normalized intensity function of the slit (pink) to show that this is a product.

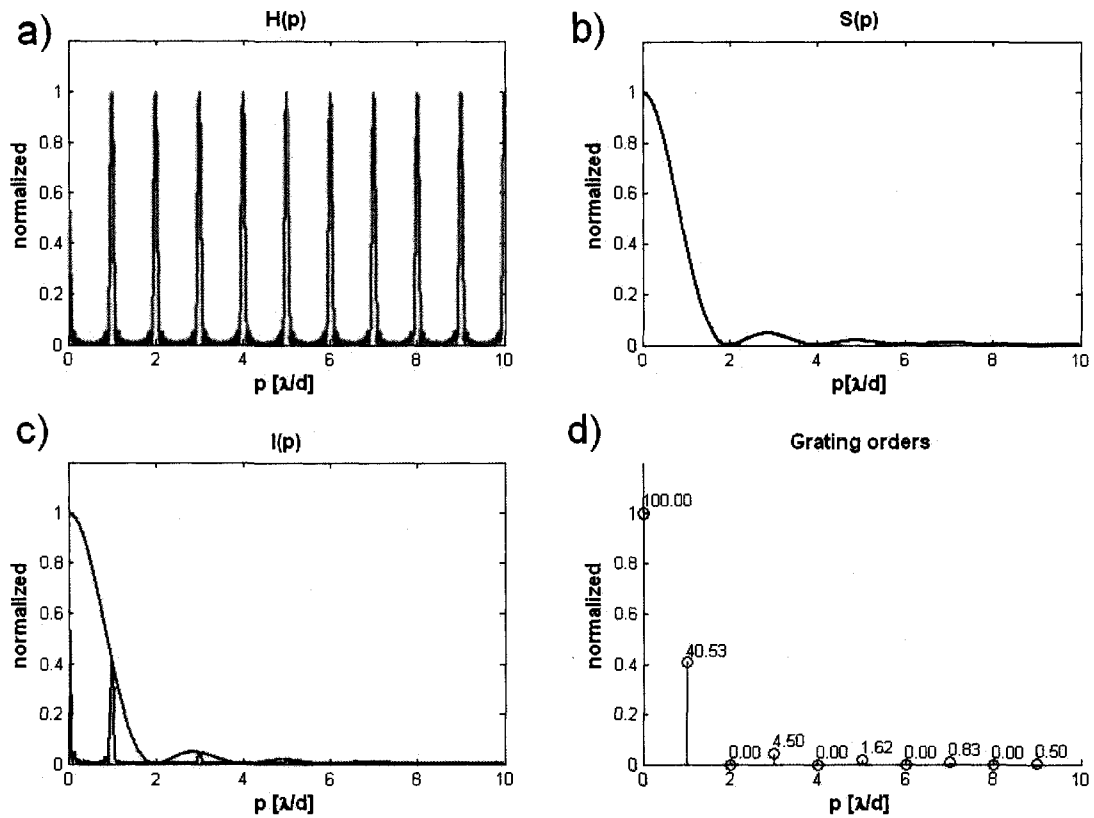


Figure 10.4.1. Transmission diffraction grating diffraction efficiency calculations. a) normalized interference function for $N=20$ sources, b) normalized intensity function of the slit, c) normalized intensity function of a grating consisting of N similar, equally spaced and parallel slits, d) relative intensities in each diffracted order normalized to the intensity in the 0^{th} order for duty cycle of 50% d .

For larger number of interfering sources N the interference function $H(p)$ will look more similar to the $\text{comb}(x)$, Figure 10.4.2a, composed of many shifted delta functions. Figure 10.4.1d show relative intensities in each diffracted order from such a grating normalized to the intensity in the 0^{th} order. Because of 50% duty cycle even diffraction orders vanish, only odd ones remain and there is $\sim 40.5\%$ intensity of the 0^{th} order in each plus and minus 1^{st} order. Practically our grating has groove width of 980nm and period 2020nm. This will give 48.5% duty cycle and almost 43% intensity of the 0^{th} order in each plus and minus 1^{st} order, as can be seen in Figure 10.4.2b.

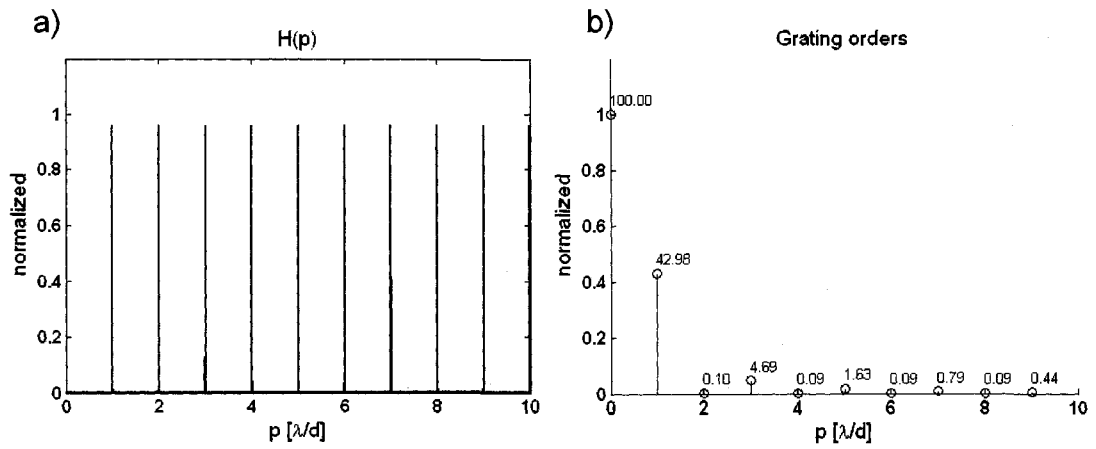


Figure 10.4.2. a) Normalized interference function for $N=300$ sources (grooves), b) relative intensities in each diffracted order normalized to the intensity in the 0th order for duty cycle of 48.5%.

[10.1] J. D. Jackson, *Classical Electrodynamics*, 3rd edition, (John Willey & Sons, Inc., chapter 7, pp. 302)

[10.2] B.L. Henke, E.M. Gullikson, J.C. Davis, "X-ray interactions: photoabsorption, scattering, transmission, and reflection at E=50-30000 eV, Z=1-92", *Atomic Data and Nuclear Data Tables* **54**, 181 (1993)

[10.3] D. Attwood, *Soft X-rays and Extreme Ultraviolet Radiation: Principles and Applications*, (Cambridge Univ. Press, 1999)

[10.4] <http://www-cxro.lbl.gov/> as in November 2007

[10.5] M. Born, E. Wolf, *Principles of Optics*, 7th expanded edition, (Cambridge University Press, 1999, pp. 451)